KU LEUVEN

ARENBERG DOCTORAL SCHOOL
Faculty of Engineering Technology

Outdoor thermal and electrical characterisation of photovoltaic modules and systems

Bert Herteleer

Supervisor:
Prof. dr. ir. J. Cappelle
Prof. dr. ir. J. Driesen, co-supervisor
Prof. dr. ir. F. Catthoor, co-supervisor

Dissertation presented in partial fulfillment of the requirements for the degree of Doctor in Engineering Technology

February 2016

Outdoor thermal and electrical characterisation of photovoltaic modules and systems

Bert HERTELEER

Examination committee:
Prof. dr. ir. W. Dewulf, chair
Prof. dr. ir. J. Cappelle, supervisor
Prof. dr. ir. J. Driesen, co-supervisor
Prof. dr. ir. F. Catthoor, co-supervisor
Prof. dr. P. Hanselaer
ing. S. Dewallef (Soltech NV)
Prof. dr. ir. J. Poortmans
Prof. dr. Wilfried G.J.H.M. van Sark
(Utrecht University)

Dissertation presented in partial fulfillment of the requirements for the degree of Doctor in Engineering Technology

February 2016

© 2016 KU Leuven – Faculty of Engineering Technology
Uitgegeven in eigen beheer, Bert Herteleer, Gebroeders De Smetstraat 1, B-9000 Gent (Belgium)

Alle rechten voorbehouden. Niets uit deze uitgave mag worden vermenigvuldigd en/of openbaar gemaakt worden door middel van druk, fotokopie, microfilm, elektronisch of op welke andere wijze ook zonder voorafgaande schriftelijke toestemming van de uitgever.

All rights reserved. No part of the publication may be reproduced in any form by print, photoprint, microfilm, electronic or any other means without written permission from the publisher.

Abstract

Current and future investors in photovoltaic systems are interested in how well the system performs, and how predictable this is over the expected lifetime. To do so, models have been developed and measurements of photovoltaic systems have been done.

This dissertation presents the outdoor measurement set-up that has been developed for thermal and electrical characterisation of photovoltaic modules and systems, aimed at measuring transient effects and changes. The main design decisions and implementations are discussed, including the ability to measure in-situ current-voltage (I-V) curves of photovoltaic modules connected to inverters and DC-DC converters, in an automated manner, without the need for physical removal from the array.

The main factors that influence photovoltaic system performance, such as irradiance, ambient temperature, wind speed and direction and module temperatures are measured and logged per second. Together with the power and energy yield measurement of a large number of photovoltaic modules and inverters at a similar rate, high resolution data is obtained on the performance of these modules and inverters. The DC values of the modules and inverters are obtained by custom-built, low-cost, galvanically isolated signal conditioning boards.

For temperature measurements, methods are adapted or introduced for steady state and transient conditions. Methods to verify, and where necessary, correct measurements are shown, which result in lowered measurement uncertainties. The intra-module and inter-module temperature behaviour of the studied modules is discussed, with results showing a dependence on the irradiance conditions, as well as the wind speed and direction. The framework of the projected wind vector is introduced and applied to the thermal analysis of the modules studied.

The electrical performance of the photovoltaic modules and systems is discussed in detail, with the introduction of a variety of tools and methods. Chief among these is the normalised efficiency η_N, which is the power equivalent of the industry-standard energy production evaluation metric, the Performance Ratio (PR). The normalised efficiency η_N can be used for system inter-comparisons, real-time monitoring, anomaly detection (such as shading), and to obtain the system temperature coefficient of power γ_{syst}.

The principle of temperature correction on power and energy values using measured temperatures is introduced, which is a powerful method which allows systems to be analysed, as if they had performed at the reference temperature. As a result, influencing factors which may be masked by the temperature can come to the fore - for example, the temperature-corrected Performance Ratio (PR^*) shows a much more stable response in time than the regular PR, whereby performance effects can be largely decoupled from temperature variations over the period studied.

A new method is introduced to obtain the coefficients for the power rating model for crystalline silicon modules from Huld *et al*, which allows the normalised efficiency η_N and normalised power P_N to more easily be modelled. The approach is expanded in application from modules to systems. The method of this dissertation is shown to be easier to implement, with less stringent measurement requirements, e.g. no need for I-V curve measurement data. The number of model coefficients that must be determined is also lowered from six to three, with no negative impact on the model results - in fact, the modified model generally outperforms the original model of Huld *et al*. The results of this work give better system-specific results as seen in the validation testing, from the normalised efficiency to power, energy and Performance Ratio. With the validated approach, the energetic impact of partial shading is quantified for the modules and systems studied.

Beknopte samenvatting

Huidige en toekomstige investeerders in fotovoltaïsche (PV) systemen zijn geïnteresseerd in hoe goed een systeem werkt, en hoe voorspelbaar dit zal zijn over de verwachtte levensduur. Hiervoor zijn modellen ontwikkeld, en zijn metingen op fotovoltaïsche systemen uitgevoerd.

Deze thesis stelt de outdoor meetopstelling voor die ontwikkeld is geweest voor de thermische en elektrische karakterisatie van fotovoltaïsche panelen en systemen, gericht op snelle transiënte variaties te kunnen meten. De belangrijkste keuzes bij het ontwerp worden besproken, waaronder de mogelijkheid om stroom-spanning (I-V) curves van fotovoltaïsche panelen te meten, die aangesloten zijn op omvormers en DC-DC convertoren, op automatische wijze, zonder de nood om de panelen fysiek te ontkoppelen en te verplaatsen van de meetopstelling.

De belangrijkste factoren die de prestatie van fotovoltaïsche systemen beïnvloeden worden gemeten en opgeslagen per seconde, waaronder de instraling, de omgevingstemperatuur, de windsnelheid en windrichting, alsook paneel temperaturen. Samen met de meting per seconde van vermogen en energieopbrengst van een groot aantal fotovoltaïsche panelen en omvormers, worden hoge resolutie gegevens bekomen over de prestatie van deze panelen en omvormers. De gelijkstroom waarden van de panelen en omvormers worden verkregen met behulp van lage-kost signaalconditioneringsborden die een galvanische scheiding bekomen tussen de vermogen- en meetzijde van de opstelling.

Aanpassingen aan methoden uit de literatuur voor steady state en transiënte temperatuursmetingen op zonnepanelen worden toegepast, en nieuwe methoden worden aangebracht. Lagere meetonzekerheden worden bekomen aan de hand van methoden en algoritmen die de meetwaarden verifiëren en waar nodig corrigeren. De variatie van temperaturen binnen panelen en tussen panelen onderling wordt besproken, waarbij de resultaten wijzen op een verband met de geldende instralingscondities, alsook de windsnelheid en windrichting. Het

concept van de geprojecteerde wind vector wordt ingevoerd, en toegepast op de thermische analyse van de bestudeerde zonnepanelen.

De elektrisch prestatie en gedrag van de bestudeerde fotovoltaïsche zonnepanelen en systemen wordt in detail besproken, waarbij een aantal extra tools, concepten en methoden worden ingevoerd. De belangrijkste van deze is het genormaliseerd rendement η_N, dat het vermogen-equivalent is van het veelgebruikte kengetal in de PV industrie, de *Performance Ratio* (PR). Het genormaliseerd rendement η_N heeft een breed gamma aan toepassingen, waarbij het gebruikt kan worden voor vergelijking van systemen, real-time monitoring, detectie van anomalieën (zoals beschaduwing), en om de systeemtemperatuurscoëfficiënt γ_{syst} te bepalen.

Het principe van temperatuurscorrectie op vermogen en energiewaarden wordt ingevoerd, waarbij de resulterende waarden aangeven hoe het systeem zou hebben gewerkt, indien het aan de referentie temperatuur zou hebben gepresteerd, dat als concept erg sterk is voor de analyse van PV systemen. Hierdoor bestaat de mogelijkheid dat andere invloedsfactoren die anders verborgen zouden blijven door het temperatuursgedrag toch zichtbaar worden. Een voorbeeld hiervan is dat de temperatuur-gecorrigeerde PR (PR^*) een veel stabieler verloop in de tijd vertoont dan de gewone PR, waardoor de temperatuur-gerelateerde effecten ontkoppeld kunnen worden van de andere invloedsfactoren.

Een nieuwe methode wordt ingevoerd om de coëfficiënten voor het vermogen *rating* model van Huld *et al* voor kristallijn silicium panelen te bepalen, dat toelaat om het genormaliseerd rendement η_N en het genormaliseerd vermogen P_N gemakkelijker te modelleren. De aanpak wordt ook uitgebreid van panelen tot systemen. De methode van deze thesis is eenvoudiger om toe te passen, met minder strenge meeteisen - bijvoorbeeld het is niet langer verplicht om I-V curve data te gebruiken om de coëfficiënten te bepalen. Het aantal coëfficiënten dat bepaald moet worden wordt ook verlaagd van zes tot drie, met in het algemeen betere resultaten dan het oorspronkelijk model van Huld *et al.* De validatie gegevens van het model van deze thesis geven betere systeem-specifieke resultaten dan het oorspronkelijk model van Huld *et al*, voor het genormaliseerd rendement, het vermogen, de energie en de *Performance Ratio*. Als toepassing wordt het gevalideerd model gebruikt om de energetische verliezen ten gevolge van partiële beschaduwing te kwantificeren voor de bestudeerde panelen en omvormers.

Preface

The process of this PhD has been like creating and solving a continuously evolving puzzle, of which you only have a crudely drawn blueprint in your mind, and not a clearly defined picture on a box. In the journey to the personal culmination in the form of a PhD, it helps to have a group of people in your corner, who can cheer you on, give wisdom and at times share the burden of your work. Luckily, the guidance, support and patience of my supervisors, colleagues and family kept me going. The cliché of "blood, sweat and tears" also applied to building and designing the measurement set-up and later interpreting the results, although the proportions were (by volume) 50 % perspiration, 49 % coffee and a few drops of blood, tears and inspiration.

Few PhD students have the luxury of three supervisors: Jan Cappelle, Francky Catthoor and Johan Driesen took the time to listen to my ideas, and had the patience to see me go through iterations of learning. Jan: thank you for the gamble you took on me. I will do my best to follow your example on showing patience and understanding, and giving others the freedom to grow. Johan: thank you for giving clarity in times of confusion with a few choice words. Francky: thank you for the patience and enthusiasm that you have shown me throughout.

A practical PhD such as mine does not happen nor work in a vacuum. It helps if you have a great group of colleagues (friends) to lean on. I would like to thank my enthusiastic colleagues in Ghent for the great times and literally sharing the burden of the work: Bram, Thomas, Hendrik, Auguste, Rien, Maarten, Bart and Jan. We not only built the physical measurement set-up twice, we also dismantled and moved it together! Having to move 6 m long aluminium rails through vents to the roof barely wide enough to fit through is an image that will stay in my mind.

Now, giving credit where credit is due: The prototype set-up was programmed in LabVIEW with the help of Boris Morel, PhD, and two Master thesis students,

Gilles Bovijn and Stijn Deweer. The design of the Signal Conditioning Boards was done in close collaboration with a colleague, Bart Huyck, PhD, over various iterations. Significant help in manufacture and testing of the final SCB design and software development was obtained from master thesis student Ahmed Latif (Hochschule Karlsruhe), as well as a colleague, Hendrik Derre, MSc. The collaboration with the colleagues at *Smart PV* has also improved the quality of the set-up and pushed me to deliver my best. Hans, thank you for the open and scientifically critical collaborations, you help me aim higher. Jonathan, thank you for the help, including being an excellent point of contact for the students with whom we've interacted. Kris, thank you for the support, in all the forms that is has taken. Among the unsung heroes, a special thank you to Veerle Duchateau, Roland Reekmans, Peter Asselman and Jan Vermeir for going beyond the call of duty - you have made a big difference. For personal growth and contributions not mentioned here I also have to thank all the Master thesis students who were so intrepid as to take me as their supervisor.

I also wish to thank the members of the PhD supervisory committee, prof. Peter Hanselaer (both as a member, and from whom I've learned much as a Master student), Stefan Dewallef for an excellent no-nonsense approach which has kept me grounded. The members of the jury, prof. Jef Poortmans for your teaching and helpful comments on my work, prof. Wilfried van Sark for insightful and interested comments on my dissertation and prof. Wim Dewulf for his help in the final steps of the PhD.

Daniel Goleman has observed that expert musicians required approximately 10 000 hours of practice to reach mastery of their craft. Daniel Kahneman's description of thinking along two paths, fast and slow, also suggests that the PhD process is an opportunity to train the System 1 (fast thinking and rapid decisions) using System 2 (deliberate, concentrated focus) thinking. Without exaggeration, I have invested more than 10 000 hours in the process of this PhD, occasionally to compensate for external circumstances. The help and support of my family and friends in this mad dash to results and expertise has been invaluable, commendable and I will cherish this in my memory. I have thanked each of you in person, but it is worth repeating. My parents for instilling a desire for knowledge and unwavering support and belief and my brothers for cheering me on. Marianne, for the amazing unwavering support and love throughout, as well as ensuring that I wouldn't forget to eat or sleep. You have been my champion and safe haven. Pieterjan for the long talks and the insights, and hearing me drone on and on about the latest brilliant concept I just read. My friends with whom I've shared much over the past years, from long dinners to profound discussions.

The research of this PhD was funded by a PhD grant (111651) of the Agency for Innovation by Science and Technology (IWT). Additional funding was obtained

by collaboration with IWT-SBO project *Smart PV* (110025). Based on my experience, I can only thank the IWT for giving me the opportunity to focus on the work, and recommend that this form of funding be continued, and if possible, expanded. The peace of mind that comes from guaranteed funding allows creativity to surface, essential in this rapidly changing world.

Lastly, I would like to encourage everyone who reads this to also take the time to consult the work of Mihaly Csikszentmihalyi, in particular the concept of *Flow*, where intrinsic motivation, skill, enjoyment and challenge come together. Moreover, it may help to develop the right type of environment in which people can flourish, as I have personally experienced. I wish each of you the possibility for *flow* in your lives.

Bert Herteleer
Ghent, January 2016

Contents

Abstract i

Beknopte samenvatting iii

Preface v

Contents ix

Glossary xiv

List of Figures xxi

List of Tables xxvii

List of Algorithms xxix

1 Introduction and overview 1

1.1 Background and general motivation for this work 1

1.2 Technical-financial motivations for this PhD 3

1.3 Description of PhD work 7

1.4 Aims of the Thesis 11

2 Design and implementation of outdoor measurement set-up for PV modules and systems 13

2.1 Descriptions in literature 13
2.2 Three iterations of the measurement set-up 14
2.3 Outdoor measurements of PV modules and systems 19
2.4 Measurements of modules to systems: overview of set-up 21
2.5 Weather-related measurements 25
2.6 Automated outdoor in-situ I-V curve measurements 28
2.7 Photovoltaic system behaviour during I-V curve measurements 35
2.8 Data and its treatment for analyses 38
2.9 Conclusions 38

3 Signal conditioning for outdoor electrical measurements 41

3.1 Introduction 41
3.2 Multi-level energy yield measurements on modules, DC-DC converters and DC-AC inverters 42
3.3 Multi-level DC logging: need for signal conditioning boards . . 44
3.3.1 Introduction, rationale and design 44
3.3.2 SCB testing, linear transformation and calibration . . . 49
3.3.3 Measurement uncertainty 56
3.3.4 Measurement uncertainty analysis applied to the SCBs . 59
3.4 Summary of results and benchmarking 64
3.5 Conclusions 66

4 Thermal characterisation of photovoltaic modules 67

4.1 Introduction 67
4.2 Long-term temperature measurements 71
4.3 Physical lay-out of array 75

4.4 Methods used to obtain improved temperature measurements: sensor attachment and placement 76

4.5 Steady-state temperature sensor bias detection and corrections 79

4.6 Over-temperatures as a metric for analyses and as a diagnostic tool 83

4.7 Cell and backsheet temperature measurements for backsheet-to-cell temperature corrections 85

4.8 Cell-backsheet temperature behaviour under variable weather conditions: theoretical considerations 91

4.9 Cell-backsheet temperature behaviour under variable weather conditions: practical considerations 96

4.10 Intra-module temperature variations 100

4.11 Inter-module temperature variations 105

4.12 Conclusions 108

5 The normalised efficiency and other tools for photovoltaic system analyses 113

5.1 Introduction 113

5.2 Theoretical background for normalisation 114

5.3 Characterisation of irradiance and power variability 119

5.4 Benefits and initial applications of the normalised efficiency . . 121

5.4.1 Performance comparison of modules and systems of different power ratings 121

5.4.2 Irradiance-dependent efficiency and effect of irradiance reference device 124

5.4.3 Identification of the system temperature coefficient of power 126

5.4.4 Calculation of the system temperature coefficient of power 131

5.4.5 Shading detection and monitoring 133

5.5 Modelling of the normalised efficiency, power and energy 139

5.5.1 Initial theoretical considerations 139

5.5.2 Least-squares approximation of the normalised efficiency model coefficients 143
5.6 Model validation 147
5.6.1 Introduction 147
5.6.2 Total Energy 148
5.6.3 Daily Performance Ratio 149
5.6.4 Longer-term evaluation of the PR and its errors 153
5.6.5 Time series evaluation of the normalised efficiency and power 157
5.7 Importance of measurement uncertainty 160
5.8 Quantifying energy losses due to shading 163
5.9 Applications of the normalised efficiency revisited 168
5.9.1 Education and outreach 169
5.9.2 Verification and comparison in multiple locations 169
5.9.3 Coefficients for model by Huld *et al* 169
5.9.4 Real-time and near-real-time monitoring 171
5.9.5 Additional comments on the determination of the system temperature coefficient of power 172
5.10 Conclusions 172

6 Conclusions and future outlook 177

6.1 Summary of the measurement set-up requirements and the results obtained 177
6.1.1 High-level goals 177
6.1.2 Actionable requirements 178
6.2 Thermal characterization and measurements 179
6.3 Photovoltaic module and system analysis 180
6.4 Performance analysis of systems 182
6.5 Future work 183

6.5.1 Normalised efficiency: measurements and modelling . . 183
6.5.2 Measurement set-up 184
6.5.3 Degradation analyses 185
6.5.4 Measurement uncertainty: absolute, relative and application 185
6.5.5 Temperature measurements and effects on energy yield calculations 186
6.5.6 Classification of irradiance variability 186
6.5.7 Signal conditioning boards (SCBs) 187
6.6 Improvements and long-term future prospects 187

A Worst-case scenario temperature measurement results 191

B Additional data for the thermal constant for other wind directions 195

C Additional information for the normalised efficiency 199

C.1 Shading detection using daily averaged values of the normalised efficiency 199
C.2 Determination of the system temperature coefficient of power . 201

D Data and its treatment for analyses 205

Bibliography 209

Curriculum Vitae 225

List of publications 227

Glossary

A_I Current amplification or scaling [A/V]. 48

A_V Voltage amplification or scaling [V/V]. 48

C_{th} thermal equivalent capacitance. xxvii, 92, 94–96

E^* temperature-corrected energy. 118

E_N normalised energy. 148

$E_{N,\tau}$ normalised energy over a period τ. 114, 181

G irradiance. xxiii, 35, 38, 65, 69, 73, 83, 85, 87, 94, 96, 104, 115, 124, 125, 127, 137, 140, 146, 206

G_N normalised irradiance. 10, 114

G_d daily irradiation. xxii, xxiii, xxv, 65, 90, 119, 120, 130, 135, 187, 202

$G_{N,\tau}$ normalised irradiation over a period τ. 114

G_{NOCT} The irradiance value for Nominal Operating Cell Conditions, 800 $\mathrm{W/m^2}$. xix

G_{STC} STC Irradiance: 1000 [$\mathrm{W/m^2}$]. 141, 143

G_τ irradiation during the interval time interval (τ). 116, 164–167, 181

$I_{m,nom}$ nominal measurement current. 47

$I_{sc,STC}$ short-circuit current at STC. 49

I_{sc} short-circuit current. 14, 22, 28, 33, 67, 73, 94

MPP_{STC} maximum power point at STC. 49

P^* temperature-corrected power. 118

P_N normalised power. xxiii, xxiv, 10, 114, 122, 124, 143, 147, 156–160, 178, 181, 185

P_N^* temperature-corrected normalised power. 11, 125, 143

P_{STC} STC Power of PV module or array [W_p or kW_p]. 24, 39, 116, 121, 123, 161

P_{th} thermal equivalent power. 93, 94

$R_{s,extra}$ Extra series resistance [Ω]. 14, 32

R_{sh} shunt resistance. 46

R_s series resistance. 8, 33, 34, 36

R_{th} thermal equivalent resistance. xxvii, 92, 94, 95

S sampling rate. 62

T_C cell temperature. 35, 81, 83, 85, 115, 146

T_o over-temperature. xxii, xxiii, xxv, 81, 83–85, 96, 110, 119, 126–131, 135, 137, 145, 172, 201–203

T_{BS} backsheet temperature. 81, 83, 85

T_{STC} STC module cell temperature: 25 [°C]. 67, 115, 118, 159

T_{amb} ambient temperature. 35, 69, 82, 92, 93, 96, 146

$T_{m,corrected}$ corrected measured temperature. 81, 83

T_m measured temperature. 81

U expanded uncertainty. 49, 56, 60, 63, 64, 66

U_E expanded uncertainty of energy. xxviii, 62, 63, 148, 149

U_P expanded uncertainty of power. 62, 63

U_T expanded uncertainty of temperature. 81

U_{PR} expanded uncertainty of the PR. xxviii, 150–156, 160

$V_{oc,STC}$ open-circuit voltage at STC. 49

V_{oc} open-circuit voltage. 14, 22, 28, 30, 32, 47, 67, 71–73, 94

$Y_{f,\tau}$ final yield over a period τ. 115, 181

$Y_{r,\tau}$ reference yield over a period τ. 115

ΔT_{CBS} cell-to-backsheet temperature difference. xxii, xxvii, 69, 78, 79, 85–91, 109

ΔT_{STC} Module temperature difference to T_{STC} [°C]. xxiv, 145, 158, 159, 169

ΔT_{bias} temperature sensor bias. xxii, 80–83

ΔT_{m-m} inter-module temperature variation. 71, 106, 107, 110, 180

Δe Difference in (total) measurement error. 56

Δt time step. 62, 63

β_0 Offset of a linear equation, may be obtained via linear regression. 53, 54

β_1 Slope of a linear equation, may be obtained via linear regression. 53, 54

ϵ random error. 53

$\eta(G)$ irradiance-dependent efficiency. 124–126

η_N normalised efficiency. xxiii–xxv, xxix, 10, 11, 94, 113, 114, 116, 117, 119, 121–129, 131, 134, 136–138, 140, 143–145, 147, 148, 156–160, 163, 168–174, 178, 180, 181, 183, 185, 199–201

$\eta_N(t)$ normalised efficiency over time. 116

η_{DCAC} DC-AC conversion efficiency. 139, 153

$\eta_{N,AC}$ AC normalised efficiency. 140

$\eta_{N,DC}$ DC normalised efficiency. 140

η_N normalised efficiency. 140, 177, 178

η_N^* temperature-corrected normalised efficiency. xxiii–xxv, 11, 94, 118, 123, 125, 127, 140–145, 163, 171, 173, 174, 200

$\eta_{PV,STC}$ STC efficiency. 10, 94, 100, 121

γ Efficiency temperature coefficient [%/°C]. xxviii, 132

γ temperature coefficient of power. 5, 67, 94, 104, 118, 126, 131, 133, 144, 156, 161, 169, 170, 183

γ_{BOS} balance-of-system (BOS) temperature coefficient. 131, 132, 177

γ_{syst} system temperature coefficient of power. xii, xvii, xxiii, xxv, xxix, 11, 126–137, 144–146, 156, 170, 172, 173, 180, 183, 201–203

κ thermal conductivity. 95

$\langle \eta_N \rangle_\tau$ averaged normalised efficiency. 116, 137

$\langle \eta_N \rangle_\tau$ Normalised average efficiency of PV module or system over a period τ [-]. 116

ν_A degrees of freedom for Type A measurement uncertainty. 60

ν_B degrees of freedom for Type B measurement uncertainty. 60

ν_{eff} effective degrees of freedom. 60, 61

ρ density. 95

σ_{PR} PR standard deviation. 182

$\sigma_{\Delta PR}$ PR error standard deviation. 156, 175, 182

$\sigma_{\gamma,syst}$ standard deviation of γ_{syst}. 132

τ time interval. xiv, xvi, xix, 61, 99, 107, 114–116, 118

$\tau_{\vartheta,eq}$ equivalent thermal time constant. 96–99, 109, 180

τ_ϑ thermal time constant. xxvii, xxviii, 94–96, 98, 99, 101, 109, 186, 195, 196

c specific heat capacity. 95

d thickness. 95

h_{Ross} Ross coefficient. 68, 85

k coverage factor. 49, 56, 57, 60, 61, 63, 65, 66, 74, 81, 185

m mass. 95

p level of confidence. 60, 61

r_{xy} correlation coefficient. 58

s sample standard deviation. 54, 59

t_p t-factor. 60

u_c combined uncertainty. 56–60, 62, 63

$u_{c,A}$ Type A combined measurement uncertainty. 58, 59

$u_{c,B}$ Type B combined measurement uncertainty. 58, 59

$v_{w,proj,EW}$ East-West projected wind vector. 9, 87, 89, 91

$v_{w,proj,NS}$ North-South projected wind vector. 9, 87, 89, 90

$v_{w,proj}$ projected wind vector. xxii, 9, 70, 87, 90, 96, 97, 109, 110, 177, 186, 197

BOS balance-of-system. xvi, 2, 131, 133, 177

c-Si crystalline silicon. 47

CSV Comma Separated Value. 14, 20, 205

DMM digital multimeter. 27, 33–36, 38, 50–54, 63, 187

e-load electronic load. 33–35, 38

ECT equivalent cell temperature. 72

EVA Ethyl Vinyl Acetate. 92, 95, 97

FS full scale. 50, 56, 64, 66

I-V curve current-voltage curve. xxi, xxiii, xxvii, 7, 8, 15, 19, 20, 22, 28–39, 43, 63, 65, 71, 100, 101, 104, 126, 129, 134, 136, 137, 139, 145, 146, 158–160, 168, 170, 171, 173, 174, 178–181, 184, 185, 205, 207

inamp Instrumentation Amplifier. 46, 47

IR infrared. 72–74, 82, 94, 107, 110, 111, 186

LCOE levelised cost of electricity. 6

MID Measuring Instruments Directive, a directive which specifies whether an energy or kWh meter can be used for billing purposes or not. 23

MPP maximum power point. 8, 12, 22, 34, 35, 37, 38, 42, 73, 119, 136, 146, 168, 179

MPPT maximum power point tracker. 32, 126, 134, 168, 173, 174

MWT Metal Wrap-Through. 21, 26, 98, 104, 132, 133, 146, 196

NOCT Nominal Operating Cell Temperature, obtained for a module held at open-circuit voltage, an irradiance G_{NOCT} and a wind speed of 1 m/s parallel to the module surface.. xiv, 69

NVI natural variability index of irradiance. xxviii, 119, 120, 125, 130, 132, 172, 173, 186, 187

NVP natural variability index of power. 120

opamp Operational Amplifier. 45, 46

open-circuit voltage Open-circuit voltage [V] of a cell or module. xix

PAC Programmable Automation Controller. 20

PCB Printed Circuit Board. 46

PR Performance Ratio. xv, xvii, xxiii, xxiv, xxviii, 10, 11, 63, 113, 114, 116, 117, 119, 137, 138, 147–157, 160–163, 173–175, 178, 181, 182, 199, 200

PR* temperature-corrected Performance Ratio. xxiii, 118, 137, 138, 163, 174, 175, 182

PR$_\tau$ Performance Ratio over a period τ. xxiii, 115–117, 175

RMS root mean square. 81

ROI return on investment. 6

RTD resistance temperature detector. 74

SCB signal conditioning board. xiii, xxii, 9, 19, 21, 23, 37, 39, 41, 44–59, 64, 66, 113, 179, 187

SSE square root of the sum of squared errors. xxix, 143–145, 159

STC Standardised Testing Conditions. xiv–xvi, 10, 14, 47, 67, 87, 89, 91, 94, 100, 107, 115, 117, 118, 121, 126, 127, 133, 147, 169, 173

TDMS technical data management streaming. 19, 205, 206

UPS uninterruptible power supply. 32, 207

VHB very high bonding. 76–79, 85

VI Virtual Instrument - LabVIEW term for program or instance of (literally) a virtual instrument. 3, 19, 23–25, 32, 34, 43, 45, 50, 51, 66, 179, 205, 207

WACC weighted average cost of capital. 6, 41

List of Figures

1.1 Photovoltaic module learning curves up to 2015 3

1.2 Global weather catastrophes worldwide 1980 – 2012, overall and insured losses with trend 4

2.1 View of prototype of measurement set-up, May 2013 15

2.2 Photograph of the second iteration of the measurement set-up, December 2013 16

2.3 Schematic bird's eye view of complete roof with indication of original and new set-up locations. 17

2.4 Multi-perspective photographs of the latest iteration of the measurement set-up, August 2015, with new roof insulation. . . 18

2.5 Schematic diagram of the measurement set-up 20

2.6 Detailed set-up bird's eye view, valid from 2015 22

2.7 Electrical equivalent diagram of PV module connections, valid from 2015 onwards. 23

2.8 Schematic overview of the switches for I-V curve commutation 30

2.9 Boolean states for I-V curve commutation contactor sequence . . 31

2.10 Schematic overview of the I-V curve measurement circuit . . . 33

2.11 Example of inverter operation with current-voltage curve (I-V curve) curve measurements 35

2.12 Example of I-V curve switching during inverter operation . . . 36

3.1 Power and energy yield measurements in a photovoltaic system 44
3.2 Simplified schematic of the initial design of the SCB. 46
3.3 Simplified schematic of the final version of the designed SCB. . 48
3.4 SCB testing and calibration schematic. 51
3.5 An example of slope and offset errors 52
3.6 Results of the slope and offset correction for one SCB 53
3.7 Example initial and calibration testing for currents, SCBs versus DMM. 55
3.8 Example calibration testing for voltages, for 1 V to 40 V SCBs versus DMM. 57
3.9 Comparison of Student's t distribution to the normal distribution 61

4.1 Bird's eye view of set-up, including poles, with focus on temperature measurements. 75
4.2 Example comparison of temperature sensor attachment and insulation methods. 77
4.3 Cell-backsheet temperature deviations measured on 5 February 2014. 78
4.4 Temperature sensor bias (ΔT_{bias}) correction comparison on 2 April 2015. 80
4.5 Detection of a loose temperature sensor using the over-temperature. 84
4.6 Example of Cell-Backsheet temperature differences on 31 July 2015 86
4.7 Cell-backsheet temperature measurements on 1-3 July 2015 . . 88
4.8 Daily filtered values of cell-to-backsheet temperature difference (ΔT_{CBS}), projected wind vector ($v_{w,proj}$) and daily irradiation (G_d), April-August 2015. 90
4.9 Cross section of a standard module with Pt100 sensors 92
4.10 Reduced thermal RC-network conduction model with cross section of a standard module 93
4.11 Cell- and backsheet-measured temperature responses to changing irradiance and wind on 9 July 2015. 97

4.12 Timeseries of intra-module ΔT_{max}, end August 2015. 102

4.13 Relative frequency histograms of maximum temperature difference inside modules for June-August 2015. 103

4.14 Module temperature deviations compared to the reference for late July–early August 2015. 106

4.15 Relative frequency histograms of temperature difference between modules for June-August 2015. 107

4.16 Maximum and minimum inter-module temperature variations for end of July and early August 2015. 108

5.1 Power and energy to calculate the PR_τ and η_N.as well as converter or inverter efficiencies. 117

5.2 Power, normalised power and normalised efficiency of modules and inverters with different power ratings 122

5.3 Comparison between pyranometer-derived and reference cell-derived normalised power P_N versus irradiance G and normalised efficiency η_N versus G. 124

5.4 Normalised efficiency η_N versus over-temperature T_o 128

5.5 Over-temperature T_o and normalised efficiency η_N for a day with multiple temperature peaks and troughs 129

5.6 Unfiltered daily values of γ_{syst}, T_o and G_d for modules of the *Smart PV* project, April-August 2015 130

5.7 Pole shading near modules in the afternoon 134

5.8 Daily averaged values of γ_{syst}, T_o and G_d for modules of the *Smart PV* project, August-October 2015, with morning shading from ∼18 September 135

5.9 Variation in the normalised efficiency due to pole shading effects 136

5.10 I-V curve measured of module *PV064* during pole shading in the morning of 30 September 2015. 137

5.11 Daily PR and PR*, April-November 2015, with morning shading from early September. 138

5.12 Comparison of initial model approximation to measured η_N^* on 21 and 22 August 2015 141

5.13 Comparison of initial model approximation to measured η_N^* - zoom on morning of 21 August 2015 142

5.14 Total DC and AC energy production comparison for June to August, models versus measurements. 149

5.15 Daily PR comparison for module *PV054* for 9-31 July 2015, models versus measurements. 151

5.16 Daily AC PR comparison for the SolarEdge inverter for 9-31 July 2015, models versus measurements. 152

5.17 PR comparison of models for modules: average daily PR and standard deviation, and mean error and standard deviation of the error for June-August 2015. 154

5.18 PR comparison of models for systems: average daily PR and standard deviation, and mean error and standard deviation of the error for June-August 2015. 155

5.19 Comparison of models for AC side of SolarEdge inverter: η_N, P_N and measured ΔT_{STC} on 22 and 23 August 2015. 158

5.20 Energy yield difference to reference module, comparison of measured and modelled energy values, April-November 2015. . 164

5.21 Total energy comparison of measured and expected (modelled) yield of individual modules, April-November 2015. 165

5.22 Comparison of measured and expected (modelled) energy yield,for September-November 2015. 166

5.23 DC and AC system yield comparison, measured and expected of the DC-DC converters and inverters measured, for April-November 2015. 167

6.1 Visual summary of PhD contributions. 181

A.1 Hot humid air from nearby pipes affecting module performance on the prototype set-up 192

A.2 Temperatures measured on a PV module, disturbed by nearby exhaust pipes 192

A.3 Irradiance, wind speed and ambient temperature measured on 1 April 2013. 193

B.1 Cell- and backsheet-measured temperature responses to changing irradiance and wind on 4 August 2015. 197

C.1 Daily averaged η_N and η_N^*, April-November 2015, with morning shading from early September. 200

C.2 Over-temperature T_o and normalised efficiency η_N for a day with multiple temperature peaks and troughs 201

C.3 Unfiltered daily values of γ_{syst}, T_o and G_d for modules of the *Smart PV* project, April-August 2015 202

C.4 Comparison of γ_{syst} values, determined using reference cell or pyranometer for April-August 2015. 203

D.1 Flow for TDMS to MAT files and *timeseries* conversion for analyses 206

List of Tables

2.1 Overview of PV modules and systems measured 24

2.2 Measurement uncertainty and amount of climatic sensors used 27

2.3 Comparison of typical electrical measurement uncertainty of I-V curves 34

3.1 Ranges of voltages and currents measured and amounts, as of 2015 49

3.2 Measurement uncertainty and amount of DC voltage and current sensing channels according to application range 64

3.3 Benchmarking of main energy and performance measurement uncertainty parameters 65

4.1 Comparison of main temperature measurement methods 73

4.2 Average wind data for Figure 4.7. 89

4.3 Average values and spread of ΔT_{CBS} for April-May and April-August 2015 per position on module *PV052*. 89

4.4 Values for thermal constant calculation of the *Smart PV* modules, as shown in Table 4.5. 95

4.5 Calculated values of thermal equivalent resistance (R_{th}) and thermal equivalent capacitance (C_{th}) for the *Smart PV* modules. 95

4.6 Calculated values of the thermal time constant τ_ϑ for the modules shown in Figure 4.11. 98

5.1 New definition of natural variability index of irradiance classes using time intervals of one second 120

5.2 Calculated values of for April to August 2015 for the three inverters and composing modules measured, for valid days. . . 132

5.3 Comparison of averaged DC module-level coefficients for the model of Huld *et al* and its modified form (this work). 146

5.4 Comparison of number of module or system models with modelled energy within expanded uncertainty of energy measurement limits, as shown in Figure 5.14. 148

5.5 Comparison of number of module or system model results with modelled Performance Ratio within expanded uncertainty of the PR measurement limits, as shown in Figures 5.17 and 5.18. . . 156

5.6 Mean and standard deviation of model daily PR errors for June-August 2015. 157

5.7 Possible sources and uses for model of Huld *et al* coefficient values.170

B.1 Calculated values of the thermal time constant τ_ϑ for the modules shown in Figure B.1. 196

List of Algorithms

3.1 Linear transformation and calibration of SCBs via successive approximations. 56
4.1 Steps to follow to ensure correct temperature measurement . . 82
5.1 Method to obtain the system temperature coefficient of power γ_{syst} from the normalised efficiency and temperature measurements. 127
5.2 Method used to obtain coefficients k_1 and k_2 for Equation (5.16) using the square root of the sum of squared errors SSE 144
5.3 Steps to obtain the model coefficients for a system's performance from measurements, using the normalised efficiency, system temperature coefficient of power and Algorithm 5.2. 145

Chapter 1

Introduction and overview

1.1 Background and general motivation for this work

Anthropogenic greenhouse gas emissions have increased since the pre-industrial era driven largely by economic and population growth. From 2000 to 2010 emissions were the highest in history. Historical emissions have driven atmospheric concentrations of carbon dioxide, methane and nitrous oxide to levels that are unprecedented in at least the last 800,000 years, leading to an uptake of energy by the climate system. – IPCC Climate Change 2014 Synthesis Report [1]

Our results expose a specific regional hotspot where climate change, in the absence of significant mitigation, is likely to severely impact human habitability in the future. – Pal & Eltahir [2]

The Economy, Stupid. – James Carville [3]

The fiscal, environmental, and welfare impacts of energy subsidy reform are potentially enormous. Eliminating post-tax subsidies in 2015 could raise government revenue by $2.9 trillion (3.6 percent of global GDP), cut global CO2 emissions by more than 20 percent, and cut pre-mature air pollution deaths by more than half. After allowing for the higher energy costs faced by consumers, this action

> *would raise global economic welfare by $1.8 trillion (2.2 percent of global GDP).* – IMF [4]

The above quotations highlight the overarching motivation for this work: by reducing uncertainties in the estimated and measured power and energy yield of photovoltaic modules and systems, the economic risks of investing in photovoltaics can be reduced. This can then contribute to a significant increase in photovoltaic installations worldwide, which leads to a faster decarbonisation of the power supply while meeting society's needs for electrical energy. The scientific consensus of the impact of human activity clearly shows the need for an electricity supply with the lowest possible greenhouse gas emissions. While photovoltaic installations only produce energy during daytime, their output is broadly predictable and emissions-free, and can play an important role in a decarbonised society, together with other technologies such as wind power.

To do this, the "trilemma" (triple dilemma) of energy supply must be solved: affordable, reliable and sustainable energy. Figure 1.1 shows how the cost of photovoltaic energy has reduced as the industry has grown, which can contribute to one aspect of the trilemma. The sustainability aspect consists of the broader picture of a technology which can positively contribute to society, from job creation, avoidance of greenhouse gas emissions to health benefits (by a local reduction of air pollution), to name a few. The reliability aspect involves ensuring that the lights stay on, day in and day out, and that the technology behaves in a predictable manner over the expected lifetime.

The cost of photovoltaic systems has seen a very strong reduction, with a learning rate of ≈20 % cost reduction for photovoltaic modules and similar for the BOS and systems, for every cumulative doubling of PV installations worldwide, since the 1970s. One example of a learning rate or experience curve for photovoltaics is given in Figure 1.1. The subsidy efforts which have been strongly felt over the past decade in Europe have resulted in the photovoltaic market growing and through scale and learning effects, with customers today being able to buy a photovoltaic system at a fraction of the cost of a few years ago.

The importance of action on climate change is highlighted in Figure 1.2, as it shows how both insured and non-insured losses due to weather-related catastrophes have been increasing since the 1980's. The scientific consensus of the International Panel on Climate Change, representing thousands of world-respected scientists is unequivocal that the acceleration in the change of the Earth's climate is mostly[1] due to human activity.

[1] The sun's activity as well as "random" events (e.g. volcanic eruptions) also play a role, but human activity has rapidly outpaced these effects in the past decades.

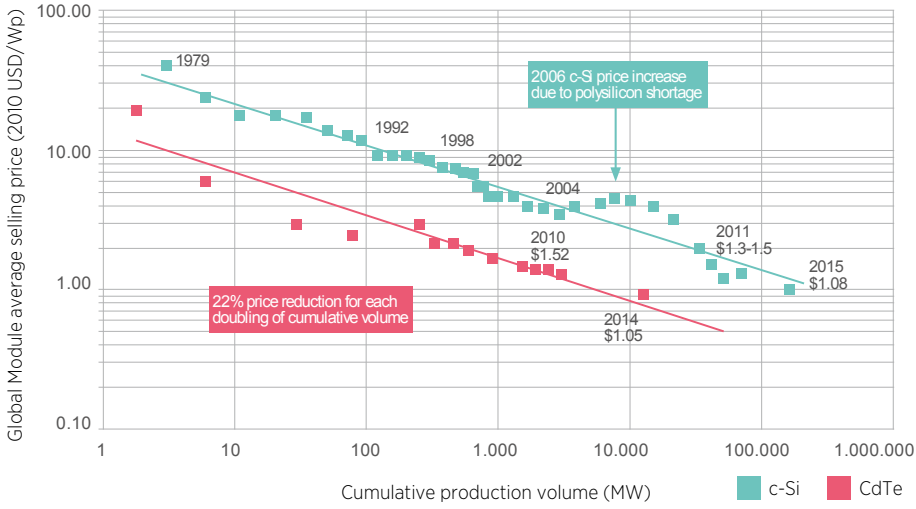

Figure 1.1: Photovoltaic module learning curves for thin-film materials and crystalline silicon, from 1979 to 2015, from [5].

The good news is that climate-neutral and climate-positive technologies will not only contribute to the welfare of society through creation of jobs, but also that their broader impacts on human health (e.g. reducing local air pollution) far outweigh their costs [4], such as insurance [6]. The costs of these climate-positive technologies are also decreasing (see e.g. Figure 1.1), in time, so that efforts in this area are also inherently rewarding. Photovoltaics is one of the key technologies that can contribute to a decarbonised society, with the expectation of growing to be a 200 billion dollar annual market by 2020 [7].

1.2 Technical-financial motivations for this PhD

The work performed in the course of this PhD has focused on providing tools in the field of renewable energy, specifically for photovoltaics, to society at large. These tools encompass hardware (the physical instruments for the outdoor measurement set-up), software (the LabVIEW Virtual Instruments VIs (programs) and other programs developed) and algorithms and processes for better measurements and analyses. The hardware and software of the measurement set-up can be used for research (e.g. energy yield measurements for the *Smart PV* project, data for photovoltaic model calibration and validation,

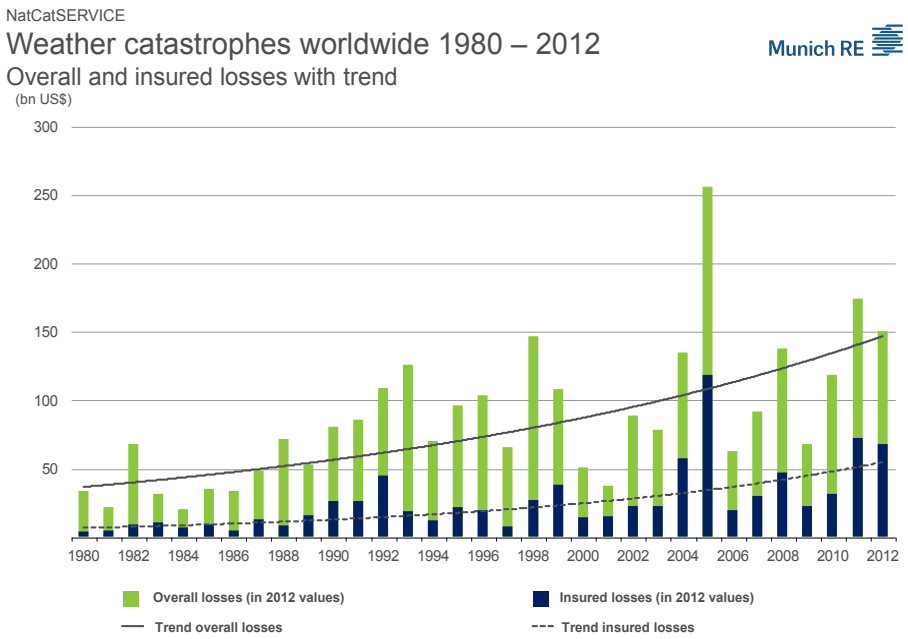

Figure 1.2: Global weather catastrophes worldwide 1980 – 2012, overall and insured losses with trend, figure from [6].

new monitoring models), industrial services (e.g. module energy yield production comparisons) and educational purposes (e.g. the small residential photovoltaic system which is measured).

From the perspective of service to industry and calibration and validation of photovoltaic models, the measurement set-up and associated software and algorithms developed are tools with which to answer a large array of possible questions. "Is the type of module or system that I bought going to perform as expected?" is one of the broadest questions that is asked regarding module performance; the other being "How much energy will the module or system produce per year?" and "How fast will my modules degrade?". Similarly, "How does a system perform under partial shading?" is a question that before has been rarely asked (sometimes due to a lack of knowledge), yet is growing in importance, as more and more systems are being installed, some of these in areas where repeated shading may occur, such as chimneys, poles, trees or even nearby buildings.

Questions may be asked regarding this work relate to why it had to be done in the first place. Is not "everything known already" about photovoltaic module

and system performance? How much does that 10 % or 1 % or even 0.1 % improvement matter? What is the purpose or benefit of measuring at a faster rate, or storing more data?

The answer to these questions will be dealt with in what follows, in parts explicitly, in others more implicitly. However, to paraphrase Lord Kelvin: not measuring is not knowing, but measure correctly and you may know a lot more.

While governments can create the legislative framework for certain technologies to thrive or not, at the end of the day it is generally the economics of the technology that determines the uptake. Investment in a photovoltaic systems entails technical and financial risks, and as is the case with any investment, there is a need for follow-up or monitoring of the performance of the investment. Given the relatively long time horizon over which the investment needs to be spread out (which is typically the expected technical lifetime of the system, 20 years to 25 years), on the technical side the reliability of the system and its components (modules, wiring, inverters, protection equipment, monitoring equipment if applicable) grows in importance. One example is the risk associated with the warranty given by photovoltaic module manufacturers, based on their model of module power degradation [8]. An overly confident ("aggressive" [8]) warranty may lead to financial ruin for a module manufacturer (and possibly many along the value chain such as installers and even insurance companies), as a significantly larger portion of the produced modules must be replaced compared to internal projections and models.

Similarly, as the general quality of photovoltaic modules and system components has improved over time and that the cost of systems has rapidly decreased, component selection has become easier and also more difficult, as the market has largely become standardised and commoditised. In the past, the reputation and technical know-how of a manufacturer would have been one of the determining factors for choosing a certain photovoltaic module type. Today, a large portion of the (silicon) photovoltaic module market has modules with power ratings of $230\,\mathrm{W_p}$ to $300\,\mathrm{W_p}$. Differentiating factors used for component selection may then be the thermal behaviour of the module (the efficiency of photovoltaic modules generally decreases with higher temperatures), so that a module with a lower value of the temperature coefficient of power (γ), e.g. $-0.40\,\%/°\mathrm{C}$ may win a contract compared to a similar module but with a value of γ of $-0.45\,\%/°\mathrm{C}$. At face value, the above decision appears to be rational, yet the variation in the determined values of γ by accredited measurement laboratories of up to 18 % [9] means that the datasheet values are subject to uncertainties which are often not known, communicated or even understood. For example, assuming an expanded measurement uncertainty for γ of $\pm 0.1\,\mathrm{pp}$ (percentage points) may make the above decision moot: the uncertainty interval is larger than the difference between the two values of γ mentioned before.

Financial models which calculate the levelised cost of electricity (LCOE) depend on the *output of technical models*, as well as the risk premium quantified by the weighted average cost of capital (WACC) [5]. A lack of knowledge by financing entities may therefore lead to too-high risk assessments (and with them, value of WACC), which may result in promising projects not being financed, or at a higher cost than necessary. Thus, measurements and monitoring of installed photovoltaic modules and systems are an essential step in verifying performance in-the-field and to refine or calibrate the technical performance models upon which the financial models depend.

For many potential customers, e.g. residential customers, investing in a photovoltaic system for electricity generation connected to the grid, is the equivalent of paying in one step for the expected electricity consumption for the future 20 years, instead of the monthly payment to the electricity utility, e.g. with net energy metering[2]. This is, in economic terms, a hedge against future rises in electricity prices. Such an investment is typically only possible for customers with sufficient savings or ability to borrow money at sufficiently affordable rates. The risks associated with photovoltaic systems, ranging from technical issues (module and inverter failures) to legal-financial issues (taxation, subsidies, permission for installations) as well as the personal risk profile of the customer, impact the rate that financial entities will set to lend money. Given the time horizon over which the photovoltaic installation needs to function and generate a return on the investment (the expected technical lifetime of 20 years to 25 years), small variations in technical and financial assumptions can lead to very large differences in economical terms, especially as the effects compound over time.

With generous subsidy policies, the sensitivity of customers to real and expected variations in the return on investment (ROI) is limited. Conversely, increased taxation, a reduction in subsidies and the *perception* (see, among others, the seminal article by Kahneman and Tversky [10] on risk perception and risk aversion) of higher technical and financial risk lead to increased accuracy demands for the energetic and economic ROI.

A very important aspect of the cost of photovoltaic systems (this also applies to wind energy) is that it is very capital intensive at the start of operation of the system and that afterwards relatively little operation and maintenance costs are incurred. While maintenance and monitoring costs have slightly increased in the past years, mostly because of increasing awareness from the initial "set and forget" philosophy for larger systems, once a photovoltaic system has been paid

[2]Net energy metering: the annual photovoltaic energy production is deducted from the annual electric energy consumption. Generally, if the production is greater than consumption, then the customer pays nothing (or a limited fixed cost). If the production is less than the consumption, the customer must pay for the difference.

for, the cost of new generated electricity is close to zero. In economic terms, the marginal cost of production is zero or close to zero, which is disrupting electricity markets worldwide, in particular where photovoltaic power and energy exceed 10 % to 20 % and 1 % respectively on a daily or yearly basis. Moreover, the financial models developed and refined over decades by utilities (e.g. for Belgium, the higher cost of electricity consumption during the day and lower at night: "dagtarief" and "nachttarief") are strongly impacted by photovoltaic systems' performance: they produce electricity at moments which before were deemed to be the most costly, eroding the profit margins that were anticipated just a few years before (this has resulted in changes in business strategies, depending on the local market conditions).

1.3 Description of PhD work

Already the period of the PhD proposal writing and start of the PhD (end 2011-start 2012) saw the transition from (overly) generous feed-in-tariff subsidies in Europe and Flanders in particular to tightening subsidy schemes. Building an outdoor measurement set-up for photovoltaic (PV) modules and systems which could provide objective comparisons of photovoltaic module performance (which comprises power, energy and temperature) for the local photovoltaic industry (installation and research oriented) was therefore an appropriate market need fit. Also at that time work at IMEC [11] already suggested that intra-module temperature variations in the scale of seconds (1 s to 30 s) could be experienced as a result of varying irradiance and weather conditions, providing an additional incentive to verify and calibrate the modelled results using outdoor measurements. The high-level goals and aims, as well as a short historical overview of the measurement set-up are detailed further in Chapter 2.

In practical terms, attempting to reach (and especially surpass) the state-of-the art of other research institutes is a challenge, especially for the measurement of current-voltage curves (I-V curves). As such, this work has focused on achieving good enough measurement uncertainty for the outdoor measurement of I-V curves using industry-standard components, and supplementing this by adding other functionalities - such as the ability to connect and disconnect modules from an inverter's string to be measured in a fully automated manner.

In general, the focus of this work has been on measuring aspects faster, such as the weather and module temperatures on a per-second basis, in order to better understand photovoltaic module and system performance, and its interaction with the environment. In so doing, well-established methods and equations from literature could not directly be applied, but required a modification to be used

for the data generated. In the course of these investigations, certain assumptions by authors (e.g. steady state behaviour, even for transient conditions) have surfaced.

For research purposes, current-voltage curve (I-V curve) are some of the most-used tools in the photovoltaic industry. If properly measured and linked to the applicable weather conditions, measurements can help to answer research questions, such as identifying module failures, determining the maximum power point (MPP) and from this the module efficiency, as well as determining additional modelling parameters, such as the series resistance (R_s). If I-V curve curves are measured in outdoor conditions, the weather, especially irradiance and module temperature, must be measured as well, in order to better determine the link between the inputs (weather, type of system) and outputs (current, voltage, power, module temperature).

The most representative I-V curve curve measurements are obtained if the module is kept at MPP in the interval between I-V curve curve measurements, mostly as this is a more realistically determined I-V curve curve: the temperature of the module measured should correspond to that measured for a module used to produce electricity. There are a number of methods available for keeping a module, and if grouped, a string of modules, at MPP, such as programming an electronic load, or using commercially available DC-DC or DC-AC converters. The benefit of the latter option is that the energy of the photovoltaic modules is not lost or converted to heat in the electronic load, which is particularly poignant when working with a technology which can and must contribute strongly to climate change mitigation practices.

The measurement set-up which is a large part of this PhD, answers the needs identified in the previous paragraphs: Joining the requirements of I-V curve curve measurements, the need to keep the module(s) at MPP between I-V curve curves using commercially available DC-DC and DC-AC converters and measurement of the produced energy of the modules connected to these converters, as well as the weather conditions that may impact the performance have lead to the measurement set-up as it is today. The description can be found in Chapter 2. The above requirements had to be fulfilled within the framework of reasonable cost and user-friendliness.

For the measurement of temperature, methods are explained in Chapter 4 which allow proper installation to be verified, to reduce sensor bias and to obtain the cell temperature, based on the measurement of the back of photovoltaic modules and irradiance.

The measurement of the DC current and voltage (which then are used to calculate the power and energy yield) are accomplished in this set-up with the

help of signal conditioning boards (SCBs) which have been custom-designed and built: these serve to isolate the power side from the measurement side, so that potential problems (e.g. a short-circuit) on one side does not affect the other. Their design and testing is described in Chapter 3. The measurement uncertainty is reduced through linear transformation and subsequently calculated using the well-established[3] methodology of the *Guide to the Expression of Measurement Uncertainty*, generally referred to as the *GUM* [12].

With the data and measurement methods verified for validity, correctness and measurement uncertainty, methods can and could be tested and developed. First proper measurement methods (sensor attachment or connection, sensor types (e.g. Pt100 sensors versus thermocouples for temperature measurements)) and corrections (backsheet-to-cell correction, linear compensation) to be applied, then the determination of measurement uncertainty, to then be able to perform analyses and reach conclusions with a known degree of uncertainty.

To aid understanding of thermal effects and interaction between module and the environment, the projected wind vector $v_{w,proj}$ is introduced and applied. By joining the (separately measured) wind speed and direction and recalculating these as the North-South projected wind vector $v_{w,proj,NS}$ and the East-West projected wind vector $v_{w,proj,EW}$, it is possible to better display time series of the wind. Coincidentally, the North-South and East-West axes are the principal wind directions for photovoltaic modules. For modules placed in a different orientation, it is possible to either use the "true" $v_{w,proj,NS}$ and $v_{w,proj,EW}$, or the system-specific $v_{w,proj,NS}$ and $v_{w,proj,EW}$.

One of the perennial questions of owners and users of photovoltaic systems is "How well is the system performing at moment X or during condition Y?". For larger systems composed of multiple arrays and inverters, often of different power ratings, such a question would be answerable, albeit after much time and effort, e.g. performing an *implicit*[4] normalisation. A first step to better answer such a question is to (explicitly) normalise the power and energy of the different components of the system. That way, if the system contains arrays of e.g. 20 $\mathrm{kW_p}$ and 24 $\mathrm{kW_p}$, the 20 % power difference is removed, and the systems performing better on a per-kW basis can be identified.

In terms of performance analysis, the collaboration with the *Smart PV* project gave access to modules with different types of technology (string configurations and number of bypass elements) to be evaluated for their individual energy yield. The *Smart PV* project was focused on researching and developing methods to increase the energy yield of photovoltaic modules and systems which could be

[3] Albeit known by too few and applied too little.

[4] Normalisation of (sub-) arrays is not yet often applied as a method for inter-system comparison, hence the focus on this term.

expected to be subjected to partial shading. Among the methods studied were modules fitted with active bypasses, with lower expected losses than standard bypass diodes. To study these effects, modules were designed and built to evaluate for improved energy yield production. The individual energy yield measurement requirement of individual modules could best be satisfied using a DC-DC converter or DC-AC inverter per module, as the performance of all modules would otherwise be impacted by the worst-performing modules in the string. The results of many of the modules, DC-DC converters and inverters associated with the *Smart PV* project are discussed in this work.

With temperature and electrical data available at high resolutions, a metric and model for photovoltaic module and system comparison is introduced in Chapter 5: the normalised efficiency η_N. Similar in approach to the industry-standard metric of the Performance Ratio (PR), it allows PV systems of different power ratings, orientations and locations to be compared to each other, in terms of irradiance-to-power conversion (instead of the irradiation-to-energy conversion analysed by the PR).

In order to compare multiple photovoltaic modules and systems, one of the first steps is to obtain the normalised power P_N defined in Equation (1.1), which is one step forward in allowing multiple photovoltaic modules and systems to be compared, both numerically and visually. Similarly, the normalised irradiance G_N in Equation (1.2) can be used for visual comparisons, as well as subsequent analyses. A step further is the normalised efficiency η_N given in Equation (1.3), as this incorporates the effect of the irradiance in the value.

$$P_N = \frac{P}{P_{STC}} \tag{1.1}$$

$$G_N = \frac{G}{G_{STC}} \tag{1.2}$$

$$\eta_N = \frac{P_N}{G_N} \tag{1.3}$$

The normalised efficiency is conceptually easy to comprehend, as it expresses which percentage of the sunlight that should[5] be converted to electric power is actually measured or delivered. For example, if one $20\,\mathrm{kW_p}$ system is performing with an $\eta_N = 95\,\%$ while its neighbour $24\,\mathrm{kW_p}$ system performs at $\eta_N = 90\,\%$, then a clear distinction between both systems can be made quickly: the $20\,\mathrm{kW_p}$ inverter system is performing *better* than its larger neighbour, although in absolute terms, it produces less power.

[5] Through the STC efficiency of the module or system.

From a monitoring perspective, the normalised efficiency (η_N) allows much easier intercomparison of large systems. In many cases, large[6] PV systems consist of multiple inverters where the array power per inverter may vary. As in the example above, an easier comparison of the power and energy performance per inverter is only possible when the values are normalised and preferably scaled to the received solar power (irradiance) and energy (irradiation).

While the normalised efficiency initially takes more effort to compute (it needs the PV power and the incoming irradiance data to be properly synchronised and linked) than the PR, it provides a large number of benefits.

The η_N can be used to determine the system temperature coefficient of power γ_{syst}, which quantifies the reduction in efficiency of the *system* (e.g. one module and DC-DC converter, or an array with its inverter). The γ_{syst} can then be used to obtain the temperature-corrected normalised efficiency (η^*_N) and temperature-corrected normalised power (P^*_N). These then are used to determine the temperature-corrected model coefficients of the power rating model for crystalline silicon modules by Huld *et al* [13], the approach of which is also expanded to encompass the performance of arrays and inverters.

The fitted model is validated for multiple modules and inverters and generally performs better than the benchmark, from individual module up to inverter. With shading present on the modules from September 2015 onwards, the fitted model is used to quantify the shading-induced losses.

1.4 Aims of the Thesis

The PhD proposal specified a number of high-level aims:

- Build a high-quality, high-speed outdoor measurement set-up, which will allow transient (rapidly changing) thermal and electrical effects to be observed.
- Contribute to the development of the detailed physics-based thermal-electrical-optical model for photovoltaic modules developed at IMEC, including providing data for model calibration and verification.
- Modelling of degradation and development/validation of test procedures for the energy rating of PV modules in the Belgian context by performing outdoor measurements and accelerated lifetime tests.

[6]Scale is relative: some define large systems from 1 MW_p. One potential definition is to look at whether the existing grid connection needs to be strengthened and whether there is a need for a low-voltage to high-voltage transformer to be in place.

Expressing the above requirements as more actionable design requirements, the following list is obtained:

- A flexible, expandable measurement set-up for distributed temperature measurements on PV modules, while also taking into account climatic and electric variables.
- Achieve the lowest measurement uncertainty within the budgetary constraints of time, skills and available resources.
- I-V curves should be measured at regular intervals, with the PV module in question held at its MPP between I-V curve measurements. I-V curves should be measured in 1 s or less, with the possibility of longer duration I-V curves if circumstances so dictated, e.g. for highly capacitive PV modules [14].
- To have the PV modules connected to a commercial converter or inverter. This resulted in the need for a commutation mechanism (which is described in (very) general terms in [15, 16]), to disconnect a PV module from a string without impeding the flow of power to the main inverter.
- All values should be measured and stored per second to characterise photovoltaic modules and systems' transient behaviour. Compared to most descriptions in literature, this is a significant increase in the frequency, as other set-ups measured and stored data at intervals between 5 s average values up to 15 min.

Chapter 2

Design and implementation of outdoor measurement set-up for PV modules and systems

2.1 Descriptions in literature

Few articles on (all) the design considerations of measurement set-ups with sufficient information to develop a similar set-up have been published. Possible reasons for this are that it is considered "standard" engineering practice, as well as that publishing an article with all the details may result in the loss of the competitive advantage for the research institution or company.

The measurement (and modelling) of current-voltage (I-V) curves has been the topic of much study [17, 18, 19, 20], as this determines critical follow-up modelling efforts, such as the energy production, shading tolerance [21, 22] and ageing or degradation [23] to name a few. Standards have served in this regard as benchmarks and represent the applicable consensus, and occasionally the preferences or methods of institutes. The International Electrotechnical Commission (IEC) has a Technical Committee (TC 82) and its working groups on the broad topic of photovoltaics, which have resulted in a large number of standards. The most well-known (in general) in this area are IEC 61215 [24] for

crystalline silicon modules from which the definition of peak power (given as W_p) and Standard Testing Conditions (STC) have spread within the photovoltaic industry and IEC 61646 [25] for thin-film modules, whereas the IEC 60904-1 [26] standard (and its associated standards 60904-2 to 60904-10) are directly related to the measurement of I-V curves. For on-site I-V curve measurements, IEC 61829 [15] gives more (similar) requirements[1]. Once the I-V curves have been measured, temperature and irradiance corrections are often performed according to IEC 60891 [27], although this is not always the case, in particular for module temperature [28].

For temperature measurements, Kurnik and Topič [29], Rustu Eke [30] and others have focused on the best and often most cost-effective method of obtaining multiple temperature measurements.

For the practical design aspects of the measurement set-up described in this work, the work of van Dyk [31], Kurnik [32], Yordanov [33] has served as an inspiration. Their work, together with the guidelines and requirements of the IEC standards and Derlab [34] informed many of the choices made.

2.2 Three iterations of the measurement set-up

The start of this PhD saw a measurement set-up capable of switching between measuring the open-circuit voltage (V_{oc}) and the short-circuit current short-circuit current (I_{sc}) of up to two PV modules at five minute intervals, with up to 3 temperature values measured and one plane-of-array irradiance value, saved to CSV–files on a computer. The data could then be retrieved using a 3.5 inch floppy disk. The shape of the current-voltage (I-V) curve was estimated using a fill factor, which then allowed an "ideal" I-V curve to be fitted. The maximum power was therefore a best estimate combination of model and measured values, rather than measured maximum power. The PV modules and the logging equipment were separated by three floors and electrically an extra series resistance $R_{s,extra} \simeq 1\,\Omega$ between the PV modules and the measurement equipment. The software and hardware did not easily permit expansion or modification, which led to the need for a new design, aimed at measuring *complete* I-V curves, energy yield and influencing weather parameters at a significantly higher frequency.

[1] This standard has taken 20 years for an update to be published (newest version: 22 Oct 2015).

During the course of the first three years of this PhD, three iterations of the new measurement set-up were run through. The first version was the prototype and proof of concept, with the PV modules and part of the measurement equipment in the original location marked on Figure 2.3. The photograph of the prototype is below.



Figure 2.1: A photograph of the outdoor set-up on 13 May 2013, view is from South-East. Note the pipes on the right, these are exhausts that give off heated air in winter, affecting the temperature measurements on the modules.

With the prototype having shown its capabilities and quite a few shortcomings, the most important being the large physical and electrical distance between the PV modules on the roof and the I-V curve measurement equipment three floors down, the second iteration of the measurement set-up was built on the location that now also serves for the final version of the measurement set-up. This location was chosen as the best compromise between far and nearby shading throughout the year (antennas on the roof, the air conditioning unit, the roof access structure) and minimising cable lengths between the new PV measurement laboratory room and the PV set-up. The photograph of the second version of the outdoor set-up is given in Figure 2.2, with the roof diagram shown in Figure 2.3.

The third and final iteration of the measurement set-up was a modification to better answer measurement needs of the *Smart PV* project and suggestions from industry. The *Smart PV* project had modules with different sub-string configurations and modules at their disposal, with the need for independent, module-level energy yield measurements. The cooperation with the *Smart PV* project, led to further modifications that had to be done to the measurement set-up, partly to accommodate a larger number of photovoltaic modules and



Figure 2.2: A photograph of the second iteration of the measurement set-up, from the access to roof vantage point. Notice the roofing material: this is covered by gravel.

inverters and corresponding amount of sensors. In particular, the need for independent, module-level energy yield measurements resulted in the use of DC-DC converters per module, with similar specifications as developed in the *Smart PV* project.

Concurrently, the roof had to be insulated, which resulted in the measurement set-up having to be dismantled for a few months (November 2014-February 2015). This period was used, among others, to modify the wiring in the original outdoor cabinet, and design and implement the mounting board in the second outdoor cabinet.

The second from top photograph in Figure 2.4 shows the nearby towers which are being demolished at the time of writing, which impede direct sunlight to reach the measurement set-up during moments of the early morning. The air conditioning unit and the inverter mounting racks cause some shading in the evening, although generally the sun is already behind the plane of the array in these moments. In general, the design and placement of the measurement set-up was done so as to minimise shading known at the time of design and installation, and if it did occur, that its influence on the annual energy yield would be limited.

The bottom photograph in Figure 2.4 shows the poles which cause shading in the morning and early afternoon, these are part of a building repair structure which were installed from early September 2015 and are expected to remain in place until September 2016. The amount of shading per module varies depending on the position of the module within the array (see also Figure 2.6), as well as the prevailing conditions: shading is most pronounced on clear sunny days.

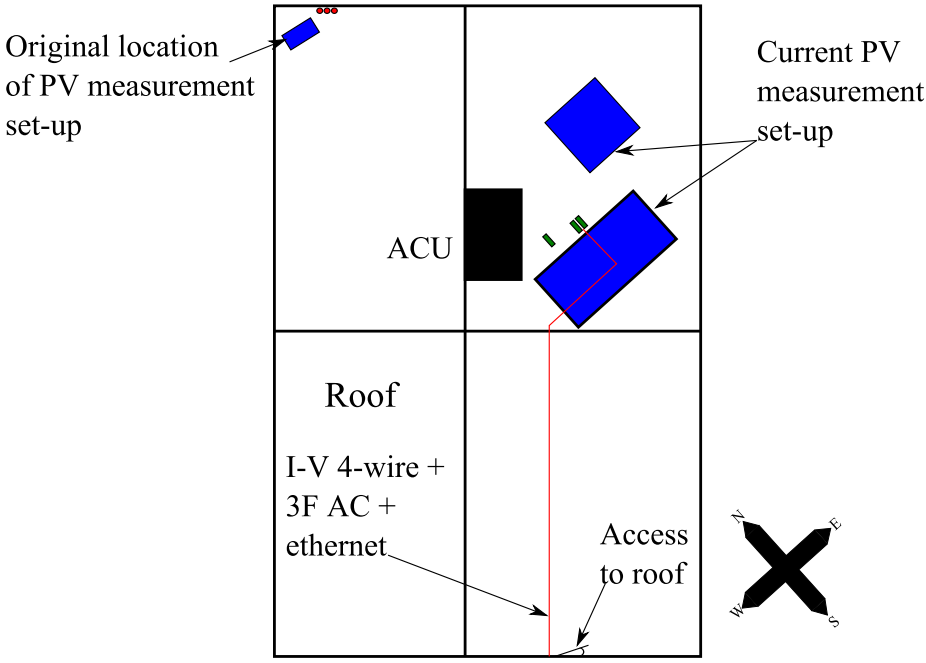

Figure 2.3: A bird's eye schematic view of the original and new location of the outdoor measurement set-up. The area occupied by the PV arrays is indicated in blue. ACU: Air Conditioning Unit. The I-V cables, communication and AC power cables run from the cabinets to the measurement laboratory, distance is approximately 55 m. Figure to approximate scale.

The advantage of the repeated shading is that the measurement set-up is subject to less-than-ideal conditions, yet with a level of measurement accuracy and granularity that is lacking with regular (non-research) photovoltaic systems, which are installed in similarly shaded environments. Many residential and commercial roofs have nearby structures (chimneys, trees, wires) which lead to losses which are often not fully known, or are difficult to attribute. With the measurement set-up having a data available from the module level up to the inverter, conclusions can be drawn regarding the impact of shading on a photovoltaic module and an array. Important here is also that there was a shading-free period of about half a year, which serves as a baseline for shading analyses on the set-up - more details are given in Chapter 5.



Figure 2.4: Multi-perspective photographs of the latest iteration of the measurement set-up. From top: views from South, West, East and North-East.

2.3 Outdoor measurements of PV modules and systems

In order to satisfy the aims given in Section 1.4, a flexible and modular outdoor measurement set-up had to be designed and built. The photographs of the various iterations partly show the visible hardware results at the different stages. In what follows, design and implementation decisions are highlighted for the main choices and parts of the work.

Figure 2.5 presents the high-level overview of the outdoor measurement set-up, showing the main methods of data transmission, and some of the connections. It also shows the number of signals measured per Virtual Instrument (VI) per second, with time-related data added as well. The software used to program the data measurement and collection is LabVIEW 2013 SP1, which runs on a dedicated PC in the PV measurement laboratory, which is located close to the roof with the PV arrays and the outdoor cabinets (see also Figure 2.3).

Four main programs (VIs) designed for the measurement of data run simultaneously on the PC:

- The I-V curve measurement VI, which is used to perform I-V curve measurements and controls the switching (connection and disconnection: commutation) of PV modules from their DC-DC converter or DC-AC inverter.
- The weather VI, which measures and logs the data from the irradiance, wind and temperature sensors.
- The SCB DC voltage (V) and current (I) measurement VI, where the DC voltage and current of PV modules, DC-DC converters and DC-AC inverters is measured and logged, together with the pulse outputs from single-phase AC energy (kWh) meters connected to inverters.
- The AC measurement VI, which takes the data from the three-phase PM3250 AC meter and stores it on the PC.

The link between the files created by the different VIs is the LabVIEW timestamp[2], assigned to each file by the computer. The data from the weather, DC voltage and current measurement and AC data measurement VIs is stored in files in the technical data management streaming (TDMS) format, with at least one[3] file created per day, with all data stored per second. Each row in

[2]This is the number of seconds since 1 January 1904.

[3]More files are created in case of (un)expected shut-downs or human interventions.

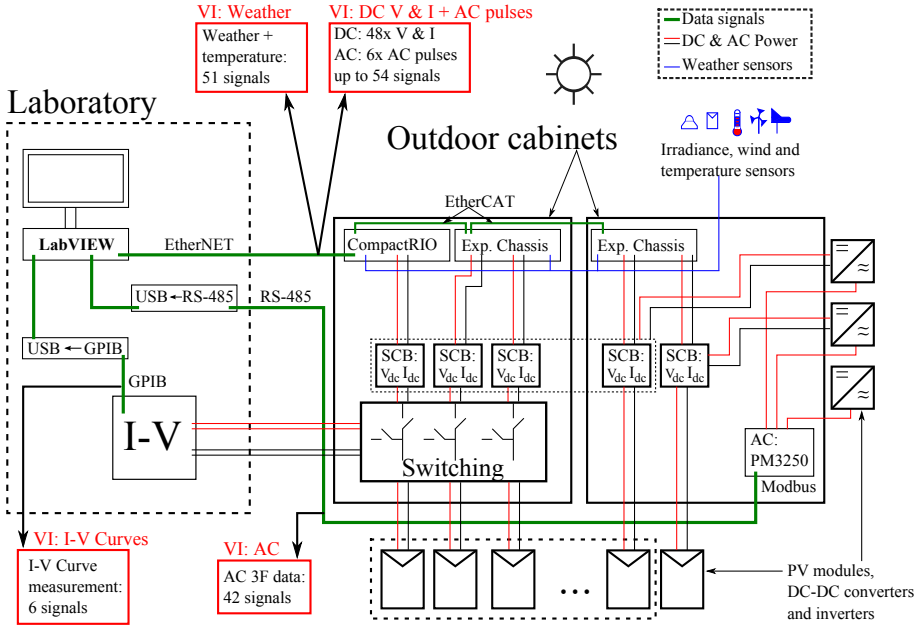

Figure 2.5: Schematic diagram of the measurement set-up.

these files contains the LabVIEW timestamp, thereby allowing the different files to be linked.

In the case of I-V curve measurements, each file is saved in the CSV format, with the name of the file containing the LabVIEW timestamp when the I-V curve measurement was performed. Each I-V curve file contains background information on the module measured, such as the project code number. For the control of the switches (the contactors) and additional measurement equipment, a controller needed to be integrated in the set-up.

The CompactRIO shown in Figure 2.5 is an National Instruments 9024 CompactRIO, a Programmable Automation Controller (PAC), essentially a programmable computer capable of reliably functioning for a long period of time under tougher circumstances than a PC. All the data obtained from the CompactRIO and the two Expansion Chassis[4] NI 9144 [35] is sent to the computer via a dedicated point-to-point EtherNET connection. (The reason for the point-to-point connection is that the CompactRIO's communication is better guaranteed using a fixed IP address, which could otherwise conflict with IT decisions on the campus.)

[4]These communicate via the EtherCAT industrial protocol, as shown in Figure 2.5.

The CompactRIO controls the switches (contactors from [36]) via NI 9472 [37] digital output cards. The NI 9024 CompactRIO and the two NI 9144 expansion chassis contain a large number of measurement cards by National Instruments, for the signals to be measured.

- There are 11 NI 9217 Pt100 temperature sensor measurement cards in use, each can measure up to four Pt100 temperature sensors in a four-wire configuration, for a total of 44 temperature values.
- Two NI 9203 analog current measurement cards (with a typical range of 0 mA to 20 mA) with 8 inputs per card are available (currently one of the two is used) to measure the irradiance, wind speed, wind direction and one temperature, on 4 mA to 20 mA loops. The benefit of 4 mA to 20 mA measurement loops is that a cable disconnection or breakage is indicated as 0 mA, which will often result in an impossible, negative value, compared to the zero line at 4 mA. Additionally, cable lengths can be much longer without reducing measurement accuracy.
- One NI 9422 digital input measurement card with 8 inputs is used to measure the digital output pulses from the AC single-phase kWh meters (see also Figure 2.7).
- Two NI 9205 and one NI 9206 analog voltage measurement cards, each with 16 differential channels are used to measure the voltage and current signals from the PV modules, DC-DC converters and DC side of inverters conditioned by the SCBs (more details are given in Chapter 3).

2.4 Measurements of modules to systems: overview of set-up

The visual lay-out of the measurement set-up, finalised in February–April 2015, is shown in Figures 2.6 and 2.7. The placement of the *Smart PV* photovoltaic modules has been done in order to best permit technology comparisons, traditional monocrystalline silicon versus MWT, as well as 3x20 substring modules versus 10x6 substring modules. In order to keep conditions similar for the core experiment modules (marked in red in Figure 2.6), the eight *Smart PV* modules chosen for more detailed analyses in the project are surrounded by 10x6 monocrystalline modules, aimed at reducing array edge temperature effects. The additional *Smart PV* modules also contributed to improved loading of the SolarEdge inverter. The data of the different modules is given in Table 2.1.

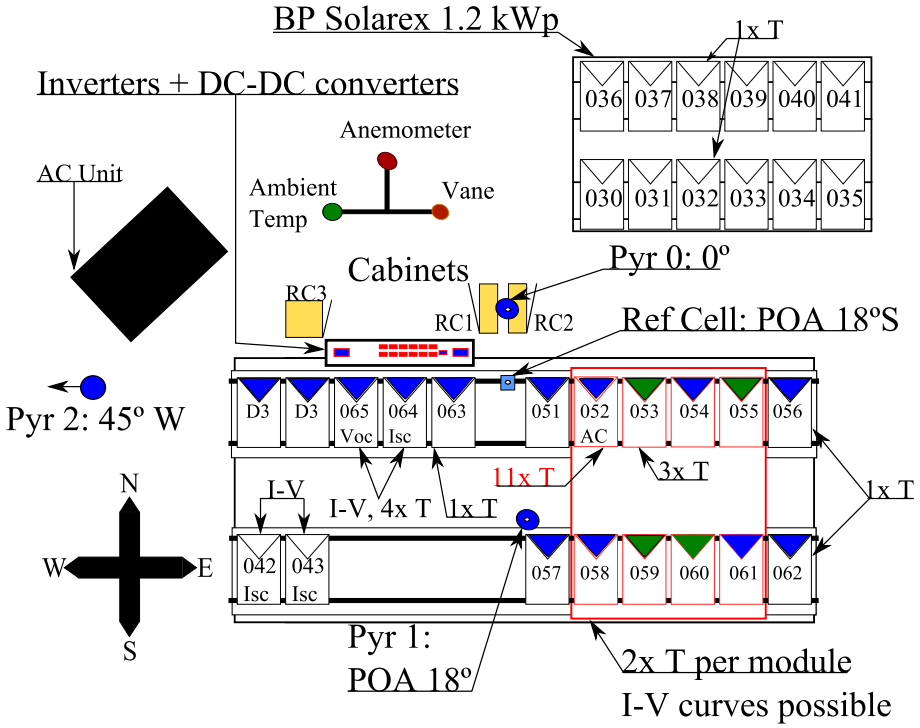

Figure 2.6: A detailed bird's eye view of the set-up, valid as of 2015. The PV modules of the *Smart PV* project (with blue or green triangles, respectively indicating diodes or active bypasses) are indicated, with number of temperature sensors per PV module. Modules 030-043 are Solarex MSX-120 modules, recovered from the dismantled set-up of KU Leuven used in [38]. The electrical equivalent of this figure is found in Figure 2.7. Scale is approximate.

The modules indicated as *064* and *065* and *D3* in Figure 2.6 are also *Smart PV* modules, of which *PV064* and *PV065* are used to obtain the I_{sc} and V_{oc}-condition temperatures. These may be compared to the temperature of the modules (*PV051* to *PV063*) which are connected to an inverter or converter and thus operate at MPP.

Additionally, as many of these modules have their I-V curves measured once per month using the equipment described in Section 2.6, their degradation may be studied at a later date, using the methodology of Jordan and Kurtz [23]. This is discussed further in Section 6.5.3.

Figure 2.7 also indicates the modules which may have their I-V curve measured on-site without interruption of the main power flow to the central inverter.

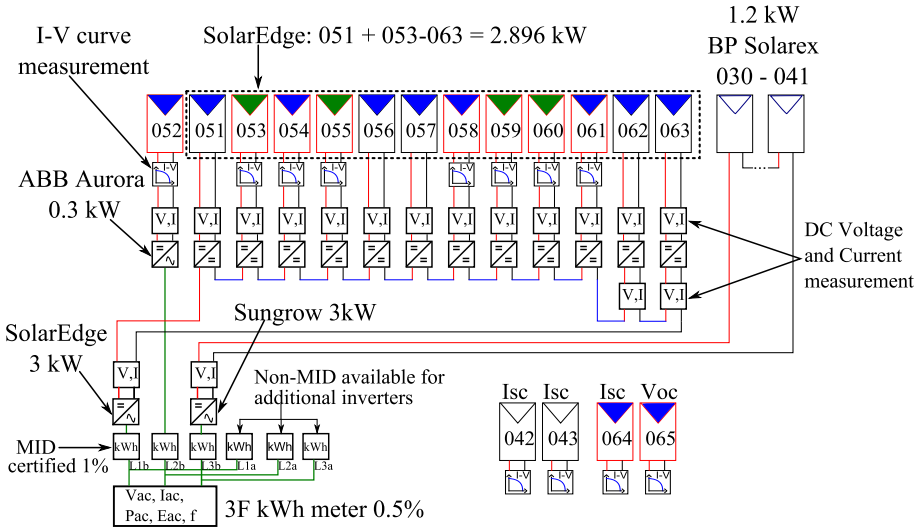

Figure 2.7: The electrical equivalent diagram of PV module connections, valid from 2015 onwards. The bird's eye equivalent diagram is found in Figure 2.6.

In total, up to twelve modules may have their I-V curve measured at regular intervals using the I-V curve measurement VI.

At the time of writing, three inverters are in use: a 3 kW SolarEdge inverter [39] and an ABB 0.3 kW micro inverter [40] for the *Smart PV* modules and a 3 kW Sungrow inverter [41] for the *Residential* system. The *Residential* system is aimed at providing data on a small-scale residential photovoltaic system, for educational purposes. The three inverters are, as shown in Figure 2.7, distributed over the three AC phases, to minimise imbalances and to have per-phase measurements.

The measurement of AC energy is performed with two types of instruments: single-phase kWh-meters with pulse output (MID: [42] and non-MID[5]: [43] certified) and a three-phase meter [44] capable of measuring power, energy and many other standard AC parameters such as the frequency and currents, total harmonic distortion, produced and consumed energy, as well as the meter temperature[6]. The pulse outputs of the single-phase kWh meters are detected using an NI 9422 digital input card [45]; this data is stored, together with the DC voltages and currents measured using the SCBs and NI 9205/9206 cards, in a TDMS file per project: *Smart PV* and the *Residential* system.

[5]Only MID-certified meters can be used for billing purposes: these have been calibrated.

[6]This further serves to verify the temperature inside the temperature-controlled cabinets and ensure that the instruments are kept within their temperature specifications.

Table 2.1: Overview of PV modules and systems measured

Identifier	Technology	Bypass[a] x Cells	P_{STC} [W_p]	Outdoor installation
SE array	mono-Si/MWT	-	2859.09	2014-2015
PV052/ABB	mono-Si	3x20 D	246.30	2014
SGW array	poly-Si	4x18 D	1209.01	2015
PV053/SE	mono-Si	3x20 AB	245.84	2014
PV054/SE	MWT	3x20 D	246.70	2014
PV055/SE	MWT	3x20 AB	243.75	2014
PV058/SE	mono-Si	10x6 D	236.51	2014
PV059/SE	mono-Si	10x6 AB	234.21	2014
PV060/SE	MWT	10x6 AB	238.60	2014
PV061/SE	MWT	10x6 D	237.04	2014
PV051/SE	mono-Si	10x6 D	237.48	2015
PV056/SE	mono-Si	10x6 D	234.57	2015
PV057/SE	mono-Si	10x6 D	233.99	2015
PV062/SE	mono-Si	10x6 D	233.54	2015
PV063/SE	mono-Si	10x6 D	236.85	2015

[a] AB: Active Bypass, D: Diode
[b] *Smart PV* modules flash-tested at Soltech, MSX-120 modules from on-site I-V curve measurements.
[c] MSX-120 modules initially installed $\sim$ 1999, removed in 2011, reconfigured to 40 V, 3 A and installed in 2015, with on-site I-V curve measurements for P_{STC} determination.
[d] Some *Smart PV* placed outdoors in V_{oc} in 2014, others kept indoors until use in 2015. This may impact ageing (and comparisons) of the modules.

The AC data measured using the PM3250 three-phase meter [44] is logged with an "AC logging" VI to a separate TDMS file per day. The data is obtained from the meter using the Modbus protocol, and transmitted using an RS-485 connection and then connected to the logging PC using an RS-485 to USB converter.

2.5 Weather-related measurements

Weather-related measurements are performed using the instruments listed in Table 2.2, with the LabVIEW Virtual Instrument (VI) for Weather measurements. From the prototype of the measurement set-up to the latest iteration, the number of temperature sensors and NI 9217 Pt100 sensing modules was increased from 24 to 44 to accommodate the larger number of photovoltaic modules to be measured.

The pyranometer oriented West at 45° tilt was placed in this orientation, to provide data for future modelling efforts on PV power peak shifting (i.e. that the West-oriented power generation curve better coincides with residential evening load curves). The horizontal and plane-of-array placement of the other pyranometers are standard photovoltaic measurement practice. In particular, pyranometers placed horizontally serve for a local comparison to satellite-derived irradiance data, with satellite-derived irradiance data having the benefit of being applicable to a significantly larger area on Earth. However, the accuracy of ground-based measurements is typically higher than satellite data, for the location measured [46]. The irradiance sensors logged in this set-up may provide additional data for irradiance transposition models (e.g. of Perez *et al* [47] or Yang *et al* [48]) as well as performance modelling of photovoltaic modules and systems for different orientations and tilt angles.

The use and preference for pyranometers or spectrally-matched reference cell devices has been and remains contested within the industry for photovoltaic measurements and analyses. Some [49, 50] prefer and recommend pyranometers, as they are (more) spectrally insensitive and the measurement represents the theoretical maximum irradiance that can subsequently be converted to electricity by photovoltaic systems. Moreover, inter-comparison of data from one location to another is easier to perform if (horizontally placed) pyranometers [51] are used, as the effect of spectral sensitivity (and thus local temporal effects) are mostly removed.

One disadvantage of pyranometers is that, as they convert the photons of sunlight to heat and then a voltage which is measured, they show a time delay compared to the irradiance-to-electricity conversion speed in photovoltaic modules and systems, which becomes pronounced during rapid irradiance changes, e.g. passing patchy clouds. As such, pyranometer-derived measurements will often lag the photovoltaic system response. Secondary standard pyranometers such as the CM11 and CMP11 used for this set-up have among the shortest time constants among pyranometers, yet they may take up to 15 s [52, 53, 54] to indicate large irradiance changes (however the CMP11 pyranometer datasheet specifies <5 s [55]). Furthermore, the response time depends on the size of the

step change in the incoming irradiance.

On the other hand, reference cells which are spectrally matched to the photovoltaic modules used in PV systems will indicate the practical maximum irradiance that can be converted to electricity. If properly calibrated they can have a lower measurement uncertainty than high-quality and high-cost pyranometers [56]. Their irradiance detecting time constant is identical to that of photovoltaic modules, as they are constructed as miniature photovoltaic modules, which is a significant advantage when looking at short-term behaviour [50].

With the above criteria and considerations in mind, the decision to use both pyranometers and a reference cell for irradiance measurement bring the benefits of each technology to the table, as well as some of their disadvantages. For example, the reference cell used (Si-420TC-T [57]) is a mono-crystalline reference cell[7], which is therefore not (fully) spectrally matched to either the MWT and poly-crystalline photovoltaic modules (see also Table 2.1).

This highlights a data and maintenance disadvantage of reference cells: in theory, for each photovoltaic module technology studied, there should be at least one spectrally matched reference cell placed in the plane-of-the-array for proper comparison. For each new technology added (to the set-up), a new, calibrated reference cell should be used, which also includes the need for additional channels and subsequent data analysis. At the time when the irradiance sensors were considered to be purchased, the broader applicability and industry consensus of the preference for pyranometers compared to reference cells won out. This consensus has shifted a little to be more favourable to reference cells, yet pyranometers are still preferred for energy yield and performance ratio analyses as well as inter-location comparisons [50, 58].

One additional aspect that is often overlooked when looking at sensor numbers used in a measurement set-up is the necessary data maintenance, quality control, installation time, available space and finally, data analysis. As Table 2.2 shows, 50 weather sensors with 51 data channels (the reference cell also has its temperature value measured) are concurrently measured in this set-up. The probability on any given day is quite high that one of these sensors will show a failure, indicate a wrong value or require maintenance in some form. If no automatic sensor failure detection mechanisms are in place, e.g. an email or SMS service to warn of errors, a quite long period of time may pass before the situation is detected, analysed, corrected and repaired to the expected value, with additional post-installation data analysis required. Thus, the cost of sensors is not always the main reason why their number in a set-up is limited.

Lastly, outdoor measurements suffer from hard-to-quantify measurement

[7] This is a standard reference cell, with likely an Aluminium back surface.

Table 2.2: Measurement uncertainty and amount of climatic sensors used

Parameter	Subcategory	Amount	Accuracy[a]	Manufacturer
Temperature	Ambient	1	±0.10 °C [59][b]	Thies Clima
Temperature	Module	43	±0.10 °C [60][b]	Omegafilm
Irradiance	Pyranometer	3[c]	±1.4 %[d] or ±1.5 %[e] [53, 55]	Kipp&Zonen
Irradiance	Reference Cell	1	±5.0 %[57]	Ingenieurbüro Mencke & Tegtmeyer GmbH
Wind speed	Cup anemometer	1	<0.2 m/s[g] [61]	Thies Clima
Wind direction	Wind vane	1	±3° [62]	Ekopower

[a] Sensor and basic equipment only; measurement and processing by the respective measurement cards adds extra measurement uncertainty.
[b] Four-wire measurement of Pt100 sensor.
[c] 1 Horizontal CM11, 1 Plane-of-array(18°, South) CMP11, 1 45° West CM11
[d] CMP11: ±1.4 %, calibration report
[e] CM11: ±1.5 %, calibration report
[f] Model Si-420TC-T
[g] Also given as class 0.5. Starting speed: 0.3 m/s

uncertainties and variabilities. It is very difficult (and not always desirable) to control the conditions to which photovoltaic modules are exposed. In this regard, the placement of sensors may not satisfy all possible research questions. For example, while the measurement of irradiance is subject to uncertainties which are one or multiple orders of magnitude larger than for electrical measurements (e.g. pyranometer: ±2 % versus digital multimeter (DMM): ±0.0040 % [63]), it is relatively speaking easier than the measurement of the wind speed and direction: the sun's path over the sky is slow and predictable, and the sensor can thus be pointed in the correct direction whereas the placement of single wind sensors can not anticipate for local turbulence effects.

Moreover, it can be argued that there is one irradiance for a location, but not one wind speed and direction: the interaction of modules with the wind result in very local effects, which would require a multitude of wind sensors to achieve the same type of one-to-one correspondence between module and measurement.

The caveat of cost of sensors from above is even more valid in this case. Follow-up questions that then arise are then related to the height and distance of the wind sensors from the modules. Wind and temperature measurements also suffer from a general lack of a reference frame: is the value indicated by the sensor correct? Perhaps the temperature sensor has come loose (as discussed further in Chapter 4) from the module surface, or the anemometer suffers an offset. While wind speed and direction have physical limitations (such as that no negative wind speeds are possible, and that the wind direction must be between 0° and 360°), it is difficult to identify whether the values are correct, until the sensors are calibrated, or subject to additional verification on-site.

2.6 Automated outdoor in-situ I-V curve measurements

For the measurement of I-V curves, the initial focus was on obtaining the highest achievable and affordable I-V curve measurement accuracy while also measuring multiple weather parameters, especially temperature and the main parameters of irradiance, wind speed and direction. This choice implied that keeping PV modules at MPP between I-V curve measurements could only be achieved in a cost-efficient manner using commercial inverters, rather than opting for (custom-made) module-level power electronics [64, 65, 66].

Methods for I-V curve measurement revolve around the need to vary the impedance at the PV module clamps, so that as much as possible of the PV module's first quadrant is measured. Ideally, the "true" open-circuit voltage (V_{oc}) and short-circuit current (I_{sc}) are measured, instead of calculated through extrapolation (this is, however, a valid approach [26]). Obtaining the first-quadrant I-V curve can be achieved by means of capacitor charging [67], by using four-quadrant source meters [68] or by varying the resistance of a programmable electronic load [69] or a (power) MOSFET [70] or similar electronic devices [71].

One determining factor for the price of measurement or conditioning equipment has been systematically seen to be power dissipation above typically 50 W or 5 A. In particular, instruments capable of dealing reliably and consistently with currents above 5 A show a significant price jump, due to the additional design requirements for dealing with the associated resistive heating inside the instrument in a safe and reliable manner.

For repeatable, accurate, I-V curve measurement for the measurement set-up, the following options were considered:

- The cost of I-V curve tracing tools was either very high compared to the available budget, e.g. the Daystar 1000 V – 100 A I-V curve tracer [72] would have cost more than 90% of the available starting budget, or the accuracy of alternatives did not meet the requirements (e.g. maximum power uncertainties of at least $\pm 5\,W_p$), or the manufacturer did not respond to inquiries.
- Four-quadrant source meters such as the Kepco BOP 1 kW [73] were a possibility, although cost and I-V curve measurement speed (the documentation specifies a time of at least 20 ms per measurement point [74]) were a concern. In particular, aiming to measure I-V curves in less than one second (cf. the interest in transient analysis from Section 1.4) would only be possible with less than fifty points per curve, which is much less than recommended by, among others, [34].
- Programming a MOSFET or other power electronic device to serve as a variable load was seen to be very time-consuming compared to the documented accuracy [70] achieved, despite the possibility of low cost for the system.
- Programmable electronic loads are situated cost-wise between custom-designed power electronic loads and (accurate) capacitive I-V curve tracers. The N33XXA family of programmable electronic loads by Agilent (now Keysight) was marketed (among other uses) for I-V curve measurement of "high-power" PV modules.

As the focus of the work was to develop a flexible, multi-purpose measurement set-up (and not specifically to develop a new/better/cheaper I-V curve sweeping and measurement method), the decision was therefore made to use an Agilent N3306A programmable electronic load inside an Agilent N3300A mainframe for the I-V curve sweeping. This configuration also provided the ability for future expansion, as two more N3306A (or similar) programmable electronic loads could fit into the N3300A mainframe.

In terms of cost, the I-V curve measurement equipment (in this case, electronic load, digital multimeters, shunt resistor and computer) is sufficiently expensive that devising a means (i.e. a commutation or switching mechanism, using a multiplexer or similar switching equipment) to re-use this for multiple modules is worth the effort (this is also done by e.g. [20, 68]). An additional benefit is that having an automated process to disconnect-measure I-V curve-reconnect a module leads to improved repeatability and user-friendliness: there is no need to manually disconnect a PV module from its string (possibly also interrupting the power flow to the inverter) to measure an I-V curve, as is the case with portable I-V curve tracers (see e.g. [22]).

The general principle of the switching or commutation mechanism shown in Figure 2.5 is given with more detail in Figure 2.8, with the detail of the I-V curve measurement circuit shown in Figure 2.10. Figure 2.8 shows the principle used to disconnect a PV module from a string connected to an inverter, and then to the I-V curve measurement circuit. This example shows two inverters that can be used, where their PV modules can be disconnected from the string, have their I-V curves measured and subsequently reconnected to the inverter string, without[8] interrupting power flow to the inverter.

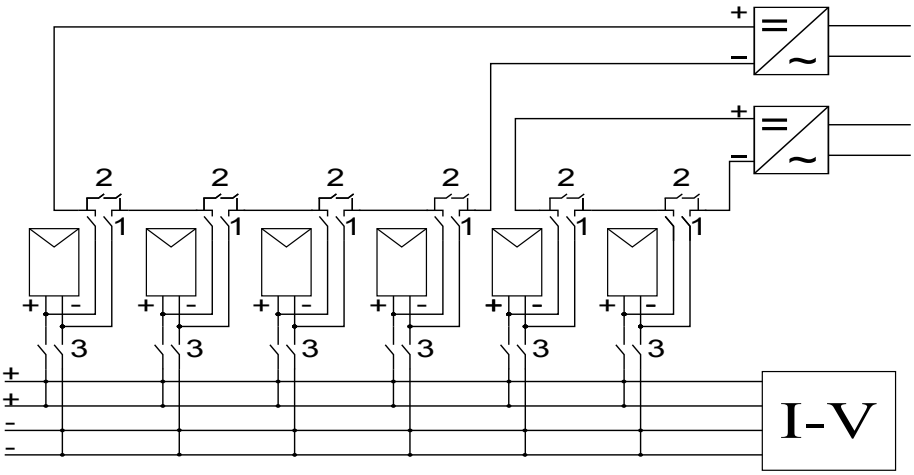

Figure 2.8: A schematic overview of the contactors for I-V curve commutation: 3 contactors per PV module are required. The I-V curve measurement circuit is shown in Figure 2.10.

The sequence of switching the contactors for the I-V curve measurement is shown below, in Figure 2.9. The current default method for the I-V curve measurement is in *sweep* mode, where the programmable load varies its voltage from zero to its maximum (or also in the reverse direction) at a rate[9] of 1 kV/s, which means that the actual I-V curve measurement duration is approximately 40 ms for a module with an open-circuit voltage (V_{oc}) value of 40 V.

The contactor "dead time" (or non-guaranteed switching time: the contact may not be fully closed or opened before the end of the interval) of 60 ms also adds to I-V curve measurement duration. To ensure a fully closed or opened contact, the dead time is assumed to last 100 ms, which should help to avoid the situation of unintended (short-circuit) current flows in the measurement set-up

[8] This is only valid if there are two or more modules in the string.
[9] This is the *slowest* rate in *sweep* mode available.

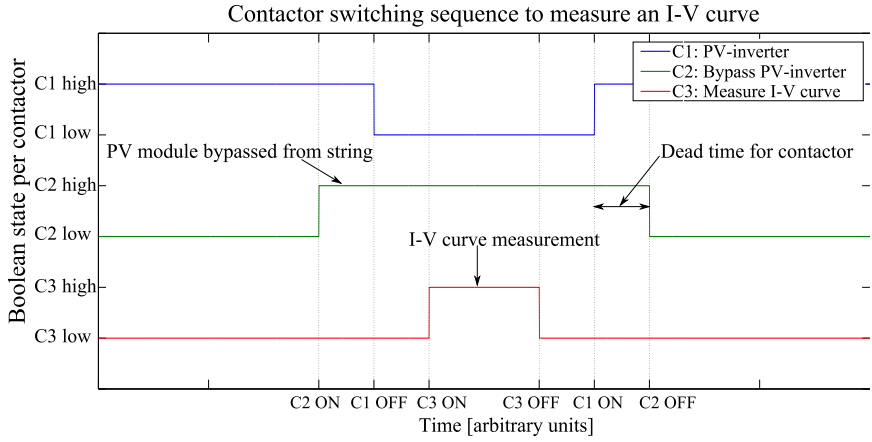

Figure 2.9: The boolean states of the three contactors used to disconnect a module from its string, measure its I-V curve and re-connect it to the string.

from happening. The time in Figure 2.9 indicated is in arbitrary units, as the duration varies from I-V curve to I-V curve measurement, although generally speaking, it takes approximately 2.5 s to disconnect a module, measure an I-V curve, reconnect the module and have the system ready for the next I-V curve measurement, if applicable.

The period indicated by the I-V curve measurement in Figure 2.9 includes instrument triggering, measurement, post-processing and file creation. The triggering serves to warn the instruments that a measurement will occur. As such, measurements are started before the I-V curve is measured and stopped afterwards, and cropped during the post-processing stage.

It could be argued that this sequence can be optimised for faster sequential I-V curve measurements (e.g. to start to measure the next I-V curve during the file creation of the previous I-V curve), but the programming cost and possibility of damage to the instruments outweighs the currently identified benefits. Moreover, as the I-V curve measurement files have the timestamp which allows them to be linked to the prevailing weather conditions, the possible variability in weather (particularly irradiance) between the measurement of one I-V curve and the next can be detected and if necessary corrected for by post-processing or filtering [26, 27].

As currently 36 contactors are available, up to twelve PV modules can have their I-V curve measured sequentially, with the total sequence (for all twelve PV modules) lasting approximately 30 s for a sequence of twelve *sweep mode* I-V curve measurements. If measurement of capacitive or otherwise special PV

modules would be called for, the I-V curve curve can also be measured in *list* mode, which is less easy to implement and slower in practice to measure. In such cases, the total I-V curve measurement sequence will be longer than N modules times 2.5 s, as the longer I-V curve measurement part (i.e. the actual variation of the electronic loads' impedance) for capacitive (or otherwise special) modules will exceed the aforementioned ∼40 ms to 100 ms.

While the interval between I-V curve measurement loops (where all the modules whose I-V curves will be measured sequentially) can be set anywhere between 1 ms and 999 999 ms, it has in practice been set at 5 min, 1 min and 30 s intervals. The interval durations have been chosen so as to disturb the maximum power point tracker (MPPT) of the inverter or DC-DC converter as little as possible. In particular for inverters, removal of too much power from the input leads to it performing a grid connection check (similar to start-up in the morning), which leads to more losses than necessary and is slower than a corresponding action for DC-DC converters, as the latter do not need to perform this grid synchronisation check. This is important for energy yield comparisons, as the philosophy is to disturb the system as little as possible to reduce the avoidable losses.

One additional aspect of the I-V curve Virtual Instrument (VI) is its use to control the contactors, even for modules which will not have their I-V curve measured at this time: all modules have a "resting" condition (e.g. connected to an inverter, or disconnected: V_{oc}), which applies to all modules at the same time. In case of a power outage or software restart, all the contactors return to their normally open (i.e. not connected) position. As a result of this decision, a human intervention is required in order to ensure that the modules are connected to the DC-DC converters or DC-AC inverters.

A delay in the human intervention thus leads to a longer-than-required energy capture loss. On the other hand, having modules at V_{oc} instead of immediately restored to their previous (possibly erroneous?) state is safer. This has led to data and energy losses in the past, as electrical maintenance work and outages have resulted in either the logging PC to temporarily shut down, or the full system turning off and back on again. The installation of an uninterruptible power supply (UPS) has remedied most of the computer-related issues, but not broader electrical outages on the campus, which affect the outdoor equipment.

The I-V curve measurement circuit (shown as the I-V block in Figures 2.5 and 2.8) is shown in Figure 2.10, with the added (extra) circuit resistance $R_{s,extra}$ between PV module and four-wire connection also shown. This $R_{s,extra}$ encompasses the wiring between cabinet and module, as well as the resistance of the contactor to the four-wire circuit, located in the measurement laboratory. (Due to the use of the contactors, a two-wire connection between module and

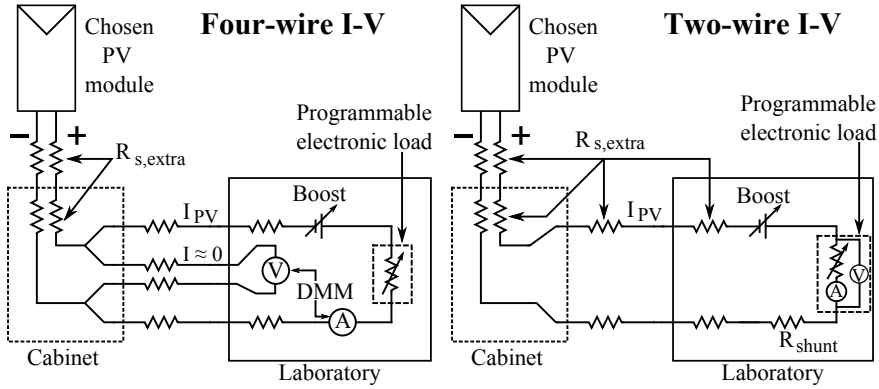

Figure 2.10: A schematic overview of the four-wire DMM I-V curve measurement circuit employed, contrasted with the two-wire measurement of the electronic load (e-load).

four-wire bus in the measurement cabinet is necessary.) Thanks to both shorter distances and thicker wiring (from 2.5 mm^2 to 10 mm^2), this resistance was reduced from $\approx 1\,\Omega$ to 69 mΩ from the prototype version to the current iteration. Reducing the R_s leads to a lower uncertainty and reduced power losses prior to measurement.

Measurement accuracy for electrical measurements is aided by the use of four-wire connections, by which the voltage drop is practically eliminated for voltage measurement. Similarly, the two-wire current and voltage measurement performed inside the programmable electronic load will be less accurate than the same measurement performed in a four-wire configuration as shown in Figure 2.10. Moreover, the Agilent 34410A Digital Multimeters used for the four-wire voltage and current measurement have a much higher accuracy (lower measurement uncertainty) than the programmable electronic load as shown in Table 2.3. Nevertheless, using and storing both the programmable electronic load and the DMM measurement data for each I-V curve measurement allows for a rapid comparison of the results, and to identify errors if and when they appear.

An example of problems would be that the boost power supply is turned off and not back on after a power outage (see also Figure 2.10). The boost supply is required in order to obtain the true short circuit current I_{sc}, and is set at 3 V, per the recommendations [75] of the electronic load[10] (otherwise, as the resistance of the e-load can not become zero, the true I_{sc} is not reached). This

[10] A higher voltage ensures that I_{sc} is reached, but the available voltage range is diminished as in $V_{range,available} = V_{range,nom} - V_{boost}$.

boost voltage is taken into account in the I-V curve measurement VI, but it also means that if the boost supply is not on, that the DMM measured voltage will be offset by 3 V, which is easily seen on graphs and subsequently corrected.

Table 2.3: Comparison of typical electrical measurement uncertainty of I-V curves

Parameter	E-load uncertainty[b] [75]	DMM uncertainty[c] [63]
Voltage[a] [V]	$1.71 \cdot 10^{-1}$	$1.55 \cdot 10^{-2}$
Current[a] [A]	$1.91 \cdot 10^{-1}$	$1.25 \cdot 10^{-2}$
Power[d] [W]	2.21 (2.79)	0.60 (0.79)

[a] Expanded measurement (k=2, 95 % confidence interval) uncertainties [12], for expected range: 0 A to 10 A and 0 V to 40 V
[b] Two-wire connection.
[c] Four-wire connection.
[d] Expanded measurement (k=3, 99.73 % confidence interval) uncertainties [12], for typical values at MPP: 0 A to 8 A and 0 V to 30 V (nominal values: ∼10 A and ∼40 V)

The choice for the contactors used was one which encompasses safety, reliability and low added series resistance (16 mΩ per contactor, 8 mΩ per path). The safety and reliability aspect was deemed to be very important, which led to the choice of over-dimensioned contactors, capable of switching up to 3 kW of AC power (although derated for DC switching to <1 kW) [36]. Compared to electronic switching equipment (multiplexers, MOSFETs, ...), the contactors chosen had both a higher withstand voltage rating, a lower on-resistance and a much simpler method of control: by using the digital output switching of the NI 9472 [37], the contactors could be turned off or on at will. For the I-V curve measurement, the voltage drop that is a result of the total R_s is compensated in the I-V curve measurement VI as well (albeit only for the four-wire measurement data), so the data saved to the I-V curve files does not require additional post-processing to correct for this aspect.

One additional remark is that the electrical measurement uncertainty of an I-V curve is but a small component of the total I-V curve measurement uncertainty budget, with Müllejans *et al* indicating this to be between 2 % and 5 % at the European Solar Test Installation ESTI. At ESTI, the rest of the uncertainty budget for outdoor measurements is mostly temperature distribution uncertainty (∼60 % and the irradiance reference device (20 % to ∼40 %)) [28]. The large uncertainty component due to temperature (in)homogeneity further stimulated investigation, with more details in Chapter 4.

2.7 Photovoltaic system behaviour during I-V curve measurements

To illustrate the functioning of the commutation mechanism, data is taken from the multiple I-V curves measured on a clear-sky day on 22 August 2015. The measured I-V curve of module *PV053* is shown in Figure 2.11, which is at the start of the measurement sequence of Figure 2.12. (No corrections for temperature and irradiance according to IEC 60981 [27] are performed in this example.)

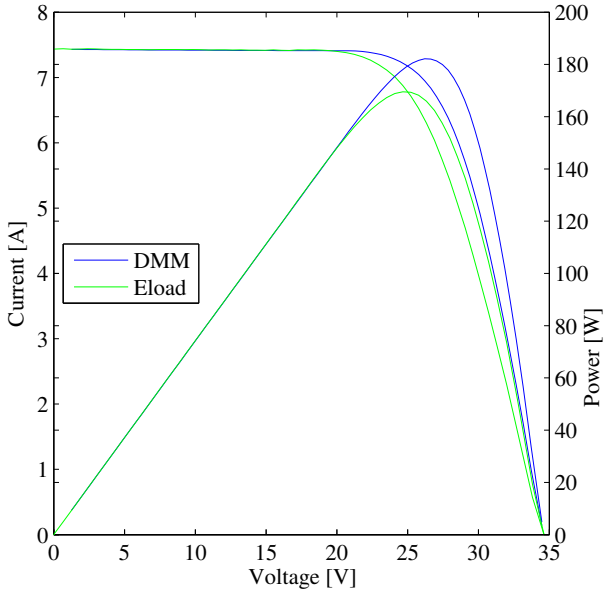

Figure 2.11: An example of an I-V curve measured on module *PV053* during inverter operation on 22 August 2015 at 13:11:59. $G = 907\,\mathrm{W/m^2}$, ambient temperature $(T_{amb}) = 28.65\,^{\circ}\mathrm{C}$, average $T_C = 47.39\,^{\circ}\mathrm{C}$. Average wind speed 1.59 m/s from SSE. The difference between the four-wire measurement of the I-V curve using the DMM and the two-wire measurement using the e-load is noticeable.

Figure 2.11 illustrates the effect of the four-wire DMM measurement compared to the two-wire internal measurement by the e-load (see Figure 2.10). The difference of the peak power measured by each instrument type is significant: the electronic load (e-load) indicates MPP $= (169.52 \pm 2.21)\,\mathrm{W}$ whereas the DMM measurements give MPP $= (182.14 \pm 0.60)\,\mathrm{W}$. The voltage drop inside

and outside[11] the electronic load thus contributes to it measuring a value that is 12.62 W lower. (Having the data from the electronic load available is useful to verify proper functioning of the DMMs, which is why it is also stored in the I-V curve files.)

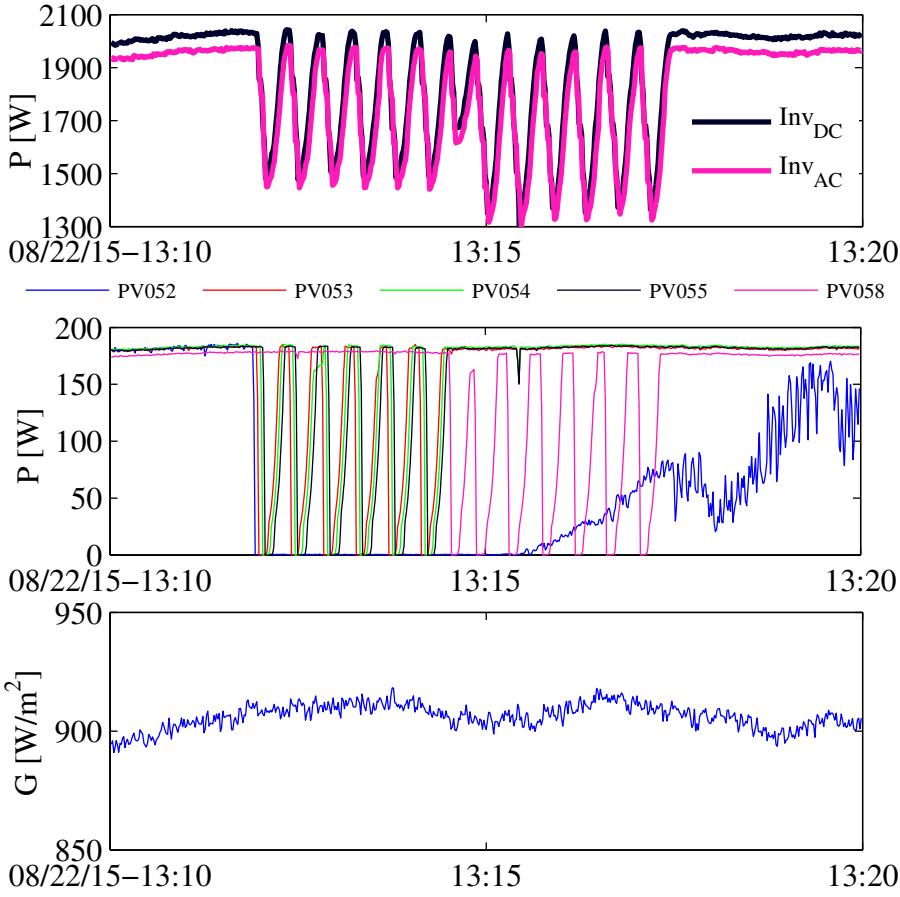

Figure 2.12: An example of I-V curve switching during inverter operation on 22 August 2015. The irradiance is quasi constant at $(906 \pm 5)\,\mathrm{W/m^2}$. See also Figure 5.19.

Figure 2.12 shows the power of the main SolarEdge inverter, while up to four modules' I-V curves are sequentially measured, for a total of 52 curves during the interval. Each large power dip in the top subplot of Figure 2.12 is a grouped

[11] The electronic load sees an additional R_s to the module, which leads to an additional voltage drop of ∼1.5 V and 11 W to 12 W loss at ∼8 A.

I-V curve measurement sequence. The modules whose I-V curves were measured were placed in these groups to keep the energy losses for all modules similar as well as the weather conditions for each group. The reference module *PV052* has a longer restart sequence than the modules connected to the DC-DC converters, as it is connected to the ABB micro inverter; the time between an I-V curve and returning to MPP takes approximately 20 s for the DC-DC connected modules, and 6.5 min for the micro inverter. Performing I-V curve measurements for all *Smart PV* modules sequentially (i.e. *PV052 to PV061*) would lead to too high energy losses for *PV052*, as the micro inverter needs to perform start-up checks: the disconnection of the PV module is treated as an error by the inverter. The duration of the (complete) power loss due to I-V curves measurement for *PV052* is thus shortened to ∼4 min instead of ∼6 min to 8 min.

Figure 2.12 illustrates how the grouped I-V curve measurement sequence results in the SolarEdge inverter losing the power of modules *PV053, PV054, PV055* and then *PV058-PV061* alternately, yet it continues to work properly. Module *PV058* has its I-V curves measured in the sequence following that of modules *PV052, PV053, PV054, PV055*: once their I-V curve measurement sequence has finished, they return to MPP. (See also Figures 2.6 and 2.7 for the lay-out and configuration of the arrays).

The grouped I-V curve measurement sequence duration for this example was ∼26 s, which comprised four sequential I-V curve measurements lasting ∼2.5 s each and a 15 s pause between I-V curve measurements[12].

The proper operation of the inverter is visible both on the DC as the AC side in the top subplot of Figure 2.12, with the power loss during the I-V curve measurement loop sequence amounting to maximum 550 W for the first half (the second half of the sequence has four modules disconnected from the SolarEdge). The maximum power, measured individually using the SCBs[13], of *PV053, PV054, PV055* is ∼183 W just before I-V curve measurement, which added together amounts to 549.3 W. Comparing the continuously measured power for *PV053* to the I-V curve value from Figure 2.11 also indicates that this is similar[14], giving further credence to these values. The measurement uncertainty of the SCBs will be discussed further in Chapter 3.

[12]The remaining one second may be either a time-rounding error in the figure plot (limited resolution) or a slightly longer I-V curve measurement duration. As LabVIEW is a sequential events-based programming language, a delay in one action results in delays in the chain. (Parallel data processing is supported by LabVIEW, but there will always be bottlenecks.)

[13]See Chapter 3

[14](182.14 ± 0.60) W (I-V) at 907 W/m^2 $\simeq$ (183.26 ± 0.60) W at 913 W/m^2 versus (182.7 ± 1.9) W (SCB) at 913 W/m^2

2.8 Data and its treatment for analyses

With few exceptions, the data shown and used in the examples of this text is daylight filtered data (filter: average G>10 W/m^2 for the three pyranometers), as this encompasses the moments of interest for photovoltaic research. The program used to analyse and generate the figures is Matlab, which required the files to be transformed to a Matlab-compatible format. The methods used and how files are linked is described in Appendix D.

2.9 Conclusions

The measurement set-up described in this chapter is flexible, modular and may be expanded with limited software and hardware modifications. Measurements of the most important parameters for photovoltaic module and system analysis, from the irradiance, ambient temperature and wind speed and direction are done at a rate of 1 Hz. The large number of temperature sensors measured permit continuous monitoring of the thermal behaviour of photovoltaic modules, with the ability to evaluate module intra- and inter-module temperatures, which can then be linked to irradiance as well as wind speed and direction. These aspects are discussed further in Chapter 4.

On the electrical side, measurements are performed with a level of granularity and flexibility that is among the state of the art, from DC measurements of individual modules up to the AC side of inverters. Measurements are done using complementary approaches, which on aggregate permit a better understanding of photovoltaic module and system performance:

- I-V curves of photovoltaic modules in outdoor conditions can be measured using a fully automated system, with currently between one and twelve modules that can have their I-V curve measured sequentially - this may be expanded in the future as the design of the system is modular. The switching methodology allows modules to be disconnected from commercial DC-DC and DC-AC converters and reconnected so that the modules can be kept at MPP, which ensures a realistic module temperature; this approach also best approximates real outdoor use of photovoltaic modules, which may be important for degradation and other performance analyses in the future.

  Full I-V curves are measured using an electronic load and two 6.5 digit Digital Multimeters, with both two-wire (e-load) and four-wire (DMM) connections and measurements as mutual verification. The I-V curves

can be used for a wide range of applications, from determination of P_{STC}, degradation analyses (e.g. using the approach of Jordan and Kurtz [23] or others [76]), they may be used for IEC 61853-1 [77] purposes, in situ self-calibration of signal conditioning board power values, calibration or validation of photovoltaic module models - e.g. the electrical-optical-thermal model of Goverde *et al* [78], ...

- SCBs are used for continuous electrical performance monitoring of multiple modules, inputs and outputs of DC-DC converters, as well as inputs of DC-AC inverters at a rate of 1 Hz. If performance deviations are observed using the continuously monitored data, the possibility of I-V curve measurement permit the cause to be ascertained, without the need for physical removal from the array, e.g. for indoor flash testing. The design, testing and measurement uncertainty of the SCBs are discussed in more detail in Chapter 3.
- The main AC parameters such as power, voltage, current, frequency and energy are measured using industry-standard equipment, and allow the complete system's performance to be measured, also at a rate of 1 Hz.

Chapter 3

Signal conditioning for outdoor electrical measurements

3.1 Introduction

This chapter discusses the design decisions, development and calibration of the signal conditioning boards (SCBs) used to measure the DC voltage and current, which are then used to calculate the power and energy of the modules, DC-DC converters and DC-AC converters measured.

The discussion of measurement uncertainty in this chapter is also applied to other values (e.g. measured temperatures - see Chapter 4), but given the similarity in methodology, not repeated.

The determination of measurement uncertainty is a vital yet complex component in the photovoltaic industry, as the magnitude of measurement uncertainty impacts the complete value chain, from investment decisions, warranty claims to final yield. The investment uncertainty in the choice of investing in a photovoltaic system with a nameplate power of 1 MWp where the module manufacturer has a power rating uncertainty of $\pm 5\,\%$ versus the same but with an uncertainty of $\pm 3\,\%$ does not scale linearly: the two percent-point difference may be judged [10] more strongly by a lender, leading to a higher rate of the project weighted average cost of capital (WACC), which may result in a project

proposal being accepted or rejected. Similarly, if data from monitoring suggests that the degradation rate of the modules in a system exceeds the manufacturer's warranty within a certain period of time, then the data must be sufficiently trustworthy for the claim to go through.

For research purposes and service to industry, a lower measurement uncertainty *together* with proper practices allows more aspects to be uncovered, from the effect of temperature on a system's efficiency to trends in the behaviour of the system.

3.2 Multi-level energy yield measurements on modules, DC-DC converters and DC-AC inverters

During the period of operation of the second iteration of the measurement set-up (December 2013 – 31 October 2014), the opportunity arose to measure the power, energy and temperature behaviour of PV modules for the *Smart PV* project, with a focus on module-level energy yield. These PV modules were designed at IMEC and manufactured by Soltech. Within the *Smart PV* project, there was the need to measure the energy yield per module, many of which were different to each other in one regard or other, such as cell technology, or internal stringing arrangement. Given the state of the existing measurement set-up at that time, it was agreed that there would be significant synergistic advantages to improving this set-up to accommodate the additional measurement needs, rather than duplicate the set-up building efforts elsewhere.

In design terms, the modification to the measurement set-up meant that instead of measuring the DC power (and by extension, energy yield) of up to three inverters, many more DC signals needed to be safely and accurately measured, and a related number of AC signals. As the requirement was to evaluate the individual energy yield of at least eight different PV modules, the set-up had to accommodate either a DC-DC converter (with MPP tracking) per module, or module-level inverters. As other aspects of the *Smart PV* project focused on a DC-DC conversion followed by DC-AC conversion, the choice was made to aim for commercial DC-DC converters with similar input specifications as within the project.

The above requirements lead to the use of SolarEdge 300 W DC-DC converters [79] per *Smart PV* module, together with their single-phase 3 kW [39] inverter. The initial STC power rating of the *Smart PV* modules was in the range of 230 Wp to 250 Wp. One industry-standard module (*PV052*: mono-crystalline

cells, three bypass diodes, each for 20 cells) was to be used as a reference for temperature behaviour, with ten Pt100 temperature sensors laminated against the cells. As a safety measure, this module had to be connected to a micro inverter as the Pt100 leads could provide an electrical fault path, especially if this module would have been connected to a high voltage DC string. This module was then connected to an ABB Micro 0.3 kW [40] inverter.

To achieve near-optimal electrical loading of the SolarEdge 3 kW inverter, twelve *Smart PV* modules with a dedicated DC-DC converter each had to be connected. As a result, the individual module energy yield measurements were not for eight modules, but the twelve SolarEdge modules and the reference module (*PV052*) on the ABB Micro inverter.

Additionally, the availability of Solarex MSX-120 modules [80] recovered from the now dismantled set-up described in the work of [81] permitted a small residential-equivalent system to be built for educational purposes, consisting of twelve (originally) 120 W_px modules connected to a Sungrow 3.0 kW inverter. The Sungrow/MSX - 120 system has a low inverter loading ratio, which affects the system behaviour, as will be discussed in Chapter 5. The power values for the MSX-120 modules have been measured[1], calculated and corrected using the I-V curve measurement equipment described in Section 2.6. The calculations and corrections were done using LabVIEW VIs which were developed for this purpose according to [26, 27], prior to the system commissioning.

As manufacturers of DC-DC converters and DC-AC inverters rarely indicate the measurement uncertainty of the DC input values and if it is done, no guarantee about their correctness is specified by the manufacturer. This led to the need to install additional measurement equipment between the individual PV modules and their DC-DC or DC-AC converters to measure the modules' individual energy yield. As the effort was already undertaken to perform measurements between PV modules and their DC-DC and DC-AC inverter, the outputs of two DC-DC converters and the main DC-AC inverter could also be measured. The AC data measurement was described in Section 2.4.

A conceptual figure which shows the measurement of power and energy between modules and the inverter(s) in a photovoltaic system is Figure 3.1. The electrical equivalent diagram for energy yield determination is given in Figure 2.7.

[1] On average, the modules have a P_{STC} value of 100 W_p. As the modules were not flash-tested prior to installation, statements regarding the extent of degradation are difficult to quantify (according to the data sheet, the initial power was 120 W_p, with likely ±5 % binning).

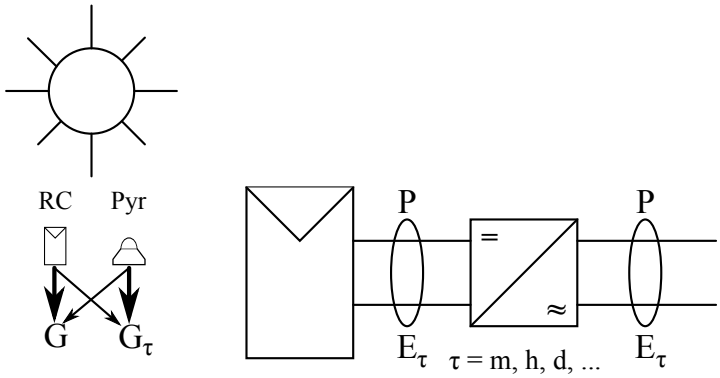

Figure 3.1: General locations of power and energy yield measurements in a photovoltaic system. RC: Reference cell, Pyr: Pyranometer.

3.3 Multi-level DC logging: need for signal conditioning boards

3.3.1 Introduction, rationale and design

As described above in Section 3.2, the need to measure a significantly larger number of DC voltages and currents (and thereby DC power and energy) led to a critical evaluation of the prior performance and whether this could be implemented in a safe, accurate and timely manner, given the deliverable requirements of the *Smart PV* project.

The safety and accuracy considerations required the DC voltage and current measurements to be performed differently than originally considered. Measuring the voltages and currents of multiple DC-DC converters in an unsafe manner could lead to the creation of ground loops which could result in inaccurate (or even incorrect) measurements being performed and worse still, introduce a safety hazard.

In order to continue using the available hardware[2] and LabVIEW software with minimal changes, the decision was made to design a signal conditioning board (SCB) which would isolate the power side from the signal side, at the same time conditioning the signals for optimal measurement by the voltage measurement cards.

[2]Specifically, the NI 9205/9206 multi-channel analog voltage cards, as well as the CompactRIO and expansion chassis.

The high-level design goals were:

- Develop an affordable and electrically safe (i.e. galvanically isolated) system which can present a stable signal to measure module currents and voltages, using the available hardware (NI 9205/9206 voltage cards) and software. Using these currents and voltages, the energy yield of at least 12 modules must be measured-calculated, with a *power* uncertainty of less than 0.5 % of full scale.
- Develop the LabVIEW VI to measure and store the data from the multiple photovoltaic modules to be logged. As the DC energy yield of the modules was to be measured, measuring the system energy yield on the AC side of the inverters was also a useful addition.

These decisions for the DC energy yield measurements had a number of design constraints:

- The cost per measured signal pair (one voltage, one current) should be as low as possible, while achieving the highest accuracy possible. The SCB must be both reliable and easy to power, in particular for multiple SCBs.
- Provide electrical safety to users and visitors to the measurement set-up: the signal conditioning board must fulfil basic IP20 protection criteria, as the set-up can be used or accessed by master thesis students. Galvanic isolation is required between power and measurement circuits; sensor responses should be as linear as possible.
- The output signals should be optimised for the NI 9205/9206 card measurement ranges (any of ±200 mV, ±1 V, ±5 V, ±10 V)[82]. Moreover, the voltage signals should have a sufficiently low output impedance (significantly below 1000 Ω) for correct measurement by the NI 9205/9206 cards.
- The dimensions of each SCB should be similar (or smaller) than the contactors used, to fit in the outdoor cabinets.

The first design iteration is shown in Figure 3.2. The isolation amplifier used is an Avago ACPL-C87BT differential amplifier [83] with unity gain for 0 V to 2 V, a high equivalent input impedance of 1000 MΩ and a low output impedance of 36 Ω. From these data sheet values, the expectation was that the output voltage would be both accurate and stable. This turned out not to be the case, with a document from the manufacturer [84] hinting at an insufficiently stable output signal, requiring an Operational Amplifier (opamp) for stabilization.

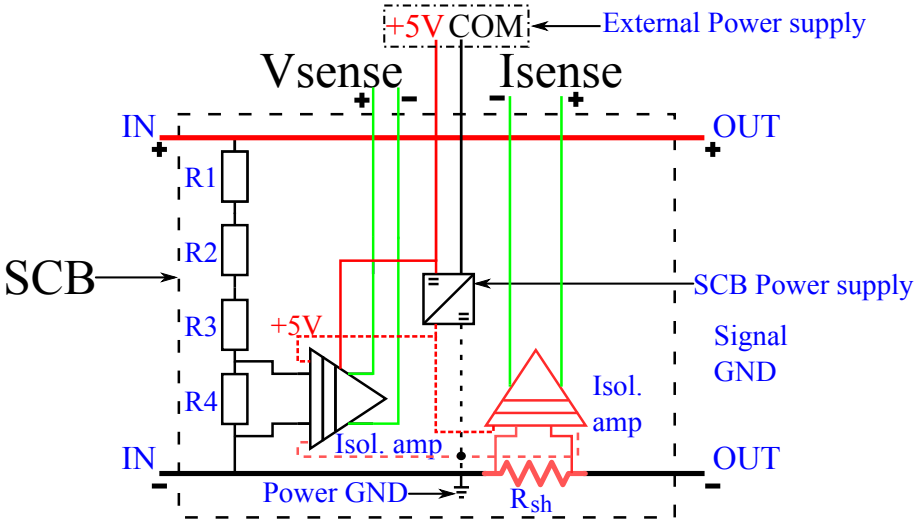

Figure 3.2: Simplified schematic of the initial design of the signal conditioning board (SCB). The dotted lines indicate galvanically isolated power to one side of the isolation amplifiers from the SCB power supply.

The DC-DC SCB power supply shown in Figures 3.2 and 3.3 provides the galvanic isolation required for the isolation amplifier(s). For the measurement of currents, the initial designs focused on measuring a voltage drop over a shunt resistance (R_{sh}), and isolating this signal using the ACPL-C87BT.

The main disadvantages experienced with the first iteration designs based on Figure 3.2 were thus the strongly non-linear and unstable (noisy) signals delivered to the voltage and current sensing terminals, as the voltage divider and the shunt resistance (R_{sh}) were not optimised for the range of the ACPL-C87BT isolation amplifiers. (An example of the stabilised, yet non-linear, behaviour of the isolation amplifiers is shown in Figure 3.8.)

Furthermore, the initial designs aimed for a signal of 0 V to 1 V (optimised for the ±1 V measurement range of the NI cards) to be transmitted by the isolation amplifier, which led to highly non-linear behaviour for values close to 0 V. These represent low measured voltages, found around sunrise and sunset, as well as low current values.

As a correctly chosen Instrumentation Amplifier (inamp) could provide improved performance compared to a single opamp and often occupy less physical space on a Printed Circuit Board (PCB), the choice fell on the Texas Instruments INA 337 inamp [85]. The benefit of the INA 337 inamp is that it came with

a standard minimum gain of two, when using the suggested values for the resistors and capacitors. This gain can be modified by changing the values of the resistors and capacitors connected to the inamp terminals. By then optimising the voltage dividing resistors R_1 to R_4 to obtain 2 V at full scale as input and output for the isolation amplifier, a stable output voltage of 0 V to 4 V can be obtained for measurement by the NI 9205/9206 cards on their ±5 V range. (In case of reasonable over-voltages (e.g. V_{oc} in winter), the 20 % margin of the isolation amplifier will not lead to damage of the NI 9205/9206 cards.)

For the current measurement, the current-shunt-isolation amplifier values were neither stable nor trustworthy, which led to searching to find the eventual solution: a Honeywell CSNX25 magnetoresistive sensor [86] with a stated full scale measurement uncertainty of ±0.32 %. The output of the sensor is $V(I) = 2.5 + R_c \cdot I_{m,sec}$, where the measured voltage represents the current, and the output current ($I_{m,sec}$) is 12 mA at nominal full scale (8 A). Depending on the direction of the current, the sensor's output ($R_c \cdot I_{m,sec}$) results in a positive or negative voltage compared to the reference value of 2.5 V. (This sensing directionality may be useful elsewhere, e.g. for battery charging and discharging measurements.)

The nominal measurement current ($I_{m,nom}$) of the CSNX25 magnetoresistive sensor is similar to the STC current of the *Smart PV* modules, and more generally, of most standard crystalline silicon (c-Si) PV modules. The summary of the relationship between the maximum (or expected) values and the applicable measurement range is given in Table 3.1.

In the present situation, multiple SCBs are powered from an external 5 V Phoenix Contact power supply, with eight SCBs powered from one external power supply in cabinet one and sixteen SCBs powered from another, identical, power supply in cabinet two (cabinets marked as RC1 and RC2, respectively in Figure 2.6). From a safety[3] and accuracy perspective, opting for this solution was better than bringing AC power to each SCB and then using an AC-to-double DC power supply on each SCB. Moreover, the power supply voltage (5 V) corresponded well with the application ranges of the active elements on the SCBs, eliminating the need for multi-output AC-DC converters per SCB.

Note that for both the current and voltage measurements, the NI 9205/9206 cards are used in differential mode, which gives the highest accuracy and transmits the least amount of noise. The reaction rate of the voltage and current sensors used in the final design iteration are in the range of nanoseconds to milliseconds (max 7 µs [83], 1.3 ms [85] and <200 ns [86]), which ensures that all current and voltage measurements are measured and transformed at a correct rate - this will be important in Chapter 5.

[3]Lower voltages, simpler cabling and lower short-circuit values at 5 V_{dc}.

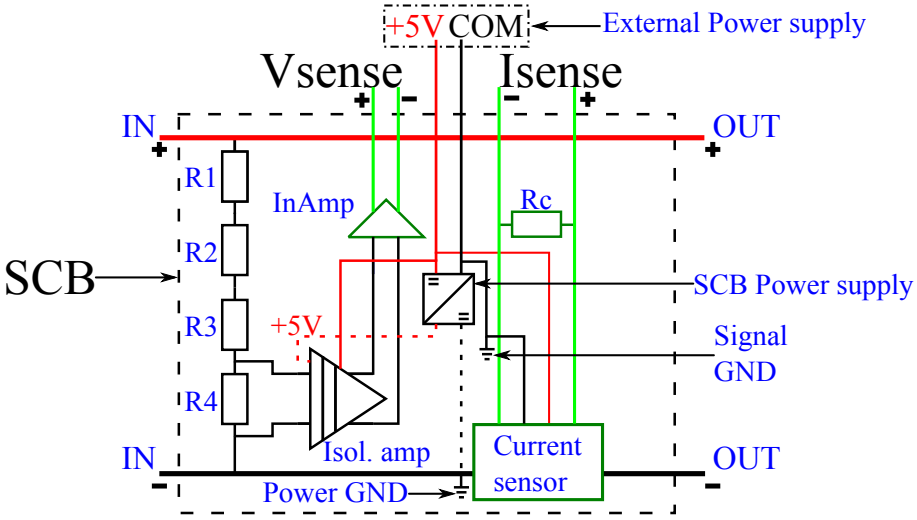

Figure 3.3: Simplified schematic of the final version of the designed signal conditioning board (SCB).

The voltages and currents that are measured are physically scaled and conditioned by the SCBs for measurement by the NI 9205/9206 voltage cards, and subsequently mathematically scaled to represent the original signals. These relationships are given by Equations (3.1) and (3.2) for the voltages and Equations (3.3) and (3.4) for the current, with the subscript *orig* indicating that this is the original value, i.e. the current and voltage as delivered by the photovoltaic device to be measured.

$$V_{orig} = \frac{V_{NI}}{A_V}, \tag{3.1}$$

with the voltage scaling A_V given by

$$A_V = \frac{R_4}{R_1 + R_2 + R_3 + R_4} \cdot A_{INA}, \tag{3.2}$$

$$I_{orig} = \frac{V_{NI}}{A_I}, \tag{3.3}$$

with the current scaling A_I given by

$$A_I = \frac{I_{m,nom,sec}}{I_{m,nom,prim}} \cdot R_c. \tag{3.4}$$

Table 3.1: Ranges of voltages and currents measured and amounts, as of 2015

System	Subcategory	Expected range [a]	Nominal measurement range [b,c]	Amount
PV module / DC-DC in / mini DC-AC in	Voltage	5 V to 39 V	0 V to 40 V	13[d]
	Current	0 A to 9 A	0 A to 8 A	
DC-DC out	Voltage	5 V to 60 V	0 V to 60 V	2
	Current	0 A to 15 A	0 A to 8 A	
SolarEdge inverter in	Voltage	100 V to 500 V	0 V to 500 V	1
	Current	0 A to 11.5 A	0 A to 8 A	
Sungrow inverter in	Voltage	150 V to 500 V	0 V to 600 V	1[e]
	Current	0 A to 10 A	0 A to 8 A	
Total	Voltage & Current	–	–	24

[a] Combination of $V_{oc,STC}$, $I_{sc,STC}$ and MPP_{STC} ranges.
[b] Nominal voltage range can be exceeded 20 %[83].
[c] Nominal current range can be exceeded 125 %, up to 18 A[86].
[d] Six more SCBs available.
[e] One more SCB available.

This scaling impacts the measurement uncertainty and achievable resolution that can be obtained, as the measurement uncertainty[4] and sensitivity of the NI 9205/9206 cards for the ±5 V range are also scaled.

3.3.2 SCB testing, linear transformation and calibration

A quick solution for the testing would have been to construct the SCBs, with the best components within the budgetary constraints, put the SCBs to use, and estimate the uncertainty on the measurements from the manufacturers' data sheets. This proved to be unrealistic for three main reasons:

[4]Expanded uncertainty (U) = 3230 µV (with coverage factor (k) = 3 [82], Type B uncertainty) and 46.4 µV sensitivity (see Section 3.3.3 for these terms).

1. The combined uncertainty of all components would be higher than the aimed-for uncertainty (below 0.5 % of full scale (FS) for power).
2. The active components (isolation amplifier, instrumentation amplifier, magnetoresistive current sensor, DC-DC power supply) in the SCB could exhibit non-linear behaviour.
3. The combination of all components, e.g. resistor-capacitor filters, could lead to offsets and measurement uncertainties not incorporated or accounted for in the manufacturers' data sheets.

Therefore, once initial tests indicated that the design of the SCB permitted "accurate" DC measurement of the current and voltage between PV modules and inverters with sufficiently linear responses to the input signals, calibration work on the SCBs was done. This consisted of:

1. Linearity testing: determining whether the measured data, as obtained using the LabVIEW VI, corresponded to the input signals, as measured using the calibrated 6.5 digit digital multimeter (DMM) [87]. An example result of this is given in Figure 3.7.
2. Slope and offset correction: ensuring that the output values are fully linear to the input values, using linear transformation, which is optimised through iteration: this is summarised in Algorithm 3.1.
3. Uncertainty calculation and outdoor verification.

The testing, and later calibration, of the SCBs was performed with a stable DC power supply (0 V to 720 V, 0 A to 15 A [88]), wire-wound rheostats as variable resistances and a calibrated 6.5 digit DMM [87] as reference. The schematic of how the tests were performed is given below in Figure 3.4.

For voltage testing and calibration, the value was measured at the input of each SCB using the DMM, to remove the effect of the voltage drop between the SCBs. The input voltages were varied in steps of 1 V, from 1 V to the maximal value for the 0 V to 40 V and 0 V to 60 V SCBs, and in steps of 5 V, from 15 V for the 0 V to 500 V and 0 V to 600 V SCBs.

Currents were varied in steps of 0.25 A from 0.25 A, (with a starting value of 0.1 A) and finishing value of 9 A. Additionally, for the voltage-current-power relationships that had to be tested, the rheostats were limited by their power dissipation capabilities, which was theoretically above 10 A and practically found at ∼9 A. While currents above 9 A can be expected for the photovoltaic modules measured, they correspond to an irradiance of $>1100\,\mathrm{W/m^2}$, for which the energy content and frequency in the year is limited.

The dimensions of the rheostats and SCBs resulted in the linearity and calibration testing being performed according to Figure 3.4. In particular, the tests were aimed at not only testing and calibrating the primary parameter (e.g. voltage in one case), but also evaluating the performance of the secondary[5] parameter (e.g. current in that case). This, together with the practical limitations of not being able to ensure identical resistances (and thus voltages at the SCBs terminals) for all SCBs tested, resulted in the need for a series connection for both current and voltage testing, with the voltage values evaluated per SCB on its input terminals.

By comparing the data obtained from the LabVIEW VI with the calibrated DMM data, a large part of the unknown aspects of the interaction of the different components for voltage or current conditioning was removed. In particular, the output data measured using the NI 9205/9206 cards should correspond to the data measured using the DMM, and any deviation from the DMM data was treated as an error (prior to completing the linear transformation, which corrects the span and zero offsets) and subsequently serve as an estimator for the measurement uncertainty.

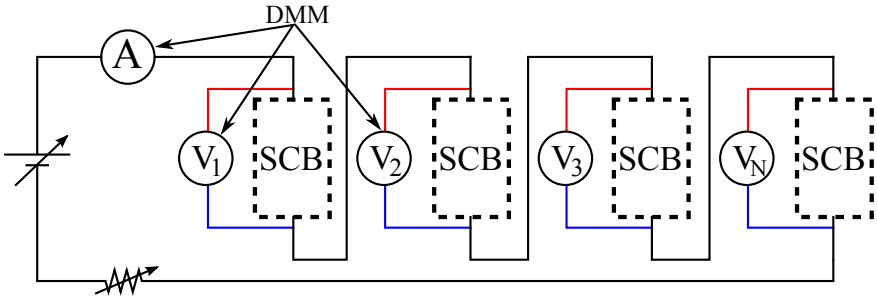

Figure 3.4: A simplified schematic of current and voltage calibration and testing of the SCBs. One calibrated DMM was used for each type of test.

Slope and offset (also known span and zero) correction in the form of linear transformation is aimed at removing all systematic aspects from the residuals (or errors), so that any remaining deviation between the reference (measured by the DMM) and the programmatically measured value is random, and can then be treated using the methods of the *Guide for the expression of uncertainty in measurement* (*GUM*)[12].

An exaggerated example of slope and offset errors is shown in Figure 3.5, with the measurements on the left and the residuals on the right side of the figure.

[5] As the SCBs were to be used for power calculations, the current and voltage values had to be measured under realistic conditions, and not only optimised for the parameter to be measured.

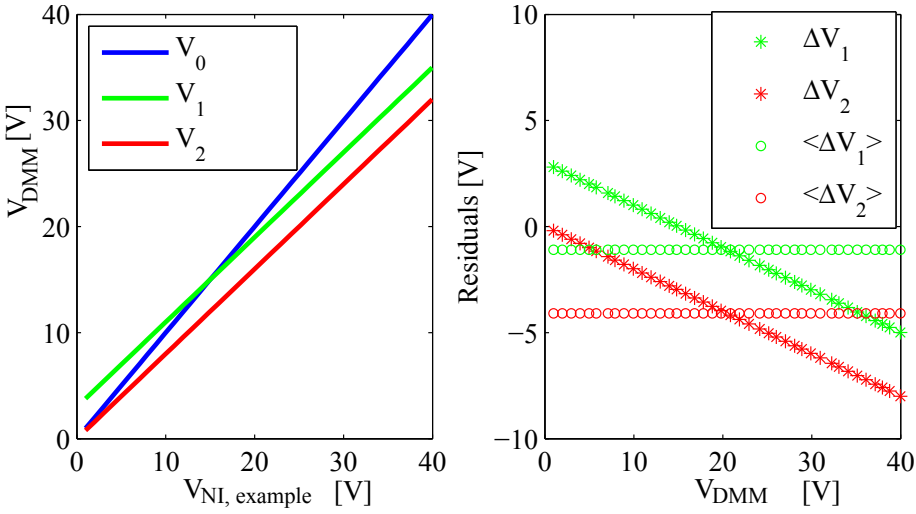

Figure 3.5: An example of slope and offset errors.

It is easy to correct the green line (V_1) to obtain the ideal line (blue, V_0): $V_0 = V_1 \cdot 1.25 - 3$. Figure 3.5 was generated from the same dataset (the DMM values V_0), so that in this case the residuals show a (perfect) linear trend. However, the mean of the residuals is *not* zero *and* the residuals show a trend[6], so the errors here can not be (easily) dealt with. So this is not an approach which meets the initial design specificatons. These residuals can also therefore not be used for the measurement uncertainty calculation according to the *GUM*. This issue can be solved by first performing the linear transformation of the data, to obtain errors which show homoscedasticity (a finite variance).

Thus, the data which is conditioned by the SCBs prior to measurement by the NI 9205/9206 cards must be characterised, and if an offset and slope error exist, they must be corrected. The method to do this is explained below.

The reference measurement data from the DMM is on the y-axis, and the (SCB) data to be characterised is on the x-axis. For each SCB, the measured values are compared to the DMM data. A regression line, similar to that shown in Figure 3.5 is calculated and drawn. The regression line equation (in general terms given in Equation (3.7)) is then used to calculate the correction to the slope and offset, so that, if the measurement would be repeated, that the now-corrected data of SCB aligns with the reference (DMM) data, with the residuals having a random trend. In the ideal case, the new regression line will

[6]In statistical terms, they show heteroscedasticity: a non-constant variance.

have a slope of one and an offset of zero, where the residuals have a mean error of zero (or the closest possible approximation).

In general statistical terms, the true value of the measurand y is never reached, as there will always be an error on the measurement. The expectation value $E(y)$ thus has an error ϵ:

$$y = E(y) + \epsilon, \tag{3.5}$$

where Equation (3.5) can further be written as

$$y = \beta_0 + \beta_1 \cdot x + \epsilon. \tag{3.6}$$

The aim is obtain the values of β_1 and β_0 for each SCB so that the residuals are minimal in value and randomly distributed with a mean of zero (or as close as possible).

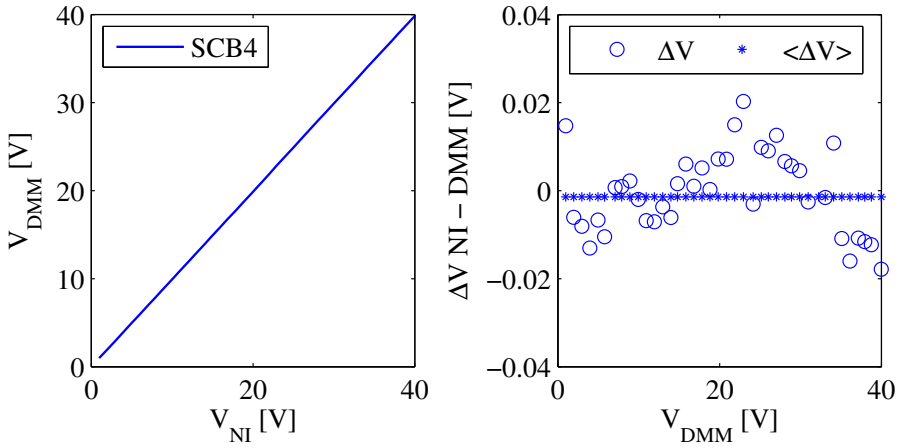

Figure 3.6: Results of the slope and offset correction for one SCB. The residuals are randomly distributed around the mean.

Temporarily assuming the random error (ϵ) to be zero, Equation (3.6) can be rewritten as

$$y(x) = \beta_1 \cdot x + \beta_0, \tag{3.7}$$

where x is the complete dataset of the SCB measured values, while y is the DMM data measured under the same conditions. The goal is now to obtain

correct values of the slope β_1 and the offset β_0 so that the SCB data "perfectly[7]" corresponds to the DMM reference data.

Using Equation (3.7), in the case that the measured residuals are too large (or more importantly, that they show a non-random trend), it is possible to modify the slope β_1 and the offset β_0, where both parameters (β_1,β_0) are initially assumed to be ideal ($\beta_1 = 1$, $\beta_0 = 0$).

The residuals can be improved on by iterative linear transformations, by obtaining the regression line of the measured points, with the subscripts $i, j, k, ...$ indicating a full measurement sequence (from close to zero to the maximum to be measured, e.g. 1 V to 40 V for the 40 V SCBs)

$$y_i(x_i) = \beta_{1,i} \cdot x_i + \beta_{0,i}, \tag{3.8}$$

$$y_j(x_j) = \beta_{1,j} \cdot x_j + \beta_{0,j}, \tag{3.9}$$

$$y_r(x) = \beta_{1,j} \cdot (\beta_{1,i} \cdot x + \beta_{0,i}) + \beta_{0,j}, \tag{3.10}$$

$$y_r(x) = \underbrace{(\beta_{1,j} \cdot \beta_{1,i})}_{\beta_{1,r}} \cdot x + \underbrace{(\beta_{1,j} \cdot \beta_{0,i} + \beta_{0,j})}_{\beta_{0,r}}, \tag{3.11}$$

where the resulting coefficients $\beta_{1,r}$ and $\beta_{0,r}$ are obtained from Equation (3.11), with the reasoning behind it elucidated by Equation (3.10): the slope of the second regression will also impact the offset $\beta_{0,i}$ of the previous regression values. In this manner, the resulting calibration coefficients are obtained in typically four to five steps, as shown in Algorithm 3.1.

The non-linear behaviour of the isolation amplifiers is evident in Figure 3.8, particularly for the high-voltage SCBs (500 V and 600 V nominal maximum): below 20 V (corresponding with 2 % to 3 % of the nominal range of the isolation amplifier), a clear non-linear trend is visible. As the inverters' start-up voltages are 160 V [41] or higher (in practice, the Sungrow and SolarEdge inverter's start-up voltages are above 200 V and 40 V respectively), this low-voltage non-linearity can be disregarded for energy calculations. The ranges of interest for measurement, and therefore the regression analysis are 1 V to 40 V, 5 V to 60 V, 15 V to 500 V and 15 V to 600 V.

Where the non-linearities may play a role, if not taken into account, is in the linear regression performed to get the linear transformation coefficients: a regression line is particularly susceptible and sensitive to outliers at the

[7] Mean error as close as possible to zero, randomly distributed residuals, with the smallest possible sample standard deviation (s).

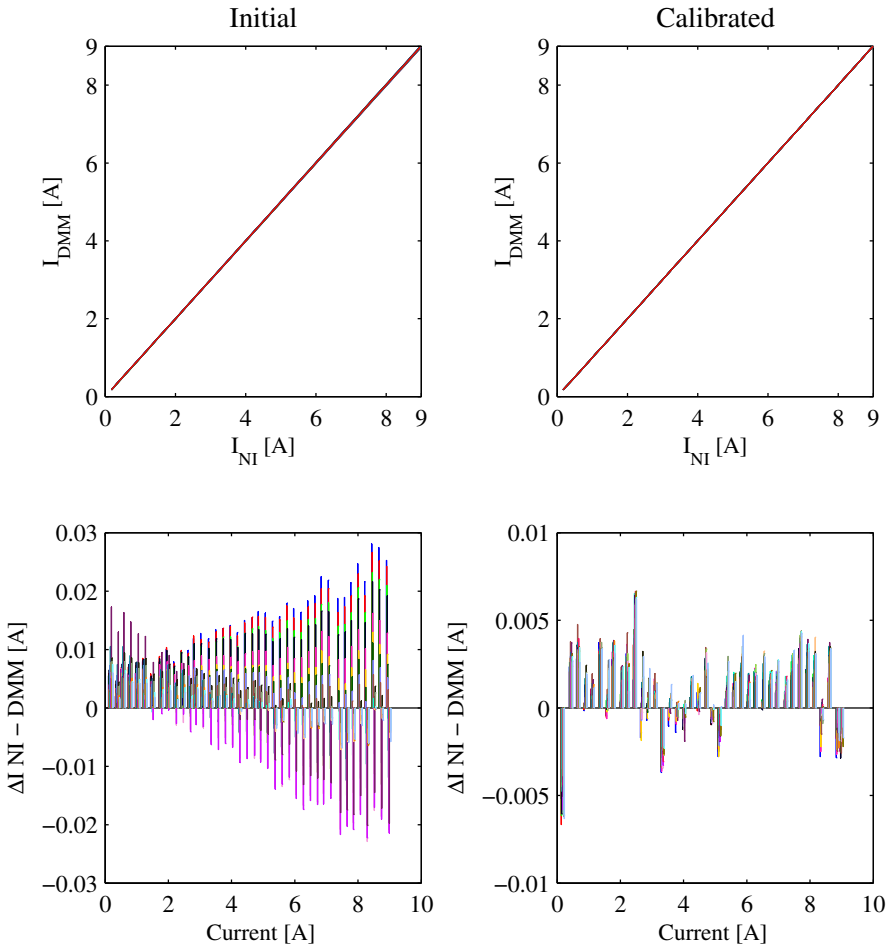

Figure 3.7: An example of the initial linearity testing (left subplots) and calibration (right subplots) for the 24 SCBs. As can be observed in the top subplots, the values obtained as output in the LabVIEW VI (I_{NI}) show a linear response to the input, as measured using the DMM reference. The residuals (bottom subplots) indicate that improved (reduced) uncertainties can be obtained by proper linear transformation, which can be seen in the bottom right subplot.

beginning and end of the range. This therefore justifies taking the starting range of the higher-voltage SCBs from 15 V.

Algorithm 3.1 and Figures 3.4, 3.7 and 3.8 hint at the laborious nature of the linear transformation and calibration of the SCBs. The effort however, results in

Algorithm 3.1 Linear transformation and calibration of SCBs via successive approximations.

1: Start: $\beta_1 = 1$, $\beta_0 = 0$. Measure values (V: 0 % to 100 % FS, I: 0 % to 113 % FS), obtain regression line, parameters $\beta_{1,i} \neq 1$, $\beta_{0,i} \neq 0$. Visualise residuals, calculate error.
2: Measure values, using $\beta_{1,i}, \beta_{0,i}$ for linear transformation. Obtain new regression coefficients $\beta_{1,j}, \beta_{0,j}$, calculate $\beta_{1,r}, \beta_{0,r}$. Visualise residuals, calculate error.
3: **while** $e > e_{criterion}$ **and** $\Delta e = e_{new} - e_{old} < 0$ **do**
4: Measure values, using $\beta_{1,r}, \beta_{0,r}$ for linear transformation. Obtain new regression coefficients $\beta_{1,k}, \beta_{0,k}$, calculate $\beta_{1,r,new}, \beta_{0,r,new}$. Visualise residuals, calculate error.
5: **end while**
6: Measure values, visualise residuals, calculate total error, verify that $\beta_{1,r}, \beta_{0,r} \Rightarrow e_{min}$.
7: **return** $\beta_{1,r}, \beta_{0,r}, e(\beta_{1,r}, \beta_{0,r})$

a strongly reduced uncertainty, as can be compared in Figures 3.7 and 3.8. The SCBs were subsequently ranked according to their uncertainty, with SCBs with the lowest uncertainties used for the *Smart PV* modules, DC-DC converters and inverters, with the remaining SCBs available for future projects.

3.3.3 Measurement uncertainty

Often (e.g. in a manufacturer's data sheet), a measurement uncertainty is given as $X \pm y\%$. What is meant by this is that the indicated (measured) value X has an uncertainty with a magnitude of $\pm y\%$. This is typically expressed (or assumed to be) for a 95 % coverage interval, i.e. that the uncertainty on the measured value is $X \pm y\%$ for 95 % of the measurements. The 95 % corresponds to a coverage factor (k), which is equal to 1.96 for a normal gaussian[8] population.

The value of y is, according to the terminology of the *GUM* [12] expressed as an expanded uncertainty (U), which is the combined uncertainty (u_c) multiplied by the coverage factor (k).

$$U_p = k_p \cdot u_c. \tag{3.12}$$

[8] 95 % of the measured values fall within the bounds of 1.96 times the standard deviation on positive and negative sides of the expected value.

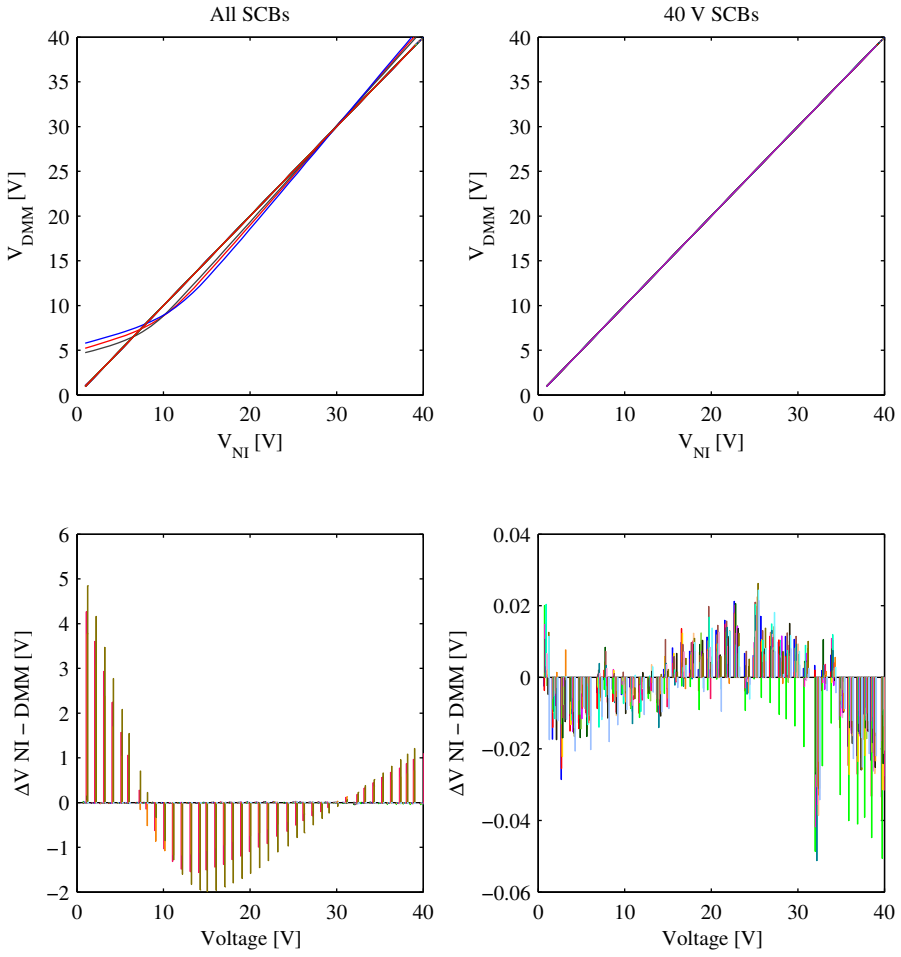

Figure 3.8: An example of the 1 V to 40 V calibration testing (left subplots: all SCBs, right subplots: 40 V SCBs) for the 24 SCBs. The non-linearity of the high-voltage (500 V and 600 V) SCBs is evident in the left subplots; the figures on the right show only 40 V SCBs.

The determination of the correct value for a certain instrument or measurement device of the coverage factor (k) depends on the Student's t distribution. The combined uncertainty (u_c) is obtained by bringing together all known and quantified sources of uncertainty for a signal.

As an example (adapted from [12] and [89]), the combined measurement uncertainty of the DC power P may be obtained from

$$P_{dc} = V_{dc} \cdot I_{dc} \tag{3.13}$$

$$P = (V \pm u_{c,V}) \cdot (I \pm u_{c,I}) \tag{3.14}$$

$$u_{c,P} = \sqrt{(I \cdot u_{c,V})^2 + (V \cdot u_{c,I})^2 + 2 \cdot r_{VI} \cdot u_{c,V} \cdot u_{c,I}} \tag{3.15}$$

with the correlation coefficient (r_{xy}) here being the correlation coefficient[9] of voltage (V) and current (I). The symbols I and V in Equation (3.15) are generally known as sensitivity coefficients [89]. In this case, their values are the nominal ranges for measurements, e.g. 8 A and 40 V. This means that not only the (combined) measurement uncertainties impact the combined uncertainty, but also the individual measurement application ranges.

If the measurement uncertainty of the voltage has no impact on the measurement uncertainty of the current (i.e. they are completely independent), then $r_{VI} = 0$ and Equation (3.15) simplifies to

$$u_{c,P} = \sqrt{(I \cdot u_{c,V})^2 + (V \cdot u_{c,I})^2}. \tag{3.16}$$

Both Equations (3.15) and (3.16) are expressions of the *Law of Propagation of Uncertainty* [12], as the uncertainties of the components (voltage and current in this example) propagate to the derived quantity (power).

Once the linear transformation and calibration are complete for each signal conditioning board, a measurement combined uncertainty (u_c) must be calculated for each signal per SCB. The measurement uncertainty of a signal, e.g. a voltage, typically comprises multiple source components.

According to the terminology of the *GUM*, a Type A combined measurement uncertainty ($u_{c,A}$) is obtained through a "statistical analysis of series of observations" [12] whereas a Type B combined measurement uncertainty ($u_{c,B}$) is obtained through "means other than the statistical analysis of series of observations" [12].

A Type B uncertainty is determined based on scientific judgement, using all available information, of which the manufacturer's specifications [90] often are key. Assuming measurement equipment with zero error (i.e. $u_{c,B} = 0$), the remaining errors can be characterised as Type A combined measurement uncertainty, provided that the experiment design, execution and analysis are

[9] From the Type A combined measurement uncertainty ($u_{c,A}$) experiments, this has been determined to be $r_{VI,A} = 0$.

properly performed. In reality, having $u_{c,B} = 0$ rarely happens, and thus the calculation of the combined measurement uncertainties requires knowledge of both $u_{c,A}$ and $u_{c,B}$.

3.3.4 Measurement uncertainty analysis applied to the SCBs

The uncertainty calculation for the calibration-derived voltages and currents per SCB is done according to the *GUM* [12], with the uncertainties from the calibration testing treated as Type A (experimentally determined) uncertainties, with each signal treated separately, and subsequently brought together, including the Type B uncertainties of the measurement instruments.

The residuals obtained from the post-linear transformation calibration are used to calculate the sample standard deviation (s), which is the estimator of the Type A combined measurement uncertainty.

The Type A combined measurement uncertainty $u_{c,A}$ and Type B combined measurement uncertainty $u_{c,B}$ are then brought together to calculate the combined uncertainty (u_c):

$$u_c = \sqrt{u_{c,A}^2 + u_{c,B}^2 + 2 \cdot r_{AB} \cdot u_{c,A} \cdot u_{c,B}}. \tag{3.17}$$

Note that $u_{c,A}$ and $u_{c,B}$ can *each* also be determined in a similar manner as shown in Equations (3.15) and (3.17), for their respective components.

For the Type A uncertainty determination, a sample of the population has to be taken. As shown above in Algorithm 3.1, generally equidistant points (e.g. for the 40 V SCBs, 1 V to 40 V with steps of 1 V) were taken for sampling, with 100 or more samples per point. The number of steps must be high enough so that the first and last points have a lower actual impact on the regression calculation: the deviation for these points has the largest potential impact on the regression line.

As the number of points between a maximum and minimum (e.g. 0.1 A and 8 A) that can be measured is infinite[10], by definition the number of samples per point is a sample of the population, and not the population.

[10] E.g. one can attempt to determine the measurement uncertainty using steps of 0.1 V instead of 1 V, but between those steps there will again be an infinite number of steps that can be measured.

Statistical theory [91] then mandates that, instead of assuming a *population* of normally distributed residuals, the degrees of freedom for the Student's t distribution must be determined for the *sample of the population*. If the degrees of freedom is infinite, the t distribution is equal to the normal distribution. The lower the degrees of freedom, the larger the deviation of the t distribution is to the normal distribution.

Knowledge of the degrees of freedom is therefore a prerequisite to be able to calculate the expanded uncertainty U as in Equation (3.12). The effective degrees of freedom (ν_{eff}) is calculated using the formulation of Welch-Satterthwaite [12]

$$\nu_{eff} = \frac{(u_{c,A}^2 + u_{c,B}^2)^2}{\frac{u_{c,A}^2}{\nu_A} + \frac{u_{c,B}^2}{\nu_B}}, \tag{3.18}$$

with the degrees of freedom for Type A measurement uncertainty (ν_A) and the degrees of freedom for Type B measurement uncertainty (ν_B) known from the statistical experiment(s)[11] together with the information from manufacturers (for ν_B).

Then, the level of confidence p must be chosen (this is most often 95 %, 99 % and 99.73 %) to determine the value of the coverage factor k. Choosing[12] $p = 99.73\,\%$, it is possible to calculate the t-factor t_p from the Student's distribution for the desired value of p

$$k_p = t_p(\nu_{eff}, p), \tag{3.19}$$

using standard statistical tables, which can then be used in the calculation of the expanded uncertainty (U).

An example which shows the impact of ν_{eff} on the coverage factor is given in Figure 3.9. The tails for the t distribution for low values of ν_{eff} diverge from the normal distribution[13], yet the value of k calculated for both distributions is similar until $k \simeq 2$. As a result of the divergence of the t distribution from the normal distribution, a low value of ν_{eff} *and* high value of p can result in k being much larger than its normal distribution counterpart and therefore the expanded uncertainty.

Up to this point, the calculation of the values has been done for a "base" signal, such as the current or voltage. The combined uncertainty for each signal then has to be used for subsequent calculations, such as the uncertainty of power.

[11] E.g. the ν_A is calculated as N samples per point minus one.

[12] Often chosen for electrical values, this gives $k = 3$ for a normal distribution.

[13] For ν_{eff} greater than 15, the normal and t distribution are mostly similar [91] and from ν_{eff} greater than 100, the t distribution is almost identical to the normal distribution. For $\nu_{eff} \to \infty$ the t distribution is equal to the normal distribution [12, 91].

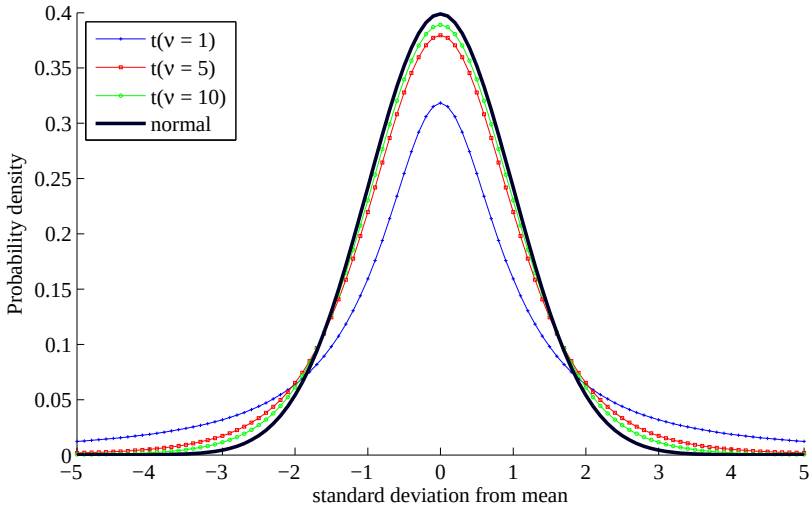

Figure 3.9: Comparison of Student's t distribution to the normal distribution, for indicated values of ν_{eff}. The coverage factor (k) corresponds to the area under the curve for the chosen value of level of confidence (p).

The uncertainty of the measured (DC) power stems from Equations (3.13) and (3.16) where the benefit of the approach is made clear: the power is calculated using $P = V \cdot I$ (Equation (3.13)), and the uncertainty can be calculated separately using Equation (3.15) or Equation (3.16).

The uncertainty can be improved by taking more samples within the chosen period and then averaging them out, according to

$$u_c(S) = \frac{u_c}{\sqrt{S}}. \tag{3.20}$$

What is not explicitly clear from Equations (3.16) and (3.20) is an issue alluded to in IEC 61724 [16]:

$$\langle P \rangle_\tau = \langle V \cdot I \rangle_\tau \neq \langle V \rangle_\tau \cdot \langle I \rangle_\tau, \tag{3.21}$$

namely that the average power over an interval τ (e.g. five seconds) calculated from the measurement multiple values of the DC voltage and current can *only*

be correct if *first* the calculations of $V \cdot I$ are done and *then* the average is calculated.

Due to the propagation of uncertainties, the calculation of the energy produced and its uncertainty is performed as in Equation (3.22), using

$$E \pm u_E = \sum_{0}^{\tau} (P \pm u_P) \cdot \Delta t. \tag{3.22}$$

As the measured power values are correlated in time (i.e. the power measured at one moment t is similar to that at $t + \Delta t$ (with $\Delta t = 1\,\mathrm{s}$)), no compensation of uncertainties is assumed to occur. As a result, Equation (3.22) for the uncertainty of energy calculation can be rewritten for the expanded uncertainty of energy (U_E), where the expanded uncertainty of power (U_P) is constant:

$$U_E = \sum_{0}^{\tau} U_P \cdot \Delta t = U_P \cdot \sum_{0}^{\tau} \Delta t = U_P \cdot N_{\Delta t} \cdot \Delta t. \tag{3.23}$$

Thus, Equation (3.23) shows that there are three aspects which can influence the total expanded uncertainty, in this case for the energy:

1. The expanded uncertainty of power (this can be generalised to the combined uncertainty) of the measurement.
2. The sampling rate (S) at which rate the data is measured, implicit in U_P (as in Equation (3.20)).
3. The time step Δt at which rate the data is stored.

Item 1 has seen the most effort, as the effect of this propagates throughout and has the largest effect of the points mentioned above.

For Item 2, the current setting is for S to be one sample per second. This can be modified in the set-up, yet Item 2 could be paraphrased as the "law of diminishing returns", as the higher the value of S becomes, the lower the effect is of one more sample per second being added. Moreover, the measurement uncertainty per point increases with a higher S, as each point is measured with an increasing amount of noise. Computationally this can also strain the equipment[14] used.

[14] (The set-up is currently close to the limits suggested by the manufacturers, in particular National Instruments for the CompactRIO.)

However, under-sampling (e.g. obtaining one power data point per 30 s) then assumes that the measured value is representative of the whole interval, which is a rough estimation of reality, and makes the calculation of the combined uncertainty more difficult. One example of such a situation is the measurement of I-V curves every 30 s and then using the determined maximum power to calculate the energy. Using such an approach, it is thus possible to have a point-by-point better[15] expanded uncertainty of power and yet a globally worse expanded uncertainty of energy, in particular if the conditions have changed between measurements.

Item 3 is determined or chosen by the rate at which aspects will be investigated, and the available storage and computational resources available. One important note to mention is that, as shown in Equation (3.23), over the period investigated (e.g. one hour), the relationship $N_{\Delta t} \cdot \Delta t = 3600\,\mathrm{s/h}$. This means that increasing time step (Δt) has no (positive) impact on the calculated expanded uncertainty of energy, as the energy content remains the same (otherwise, by the same token, the energy calculated from the measured data would also be a fraction of the real amount of energy produced).

Equations (3.17) and (3.23) highlight the sensitivity of the final expanded uncertainty to the initial composing combined uncertainties, due to the law of propagation of uncertainties. Efforts to reduce the initial combined uncertainties can therefore lead to a large difference in the final expanded uncertainty U, as well as the parameters that depend on the measured or calculated values, e.g. efficiencies or the Performance Ratio, as will be discussed in Section 5.7. The results of linear transformation, scaling of uncertainties and finally, expanded measurement uncertainties are summarised in Table 3.2. These results are of importance, as they are the foundation upon which many of the conclusions of this (and derivative) work are built on.

Note also that the calculation and use of the expanded uncertainty U is often done as a last step, otherwise the coverage factor k carried through leads to an erroneously large final expanded uncertainty U.

As a side note: it is possible to obtain a reasonable estimate of the combined uncertainty of the composing values and use these as design goals by first specifying a goal, e.g. for the U_P and U_E. Thus, an "expanded uncertainty of $\pm 1\,\%$ for power for a coverage interval of 95 %" may become "0.3 % combined uncertainty for current and 0.5 % combined uncertainty for voltages for the chosen measurement ranges". The sum of 0.3 % and 0.5 % is *not* immediately equal to 1 %, as the measurement ranges of current and voltage also play a role, as seen in Equation (3.15).

[15] Assuming that the I-V curves are measured with e.g. 6.5 digit DMMs.

3.4 Summary of results and benchmarking

The averaged absolute measurement uncertainty achieved using the SCBs is summarised in Table 3.2.

Table 3.2: Measurement uncertainty and amount of DC voltage and current sensing channels according to application range

Parameter	Application	Amount	Mean[a] expanded uncertainty U^b	Range[c,d]
Voltage	Module out / DC-DC or DC-AC converter in	19	$\pm 6.0 \cdot 10^{-2}$ V (± 0.15 %)	1 V to 40 V
Voltage	DC-DC converter out	2	$\pm 1.1 \cdot 10^{-1}$ V (± 0.18 %)	1 V to 60 V
Voltage	Inverter in	3	$\pm 6.9 \cdot 10^{-1}$ V (± 0.14 %) / $\pm 9.3 \cdot 10^{-1}$ V (± 0.15 %)	15 V to 500 V / 15 V to 600 V
Current	All	24	$\pm 4.5 \cdot 10^{-2}$ A (± 0.56 %)	0 A to 8 A
Power	Module out / ...	19	± 1.9 W (± 0.58 %)	0 W to 300 W
Power	DC-DC converter out	2	± 2.9 W (± 0.59 %)	0 W to 300 W
Power	Inverter in	3	± 23 W (± 0.58 %) / ± 28 W (± 0.58 %)	0 W to 3000 W

[a] The mean accuracy is taken as a representative value in this table; calculations are performed using the value per module or converter.
[b] Expanded uncertainty, $k = 3.06$ for 99.73 %, absolute and relative to the FS.
[c] Voltage range can safely be exceeded up to 20 %, current: at least up to 60 %.
[d] For power: practical or intended range. This range is in reality 0 to $P_{max} = V_{max} \cdot I_{max}$.

In terms of comparison to other results in literature, Table 3.3 gives a brief overview. In particular, module-level measurements have typically been performed using I-V curves, and much less using other means, e.g. a module connected to a micro inverter. The results of this work approximate the state of the art (the best results in the table), although the investment cost to achieve these values is lower.

Table 3.3: Benchmarking of main energy and performance measurement uncertainty parameters

Application	Expanded measurement uncertainty (this work)	(Expanded[b]) measurement uncertainty (Literature)
Irradiance G	±5 %	±4 % to 8 %
Daily irradiation[a] G_d	±2 %	±2 % to 5 %
Module out (converter in) (DC)	±0.15 % (V), ±0.56 % (I), ±0.58 % (P), ±2.5 % (E)	±0.1 % (V), ±0.2 % (I), ±0.23 % (P)[c] [28], ±2.5 % (P) [92], ±2.5 % (V, I, P), ±5 % (E) [93]
DC-DC converter out (DC)	±0.18 % (V), ±0.56 % (I), ±0.59 % (P), ±3.7 % (E)	±2.5 % (V, I, P), ±5 % (E) [93]
Inverter in (DC)	±0.15 % (V), ±0.56 % (I), ±0.58 % (P), ±2.5 % (E)	±2 % (V) & ±1.5 % (I) [94], ±2 % (V & I) [95], ±0.015 % (V), ±0.75 % (I) & ±0.765 %[d] (E) [96], ±4 % (P) [97]

[a] Some irradiance errors compensate each during the day for irradiation values [50, 98]
[b] It is not always clear whether an expanded measurement uncertainty is applicable, and which confidence interval is used.
[c] Estimate from [28], *electrical* uncertainty only, $k = 2.586$ for 99 %.
[d] Value appears to be too optimistic: ranges are 20 V to 1000 V and 0 A to 10 A [96].

3.5 Conclusions

The high-level goals of Section 3.3.1 are repeated here and updated with the information of this chapter. In general, the achieved measurement uncertainty approximates the published state of the art.

- *Develop an affordable and electrically safe (i.e. galvanically isolated) system which can present a stable signal to measure module currents and voltages, using the available hardware (NI 9205/9206 voltage cards) and software. Using these currents and voltages, the energy yield of at least 12 modules must be measured-calculated, with a* power *uncertainty of less than* 0.5 % *of full scale.*
- **Broadly achieved:** The solution devised is a scalable signal conditioning board (SCB) design which galvanically isolates the power from the signal side. The SCB design has shown to be amenable to repeat manufacturing and stability in operation. While the hardware design allows the SCB to be used "out of the box" with good linearity, the linear transformation methodology, calibration and uncertainty determination have shown that uncertainties and offsets can be strongly reduced. The full scale (FS) uncertainty of power *for a coverage interval of* 99.73 % exceeds the ±0.5 % design requirement[16]. For the modules and inverters currently measured for the *Smart PV* and *Residential* systems, the relative value of the expanded uncertainty (U) is higher, at $\sim \pm 0.8\,\%$. The SCB design is affordable (material cost per SCB is ∼€75), which together with the cost of the use of measurement channels of the NI 9205/9206 cards delivers a per-signal cost of ∼€100 to €120.
- *Develop the LabVIEW VI to measure and store the data from the multiple photovoltaic modules to be logged. As the energy yield of the modules was to be measured, measuring the system energy yield on the AC side of the inverter was also necessary.*
- **Achieved:** The "V, I DC + AC pulses logging" LabVIEW VI allows up to 24 voltage-current pairs and 6 AC energy counters to be logged per second, with the data stored in up to four project-specific files. More AC data (e.g. power, frequency) is measured using a three-phase PM3250 logger, for which another "AC logging" LabVIEW VI was developed and modified. The overview and electrical diagrams of this were given in Figures 2.5 and 2.7.

[16] One option would be to use $k \simeq 2$ for a 95 % coverage interval, in which case design requirement would be met, at the cost of 4.73 pp added probability of values exceeding the limits (i.e. 95 % "certain" versus 99.73 %).

Chapter 4

Thermal characterisation of photovoltaic modules

4.1 Introduction

The primary effect that explains the energy yield of photovoltaic modules and systems is the received irradiation, together with effects which modify the received irradiance, such as shading and non-uniform irradiance [99]. The temperature behaviour of photovoltaic modules has then been identified as one of the leading secondary causes of a reduction of efficiency and power, and as a consequence, the energy yield [50, 100, 101, 102, 94].

For crystalline silicon cells and modules, an increase in the temperature above STC leads to a reduction[1] in the open-circuit voltage (V_{oc}) and a smaller increase[2] in the short-circuit current (I_{sc}). The combination of these two effects lead to a reduction in efficiency and power, which is often described using the temperature coefficient of power (γ), with typical values for crystalline silicon in the range of $-0.30\,\%/°\mathrm{C}$ to $-0.50\,\%/°\mathrm{C}$. Thus, a module's temperature rise above the reference value (T_{STC}) by $10\,°\mathrm{C}$ may lead to a reduction in the efficiency (and hence, power) of the module by $5\,\%$. As a result, modules installed in warmer climes perform generally less well than those in the cooler

[1] V_{oc} typical values: $-0.25\,\%/°\mathrm{C}$ to $-0.45\,\%/°\mathrm{C}$.
[2] I_{sc} typical values: $0.05\,\%/°\mathrm{C}$ to $0.06\,\%/°\mathrm{C}$.

location with the same irradiance and irradiation[3]. This also points to the need for temperature measurements on modules, as a module's temperature is influenced by a host of variables such as irradiance, wind, ambient temperature and the mounting structure. It therefore does not suffice to only measure irradiance (as the input) and the module or system power (as the output) to fully characterise a photovoltaic module's or system's performance.

When performing temperature measurements, how can one be sure that the results are correct? Are the temperature variations measured an effect of a "normal" module-environment interaction, or are the results due to a loose sensor or poor connection to the module's surface? At which rate does the module temperature vary, and at which rate are the measurements performed? Are the measurements focused on steady state, or are dynamic effects measured as well?

The above questions highlight some of the issues that challenge performance analyses, and may lay at the root of over- and under-estimations in literature. The issue of the most accurate and practical temperature measurement has been tackled by many authors, such as [100, 103, 104, 105, 106, 107]. The summarising work of Skoplaki and Palyvos [108, 109] is particularly noteworthy in this area, and provides a good overview of temperature measurements and models used.

Two of the simplest and thus most used models for the module temperature are Equation (4.1) [110] and Equation (4.2) [111].

$$T_C = T_{amb} + h_{Ross} \cdot G \tag{4.1}$$

$$T_C = T_{amb} + \frac{NOCT - T_{amb,NOCT}}{G_{NOCT}} \cdot G \tag{4.2}$$

Equation (4.1) uses the Ross coefficient (h_{Ross}), introduced by Ross [110] and is regression-based using measured data. Typical values for the h_{Ross} are $0.02\,°C \cdot m^2/W$ to $0.04\,°C \cdot m^2/W$ [108] for open-rack mounted modules, with Ross originally reporting h_{Ross}=$0.03\,°C \cdot m^2/W$ [110]. As such, Equation (4.1) is most applied for measurement set-ups, where the regression analyses can be performed.

Equation (4.2), as it is defined in the standards (e.g. IEC 61215 [24]) and a required value for reporting in data sheets [112], is often used for modelling of installed and future photovoltaic installations. The difficulty in measuring the

[3]Generally, the increase in temperature corresponds to an increase in irradiation. That said, for a same latitude, there are indeed areas where the temperature is lower with a constant level of annual irradiation, e.g. coastal areas compared to more inland.

NOCT outdoor in the Belgian climate, is that the conditions (T_{amb} = 20 °C, wind speed 1 m/s *parallel to the module surface* and G = 800 W/m^2) occur so few times in the year that the regression methodology of Ross is much more useful. However, the easier determination of NOCT indoors and its simplicity explain why Equation (4.2) has been popular in use [111, 103].

For thermal model calibration or application, a number of data or modelled sources may be required, depending on the model complexity. For Equation (4.2), the NOCT, the ambient temperature T_{amb} and the irradiance G are required, and may be obtained from a variety of sources (e.g. national meteorological services, or a measurement set-up in a location of interest). Other models also incorporate the wind speed [111, 113], or the (full) physical properties of the modules [78].

What both Equations (4.1) and (4.2) share is that they relate the module temperature to the ambient temperature, and attribute the increase in a module's temperature to irradiance. Similarly, measured temperatures on the cell backside of modules and on the backsheet are often also corrected using

$$T_C = T_{BS} + \Delta T_{CBS} \cdot \frac{G}{G_{STC}}, \tag{4.3}$$

which was given by King *et al*, where the value of the ΔT_{CBS} was given as "2 °C to 3 °C at 1000 W/m^2 [...] for modules in rack mount" [114].

What is *not* clear from the formulations of e.g. Equations (4.1) and (4.3) is up to which rate they are valid: is this per second, per minute, per...? As the measurements and data treatment in this work has primarily focused on data measured per second, some issues have appeared with the attempting to use either of the above formulations. In particular, the rate of change of the irradiance G may be much faster than the rate of change of the temperature, and thus gives a modelled temperature with noise. Thus, some of the steps undertaken have been to identify to which extent these equations (or similar ones) may be used, and which modifications can be done.

In practical terms, the temperature measurements per second used in this work are typically much faster than previously applied (which were generally in the range of minutes[4]). The temperature data is thus often measuring during dynamic conditions, and much less during steady state[5]. Since temperature data

[4]Either the reported or sampled data, with the reported data in the range being per minute or longer.

[5]If steady state is defined as indicated in the IEC standards, e.g. ±2 % irradiance deviation in the previous minutes and an (average) wind speed of less than 2 m/s, then almost no days qualify - especially the wind speed requirement is challenging. Focusing purely on steady

is of interest during the whole day for energy yield analyses, the temperature data must be measured as correctly as possible for all applicable weather conditions, and thus not only steady state. As a result, much effort went into using the right type of sensor, attaching it correctly, correcting for biases and irradiance-induced temperature differences, all for both steady-state and dynamic conditions. These steps and choices are highlighted in the following sections.

For temperature sensors and attachment methods, an inter-comparison has been done by Jankovec and Topič [115], with other methods to develop cheap, or easy-to-use sensors by Rustu [30] and Bohorquez [116].

Regarding the more prosaic aspects of temperature measurement, few articles have been published in this area. In practical terms, the sensor type, attachment method and choice to insulate or not play a role in temperature measurements. The article by Jankovec and Topič [115] discusses the use of insulation, as well as keeping a sensor in contact with the module surface using a support structure (the latter being impractical, and may modify wind access to the back surface). Tape is often used to attach a sensor to the back surface, and (slightly) insulate the sensor from the ambient conditions [100], although epoxy glue [105] has also been used. In general terms, practices have typically been to install sensors with some form of tape, and depending on the research group, to also add insulation. Adding insulation to temperature sensors increases their indicated temperature under steady state conditions, but also results in a worse transient or dynamic temperature indication [117], a result which can be understood from the RC-equivalent thermal networks presented by Jones [118] and Armstrong [119].

Among the applications of temperature measurements using the measurement set-up, two groups of assumptions have been of interest: temperature differences inside a module (intra-module) and temperature differences among modules (inter-module).

With the mounting conditions of the measurement set-up of this work (fixed, open rack, oriented due South, tilt angle 18°), the effect of wind access to the modules plays a role. Throughout this chapter, the projected wind vector ($v_{w,proj}$) is used to better illustrate and understand wind effects on module temperatures, with details about the method in a.o. Section 4.7.

Intra-module temperature inhomogeneities (non-uniformities) for outdoor calibrations were identified by Müllejans *et al* at ESTI [28] to amount to 60 % of their uncertainty budget. They *assumed* the temperature inhomogeneity values

or slow-changing irradiance conditions still limits the amount of days (or even hours) to a fraction of the year, and thus impoverishes analyses.

for the modules to be ±3 °C (i.e. $\Delta T_{max} = 6\,°C$), and with a rectangular type of probability distribution. Together with the model results from IMEC (e.g. [11]), this has suggested an avenue of investigation, with the results given in Section 4.10.

A reduction in the intra-module temperature homogeneity uncertainty may then lead to reduced uncertainties in module power and ultimately, energy [120]. In particular, for the fixed-rack outdoor method[6] outlined in the IEC 61853-1 standard [77] and applied by a.o. ESTI [121, 122], often occurring (e.g. daily) temperature non-uniformities play a role for the uncertainty determination.

Inter-module temperature differences are of interest as larger arrays are generally assumed to operate at a homogeneous temperature (occasionally with a stated inter-module temperature variation (ΔT_{m-m})), which then permit the use of a limited amount of representative temperature measurements to characterise the whole [123]. The results obtained for this measurement set-up are discussed in more detail in Section 4.11.

With better temperature data, the effect of temperature may then be used for power and energy modelling efforts, see e.g. [29, 119, 124, 13, 125], in particular to reach the lowest model uncertainties compared to measurements: ignoring temperature in modelling leads to errors [126].

The need for (continuous) temperature measurements on photovoltaic modules is mandated by standards (e.g. [15, 16]), as well as recommended to verify and characterize the thermal behaviour of the photovoltaic modules studied [127]. Moreover, continuous module temperature measurements are useful for energy yield evaluations and modelling purposes - this will also be discussed further in Chapter 5.

4.2 Long-term temperature measurements

As models have historically been ported from indoor laboratory measurements on naked cells to encapsulated cells (indoors and outdoors) and ultimately modules (indoors and outdoors), the methods and descriptions in literature have focused on cell temperatures. Moreover, as the type of encapsulation materials has varied over time, the most constant aspect has been the photovoltaic cells inside the modules. As a result, almost all data reporting has focused on the initially indoor-determined relationships between the open-circuit voltage V_{oc}

[6] Which requires the measurement of large number of I-V curves for subsequent binning according to temperature and irradiance.

and temperature, and using this as a basis for encapsulated cell and module temperature measurements, both indoors and outdoors.

The outdoor measurements using e.g. contact measurements then often reported temperatures lower than suggested by the measured V_{oc} - leading to corrections being proposed, such as the backsheet-to-cell correction by King *et al* [114].

The work at Sandia National Laboratories by King *et al* [114] and others such as Tina [128] indicate that there are temperature differences between cell and backsheet, and that these may vary with the irradiance. As a module's backsheet has been designed to prevent environmental elements such as moisture[7] to enter the module, it is therefore generally not possible in practice to directly measure a photovoltaic modules' cell temperature using a contact method (i.e. with the thermal sensor directly touching the cell surface).

The main alternatives for outdoor measurements are therefore a backsheet contact temperature measurement (with, or without a backsheet-to-cell correction applied), a V_{oc}-derived[8] method such as the equivalent cell temperature (ECT) [129] or a non-contact measurement such as infrared (IR) thermography [130]. More methods (often aimed at failure detection), generally in the non-contact method field are also given in [131]. Some of the methods of [131] may become more popular in the future, provided their repeatability, cost and accuracy improves.

Table 4.1 gives an overview of the advantages and disadvantages per measurement method. For research purposes, contact temperature measurements are often combined with V_{oc} (this is also specified in the standards, e.g. [129]), with IR measurements complementing these results, either as verification or to determine discrepancies between measurement methods, e.g. [132]. For monitoring purposes of (large) photovoltaic installations, contact temperature measurements and IR measurements are most often combined, although V_{oc}-only methods are used as well [123]. In general, temperature values of photovoltaic modules in (large) photovoltaic systems are rarely continuously monitored, and when they are, the number of temperature sensors and modules monitored is limited. For larger arrays and systems, the most applied method is where one module or array is deemed to be representative of the whole [123].

The focus of this work on detecting, analysing and characterising thermal transient behaviour of photovoltaic modules and the possibility of intra-module (and also inter-module) temperature differences and variations led to contact temperature measurements being the preferred method. In particular, a number

[7] Moisture can lead to undesirable current paths, which lead to short-circuits and damage the cells, as well as corrode the contacts.

[8] The temperature may be deduced from the V_{oc}, as the V_{oc} has (generally) a predictable relationship to temperature.

Table 4.1: Comparison of main temperature measurement methods

	Contact measurement	V_{oc} methods	IR methods
Applicable measurement conditions	All	All; best for stable weather	G>600 W/m^2 recommended[a]
Advantages / strong points	Standardised [15, 16, 27, 77]	Standardised [129]	Being standardised [133]
	Module @ V_{oc}, I_{sc}, MPP	Module @ V_{oc}	Module @ V_{oc}, I_{sc}, MPP
	Continuous measurements ⇒ Timeseries analysis	"Most accurate"	Very broad overview: rapid failure detection
Disadvantages / weak points	>1 sensor required for ΔT determination	Assumes non-faulty cells.	Snapshot measurement.
	Point-based measurement	Assumes temperature homogeneity.	Relatively low accuracy & resolution.
	Multiple points of failure possible per sensor	Module not @ MPP: not practical for monitoring	Human interaction needed

[a] Lower values of G possible, but temperature differences will be lower.

of factors pointed to contact measurements as being the main[9] or only method to use, as contact temperature measurements have the following key advantages:

- They are the main method for continuous temperature monitoring, as evidenced by the number of standards that depend on them (see Table 4.1).
- If well executed, the measurements have little to no impact on the studied module's temperature and electrical performance. V_{oc}-methods for example require the module to be at V_{oc}, even for a short while, which

[9] If organisationally feasible, temperature method determination inter-comparison and inter-calibration can lead to better results: combining at least two of the methods of Table 4.1.

leads to electrical losses (in some cases, the inverter needs to restart) and a modification of the module's temperature.

- The higher accuracy and improved resolution compared to non-contact methods such as IR thermography.
- The cost-benefit relationship is also better than the alternatives in Table 4.1, especially for higher accuracy demands where the (total) measurement uncertainty[10] is "±1 K"[129]: many IR thermographic cameras have a similar or larger uncertainty. Achieving this uncertainty is also not as straightforward as it appears with "high accuracy" contact thermal sensors: many are provided with uncertainty values ∼0.8 °C at the higher end of the measurement range (80 °C or higher). Due to the law of propagation of uncertainty (see Section 3.3.3), these uncertainties approach the limits mentioned in the standards, and if erroneously installed, may easily exceed the limit.

Having thus determined to opt for contact measurements, the sensor type must be chosen. As the focus was on transient thermal analysis *and* temperature homogeneity measurements, a large number of temperature sensors were to be logged, preferably on the NI CompactRIO measurement platform. The two main sensor types that can be measured using National Instruments C-series cards are thermocouples and resistance temperature detector (RTD), the latter generally being of the Pt100 variety. In terms of accuracy, the best thermocouple measurement card available by National Instruments gives an instrument uncertainty of ±0.29 °C [134]. The Pt100 measurement cards chosen (NI 9217) have a worst-case uncertainty of ±0.35 °C for a four-wire connection [135].

A Pt100 temperature sensor's resistance varies with a known relation to its temperature, as the Platinum (Pt) in the sensor has a well-known thermal response. The sensors are then constructed to have a resistance of 100 Ω at 0 °C, hence the name Pt100.

The deciding factor between these two types of sensors was then accuracy, practicality and cost: more accurate Pt100 sensors ([60]) can be bought at a cheaper price, and their wiring is much easier to obtain and at a significantly lower cost[11]. The maximum, yet typical, distance between the module to measure and the cabinet where the readout happens is (see also Figure 2.6) approximately[12] 12 m to 18 m. For 44 temperature sensors, the total cable

[10] Note also that the coverage factor (k) for this and other uncertainty values is *not* mentioned. It may, generally speaking, be assumed to be $k = 1.96$ for 95 % coverage.

[11] About one third the price of thermocouple cabling, per meter.

[12] 6 m from cabinet to front row of modules (of e.g. *PV062*) + 6 m to the modules.

length, associated cost and possible impact on measurement uncertainty were therefore not a trivial choice. Moreover, the easier extension of the measurement leads of Pt100 sensors with no impact on measurement uncertainty (because of the use of four-wire connections) was also a deciding factor.

4.3 Physical lay-out of array

To aid the interpretation of some of the figures in this chapter, Figure 2.6 was modified to Figure 4.1, and the approximate placement of poles also indicated (these will be discussed in Chapter 5). Most of the temperature discussions and measurements relate to the *Smart PV* modules, which are indicated by a blue or green coloured triangle. Module *PV052* has 11 temperature sensors installed, of which 9 are laminated against the backside of the cells, and two backsheet sensors, used to verify the backsheet-to-cell relationship.

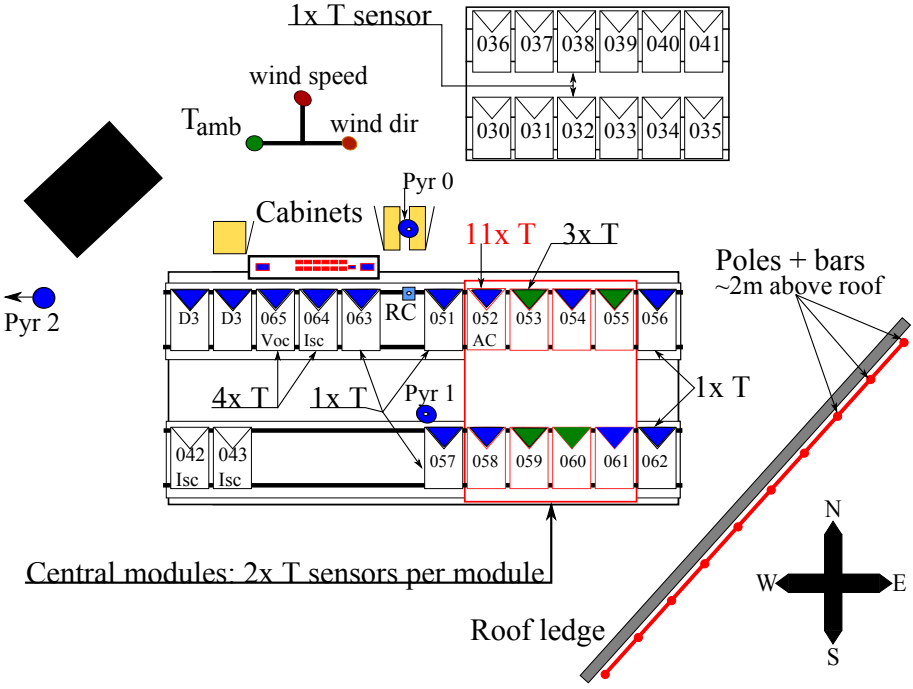

Figure 4.1: Bird's eye view of set-up, with focus on temperature measurements. Poles which cause shading in the morning and early afternoon were installed from 1 September 2015 onwards. Figure to approximate scale.

4.4 Methods used to obtain improved temperature measurements: sensor attachment and placement

The impact of correct, temperature sensor attachment on the surface[13] to be measured may often be larger than the sensor measurement uncertainty itself: removing or reducing *operator error* and application of correct practices thus leads to improved and comparable results. The importance of having reliable, trustworthy measurements is that errors in measurements may lead to erroneous conclusions, such as the effect of a module's temperature on its efficiency. As mentioned before, it is unrealistic nor practical to have temperature sensors placed directly against a photovoltaic module's cells (except for custom-made modules), especially as this may lead to an accelerated degradation process, compared to a module where the backsheet is intact.

As the goal is to have temperature measurements and practices that are valid today *and* for use in the future[14], the sensors, attachment methods and corrections had to be tested. In this regard, the maxim of "trust but verify" applied: the sensors and read-out equipment chosen should be trustworthy, but perhaps there may be steps to take to ensure repeatability and quality of measurements. These are evaluated in the following sections.

The method of sensor attachment in Algorithm 4.1 (line 3, see further) is a (very short) practical summary of the conclusions from the paper presented at EU PVSEC 2014 [117]. There, experimental methods to attempt to measure a cell temperature while measuring against the backside of the module were shown. This was aimed at testing some of the methods presented by Jankovec and Topič [115], while keeping in mind the general thermal transfer model of Armstrong and Hurley [119].

The method of sensor attachment was investigated in a number of experiments. The experience from the first iteration and early use of the second iteration of the measurement set-up indicated that sensors could come loose due to a combination of low adhesive strength, sensitivity to humidity and heat. The choice for the method of temperature sensor attachment further had to satisfy user-friendly constraints: the sensor must be easy enough to attach, stay stuck for the intended duration, and be removable when that period has passed. The solution found in this case was very high bonding (VHB) tape [136] of the 4910

[13] Which has generally been the photovoltaic modules' backsheets.

[14] It was anticipated that few modules would have temperature sensors laminated against cells in the future, hence the importance on the method.

family: transparent viscoelastic tape, aimed at surfaces with high surface energy such as glass, many metals and plastics.

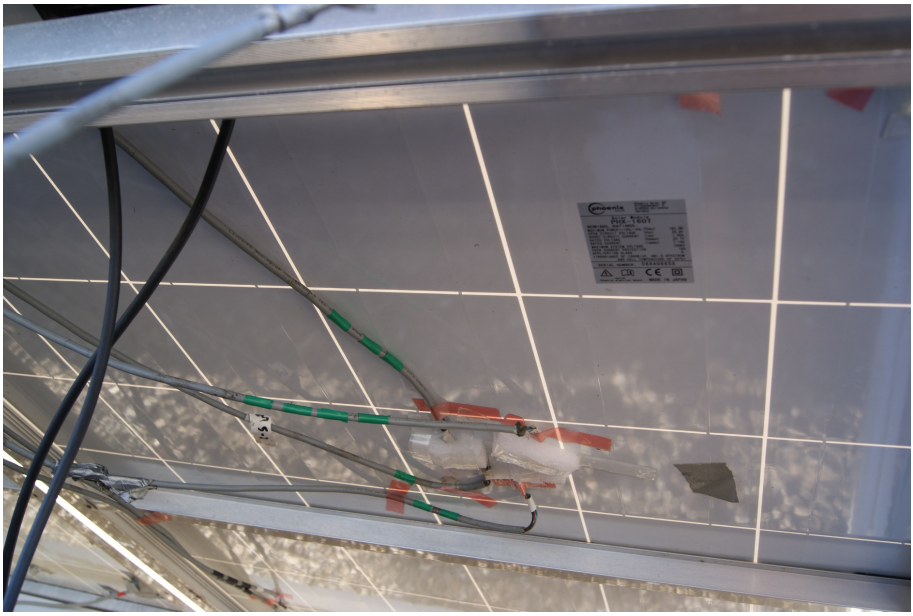

Figure 4.2: Photograph of a comparison of temperature sensor attachment and insulation methods tested, with backsheet and cell temperatures measured, taken on 10 January 2014. Module shown: PV004 [137].

With the attachment method (VHB tape) more trustworthy, experiments were performed to determine whether additional insulation was required for temperature sensors and if so, what dimensions and type of insulation should be used. One example of such an experiment is shown in Figure 4.2, where the insulation methods were compared, as well as cell and backsheet temperatures. By placing the sensors on the same cell, the expectation was to measure (e.g. at night, and during the day) the same temperature, and then be able to attribute a deviation to the insulation method. The cell was made accessible by carefully cutting into the backsheet (similar to a skin lift cut), and then placing the sensor against the cell.

An illustrative figure for backsheet-to-cell temperature differences is given in Figure 4.3, where another of the experiments is illustrated, which was performed to determine the best (or most practical) insulation and attachment methods. The top left (1x1) and bottom left (1x8) cells of the module had an identical attachment and insulation method, where a single layer of VHB tape

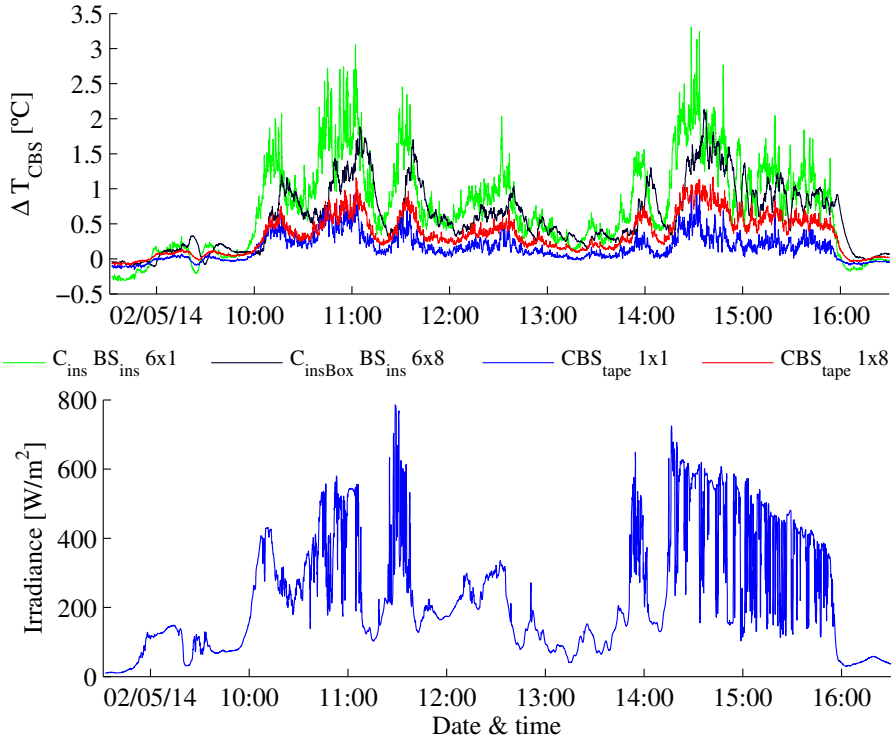

Figure 4.3: Cell-backsheet temperature deviations measured on 5 February 2014. Subscripts: "t" tape, "ins" insulation, "insBox" insulation in box. Position on module: 1x1 top left, 1x8 bottom left, 8x6 bottom right. Module measured: PV001 [137]. Backsheet temperature sensors (green and black lines) with insulation show unexpected and thus undesireable ΔT_{CBS} peaks and significant time delays to cell temperatures.

was placed over the sensor heads. The top right (6x1) cell had the cell and backsheet sensors placed with a layer of insulation (∼2 cm thick, 4 cm wide) over it, with the insulation stuck in place using the same[15] VHB tape. The bottom right (8x6) cell had the cell sensor covered with insulation placed inside a box (so the thickness of insulation could be higher: ∼3 cm), while the backsheet sensor was covered with insulation as in the case of the 6x1 cell.

For the day shown in Figure 4.3, with quite large and repeated irradiance fluctuations, it is clear that the smallest backsheet-to-cell temperature differences ΔT_{CBS} are observed for the tape-only sensors. By contrast, the two cells with insulation on the temperature sensor have a delayed temperature response (e.g.

[15]The tape in this case was not placed on top of the insulation over the sensor head.

the black line clearly lags the red and blue lines). Thus, the temperature indicated by the backsheet sensor with VHB tape is more similar to the sensor placed on the same cell than using insulation methods. Moreover, both "high"-insulation methods on the module show higher values of ΔT_{CBS}, which is undesirable - the purpose is to achieve the smallest possible temperature deviations in magnitude *and* temporal response using physical means (i.e. tape).

The above results were obtained and repeated for multiple modules measured over several weeks, which lead to the following conclusions. Using (too much) insulation to physically "correct" a measurement leads to results which are:

- Untrustworthy or not translatable to a different set-up. For example, the 6x1 ΔT_{CBS} value in Figure 4.3 shows that the cell also suffers from sensor heating: the insulation over the cell sensor leads to a faster temperature rise than the backsheet, as the heat cannot be dissipated as fast as should be the case to the environment.
- Too different from the cell data. Both tape-only cell-backsheet temperature plots in Figure 4.3 show a consistently smaller deviation from the cell than the insulation-method data.
- Delayed in time, compared to the "true" change in the module. This result can be anticipated from the model of Armstrong and Hurley [119], as the added insulation means a local artificial increase in the thermal resistance and mass (or capacitance), which leads to a time-delayed measurement response.

Lastly, from a practical perspective, opting for a tape-only attachment and insulation method is both more practical (faster to install each sensor), repeatable and translatable. Thus, from the above, it is now possible to look in more detail at the most desirable measurement of temperature, to then evaluate the relationship between the cell and backsheet temperature, and how these interact with the prevailing weather conditions.

4.5 Steady-state temperature sensor bias detection and corrections

The above discussion has shown some of the issues that occur for dynamic measurements, and some of the effects of temperature sensor placement and insulation methods. With a valid and repeatable temperature sensor placement

method available, steady state sensor deviations (biases) may be detected and corrected.

The value of the temperature sensor bias (ΔT_{bias}) has to be determined for each temperature sensor placed on a PV module. The best situation in which to determine ΔT_{bias} is where the conditions allow a quasi-ideal temperature homogeneity to be assumed, both for the ambient temperature and surfaces.

These would be very cloudy (so thermal radiation from modules is minimised), low or no irradiance (so external heating effects are eliminated), low wind speeds (<1 m/s) and rain (as the larger heat capacity of water versus air maintains a more constant temperature, for longer). Obviously, not all of the aforementioned conditions can always be satisfied, although heavy rain typically outweighs high wind speeds, and rain episodes automatically lead to heavy cloud cover and a reduction in irradiance. For areas that do not have rain at regular intervals such as Belgium, a more detailed data analysis can still provide a reduction in measurement uncertainties, albeit possibly smaller than the situation mentioned here.

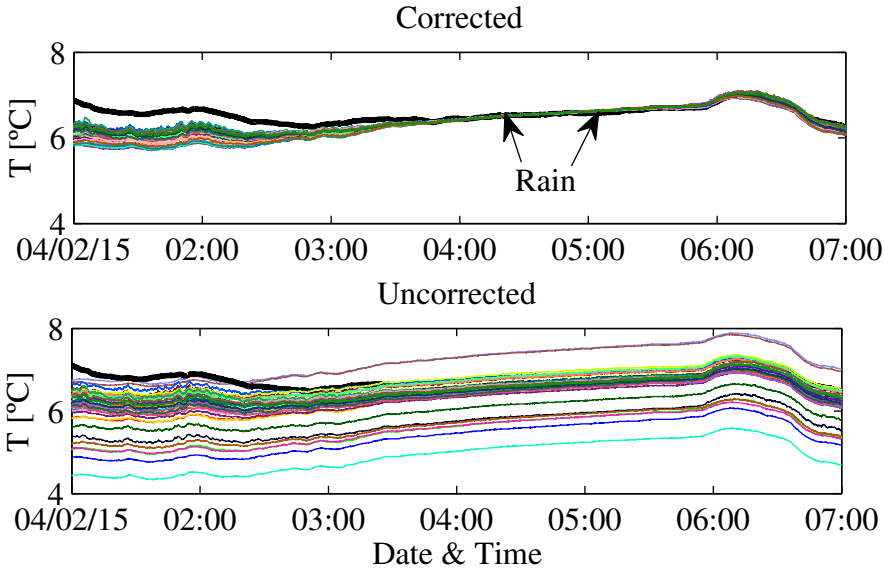

Figure 4.4: Correction using ΔT_{bias} and comparison to raw data on 2 April 2015. All temperature sensors shown, ambient sensor is thick line.

The temperature bias correction that can be calculated based on the rain events shown in Figure 4.4 leads to a maximum sensor deviation before 06:00 of

<0.05 °C (maximum - minimum value), whereas ΔT_{max} without correction is 2.25 °C (maximum - minimum value). The need for this individual temperature sensor bias correction is that without it, all results and calculations (see, e.g. Chapter 5) are impacted, leading to a higher uncertainty, which as shown above, can be avoided.

Contrasting the maximum deviation under arguably ideal conditions with the indicated night-time measurement uncertainty of Faiman [105] (root mean square (RMS) uncertainty of ±0.26 °C), the benefits of this approach are clear: by characterization, evaluation and where necessary correction of the measurement instruments, it is possible to achieve a significantly improved measurement accuracy, in this case, using the same RMS uncertainty metric, of ±0.02 °C.

However, the value of the expanded uncertainty of temperature (U_T) is limited by the measurement uncertainty of the read-out equipment, the NI 9217 measurement cards [135]. As a result, the value of U_T for one temperature measurement is not ±0.02 °C, but rather ±0.40 °C, for a coverage factor (k) = 1.96 (95 %). For temperature data comparison between sensors on modules[16], U_T = ±0.80 °C, whereas for the over-temperature (T_o) (see Section 4.6) U_T = ±0.57 °C.

Without the temperature corrections, the *average* $U_T \geq \pm 1.8$ °C, thus indicating that the expenditure of effort results in a reduction in uncertainty by approximately 75 %, from ±1.8 °C to ±0.4 °C. Moreover, it is good practice to first minimise all predictable sources of measurement uncertainty and then calculate the uncertainty on the remaining random residuals - as was shown in Chapter 3.

The temperature bias value is not necessarily a fixed value in time (as sensors may come loose or degrade), and must be checked at regular intervals, e.g. per month, or sooner, if a sensor has been (re)moved. Otherwise, the quoted or calculated uncertainty values no longer apply. The sensors shown in Figure 4.4 were installed and verified at regular intervals, yet the results from this section do caution against blindly believing sensor data.

The temperature value that is thus corrected using the value of ΔT_{bias} in subsequent calculations according to

$$T_{m,corrected} = T_m + \Delta T_{bias}, \tag{4.4}$$

where the corrected measured temperature ($T_{m,corrected}$) and measured temperature (T_m) can be either a cell temperature (T_C) or backsheet

[16] Where the data can be assumed to be fully correlated.

temperature (T_{BS}). (At this point, the correction is for the sensor and the attachment method, *not* yet the relationship between cell and backsheet - this is done in Sections 4.7 and 4.8.)

On a practical note, it is possible to save the corrected temperature data immediately to the logging file. The choice was made to do this in the post-processing stage, where the data is checked for consistency and quality, which also allows greater flexibility in assigning a value to ΔT_{bias}. Moreover, if the previous ΔT_{bias} deviates from the current month's ΔT_{bias}, the post-processing step must be applied again, thus not saving on effort. (Saving and comparing the values of ΔT_{bias} may be used for sensor degradation monitoring and analyses.)

A summary of the steps to follow for bias detection and correct sensor placement is given in Algorithm 4.1. (The order of execution of the steps may vary, as shown in this chapter).

Algorithm 4.1 Steps to follow to ensure correct temperature measurement

1: **Start**: ensure proper functioning of sensor, cable and read-out after initial installation.
2: Optional: If available, use IR thermographic camera to determine correct functioning of module and cell for desired sensor location - see Table 4.1 and [131].
3: **Attach** sensor to desired location on module, using a single layer of (VHB) tape over sensor head; as little additional tape as possible against module surface (minimise self-heating). Fix cable with tie wraps. Record position on module, module code, installation date. Verify correct functioning of sensor.
4: **Compare** output of sensor to > 3 sensors, including T_{amb} during day(s) after installation: evaluate night-morning transition, noon peak and evening-night transition.
5: **Determine** bias offset value: compare output to similarly placed sensors (if possible previously calibrated) at night or low irradiance ($<50\,\mathrm{W/m^2}$) during cloudy, low-wind conditions ($<1\,\mathrm{m/s}$) **or** during period of heavy rain. $\Delta T_{bias} = T_{sensor} - \langle T_{sensor,others} \rangle$
6: **return** ΔT_{bias} per sensor.

Line 2 in Algorithm 4.1 depends on the availability of an IR thermographic camera to verify correct functioning of the photovoltaic module. This is a snapshot verification, as mentioned in Table 4.1, which also depends on high enough irradiance, due to the limited resolution of the IR thermographic camera. Assuming a non-faulty module and sufficient irradiance, the IR measurement can suggest the point(s) to place temperature sensors. The IEC standards [77, 27] mention the centre of the module and at least one corner location, as this is

generally where the largest temperature differences may be measured of the module. (The edges of PV modules are expected to be cooler than the centre, as there are less surrounding cells.)

In summary, live monitoring (and logging) of module temperatures is best served using the corrected measured temperature ($T_{m,corrected}$) of Equation (4.4), if the ΔT_{bias} value is verified and updated at regular intervals. For temperature values evaluated after the fact, the data quality control step must be performed in any case, and the marginal benefit of having logged $T_{m,corrected}$ is reduced.

4.6 Over-temperatures as a metric for analyses and as a diagnostic tool

Both as a diagnostic tool and for analyses, the over-temperature (T_o) (mentioned in, a.o. [29, 138]) is a powerful temperature comparison metric:

$$T_o = T_c - T_{amb}, \tag{4.5}$$

as the value of T_o incorporates the ambient temperature. In essence, Equations (4.1) and (4.2) and similar temperature models and equations all attempt to model the over-temperature as the ambient temperature is then taken from current or historical measurements. A rise in the ambient temperature (due to the heating by the sun during the day) is therefore compensated and visually removed, as in Figure 4.5.

Line 4 in Algorithm 4.1 refers to what is shown in Figure 4.5: the night-time high and noon low over-temperature indicate a loose temperature sensor (the thick line of the temperature values shown). As a result, daytime (G>10 W/m^2, ideally G>500 W/m^2) indicated temperatures are between the ambient temperature and the module temperature. During the day, this manifests as a consistently lower temperature than other sensors, whereas at night the value is closer to the ambient temperature (which is often higher than module temperatures, as the ambient sensor has a radiation shield). As can be seen in Figure 4.5, the effect of the loose temperature sensor is identified better and faster with T_o (and then possibly ΔT to other sensors) than by comparing absolute module temperatures (either of T_C or T_{BS}), as these temperatures are also affected by the ambient temperature.

The use of T_o in figures such as Figure 4.5 leads to an improved relative resolution to identify temperature differences. The temperature differences in the measured values and the over-temperatures is identical, yet the scale on

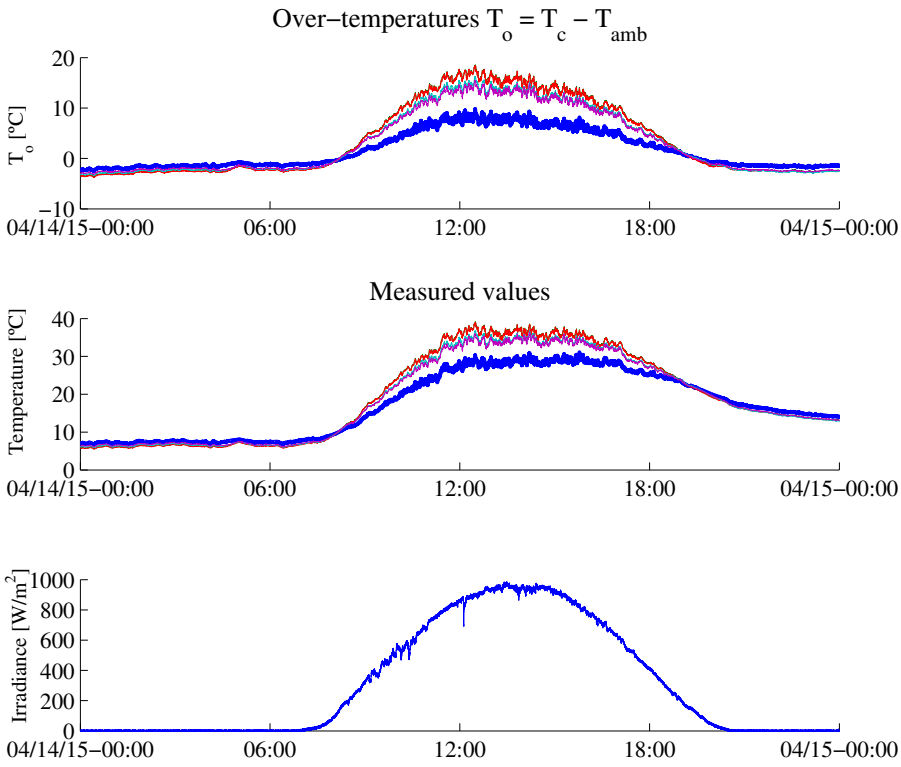

Figure 4.5: Detection of a loose temperature sensor (thick line) using the over-temperature: its temperature is too high at night and the peak daytime value too low, compared to other sensors.

which they are displayed differs, with the maximum temperature difference for T_o smaller than that of the measured cell or backsheet values. As such, a temperature difference between sensors or modules is larger in relative terms. For example, the temperature difference between midnight and the peak is $\Delta T_o = 21\,°\mathrm{C}$ using T_o and $\Delta T_{sens} = 31\,°\mathrm{C}$ for the red line on Figure 4.5. In this example, using T_o, a sensor-to-sensor temperature difference of 1 °C is $\sim$5 % of the visual scale[17], compared to $\sim$3.3 % for measured sensor values.

The use of the T_o appears to be straightforward, and the above paragraph may be seen as superfluous. The issue is that the detection of loose temperature sensors (or in general sensors with a type of degradation process) is not an easy

[17] Assuming that both temperature axes have adapted temperature ranges.

task. The above example is more extreme than often encountered - it may just be that a sensor indicates a value at 80 % of what it should indicate, and that real-time visual analyses cannot easily distinguish between genuine temperature differences and sensor issues. Hard-to-see temperature errors of 2 °C to 3 °C result in a measurement error for the power of ∼1 %, and thereby a misdiagnosis of the performance. On that note, concepts such as the over-temperature have been applied too little, and when they have, authors have often devised a new name (e.g. ΔT [139], or no name), hindering the use of this and similar tools for analyses. In this regard, the work of the PV Performance Collaborative [140] is useful in establishing an industry-standard terminology.

The over-temperature T_o also makes the interaction between a module's temperature and the environment more explicit, and may thus serve for educational purposes. For example, the Ross coefficient h_{Ross} and the G together in Equation (4.1) are equal to the T_o. Similar interpretations for other similar thermal models (e.g. some that incorporate the wind speed) may be done, which allows a deeper understanding of the topic at hand.

4.7 Cell and backsheet temperature measurements for backsheet-to-cell temperature corrections

Up to this point, the method to attach (Pt100) temperature sensors (using VHB tape), whether they need insulation or not and steady-state errors have been dealt with. The next step is then using the improved measurement methods to determine the difference between temperatures measured against the cell's backside surface and the backsheet of a module.

One formulation for the expected backsheet-to-cell correction was given by King et al, where the value of the ΔT_{CBS} was given as "2 °C to 3 °C at 1000 W/m^2[...] for modules in rack mount" [114], to be used in Equation (4.6), also from [114]:

$$T_C = T_{BS} + \Delta T_{CBS} \cdot \frac{G}{G_{STC}}. \tag{4.6}$$

The method to determine ΔT_{CBS} appears easy enough: measure the T_{BS}, the T_C and the irradiance (G), then calculate ΔT_{CBS}, e.g. using a regression method. An example for 31 July 2015 is shown in Figure 4.6, which was a variable irradiance day.

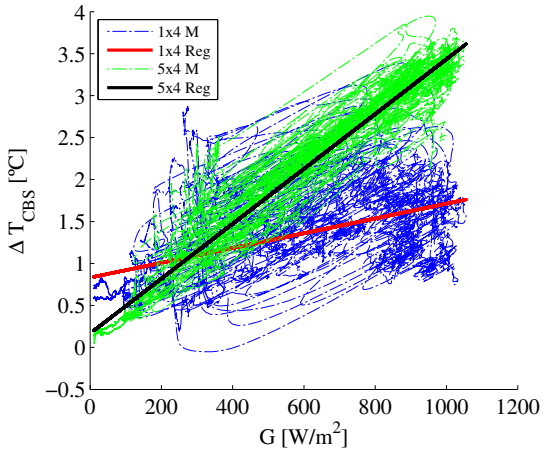

Figure 4.6: Example of Cell-Backsheet temperature differences versus irradiance on 31 July 2015, for module *PV052*. Top centre (1x4) and middle centre (5x4) positions. M: measured, Reg: Regression line.

Assuming that a representative[18] module is available, it would be possible to perform measurements during one or more days, to determine the backsheet-to-cell temperature relationship. Such a module can be constructed with temperature sensors laminated against the cell backsides and a few on the backsheet, in this example, module[19] *PV052*, with the comparison shown for the 1x4 (top centre) and 5x4 (middle centre) positions.

The issue with the assumption about the ease of measurements to determine the ΔT_{CBS} is that the sensors may have biases (offsets), and the sensors may be incorrectly attached, which both can lead to an incorrect determination of ΔT_{CBS}. Moreover, the impact of wind (both speed and direction) affects the temperature, and the measurement thereof.

Equation (4.3) was determined for steady-state conditions [114], and no statement or clarification given for dynamic conditions. As such, an unqualified use of the value of ΔT_{CBS} for second-based data may have the backsheet-corrected data show faster fluctuations (i.e. noise) than encountered in reality. Additionally, steady-state (i.e. clear-sky) conditions with an irradiance above $800\,\mathrm{W/m^2}$ occur too little throughout the year in Belgium for only these moments to be used. Moreover, modules are in reality *also* subjected to variable

[18] If possible, identical module from the same manufacturer, in particular same encapsulation materials and backsheet colour.

[19] All laminated sensor positions: 1x1, 1x4, 1x6, 5x1, 5x4, 5x6, 10x1, 10x4, 10x6.

conditions, so a value for ΔT_{CBS} should also be determined under a similar variety of conditions.

The difficulties with obtaining a single value for the cell-to-backsheet temperature difference ΔT_{CBS}, apart from the measurement uncertainty and bias reduction techniques described above, are illustrated in Figures 4.6 and 4.7.

The data in Figure 4.7 is shown for three consecutive days in July, with the top subplots indicating the cell-to-backsheet temperature difference versus the irradiance G, which can be used to calculate the value of ΔT_{CBS} at STC to be used in Equation (4.3), or its more correct formulation: Equation (4.15), given further below. The middle subplot shows the projected wind vector ($v_{w,proj}$). The bottom subplot shows the irradiance profile for those days.

The projected wind vector ($v_{w,proj}$) joins the wind direction and wind speed in two values which can be displayed on the same graph for the main directions of importance for PV modules, namely the front-back axis (North-South) and the sides (East-West). The North-South projected wind vector ($v_{w,proj,NS}$) is positive for wind *from* North and similarly the East-West projected wind vector ($v_{w,proj,EW}$) is positive for wind *from* East.

Compared to displaying the wind speed and the wind direction separately, the $v_{w,proj}$ has a range of advantages, of which one of the most important ones is the ability to calculate the mean wind direction[20]. Figure 4.11 further in the text also illustrates the use of $v_{w,proj}$.

The average wind data for the days shown in Figure 4.7 is given in Table 4.2.

The larger variability in the measured values of ΔT_{CBS} on variable days (which can be seen for 2 and 3 July in Figure 4.7), has the possible effect that a regression line through the data may be subject to significant errors. This is due to the sensitivity of the regression methodology to outliers at the start and end of the data ranges (in this case $<100\,\mathrm{W/m^2}$ and $>900\,\mathrm{W/m^2}$) - this is particularly pronounced for the data for position 1x4, at the top of the module.

The effect of the wind speed and direction on the relationship of ΔT_{CBS} per position is clearly visible in Figure 4.7 and Table 4.2. The combined effects of solar and wind variability also contribute to a larger spread in the values of ΔT_{CBS}. For modules whose back surface cannot easily be reached by wind (e.g. mounting flush with the tilted roof in the residential sector), the data could[21] be filtered for wind directions from South only (and from North in the Southern

[20] By contrast, if the wind was from NNE at 15° and then NNW at 345°, the mathematical average would equal 180° (S): the wind would suddenly be pointing in the opposite direction of reality (0°) (N).

[21] It is however recommended to install physical barriers to better simulate such conditions.

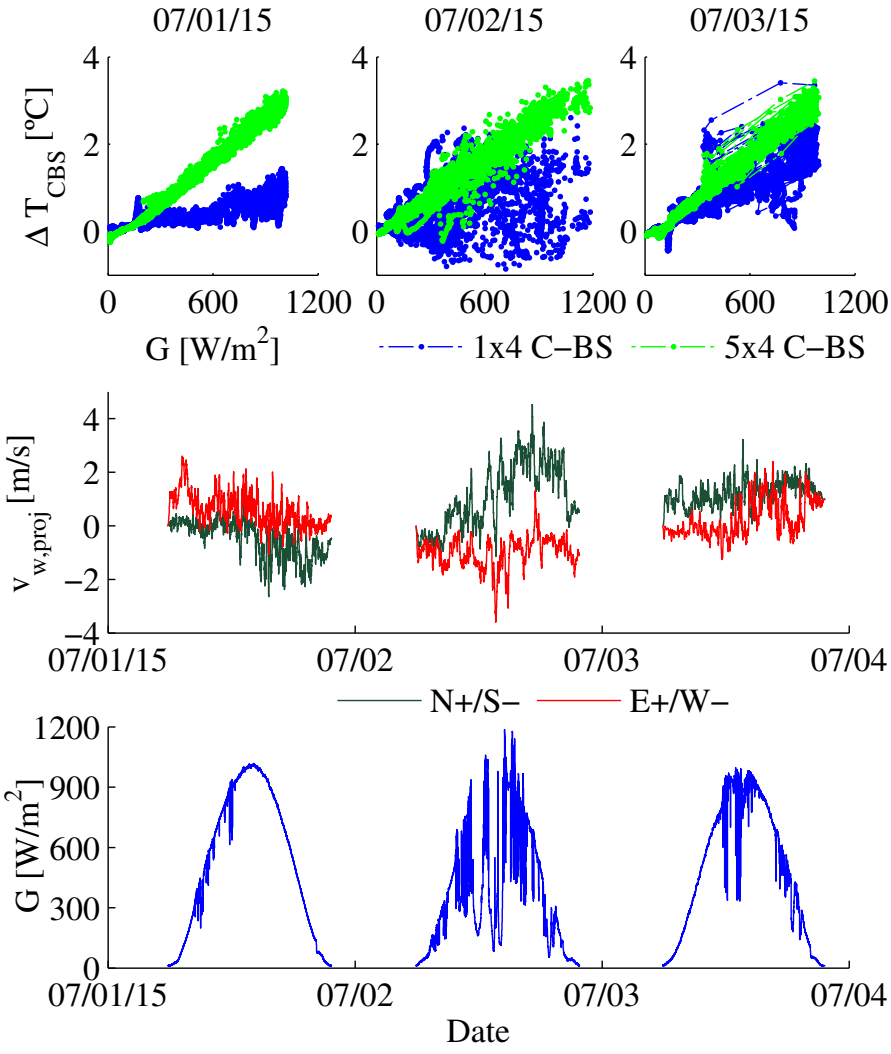

Figure 4.7: Cell-backsheet temperature measurements on 1-3 July 2015.

hemisphere).

By then applying the same methodology of linear regression on the ΔT_{CBS} versus G data as shown in Figure 4.7 for April and May 2015, a longer-term average value for ΔT_{CBS} was computed, and subsequently used in data analyses,

Table 4.2: Average wind data for Figure 4.7.

Parameter	1 July	2 July	3 July
$v_{w,proj,NS}$ [m/s]	−0.48	1.07	1.23
$v_{w,proj,EW}$ [m/s]	0.59	−0.99	0.24
$\sigma_{v,wind,NS}$ [m/s]	0.67	1.21	0.45
$\sigma_{v,wind,EW}$ [m/s]	0.62	0.57	0.67
$\lvert\vec{v_w}\rvert$ [m/s]	0.76	1.46	1.25
$\angle\vec{v_w}$ [°]	129 (SE)	317 (NW)	11 (NNE)

with the data in Table 4.3.

Table 4.3: Average values and spread of ΔT_{CBS} for April-May and April-August 2015 per position on module *PV052*.

	April-May	April-August
ΔT_{CBS}@STC Top (1x4) [°C]	0.21 ± 0.93	0.23 ± 0.90
ΔT_{CBS}@STC Centre (5x4) [°C]	2.87 ± 0.18^a	2.91 ± 0.18

Table 4.3 also indicates that it is possible to obtain a value for ΔT_{CBS} in limited amount of time (two instead of four months), if the daily irradiance in that period is high enough.

As the other modules on the set-up have the temperature measured at a central position, the value of $\Delta T_{CBS} = 2.87\,°C$ at STC was used throughout, for all *Smart PV* modules. This value is at the higher end of what King *et al* [114] use (they mention 2 °C to 3 °C at STC). This is module and encapsulant technology-specific, and thus suggests that similar tests as described here may be needed, if lowest measurement uncertainty is required. This methodology was also tested prior to this on modules *PV001-PV004*, with similar, albeit occasionally higher results [117].

The assumption for subsequent use is that, as all the *Smart PV* modules were constructed with the same encapsulant and backsheet materials, that the value of ΔT_{CBS} obtained from module *PV052* applies to all *Smart PV* modules, as the parameter ΔT_{CBS} characterises the thermal behaviour of the layers between the cell and ambient, as will be discussed further below.

Figure 4.8 shows that the sensitivity of the value of ΔT_{CBS} for the top middle position (1x4) has a pronounced correlation to wind direction, which is almost absent for the centre position. While the dominant effect is the North-South

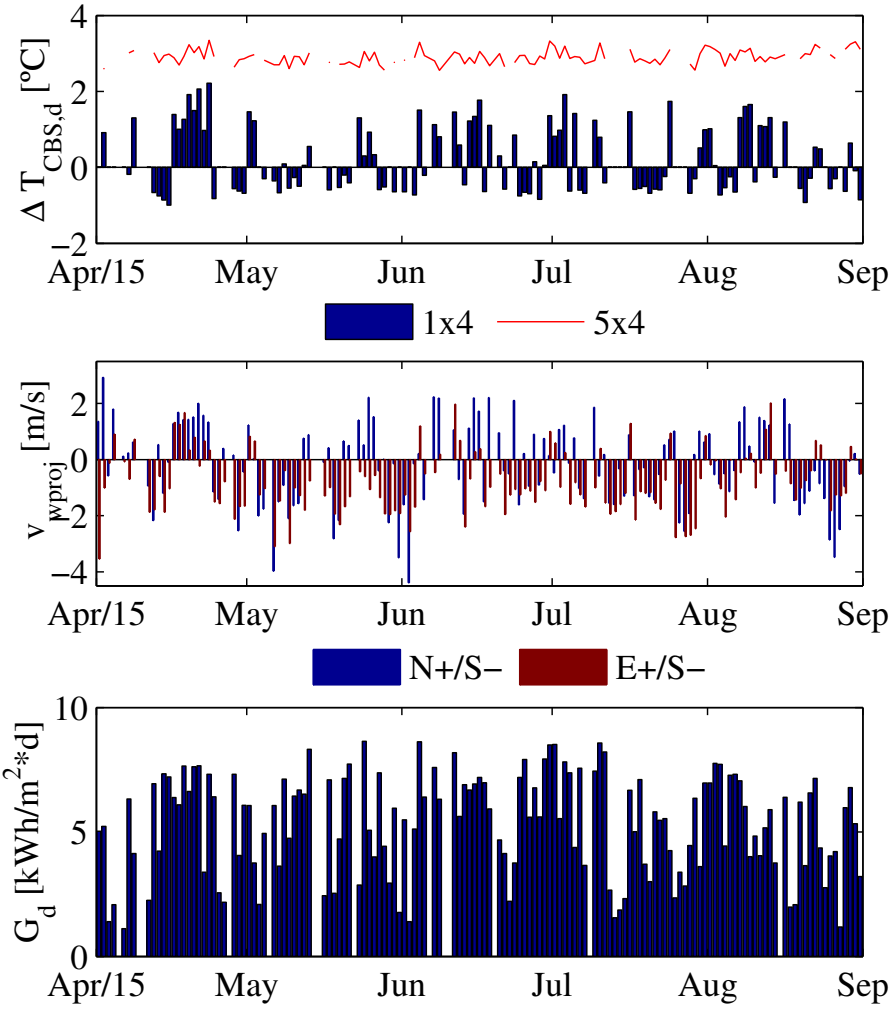

Figure 4.8: Daily filtered values of ΔT_{CBS} for top (1x4) and centre position (5x4) on module *PV052*, $v_{w,proj}$ and G_d, April-August 2015. Data removed for filtered days. The ΔT_{CBS} for position 1x4 shows a much stronger correlation to $v_{w,proj,NS}$ than position 5x4.

projected wind vector ($v_{w,proj,NS}$) (this can be noticed for April: the magnitude and direction of ΔT_{CBS} corresponds with the value of $v_{w,proj,NS}$), if the

$v_{w,proj,EW}$ is very strong, then it also affects the determined ΔT_{CBS} on those days.

As can be observed in Figure 4.8, the values of ΔT_{CBS} for the top middle position (1x4) show a correlation to the variation in the wind speed and direction, which is much larger than in the centre of the module. This may in part be due to a higher effective wind speed at the top of the module, compared to the centre position - a conclusion similar to that voiced by Goverde *et al* [141]. The variation in the ΔT_{CBS} due to the variation in the wind speed and direction can also be seen in Table 4.3, where the standard deviation for position 1x4 is 0.90 °C, whereas for the centre this is 0.18 °C. As all sensors have been attached using an identical method (as described in Section 4.4), the variation may be attributed to sensor variation and wind effects, of which wind effects are the more likely explanation.

4.8 Cell-backsheet temperature behaviour under variable weather conditions: theoretical considerations

Up to this point, the installed Pt100 sensors have been verified, their steady state biases have been corrected and the value of ΔT_{CBS} at STC has been determined. Now, the relationship of Equation (4.3) must be verified for time series, and to identify the rate at which the corrections may be done. The conclusions can then be discussed using the framework of the model of Armstrong and Hurley [119].

Important to note here is that the concepts discussed in this section are used to have a *qualitative* framework for temperature behaviour analysis, and not a fully predictive *quantitative* framework. The complexities of the thermal-electrical interaction between photovoltaic modules and their environment are such that their study is outside the scope of this work[22].

As past analyses have used data averaged over longer time periods than used in this work, their conclusions and methods cannot be directly applied. In particular, equations that use "the irradiance" have actually been using the *average* irradiance over the chosen interval (one minute, five minutes, up to fifteen minutes). For temperature, this averaged irradiance corresponds to energy and *not* power (this will be explained in more detail further below). Thus, one of the questions to answer with this knowledge in mind, is "which period of

[22]The reader is invited to consult the work of Palyvos and Skoplaki [111] as well as that of Goverde *et al* [78, 142].

time is appropriate to average the irradiance, for temperature corrections of temperatures measured per second?".

To examine this in more detail, a few modifications are done to the model of Armstrong and Hurley [119], primarily of the area of the photovoltaic module (they use a smaller, older module), glass thickness and number and location of Ethyl Vinyl Acetate (EVA) layers. The model is an RC-equivalent thermal model, which uses the known, or estimated, properties of the main photovoltaic module components.

These main photovoltaic module components are drawn in Figure 4.9, with a number of items omitted, such as cell-cell electrical connections, the aluminium frame around the edges of the module and the junction box (from where the main electrical leads of the module leave). The Pt100 sensors displayed touching the cells may either be laminated against the cells back surface (this is the case for module *PV052*) with the leads passing through the backsheet, or reached by a "skin lift"[23] cutting away of the backsheet (this was the case for modules *PV001 – PV004*).

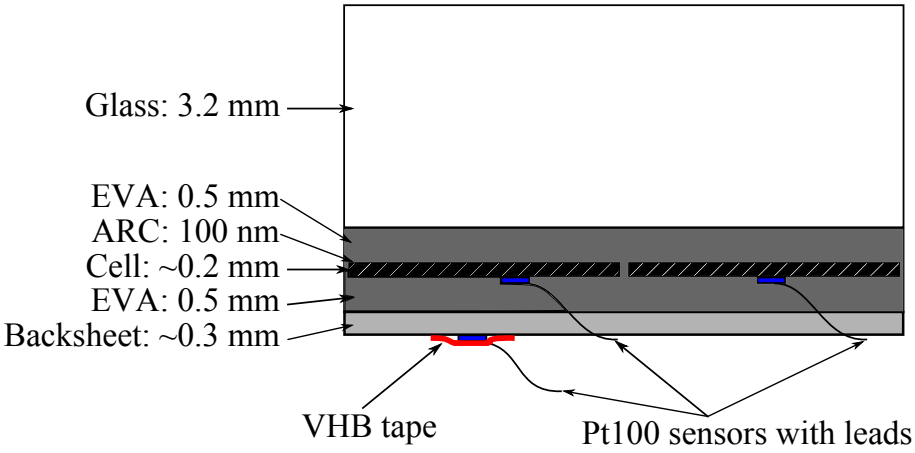

Figure 4.9: A cross section of a standard crystalline silicon module, with placement of Pt100 temperature against cells and the backsheet. ARC: Anti-Reflection Coating. Vertical dimensions to approximate scale. Figure inspired by [143].

The reduced equivalent thermal network of a module is a front-facing (glass side) thermal equivalent resistance (R_{th}) and thermal equivalent capacitance (C_{th}) and a backside-facing R_{th} and C_{th} as in Figure 4.10. The ambient temperature

[23] Carefully cutting three sides of a rectangular area on the backsheet to be able to insert a temperature sensor while maintaining the backsheet integrity as much as possible.

(T_{amb}) is shown in Figure 4.10 to be a thermal heat sink, on the front and the back.

Depending on the complexity of the model, the front-facing equivalent value of T_{amb} may be different to that of the backside of the module. One such situation occurs for tilted modules, where the sky temperature may be up to 20 °C lower than the ambient temperature during clear sky moments, which affects the upward-facing side of the module more strongly than the backside [113, 118] through radiative losses. In the case of roof-integrated or close-to-roof photovoltaic system mounting conditions, the back surface will indeed have a very different T_{amb} value than the front.

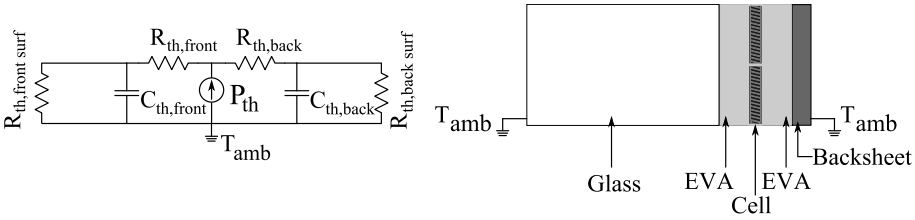

Figure 4.10: Reduced thermal RC-network conduction model with a cross section of a standard module.

Figure 4.10 shows that the thermal power generated in the cell (as a result of absorption of irradiance) can be dissipated to the environment via either the front side through the glass or via the back side of the module through the encapsulant and backsheet. Of interest here for temperature measurement and correction is the speed at which heat can travel through the module's surface, in which direction this primarily happens, and how this interacts with the environment.

The thermal equivalent power (P_{th}) can be calculated using the First Law of Thermodynamics (conservation of energy) as

$$P_{th} = G \cdot A_{PV} \cdot (1 - \eta_{PV,STC} \underbrace{T_{corr} \cdot \eta_N^*}_{\eta_N}), \tag{4.7}$$

where the reduction in the heat absorbed by cells[24] in the module is due to the amount of electrical power removed from the module. In the simplified form of

[24]The photons that reach the module as irradiance are reflected at the surface and absorbed throughout the module, e.g. partly in the glass, with efforts to maximise absorption in cells, hence the simplification. In reality, the situation is more complex than in Equation (4.7). The irradiance signal used to calculate the P_{th} may need to be corrected, depending on whether it has been measured using a pyranometer or reference cell. More complex models, e.g. that

Equation (4.7), the P_{th} is primarily impacted by the change in the module's efficiency due to the temperature being different from that measured at STC as in Equation (4.8):

$$T_{corr} = 1 + \gamma \cdot (T_{cell} - T_{STC}) = 1 + \gamma \cdot \Delta T_{STC}, \tag{4.8}$$

with the temperature coefficient of power (γ) typically $-0.35\,\%/°\mathrm{C}$ to $-0.50\,\%/°\mathrm{C}$ for crystalline silicon. The normalised efficiency (η_N) and temperature-corrected normalised efficiency (η_N^*) are discussed in more detail in Chapter 5. Nevertheless, the most important aspect of the η_N and η_N^* here is that a module or system's performance deviation from the theoretical maximum at MPP, e.g. due to MPPT errors or shading, is contained in these metrics.

Intuitively, a higher STC efficiency ($\eta_{PV,STC}$) leads to a lower module temperature as more of the incoming irradiance (G) is converted to electrical power and removed from the module. However, if the module is not operating at MPP, e.g. at at V_{oc} and I_{sc} whereby η_N^* (and therefore also the η_N) becomes zero, then Equation (4.7) becomes Equation (4.9).

$$P_{th,max} = G \cdot A_{PV}. \tag{4.9}$$

Under steady weather conditions at high sustained irradiance ($>600\,\mathrm{W/m^2}$), Equation (4.9) leads to IR thermography being practical for detection of electrically disconnected modules or parts of modules [131], as their temperature is higher than the surrounding areas.

The calculation of R_{th} and C_{th} is done using Equations (4.10) and (4.11), which are from [119], with Equation (4.12) the standard definition of a time constant for an RC network.

$$R_{th} = \frac{d}{\kappa \cdot A_{PV}} \tag{4.10}$$

$$C_{th} = \underbrace{\rho \cdot d \cdot A_{PV}}_{m} \cdot c \tag{4.11}$$

$$\tau_\vartheta = R_{th} \cdot C_{th} \tag{4.12}$$

With the data from Table 4.5 and the formulation of Equation (4.12), a discrepancy comes to the fore: the units of R_{th} times those of C_{th} give a time in seconds[25] for the thermal time constant (τ_ϑ), yet measurements and

of Goverde *et al* [78] can more faithfully reproduce the described effects. For the present discussion, the effect of temperature on the module's efficiency and thus removal of electrical power and its relationship to irradiance and the final module temperature are of interest.

[25] $\mathrm{W} = \mathrm{J/s}$ and $R_{th} \cdot C_{th} = \tau_\vartheta [\mathrm{J/°C}] \cdot [\mathrm{°C/(J/s)}] = [\mathrm{s}]$

Table 4.4: Values for thermal constant calculation of the *Smart PV* modules, as shown in Table 4.5.

Layer	d [m]	κ [W/m°C][a]	ρ [kg/m^3]	c [J/kg°C]
Glass	$3.2 \cdot 10^{-3}$	1.8	3000	500
EVA	$500 \cdot 10^{-6}$	0.35	960	2090
ARC	$100 \cdot 10^{-9}$	32	2400	691
PV cells	$200 \cdot 10^{-6}$	148	2330	677
EVA	$500 \cdot 10^{-6}$	0.35	960	2090
Backsheet	$300 \cdot 10^{-6}$	0.2	1200	1250

[a] Note that the *use* of this value in literature, e.g. [118, 119] is with data averaged over one-minute intervals or longer.
[b] Table is modified from [119].

the conclusions of [118, 119, 142] indicate that the module τ_ϑ is in the range of minutes. The most likely reason for this is the use of the one-minute averaged data by a.o. [119, 118], which leads to the result of the τ_ϑ *also* being expressed in minutes. This is not a trivial choice, as it means that the "irradiance" or average irradiance measured actually corresponds to an *irradiation* over the one-minute interval ($N = 60$ s in Equation (4.13) for one minute data).

Table 4.5: Calculated values of R_{th} and C_{th} for the *Smart PV* modules.

Layer	m [kg]	R_{th} [°C/W]	C_{th} [J/°C]	τ_ϑ [min]	τ_ϑ [s]	Relative τ_ϑ [%]
Glass	14.5	$1.0 \cdot 10^{-3}$	7270	7.50	450	67.9
EVA	0.8	$8.8 \cdot 10^{-4}$	1620	1.43	86	13.0
ARC	0	$1.9 \cdot 10^{-9}$	0	0	0	0.0
Cells (F)	0.4	$4.7 \cdot 10^{-7}$	290	0.0001	0.01	0
Cells (B)	0.4	$4.7 \cdot 10^{-7}$	290	0.0001	0.01	0
EVA	0.8	$8.8 \cdot 10^{-4}$	1620	1.43	86	13.0
Backsheet	0.6	$9.3 \cdot 10^{-4}$	730	0.68	41	6.1
Front	15.7	$1.9 \cdot 10^{-3}$	9180	8.9	536	80.9
Back	1.8	$1.8 \cdot 10^{-3}$	2640	2.1	127	19.1
Total	17.5	$9.24 \cdot 10^{-4}$	11 820	5.6	337	100

[a] Environmental effects, such as forced convection by wind, can modify this duration. For similar values, Armstrong and Hurley give ~ 5 min to 7 min, from measurements and modelling [119].
[b] Data also from [119], here: $A_{PV} = 1.616\,\mathrm{m}^2$, additional data from the module manufacturer, Soltech.
[c] Additional data used to calculate these values can be found in Table 4.4, in Appendix B.

$$\langle G \rangle_\tau = \frac{\sum_{i=1}^{\tau} G_i}{N} \equiv \frac{G_\tau}{N} \tag{4.13}$$

The relevance of this is that the *energy* content obtained from the sun interacts with the different layers of the photovoltaic module, and that the energy content of 1 s of irradiance (G) is generally too low to strongly impact the module temperature (the effect is cumulative, however). As can be seen in Table 4.5, the thermal equivalent capacitance (C_{th}) gives an indication to the amount of energy required to raise each layer by 1 °C, or the amount of energy that each layer can store.

4.9 Cell-backsheet temperature behaviour under variable weather conditions: practical considerations

The calculation of the total thermal time constant (τ_ϑ) in Table 4.5 recognises from Figure 4.10 that the heat in the cells has two possible paths to reach the lower-temperature sink at T_{amb}. As a result, the module's temperature will react to a change in the irradiance (e.g. a step) at a rate that ranges between two and nine minutes. The effect of the glass thickness tends to dominate the total thermal time constant [142].

Additionally, the different values of the τ_ϑ for the front and back surfaces indicate that module temperatures will show a difference, depending on the mounting condition and prevailing wind condition: wind which can reach the back surface of the module will cool the cells faster than from the front. Here, the projected wind vector ($v_{w,proj}$) again can show its usefulness to understand and evaluate temperature measurements.

Thus, with the framework of Figures 4.9 and 4.10 and the data from Table 4.5, it is now possible to qualitatively discuss cell and backsheet temperature measurements, and to which extent a backsheet-to-cell temperature correction can be performed.

For this, a first look at the temperature changes due to large irradiance steps can help to verify whether there is a equivalent thermal time constant ($\tau_{\vartheta,eq}$), and whether this can be seen for both cell-measured (*PV052*) and backsheet-measured modules. Figure 4.11 shows the over-temperature for two groups[26]

[26] One group on the back row, the other on the Southward row on the mounting structure - see Figure 2.6.

of adjacent modules, and how their measured temperatures vary due to the irradiance as well as the wind. The backsheet temperature values have been corrected to cell-equivalent temperatures, using Equation (4.15) (given below).

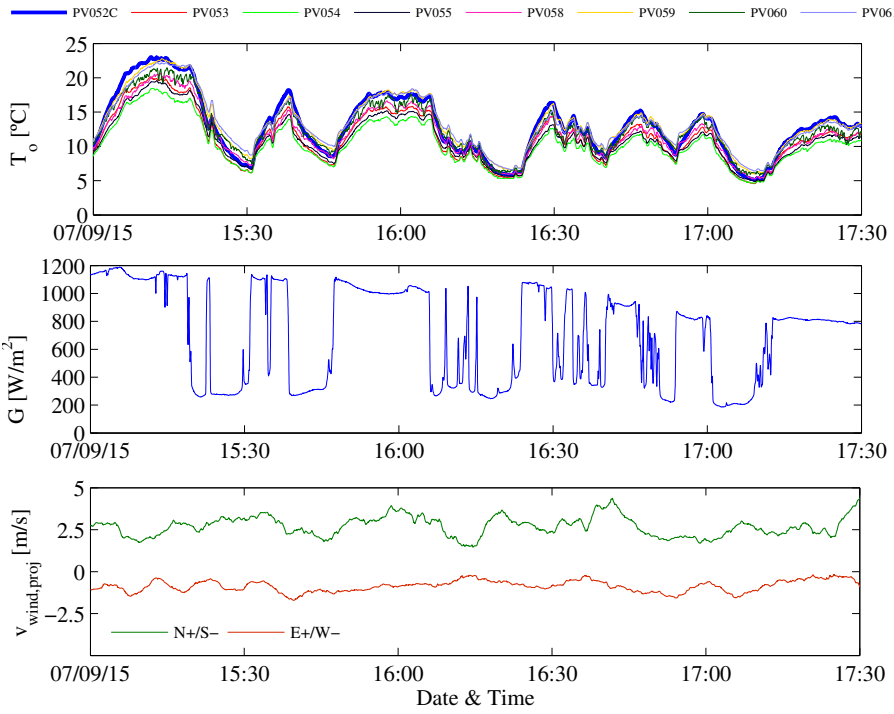

Figure 4.11: Cell- and backsheet-measured temperature responses to changing irradiance and wind on 9 July 2015 for central *Smart PV* modules. Projected wind vector averaged over 5 min. Physical module lay-out: Figure 2.6.

Figure 4.11 shows that the module temperatures do change due to the irradiance, but that this change is slower than the irradiance variations: the modules' thermal response can indeed be characterised by a single equivalent thermal time constant ($\tau_{\vartheta,eq}$), which may be determined from figures such as the one displayed.

From Table 4.5, Equation (4.12) and Figures 4.9 and 4.11, it can be understood that a temperature change measured by a (Pt100) temperature sensor against the backside of the cell will be detected earlier than an identical temperature sensor placed against the backsheet, as part of the heat must travel through the EVA and backsheet layers, if the wind hits the module from the front (South) side. Conversely, the impact of wind from North can be expected to *first* be

detected by a temperature sensor on the backsheet and then by those on the cell backside. Table 4.6 illustrates the latter effect (additional information can also be found in Appendix B).

Table 4.6: Calculated values of the thermal time constant τ_ϑ for the modules shown in Figure 4.11.

Module	Heating τ_ϑ [min:s]	Cooling τ_ϑ [min:s]	Average = $\tau_{\vartheta,eq}$ [min:s]
PV052 (N,ref)[b]	3:24	3:53	3:38
PV053 (N)[b]	3:23	3:10	3:16
PV054 (N)[c]	3:55	3:14	3:34
PV055 (N)[c]	3:45	3:16	3:30
PV058 (S)[b]	3:54	3:13	3:33
PV059 (S)[b]	3:54	3:37	3:46
PV060 (S)[c]	3:33	3:34	3:34
PV061 (S)[c]	4:25	3:52	4:09
Average (N)	3:37	3:23	3:30
Average (S)	3:57	3:34	3:45
Average all	3:47	3:29	3:38

[a] Prevailing wind direction during measurements: NNW.
[b] Mono-crystalline silicon cell technology.
[c] MWT cell technology.

The effect of the prevailing wind direction (from North-North-West) on the values in Table 4.6 is that the calculated values of the τ_ϑ are lower than the $\tau_{\vartheta,eq}$ from Table 4.5. The values are closer to what is suggested by the τ_ϑ for the back surface ($\sim$2.1 min versus $\sim$3.5 min in Table 4.6). The cooling-determined τ_ϑ is lower than during the heating phase: in a cooling phase, the effects of wind and the reduction of irradiance reinforce each other, while during heating, the wind counteracts part of the irradiance heating effect.

Interestingly, the average of the heating-cooling calculated values for the τ_ϑ is quite similar for the modules, irrespective of whether the measurement is performed on the cell or on the backsheet. (The physical placement on the array does play a role, however.) This can again be discussed using the RC-equivalent formulation: heating of the cell will be detected faster by the sensor against the cell surface, which leads to a lower value of the τ_ϑ. By contrast, cooling of the module is detected later by the cell temperature sensor, compared to the backsheet sensors, and thus leads to a higher value of the τ_ϑ.

$$\tau_{\vartheta,eq} = \langle \tau_{\vartheta,heating} + \tau_{\vartheta,cooling} \rangle \tag{4.14}$$

Averaging of the heating-cooling determined values as in Equation (4.14) of τ_ϑ thus leads to more reproducible results[27]. The additional benefit is that the above approach shows that backsheet-measured values *can* be used, as the module temperature changes are detected in a similar manner to cell-measured temperatures.

For temperature measurements per second, which value of $\Delta t = \tau$ should then be used in Equation (4.15), so that the backsheet-measured value can be corrected to the cell temperature with the lowest achievable error? If the interval $\Delta t = \tau$ is too short, then the changes in irradiance will not yet be transmitted as heat throughout the module surface, and the backsheet-to-cell temperature corrected value will show irradiance-induced peaks and troughs which are absent in reality.

Equation (4.15) contains a running mean of the irradiance over a time interval (τ) (i.e. the energy over that interval). Compared to Equation (4.3), the impact of irradiance averaging is made more explicit.

$$T_C(t) = T_{BS}(t) + \Delta T_{CBS} \cdot \frac{\langle G(t) \rangle_\tau}{G_{STC}} \tag{4.15}$$

The value for τ that is proposed here as a heuristic:

$$\tau \simeq 0.1 \cdot \tau_{\vartheta,eq}, \tag{4.16}$$

benefits from the linear approximation of the exponential function. Rounding the value $\tau = 0.1 \cdot \tau_{\vartheta,eq}$ using the "steady-state"[28] $\tau_{\vartheta,eq}$ from Table 4.5 then gives $\tau = 0.1 \cdot 337 \simeq 30\,\text{s}$. As with any fixed heuristic approximation, there may be more exact results *a posteriori*[29], yet for monitoring purposes and live data analysis, Equations (4.15) and (4.16) serve the purpose of correcting temperature measurements at faster rates than per minute.

Lastly, as historically many temperature measurements were taken over longer periods (in the range of minutes), the corrections of backsheet temperatures may underestimate temperature changes. The effect of this is discussed further in Section 6.5.5.

[27] These should, however, be determined in as similar conditions as possible - e.g. within a few hours of each other so that the wind speed and irradiance conditions for heating and cooling are similar.

[28] Situation with low wind, for a step change in irradiance - e.g. after intentional shading is removed from a module.

[29] E.g. use of a heating τ_ϑ and a cooling τ_ϑ. This could require a situation-aware algorithm: "is the trend of irradiance changing sufficiently?".

4.10 Intra-module temperature variations

For generally error-free mounting conditions and system behaviour, it can be assumed that an outdoor mounted module's temperature will be homogeneous, as the irradiance is expected to be collimated. It has been observed that modules mounted outdoors do have intra-module temperature variations, although these have not yet been studied in much detail. (Modules with damaged or disconnected areas do suffer from temperature deviations, but the focus here is on error-free modules.) These intra-module temperature variations are primarily a result of the interaction of the module with the surroundings, in particular wind access to the module surface, which is impacted by the mounting structure.

For the most important measurements outdoors, e.g. to determine a module's STC efficiency ($\eta_{PV,STC}$) temperature conditioning equipment is used, primarily to ensure that the module temperature is at 25 °C. However, the outdoor fixed-rack method of IEC 61853 requires the measurement of I-V curves over a relatively long period, in which temperature conditioning equipment becomes impractical. Moreover, photovoltaic modules in the field do not have temperature conditioning equipment installed. Thus, with the methodologies described in the previous sections, it is now possible to answer two questions which are of interest for practical data evaluation (such as performance and quality assessments) and for calibrations:

1. What is the relative frequency histogram of maximum intra-module temperature deviations as they have been measured?
2. How large are the maximum temperature differences measured over the surface of one module? How does this profile look over a day or more?

Both Item 1 and Item 2 are related, yet the manner to answer each question varies slightly.

The question of Item 1 was inspired by the seminal article by Müllejans, Zaaiman and Galleano [28], which assumes two sources of uncertainty due to module temperature:

1. The stability of the module temperature during the (I-V curve) measurement: ±2 °C with an assumed rectangular probability, which gives a standard uncertainty (1σ) of ±1.15 °C.
2. The module temperature non-uniformity during the (I-V curve) measurement: ±3 °C with an assumed rectangular probability, which gives a standard uncertainty (1σ) of ±1.73 °C.

As an extra note, King *et al* also mention intra-module temperature differences of less than 5 °C for wind speeds <3 m/s [114].

Through the *Law of Propagation of Uncertainties* (see Section 3.3.3), these two sources of measurement uncertainty impact the measurement uncertainty of voltage and current, and ultimately the measurement uncertainty of power of the modules being tested. According to Müllejans *et al*, these temperature uncertainties contribute to approximately 60 % of their total outdoor uncertainty budget [28].

As module I-V curves are recommended to be measured under stable irradiance (and wind) conditions [15, 26], the magnitude of the temperature change in a module depends on the (total) duration over which the measurements happen. If the sequence of multiple I-V curves is measured in a time frame of less than one minute, then for steady wind and irradiance conditions the temperature change will be limited, and very likely be less than 1 °C. In part, this is a result of what was discussed above in Section 4.8, namely that the module's total thermal capacitance and the τ_ϑ ensure that temperature changes will be limited, *especially* for steady wind and irradiance conditions.

From previous measurements (using the first and second iterations of the measurement set-up) - see e.g. [117, 138], the data suggested that the highest temperatures experienced by the modules was at the bottom. This is due to the roof mounting tilt angle of the array (18°), with the bottom of the module ∼20 cm from the roof surface, which likely reduces convective heat losses in that area. The limited distance between module and roof may also lead to higher radiative and convective heat transfer from roof to module. The bottom of the module is thus one area of interest, compared to the standard placement in the centre of the module.

Figure 2.6 indicates that the 8 modules which were of most interest were fitted with 11 (*PV052*), 3 (*PV053*) and 2 (*PV054, PV055, PV058-PV061*) temperature sensors per module. The placement of the temperature sensors was then one sensor in the centre (on the cell on row 5, column 4: 5x4) and one on the bottom left (10x1) cell. Module *PV053* also has a sensor on position 1x6. *PV052* has sensors on the left, centre, right of the module on three rows: rows 1, 5 and 10 and columns 1, 4 and 6.

From Figure 4.12, it is possible to assume that the maximum measured temperature inhomogeneity for the modules measured may exceed 6 °C. By contrast, from Figure 4.13, it would be possible to leap to the conclusion that "temperature deviations inside a module are maximum 6 °C, and often ≤4 °C". The combination of the knowledge from Figures 4.12 and 4.13 allows to qualify the above statements, to claim that intra-module temperature inhomogeneities

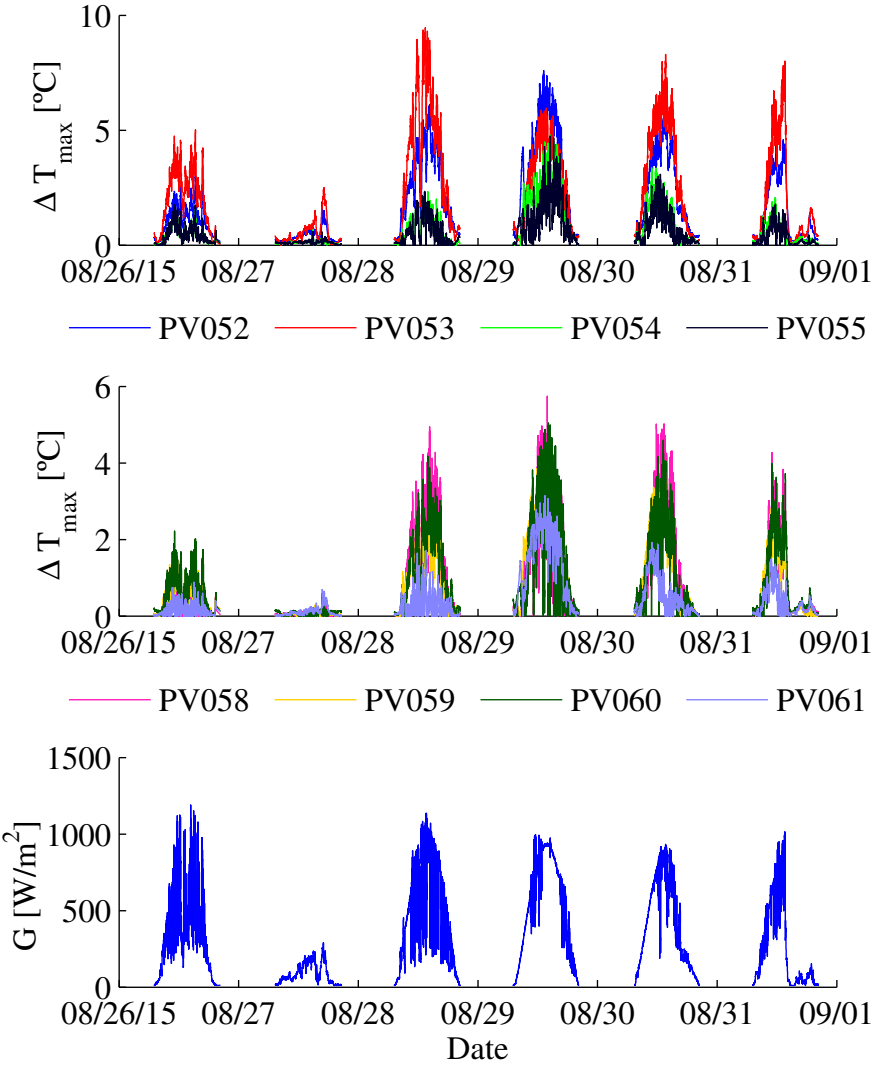

Figure 4.12: Timeseries of intra-module ΔT_{max}, end August 2015.

may exceed 6 °C, but that their occurrence is limited. In short, taking either of Figure 4.13 or Figure 4.12 at face value can lead to erroneous conclusions regarding the performance of photovoltaic modules, and due care must be taken with the interpretation of the data.

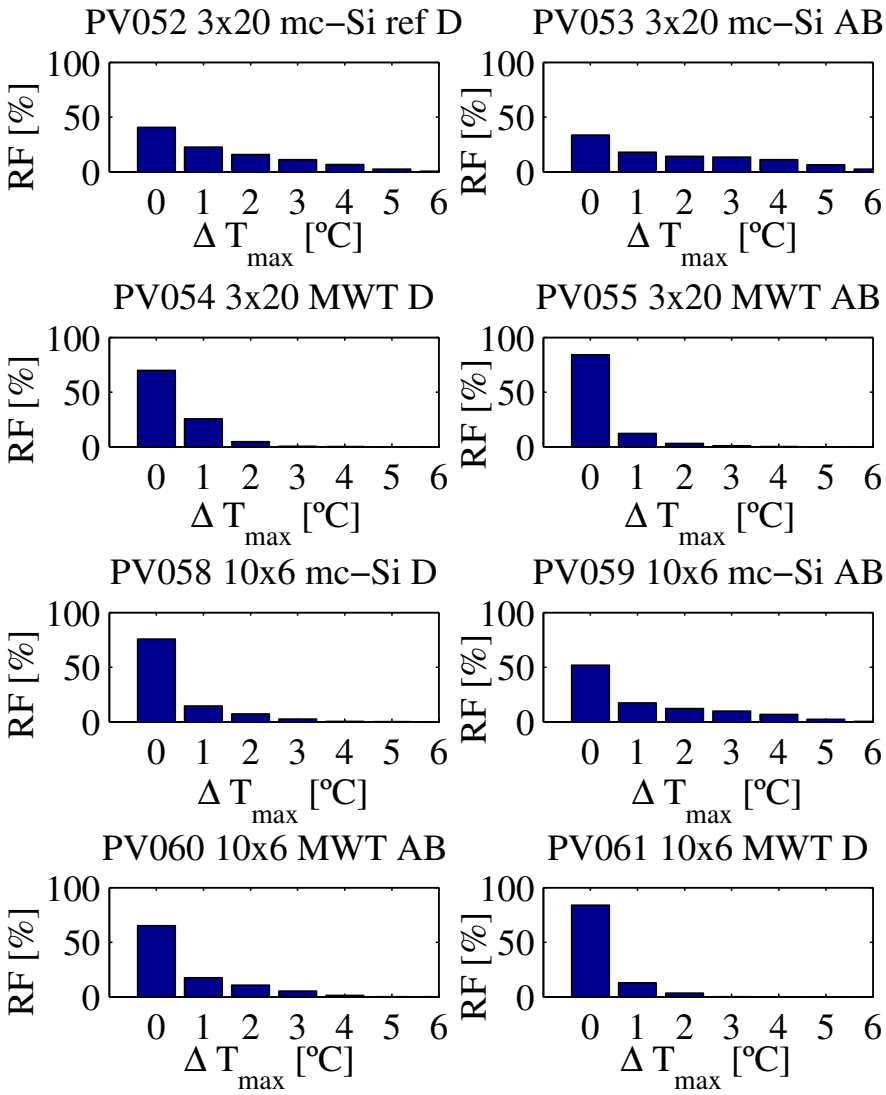

Figure 4.13: Relative frequency (RF) histograms of maximum temperature differences measured inside modules for the period June-August 2015.

Taking the measured and corrected temperature data for the months of June to August (the hottest months of the year, and generally with the highest irradiance), the absolute number of maximum temperature variations for the

eight modules was calculated. By then recalculating this to a relative frequency histogram, Figure 4.13 was generated. It clearly indicates that intra-module temperature differences of up to 4 °C may be detected at a regular rate, with the frequency of higher temperature deviations rapidly decreasing.

The intra-module maximum temperature non-uniformity ($\Delta T_{max,intra-module}$) was $\geq 4\,^{\circ}\mathrm{C}$ only 9 % of the time for module *PV053*, ∼3 % for modules *PV052 & PV059* and less than 0.1 % for the remaining modules. These results suggest that the temperature uncertainty assumed by Müllejans *et al* can be reduced, without the need for module temperature conditioning equipment (e.g. cooling equipment around the module's backside, to keep it at a fixed temperature). In particular, the assumed rectangular probability distribution of $\pm 3\,^{\circ}\mathrm{C}$ (which gives $\Delta T_{max} = 6\,^{\circ}\mathrm{C}$), suggests that for one third of the time, a value of $\Delta T_{max} \geq 4\,^{\circ}\mathrm{C}$ can be expected. Compared to measured 0 % to 9 % of the time for $\Delta T_{max} \geq 4\,^{\circ}\mathrm{C}$, this is a large over-estimation of the magnitude and frequency of the temperature non-uniformity for a module.

Only by filtering the data for irradiance values larger than $600\,\mathrm{W/m^2}$, do the temperature non-uniformities start to approach the values assumed by Müllejans *et al.* This then contradicts the intended use of long-term, fixed-rack measurements of I-V curves according to IEC standards. These measurements are concerned with the performance of photovoltaic modules and systems over *all* weather conditions, not only $G > 600\,\mathrm{W/m^2}$. Regardless, temperature inhomogeneities become more pronounced for sustained high irradiance conditions, and may reach temporary peaks during irradiance and wind oscillations.

In case of fixed mounting-rack long term I-V curve measurements for IEC 61853-1 [77] and similar standards, where the use of module temperature conditioning equipment is impractical or unrealistic, these results also suggest that temperature differences inside a module *do occur on a regular basis*, yet the magnitude of the temperature non-uniformities and probability distributions can be assumed to be lower for non-faulty modules.

Figure 4.13 also shows that the modules with MWT cells appear to have a more uniform temperature profile than the standard monocrystalline silicon modules. This may partly be explained by the better packing factor (practical use of the module's surface area) of the rectangular MWT cells compared to the pseudo-square monocrystalline cells, as well as the lower value of the temperature coefficient of power (γ) of the MWT cells. (These are given in Table 5.2 in Chapter 5.)

While not shown, the temperature deviations and module homogeneity were also verified with an infra-red camera, giving results in line with the contact

measurements described above. Lastly, it could be argued that the methodology and placement of sensors on the modules employed may underestimate the maximum intra-module temperature deviation values, as more locations could be measured. Nevertheless, the results shown do suggest that intra-module temperature deviations are generally less than assumed by Müllejans *et al.* These conclusions are drawn however for this set-up – it bears evaluating local mounting and wind access effects for modules in other locations - see Section 6.5.5.

4.11 Inter-module temperature variations

Depending on the complexity of photovoltaic *system* models, temperature differences between modules in photovoltaic arrays may, or not, be taken into account. While the current set-up is limited in physical and electrical size, the data may serve for similar analyses in larger photovoltaic systems.

Figure 4.14 shows how the average module temperatures vary compared to the reference, module *PV052*. A number of effects can be observed, of which the variation of temperature of the modules on the edges (*PV051, PV056, PV057, PV062* and *PV063*) due to wind are pronounced. For example, the temperature variation of modules *PV056* and *PV062* on 2 August cross paths: *PV056* is hotter in the morning, while *PV062* becomes hotter in the afternoon. In part, this validates the approach of IEC 61724 [16] and the Australian PV Monitoring Technical Guidelines [144], which recommend the use of at least one centrally located module as reference for the whole. That said, for utility-scale (megawatt) photovoltaic systems, neglecting edge effects can lead to other systematic effects (e.g. inverters performing less well than expected) being masked.

The temperature variations for the more central modules (visible in the top subplot of Figure 4.14) also show sensitivity to the wind direction: contrasting 29 with 31 July, the temperature variations follow a different profile, yet the irradiance profiles are similar. For example, the temperature difference of module *PV058* to *PV052* is significantly higher on 29 July than on 31 July.

For assumptions on the array or system temperature homogeneity, Figure 4.15 indicates the probability distribution (top subplot) and frequency of maximum temperature differences, for the modules measured using the set-up of this work. The centre modules are indicated in Figure 4.1, these are *PV052–PV055* and *PV058–PV061*. The modules at the edges are *PV051, PV056, PV057, PV062* and *PV063*.

From Figures 4.15 and 4.16, it is possible to suggest a formulation for the

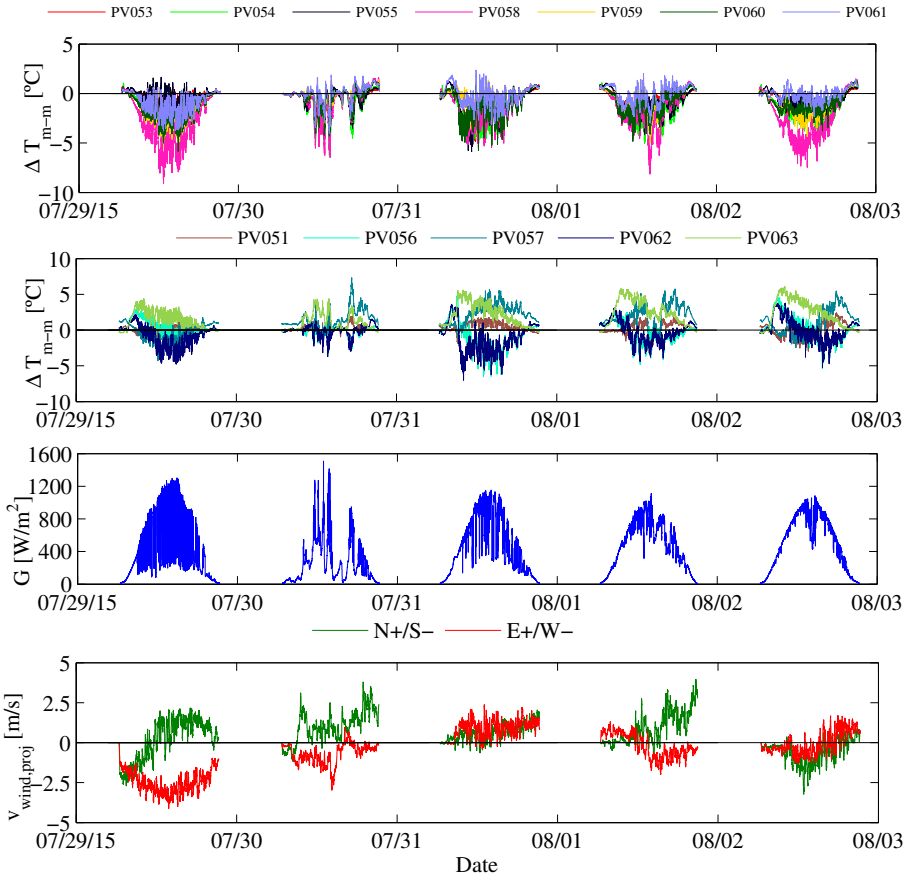

Figure 4.14: Module temperature deviations compared to the reference (*PV052*) for late July–early August 2015.

expected inter-module temperature variation (ΔT_{m-m}), which can be used to quantify the variation in the array temperature

$$T_{array} = T_{ref,module} \pm \Delta T_{m-m} \cdot \frac{\langle G \rangle_\tau}{G_{STC}}, \tag{4.17}$$

recognising that temperature deviations among modules will increase with increasing irradiance. (Equation (4.17) may further be modified using wind effects - which still need to be quantified.) Figure 4.15 also indicates that the inter-module temperature deviations are almost normally distributed, so that Equation (4.17) is a reasonable approximation.

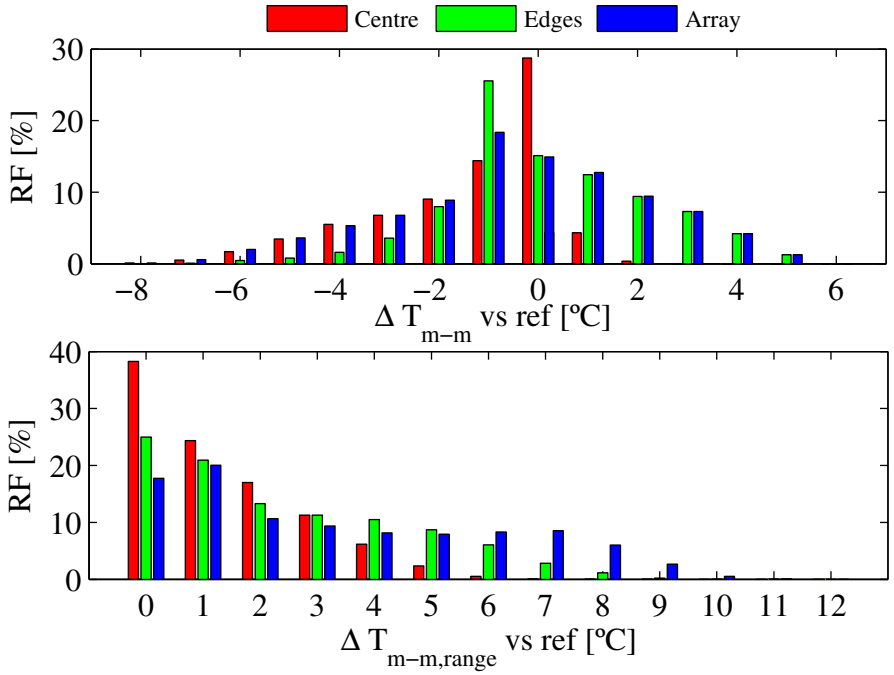

Figure 4.15: Relative frequency (RF) histograms of temperature differences measured for the period June-August 2015. Values are module average temperatures, compared to each other and the reference (*PV052*).

Equation (4.17) also uses the heuristic value of τ from Equation (4.16), and similar to Equation (4.15), the irradiance should also be calculated as the running mean for the interval τ. The value of ΔT_{m-m} at STC is $\simeq$4 °C, for the data shown[30].

As can be observed from Figure 4.14, the instantaneous values of temperature differences between modules may be larger than $\Delta T_{m-m} = \pm 4$ °C and impacted by wind effects, yet in general terms, the maximum inter-module temperature deviation is below 8 °C for 90 % of the time, for the months of June to August.

While IR thermography has been useful in large-scale fault determination of photovoltaic plants, few long-term (continous) analyses of the inter-module temperature variation have occurred. Through further study, the assumptions

[30]This is an approximation: in reality, it is $\Delta T_{m-m} \simeq 3$ °C for the higher temperatures and $\Delta T_{m-m} \simeq 5$ °C for the temperatures below that of the reference module. Many statistical treatments assume a fully symmetrical deviation, hence the use here.

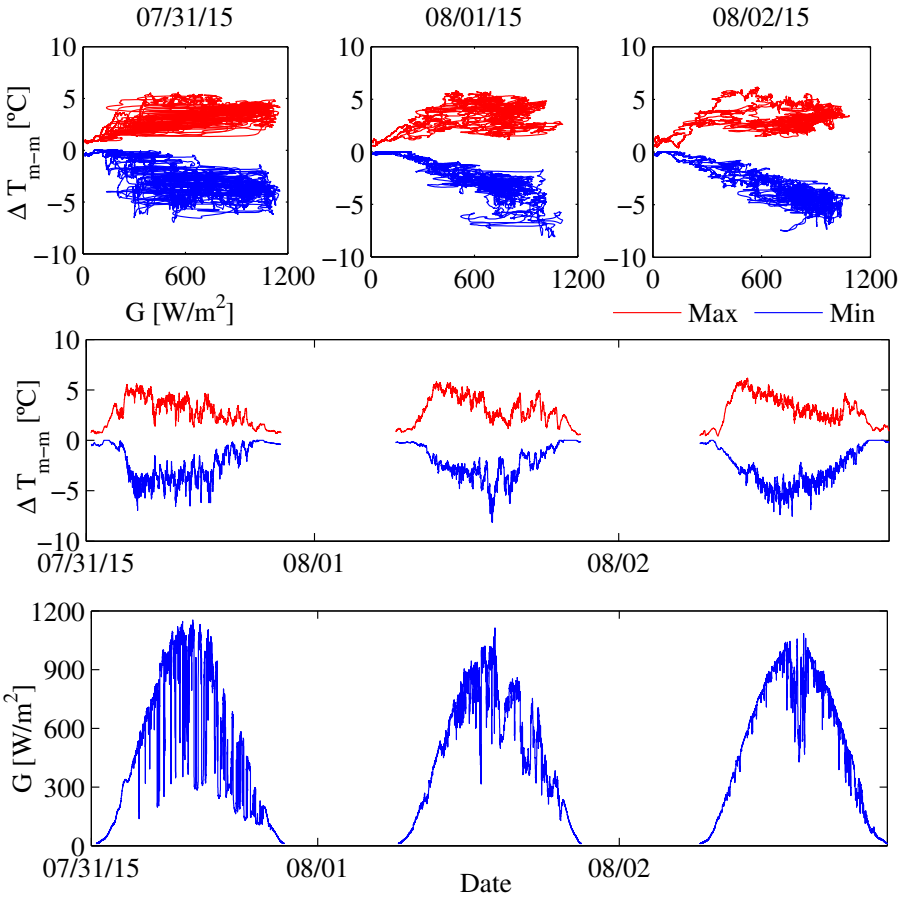

Figure 4.16: Maximum and minimum inter-module temperature variations for end of July and early August 2015.

of system temperature homogeneity can be optimised, or where required, made location-specific.

4.12 Conclusions

Contact temperature measurements are a useful tool to understand and analyse the performance and behaviour of photovoltaic modules. As with any tool, better and more meaningful results are obtained through careful application

and interpretation of the data. The methods used to attach temperature sensors to the module surface may be seen as prosaic, yet these, together with the subsequent sensor bias corrections, are part of the vital data chain: a loose yet very accurate temperature sensor may end up giving worse data than a well-attached, inspected temperature sensor. Furthermore, erroneous or untrustworthy data is difficult to correct a posteriori, and care must be taken when performing corrections.

To verify proper functioning of temperature sensors and correct for inter-sensor biases, Algorithm 4.1 gives the steps to follow.

Equation (4.18) from King *et al* [114] is modified in this work to Equation (4.19). Backsheet temperature measurements performed at faster rates (e.g. 1 Hz) can now be corrected while limiting noise from the irradiance data. The formulation shown here makes aspects more explicit, such as the time interval over which the irradiance data must be averaged.

$$T_C = T_{BS} + \Delta T_{CBS} \cdot \frac{G}{G_{STC}} \tag{4.18}$$

$$T_C(t) = T_{BS}(t) + \Delta T_{CBS} \cdot \frac{\langle G(t) \rangle_\tau}{G_{STC}} \tag{4.19}$$

For the correction of temperature values measured and used at rates below one minute, the heuristic value of $\tau \simeq 0.1 \cdot \tau_{\vartheta,eq}$ for use in Equation (4.19) is proposed. As with any contact temperature measurement not performed against a cell, a backsheet temperature measurement will not be able to perfectly capture the thermal behaviour, although the proposed methodology aims to reduce these errors during transient conditions. The similarity in the determined values of the equivalent thermal time constant $\tau_{\vartheta,eq}$ for cell- and backsheet-measured point in this direction. However, wind effects can give very different values in the thermal time constant τ_ϑ, depending on the module's position in the array - an issue that resurfaces for the inter-module temperature differences.

Therefore, if possible, it is recommended to perform the steps described in this chapter to determine the value of the cell-to-backsheet temperature difference ΔT_{CBS} for the primary module technology studied, and for the applicable mounting conditions. With regard to future work, measurement of the temperature of the back surface of glass-glass modules is an aspect worthy of further study.

The projected wind vector has shown its usefulness in this chapter to better illustrate wind speed and direction time series. Moreover, not only is the display of the wind vector over time simplified, systematic effects which affect the module temperatures differently in the array can be identified. From a visual

analysis perspective, there has been a need to calculate and display the projected wind vector using a relatively long-term running mean of 5 min: the variation in wind has often been much higher than that of the irradiance. Depending on the time scale in which analyses are performed (minutes, hours or days), there may be more appropriate time periods to calculate the running mean of the projected wind vector. Compared to the use of *only* the wind speed in other articles, e.g. [145], the projected wind vector has much more explanatory power, both for time series and summary statistics.

The inter-module temperature differences also show irradiance and wind-related effects, such as the well-known effect of wind for modules at the edges of the array. A formulation for the deviation of temperature from the reference module's value is suggested in Equation (4.17), which also uses $\tau \simeq 0.1 \cdot \tau_{\vartheta,eq}$ for sub-minute measurements. This formulation may be used to estimate the uncertainty due to inter-module temperature differences in an array, or as a quality control value: if measured temperatures routinely exceed the ΔT_{m-m}, this may point to either module problems (e.g. hotspots [146]), sensor issues, or local mounting effects. Regardless of the root cause of the problem, the approaches described in this chapter (e.g. using the over-temperature to detect loose sensors) can be used to more rapidly identify and correct the issue, if need be.

From the above analyses and figures, the data from the hottest months of the year (June to August) suggests that the assumptions of intra-module temperature non-uniformity by Müllejans *et al* are too pessimistic. Moreover, many research laboratories use temperature-controlling methods for outdoor measurements of photovoltaic modules (see e.g. [123]), so temperature non-uniformities in such cases will largely be limited.

However, the *combined* effect of intra-module and inter-module temperature deviations may lead to larger values than assumed by Müllejans and King *et al*, in particular when using one module's temperature measurements to be representative of other modules on the mounting rack(s). If highest accuracy is required, there is no alternative to measuring the temperature of the module(s) under consideration. It is suggested to perform continuous temperature monitoring using contact measurements on at least two locations per module.

Care must also be exercised with the interpretation of "snapshot" type temperature measurements - such as IR thermography: as the results of this chapter have shown, temperature variations may appear, or not, depending on the mounting of the modules and prevailing wind conditions *at the time of measurement*. If snapshot type measurements are performed, it is suggested to repeat these at least once with five to twenty minutes in between, for verification of the measurement. Cost reductions and camera improvements may lead to

automated IR movies or timelapse analyses becoming possible instead of human-interaction snapshots, although this is certainly not yet widespread.

For increasing irradiance, as shown for example in the formulation of Equation (4.15), temperature deviations between both cell and backsheet and between cell positions on a module increase. This poses some measurement and interpretation challenges, as well as limits the achievable measurement uncertainty for contact temperature measurements. Possible methods for improvements of measurements may be to also include a thermal model of the sensor-module interaction, based on the work of e.g. of Goverde *et al* [78, 142, 147] for the corrections - although this limits temperature measurements to be corrected post-facto with irradiance data, and assumes lower errors due to the use of thermal models. Real-time measurements and corrections may use some of the tools detailed in this chapter, although ensuring good real-time data quality may be a challenge.

Chapter 5

The normalised efficiency and other tools for photovoltaic system analyses

5.1 Introduction

This chapter synthesises and puts to use most of the work that has been described in the previous chapters, from the SCBs for the DC energy yield measurements to the weather, module temperature and AC energy yield measurements. By the end, the performance of the photovoltaic modules of the *Smart PV* project will have been analysed, and the advantages of the modelling approach for the normalised efficiency will have been put to the test, in order to quantify module and array energy losses due to shading.

This chapter presents a number of methods and tools for photovoltaic analysis, which range from instantaneous normalised power and normalised efficiency, to temperature corrections and fitting of an empirical model. One of the main goals is to understand and where possible quantify energy yield variations, keeping in mind changes in the environment. In order to do so, it may be necessary to dive to the level of the instantaneous normalised efficiency, at other times the longer-time perspective of the Performance Ratio can serve to explain

deviations in performance between systems.

Traditionally, analyses and monitoring of photovoltaic systems have been limited to timescales of minutes [50] or longer, mostly due to data availability and computational limitations, as well as engineering design choices. As such, the analyses focus on well-established and well-known metrics, such as the Performance Ratio (PR), the daily/weekly/monthly (normalised) energy yield, the mean daytime module temperature, ... In short, the time interval on which traditional analyses focus is in the range of minutes-hours-days, with longer time frames of months and years as well.

The core idea behind this chapter is that using data available at shorter time frames allows fluctuations in power (and therefore as a result, in energy) to be observed, providing new insights into the functioning of PV systems. To this end, the methodology of normalising the output power and energy and using the normalised efficiency is applied as a first step, which allows similar photovoltaic systems with different power ratings to be compared.

5.2 Theoretical background for normalisation

The Performance Ratio (PR) has been the most widely used [16, 50], reported and standardised measure to quantify the performance of photovoltaic (PV) systems to date. Improvements to the original definition of the PR by including (and correcting for) temperature effects were given, in [148, 149] among others, with a report on the work in progress on IEC 61724 given by [150]. David King [151] introduced the use of the regular (i.e. not normalised) AC (system) *energetic* efficiency and Copper *et al* [144] extended this approach to the DC side of the photovoltaic array. Huld *et al* [13, 124] used and defined a module-level model of the instantaneous relative efficiency η_{rel} and its hourly and yearly equivalent, by modifying the model of King *et al* [114].

The method of normalising values similar to the PR in Equations (5.1) to (5.4) is the explicit formulation for the normalised power (P_N), the normalised irradiance (G_N), the normalised energy over a period τ ($E_{N,\tau}$) and the normalised irradiation over a period τ ($G_{N,\tau}$).

$$P_N = \frac{P}{P_{STC}} \tag{5.1}$$

$$G_N = \frac{G}{G_{STC}} \tag{5.2}$$

$$Y_{f,\tau} = \frac{E_\tau}{P_{STC}} = \frac{\sum_0^\tau P(t) \cdot \Delta t}{P_{STC}} \tag{5.3}$$

$$Y_{r,\tau} = \frac{G_\tau}{G_{STC}} = \frac{\sum_0^\tau G(t) \cdot \Delta t}{G_{STC}}. \tag{5.4}$$

The definition of the Performance Ratio over a period τ (PR_τ) is typically given as the ratio of the final yield over a period τ ($Y_{f,\tau}$) to the reference yield over a period τ ($Y_{r,\tau}$), where τ is generally taken in the range of days, and occasionally shorter periods (e.g. 5 minute intervals [50]). Equations (5.3) and (5.4) are then taken to calculate the Performance Ratio:

$$PR_\tau = \frac{Y_{f,\tau}}{Y_{r,\tau}}. \tag{5.5}$$

The PR_τ indicates how much of the incident solar energy has been captured and converted to electrical energy, where the theoretical maximum depends on the definition of the Standardised Testing Conditions (STC): the power produced by one or more photovoltaic modules whose cell temperature (T_C) is 25 °C, when an irradiance (G) of 1000 $\mathrm{W/m^2}$ with an Air Mass (AM) AM1.5 spectrum is perpendicular to the module surface.

The reference yield over a period τ ($Y_{r,\tau}$) is defined as a lossless photovoltaic system installed with the same tilt angle and orientation working at all times at its STC efficiency, which includes the temperature. As the efficiency of photovoltaic modules decreases for a cell temperature above 25 °C (and conversely, increases when $T_C < T_{STC}$), the PR_τ typically shows a seasonal effect, with a peak in winter and a low in summer, due to the variation in the ambient temperature and irradiance (and to a lesser extent the spectrum). As such, when the actual module temperatures over the interval τ are below the STC temperature, the value of the PR_τ can exceed 1, e.g. during a day.

By fully writing out the equation of PR,

$$PR_\tau = \frac{\frac{1}{P_{STC}} \cdot \sum_0^\tau P(t) \cdot \Delta t}{\frac{1}{G_{STC}} \cdot \sum_0^\tau G(t) \cdot \Delta t} = \frac{\langle P_N(t) \rangle_\tau}{\langle G_N(t) \rangle_\tau}, \tag{5.6}$$

it becomes clear that the Performance Ratio is also a mathematical expression for the arithmetic mean of the (scaled, or normalised) power divided by the mean of the irradiance, as in both cases the energy is calculated over the same time interval τ. Important to note here is that the time-dependent nature of photovoltaic power and energy generation is mostly removed by calculating PR, or any other summary metric.

Depending on how the STC power P_{STC} has been obtained (calculation, module datasheet, measurement, ...), it can be seen as a (mathematical) scaling factor or a normalising factor. In either case, it permits the comparison of power production of modules (and even systems) of different values, so that a difference seen is due to the module's behaviour, rather than a natural effect of a difference in P_{STC} (e.g. that a 250 $\mathrm{W_p}$ module produces more power than a 230 $\mathrm{W_p}$ module for the same weather and mounting conditions).

Introducing the normalised efficiency (η_N)

$$\eta_N = \frac{P_N}{G_N}, \tag{5.7}$$

and expressing it more explicitly as the normalised efficiency over time ($\eta_N(t)$) and the averaged normalised efficiency ($\langle \eta_N \rangle_\tau$):

$$\langle \eta_N \rangle_\tau = \left\langle \frac{\frac{1}{P_{STC}} \cdot P(t)}{\frac{1}{G_{STC}} \cdot G(t)} \right\rangle_\tau = \left\langle \frac{P_N(t)}{G_N(t)} \right\rangle_\tau = \langle \eta_N(t) \rangle_\tau, \tag{5.8}$$

the similarity to the calculation of PR_τ becomes apparent. The main difference is that for $\langle \eta_N \rangle_\tau$ the input (irradiance) is *first* linked to the output (power) on a moment-by-moment basis and *then* averaged. Conceptually, this is not a trivial distinction between PR and $\langle \eta_N \rangle_\tau$: for the (mathematical) calculation of PR, the sequence of PV power (and energy) and whether this is seen at the same time as the irradiance (and irradiation) is of no consequence, which does not represent reality.

The visual summary of Equations (5.5) and (5.8) for the Performance Ratio over a period τ and the normalised efficiency η_N is given in Figure 5.1, showing the main areas where the power and energy may be measured: on the DC side between module(s) and inverter (or converters) and on the AC side, after the inverter.

As shown in Figure 5.1, a reference cell and a pyranometer may be used for both irradiance and irradiation measurements, although their most appropriate or preferred application are still subject to discussion. A pyranometer is generally recommended for energetic performance analyses (so irradiation G_τ and PR),

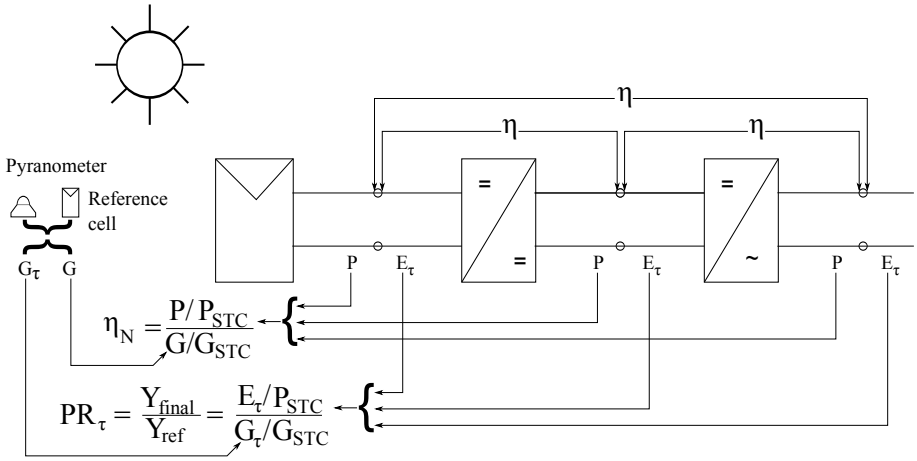

Figure 5.1: Measurement of power and energy , to calculate the PR_τ and η_N as well as converter or inverter efficiencies. Depending on the system configuration, either the DC-DC converter or DC-AC inverter may not be present..

whereas a reference cell is recommended for analyses which anticipate rapid changes in time (e.g. irradiance per second, and the normalised efficiency) [50]. A pyranometer will indicate the maximum power or energy that could have been captured by a photovoltaic system, whereas a reference cell will better indicate the maximum power or energy that could have been produced (if it is properly spectrally matched to the module technology studied). The calculation of the normalised efficiency is shown in this text using both reference cell and pyranometer data. In general terms, the pyranometer data is used for temperature-related effects (Sections 5.4.3 and 5.4.4) and Performance Ratio calculations, whereas the reference cell data is primarily used for power-related effects, such as model fitting (Section 5.5).

The normalised efficiency has been called the relative efficiency η_{rel} by other authors in the past, and typically discussed for modelling purposes. David King considered the "true" or nameplate system AC efficiency[1] to be more useful [151], although in his case, the focus was on using the nameplate system *energetic* efficiency as a tool to compare different systems for investment decisions and monitoring purposes.

In both cases of η_N and PR_τ, the value equals 1 when the module or system performs at STC conditions, and may be exceeded if the temperature is below

[1] $\eta_{syst} = \frac{E_{ac,\tau}}{G_\tau \cdot A_{syst}}$

the STC temperature. The decrease in a module's efficiency and power output is often given as

$$P(T) = \underbrace{P(T_{STC})}_{P^*} \cdot (1 + \gamma \cdot (T_{cell} - T_{STC})) = P^* \cdot \underbrace{(1 + \gamma \cdot \Delta T_{STC})}_{T_{corr}}, \qquad (5.9)$$

with the temperature coefficient of power (γ) expressing the change in a module's power (or efficiency) as a result of a deviation from the STC temperature[2].

Equation (5.9) is used in models which start from a power assumed to be at the STC temperature and then correct this by modelling the temperature and then use this effect to reduce the system's efficiency. By reorganising Equation (5.9) to counteract the effect of a change in temperature, the temperature-corrected power (P^*) can be calculated as

$$P^* = \frac{P(T)}{1 + \gamma \cdot \Delta T_{STC}} = \frac{P(T)}{T_{corr}}. \qquad (5.10)$$

Important here is that in Equation (5.10), the temperature-corrected power may be calculated from measured or modelled values, and worth emphasising: while Equation (5.9) is focused on the physical process (i.e. that the deviation in temperature from T_{STC}) results in a change in power, and is thus often used in modelling, Equation (5.10) reiterates that the process can be mathematically reversed (a step which was historically rarely done). For most of the discussions in this chapter, the values used to calculate a temperature-corrected form of the power or normalised efficiency will be measured values, except where otherwise noted, e.g. in Section 5.6.

The temperature-corrected power P^* is the building block with which to obtain the temperature-corrected normalised efficiency (η_N^*), the temperature-corrected energy (E^*), and the temperature-corrected Performance Ratio (PR^*). (It is possible to perform a similar temperature correction on the energy or Performance Ratio, at the cost of using data averaged over the interval τ for the calculation of these parameters.)

By using temperature-corrected data, the opportunity arises to identify otherwise hidden system effects. For example, the (normalised) efficiency of a system may decrease at higher irradiances, which typically result in a higher module temperature. The temperature-corrected normalised efficiency can then be used to examine this theory. A figure which illustrates this is Figure 5.2.

[2](Part of Equation (5.9) was also given as Equation (4.8) in Chapter 4).

Semantically, the choice was made to name η_N the normalised efficiency, and not, as others in the past have, the relative efficiency - e.g. [124]. Its use helps to keep distinctions clear, in particular for comparisons[3].

5.3 Characterisation of irradiance and power variability

Many analyses of photovoltaic performance start from daily summary data, using displays of parameters such as the PR and the daily irradiation G_d to understand the performance. The effect of summary metrics is that what transpired throughout the day is generally averaged in some form. As a result, two days may have a similar total value of the G_d and perhaps even of the over-temperature, yet the PR differs. One explanation for this may be the variability in the solar resource, and as a result, of the generated power. Moreover, large and frequent irradiance fluctuations will result in more losses, as the MPP tracking algorithms of inverters and DC-DC converters cannot yet follow all irradiance variations immediately.

Thus, a summary metric for irradiance and power variations can help to ascertain whether the deviation in daily performance was due to irradiance fluctuations, or whether more analyses must be performed - e.g. plotting the η_N and the irradiance over the day.

To characterise irradiance variability over a day, three metrics were compared for use in this work: the *Variability Index* by Stein *et al* [152], the natural variability index of irradiance (NVI) from Willy *et al* [153] and the *Output Variability* by Hoff and Perez [154]. Two of the three concepts use the standard deviation (the NVI and the *Output Variability*) to help quantify variability. The *Variability Index* compares the (averaged) ratio of the change in measured horizontal irradiance to the change in clear-sky (theoretical) horizontal irradiance. In terms of applicability for measured data for a single site, the *Variability Index* and the NVI are very similar, with the difference that the *Variability Index* requires the computation of the expected clear sky irradiance, for each moment of the day. The *Output Variability* is aimed more for use in large fleets of PV systems, and thus not used here. Given its easier determination, the NVI was chosen for use in this work, although the *Variability Index* is kept in mind for future implementation. (The reader may also wish to consult [155, 156, 157] for additional irradiance variability metrics.)

[3]For example “A relative change in the normalised efficiency” versus “a relative change in the relative efficiency”.

The natural variability index of irradiance (NVI) was proposed by Willy *et al*, as a transfer of the concept from the wind industry (there it is used to characterise wind resource turbulence) [153]. The initial definition focused on data over longer time intervals, e.g. 10 min. It permits days to be classified according to the standard deviation in the irradiance changes. A very low value of the NVI indicates either of two cases: a clear sky day, or a fully overcast day. A very high value of the NVI indicates a day with many and large irradiance fluctuations. Similarly, the natural variability index of power (NVP) [153] can be determined for the measured power of a system.

$$NVI_\tau = \frac{\sigma_{\Delta G}}{\langle G \rangle_\tau} \tag{5.11}$$

$$NVP_\tau = \frac{\sigma_{\Delta P}}{\langle P \rangle_\tau} \tag{5.12}$$

When using a much shorter interval than that of Willy *et al* [153] (e.g. per second, instead of ten minutes), many of the values which correspond to a variable day fall into a lower (calmer day) category, if using the originally defined classes[4]. Hence, for per-second data, the classification of a day according to the variability must be done with new categories, which are proposed in Table 5.1. These categories are chosen here to be of equal size, which differs from the approach of Willy *et al* [153] who opted for equally-likely intervals. The definition of the intervals may be suject for further study.

Table 5.1: New definition of natural variability index of irradiance classes using time intervals of one second

NVI class	1	2	3	4	5	6	7	8	9
Value	<0.005	0.005–0.010	0.010–0.015	0.015–0.020	0.020–0.025	0.025–0.030	0.030–0.035	0.035–0.040	≥ 0.040
Condition		Calm[a]			Variable			Extremely Variable	

[a] Applies to *both* fully overcast and clear sky days. Identify using G_d or clear-sky index.

Lastly, the NVI is technology-specific: the NVI calculated for reference cell-determined data will typically be higher than the corresponding value for a pyranometer. In part, this is a result of pyranometer-measured irradiance data generally being higher than reference cell data, because of the pyranometer's

[4] The magnitude and probability of large irradiance change from one second to the next is much smaller than within a period of minutes.

better cosine response, lowered reflection losses and broadband spectral response. The value of $\langle G \rangle_\tau$ in Equation (5.11) will generally be higher for pyranometer data than reference cell data, and as a result the NVI for pyranometer data will be lower. More work can be done in this area, which will be discussed in Section 6.5.6.

5.4 Benefits and initial applications of the normalised efficiency

5.4.1 Performance comparison of modules and systems of different power ratings

One of the perennial questions of owners and users of photovoltaic systems is "How well is the system performing at moment X or during condition Y?". For larger systems composed of multiple arrays and inverters, often of different power ratings, such a question would be answerable, albeit after much time and effort, e.g. performing an *implicit*[5] normalisation. A first step to better answer such a question is to (explicitly) normalise the power and energy of the different components of the system. That way, if the system contains arrays of e.g. $20\,\mathrm{kW_p}$ and $24\,\mathrm{kW_p}$, the 20 % power difference is removed, and the systems performing better on a per-kW basis can be identified.

Thus, the normalised (regular, or temperature-corrected) power is one step forward in allowing multiple photovoltaic modules and systems to be compared, both numerically and visually. A step further is the normalised efficiency, as this incorporates the effect of the irradiance in the value. The normalised efficiency is conceptually easy to comprehend, as it expresses which percentage of the sunlight that should[6] be converted to electric power is actually measured or delivered. For example, if one $20\,\mathrm{kW_p}$ system is performing with an $\eta_N = 95\,\%$ while its neighbour $24\,\mathrm{kW_p}$ system performs at $\eta_N = 90\,\%$, then a clear distinction between both systems can be made quickly: the $20\,\mathrm{kW_p}$ inverter system is performing *better* than its larger neighbour, although in absolute terms, it produces less power.

Figure 5.2 illustrates the above issues for the measured set-up: it shows the measured power, the normalised power and the normalised efficiency for a module (*PV053*, $P_{STC} = 245.84\,\mathrm{W_p}$, DC measurement), the SolarEdge inverter

[5] Normalisation of (sub-) arrays is not yet often applied as a method for inter-system comparison, hence the focus on this term.

[6] Through the STC efficiency of the module or system.

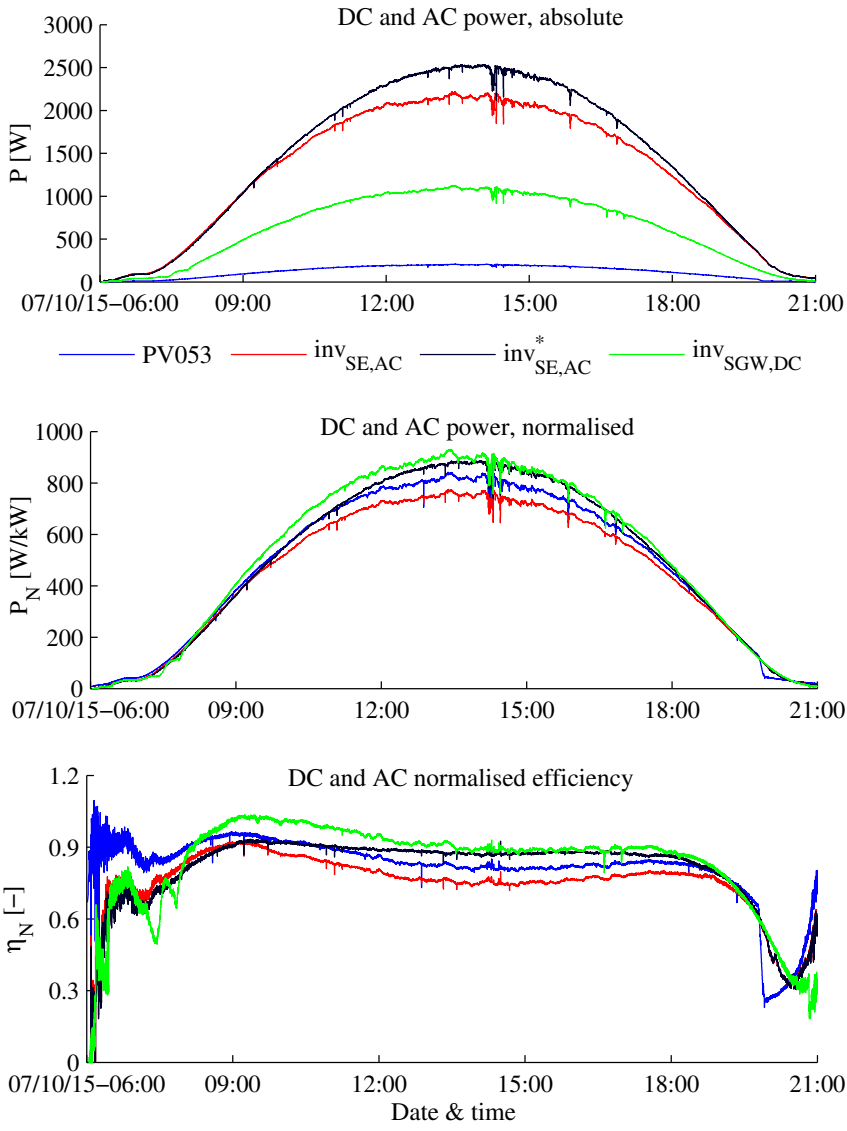

Figure 5.2: Absolute and temperature-corrected (*) displays of power, normalised power P_N and normalised efficiency η_N, of a module and two inverters (SE: SolarEdge, SGW: Sungrow) with different power ratings.

($P_{STC} = 2859.09\,\mathrm{W_p}$, AC measurement, also temperature-corrected) and the Sungrow inverter ($P_{STC} = 1209.01\,\mathrm{W_p}$, DC measurement).

The top subplot of Figure 5.2 does not allow the module or the Sungrow inverter to be easily compared to the SolarEdge inverter, as the scale has been optimised for the power of the SolarEdge inverter which differs significantly from the other power values. To a certain extent, it does show the impact of the temperature on the system functioning, as the temperature-corrected power output of the SolarEdge inverter rises above the measured power, particularly between ∼09:30 and ∼18:30. Generalised shading can be identified with some difficulty at the beginning and end of the day.

The middle subplot of Figure 5.2 allows a much better inter-comparison of *PV053* to the inverters, and among the inverters. It shows how the inverters and the module react to changes in the irradiance (limited cloud movement around 14:00) in a similar manner. The Sungrow inverter appears to function better proportionally than the rest for much of the day. At ∼20:00, a drop in the (normalised) power of *PV053* can be seen, which is larger than for the inverters.

Lastly, the bottom subplot of Figure 5.2 allows the morning and evening shading of the systems to be better identified. The Solarex-Sungrow system works proportionally better than the other systems shown, in particular between ∼08:30 and ∼19:30. The Solarex array is undersized compared to the Sungrow inverter, and thus the inverter has proportionally less variable losses for an increasing irradiance. Comparing the AC η_N^* to the η_N of the SolarEdge inverter, the relative efficiency drop due to the increase in module (and ambient) temperatures is clearly noticeable. For example, at 14:00, the SolarEdge system efficiency decrease due to higher module temperatures is 14.72 pp (percentage points).

The shade that falls on *PV053* from ∼19:45 to ∼20:30 is clearly more noticeable than in either of the two other subplots. This shading is due to the sun moving behind the plane of the array, with the measurement cabinets casting *beam* shading on the module, while it produces energy from diffuse sunlight. The increase in the normalised efficiency after 19:45 is due to comparatively *more* shading on the reference cell than on the modules (many are also shaded at that time by the AC unit - see Figures 2.4, 2.6 and 4.1). The inverter mounting rack casts *beam* shading on the nearby elements (module *PV063*, the reference cell) when the sun is behind[7] the plane of the array, in the summer period.

[7]This relative movement of the sun beyond the traditional East-West limits is a result of the Earth's axial tilt and eccentricity of motion around the sun.

5.4.2 Irradiance-dependent efficiency and effect of irradiance reference device

Whereas most crystalline silicon modules and systems can be reasonably assumed to show a linear response to the irradiance, this is for the power as a function of the irradiance, and for a sufficiently high irradiance G. By plotting the (normalised) efficiency versus the irradiance, an irradiance-dependent efficiency $\eta(G)$ can be obtained.

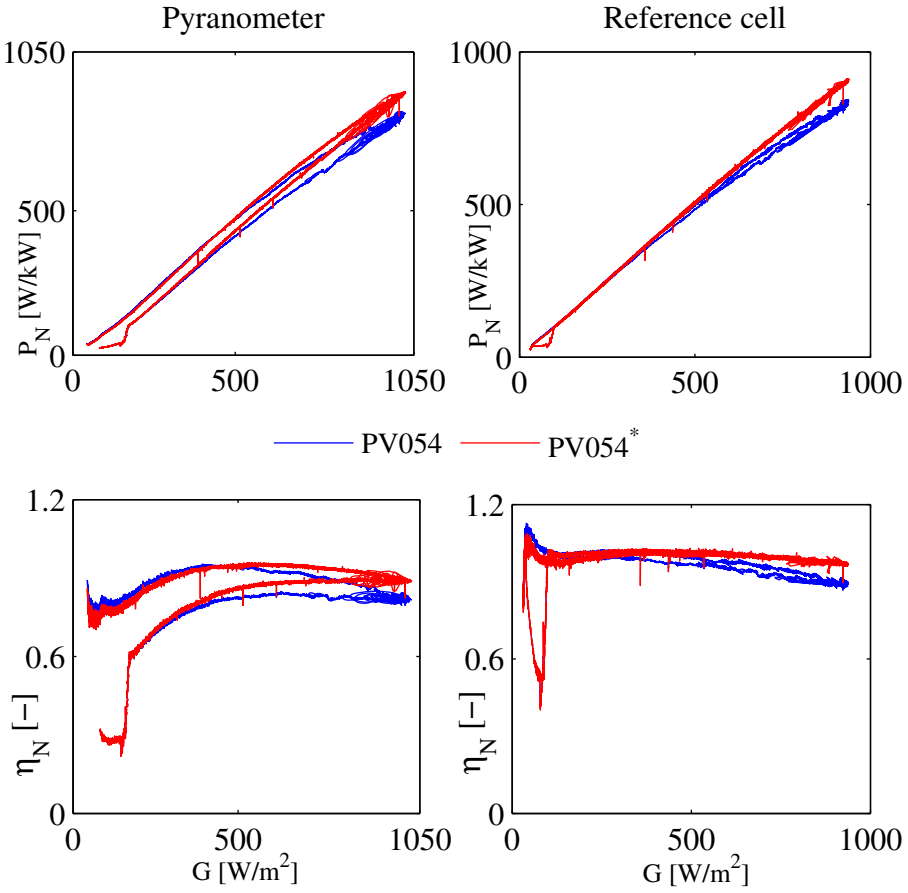

Figure 5.3: Comparison between pyranometer-derived and reference cell-derived normalised power P_N versus irradiance G and normalised efficiency η_N versus G for module *PV054*. Temperature corrected: (*). Measured on 10 July 2015.

The $\eta(G)$ of photovoltaic modules may be obtained from datasheets [158], and can, also be obtained from measurements - e.g. by fitting a polynomial to a plot of the η_N versus G. The data and trends obtained for [158] suggest that pyranometer-derived data was used for the datasheets analysed.

The top subplots of Figure 5.3 for 10 July 2015 (a clear sky day), shows that the (normalised) power exhibits a (mostly) linear response to the irradiance. The trend of the temperature-corrected normalised power (P_N^*) is closer to the ideal of the irradiance. When using the pyranometer as reference irradiance instrument, it exhibits hysteresis, whereas using the reference cell leads to much less hysteresis. This is due to the different measurement principles of the instruments, in particular their spectral response: the broadband response of the pyranometer results in it indicating a higher irradiance value than the more spectrally narrow reference cell. Moreover, angle-of-incidence effects are minimised by design in a pyranometer, whereas a reference cell has no physical cosine correction built in. As a reference cell is in essence a miniature photovoltaic module, it shows the same response as the modules to the incoming irradiance, for both spectrum and angle, and the result is a much more linear relationship with little to no hysteresis.

This effect is more pronounced in the bottom subplots of Figure 5.3, where the pyranometer-calculated temperature-corrected normalised efficiency shows a very similar hysteresis to the regular normalised efficiency: *some* temperature effects can be remarked, but in general, the pyranometer data exhibit hysteresis. The reference cell-calculated η_N^* shows much less hysteresis than its regular (non-temperature-corrected) counterpart, again suggesting that some effects are due to module temperature. In both subplots of the η_N, partial shading can be remarked by the large drop in the normalised efficiency for $G \sim 100\,\mathrm{W/m^2}$ to $150\,\mathrm{W/m^2}$, with the different responses for the reference cell and pyranometer also due to their placement on the mounting structure.

Figure 5.3 thus suggests that using a reference cell to calculate the normalised efficiency η_N will result in a more linear response with less hysteresis, which will be useful in a.o. Section 5.5. However for thermal analyses, the pyranometer-calculated values of the normalised efficiency show much less irradiance-induced variability[8], which is a useful property for linear regressions on the data, such as in Sections 5.4.3 and 5.4.4.

[8]The natural variability index of irradiance (NVI) discussed in Section 5.3 is lower for pyranometer data than for reference cell data. As a result, regression analyses will generally have less outliers using pyranometer data.

5.4.3 Identification of the system temperature coefficient of power

The temperature coefficient of power is one of the most used parameters to model and evaluate the performance of a type or brand of photovoltaic module. With the increased commoditisation (because of increased quality and standardisation) of photovoltaic modules, buyers and investors no longer just look at a brand as the deciding factor for a purchase. When comparing two modules from competing brands which otherwise appear identical (e.g. technology, STC power, ...), the γ becomes one of the technical parameters which leads to the decision for either option A or B. The determination of the temperature coefficient of power γ is not an easy task, as David King *et al* [127] and others [132, 159] have remarked. Recently, the round-robin inter-comparison of measurement laboratories in Europe also indicated a similar issue, with up to 18 % [9] difference in the calculated value of γ for the same modules.

The normalised efficiency can be used to calculate the γ, which in this case is the system temperature coefficient of power (γ_{syst}), as the influencing factors of the system (cabling, MPPT quality, other losses which have a link to the module temperature) are encapsulated in the value of γ_{syst}. Employing the normalised efficiency to calculate γ_{syst} requires a significantly reduced amount of effort, compared to the methodology of King *et al* [127] to calculate the temperature coefficient of power γ: the amount of manual labour is minimised (e.g. no need to cover-uncover modules on clear sky days) while the system continues to perform.

The steps to calculate the γ_{syst} are summarised in Algorithm 5.1. The methodology described here is a novel application and extension of concepts, such as displaying the (normalised) efficiency versus temperature. The filtering criteria have been developed within this work, and thus permit the almost fully automated determination of the γ_{syst}, which may lead to significant time saving compared to the I-V curve method of [127]. In particular, the γ_{syst} may be determined *without* the need for I-V curve measurement equipment, and can thus be applied much more broadly. To illustrate for one day, Figure 5.4 shows an example regression for module *PV055*.

(Note that for step 2 of Algorithm 5.1, the time interval chosen is such as to reduce the effect of local shading and a marked reduction in the irradiance-dependent efficiency $\eta(G)$. This occurs e.g. in the evening when the sun's position is such that the irradiance measured is $\sim$150 W/m^2 to 200 W/m^2 as seen in a.o. Figures 5.3 and 5.4.)

The top subplot of Figure 5.4 shows how the normalised efficiency varies versus the module over-temperature for the clear-sky day. Comparing the normalised

Algorithm 5.1 Method to obtain the system temperature coefficient of power γ_{syst} from the normalised efficiency and temperature measurements.

1: Start: **Calculate** the normalised efficiency (η_N) for each measurement step Δt using measured module (or system) power, the irradiance (G) and the module (or system) STC power. **Measure** the module (or system) temperature at the same rate as the η_N. **Note** use of pyranometer or reference cell data.
2: **Plot** η_N versus the module (or system) temperature, for the *time* between sunrise + 1 to 2 hours and sunset - 1 to 2 hours, where the start and end points approximately correspond with $G \geq 200\,\mathrm{W/m^2}$ for each day.
3: **Fit** least-squares regression line through points, save slope. Slope = γ_{syst}.
4: **Calculate** *filtered* long-term (e.g. per month or more) mean of daily values of γ_{syst}.
Filter for *pyranometer*: $\langle T_o \rangle_d > 5\,^\circ\mathrm{C}$ and $NVI_{pyr} < 0.020$. Filters for *reference cell*: $\langle T_o \rangle_d > 5\,^\circ\mathrm{C}$ and $NVI_{RC} < 0.020$ (if enough data: $NVI_{RC} < 0.010$).
5: **Verify** proper value of average γ_{syst}: plot η_N^* and η_N for a clear sky day (or closest approximation). The graph of η_N^* should be flat and close to 1, and higher than the graph of η_N for stable irradiance conditions and module temperatures above 25 °C and a properly functioning module or system.
6: **return** Averaged and daily values of γ_{syst}.

efficiency at 9:00 and 19:00 shows a decrease, as the module temperature in the evening is higher than the morning, for an identical irradiance. This is a result of the rise in the ambient temperature, and can not be compensated for, even by using the concept of the over-temperature T_o (the *absolute* temperature is higher in the afternoon than in the morning, for an identical T_o). For a clear-sky day such as shown here, a hysteresis curve can be remarked (it is less pronounced when using a reference cell). The regression line, whose slope is the value of the system temperature coefficient of power γ_{syst} fitted through the subset of the day's data, is the average of what would be the morning γ_{syst} regression line and the afternoon γ_{syst} regression line.

This would suggest that, rather than use a single parameter (the system temperature coefficient of power γ_{syst}) to characterise the change in a photovoltaic module's efficiency due to its temperature deviating from its STC temperature, two parameters should be used: the "morning" γ_{syst} and "afternoon" γ_{syst}. This is neither practically feasible nor desirable, as the temperature profile of a (clear sky) "morning" is an increase in a module's temperature from sunrise to midday. An "afternoon" would then be characterised by starting at a high temperature at midday and ending at a lower

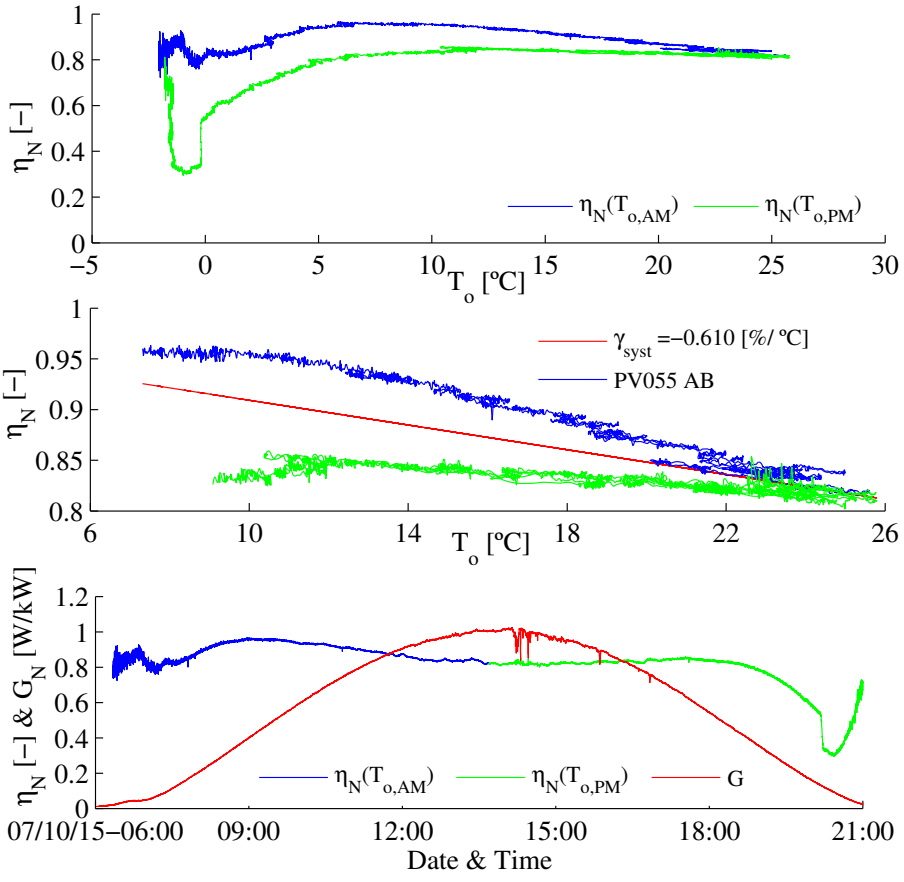

Figure 5.4: Pyranometer-normalised efficiency η_N versus over-temperature T_o, with a polynomial regression line for the system temperature coefficient of power γ_{syst}.

temperature at sunset. As an example of a day with multiple temperature peaks and troughs, Figure 5.5 was generated. The time-based definition of daylight morning and afternoon for the module's temperature thus fails to be of benefit.

As photovoltaic modules and systems are rarely exposed to the ideal conditions employed for standardised or well-established measurement methodologies, a natural discrepancy between theory and practice arises. The philosophy here is to take all (reasonable) weather conditions into consideration, and to characterise a system as it performs under most of these conditions.

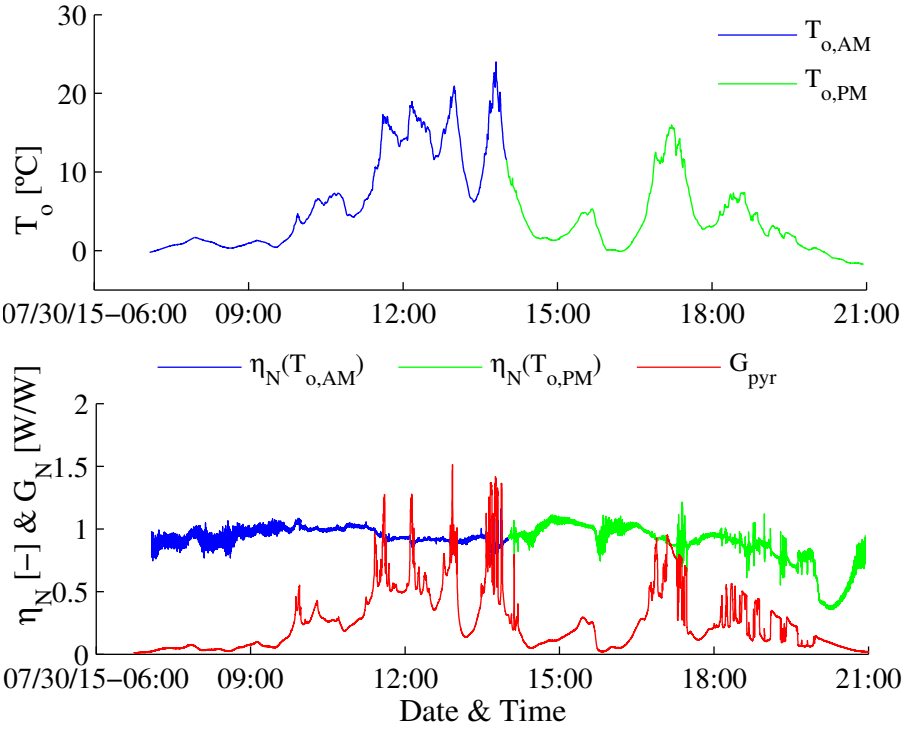

Figure 5.5: Over-temperature T_o and pyranometer-normalised efficiency η_N for a day with multiple temperature peaks and troughs.

Hence, by calculating the system temperature coefficient of power (γ_{syst}) as a value per day, filtering for appropriate days (as shown in step 4 of Algorithm 5.1) and then taking the average over a long period (e.g. one month), a representative value of the γ_{syst} is obtained[9].

The determination of this value is thus much less dependent on the amount of clear-sky days in a period[10] or availability of personnel. The additional benefits include that there is no need to perform actions which impact the energetic performance of the system, such as manual cover-uncover steps, or the need to measure I-V curves and temperature at regular intervals.

[9] A comparison of reference cell-determined versus pyranometer-determined γ_{syst} is given in Figure C.4 in Appendix C

[10] There were 11 clear-sky (or almost perfect clear sky) days in the period of April-October 2015, i.e. roughly one day per three weeks, although July-September saw only four such days.

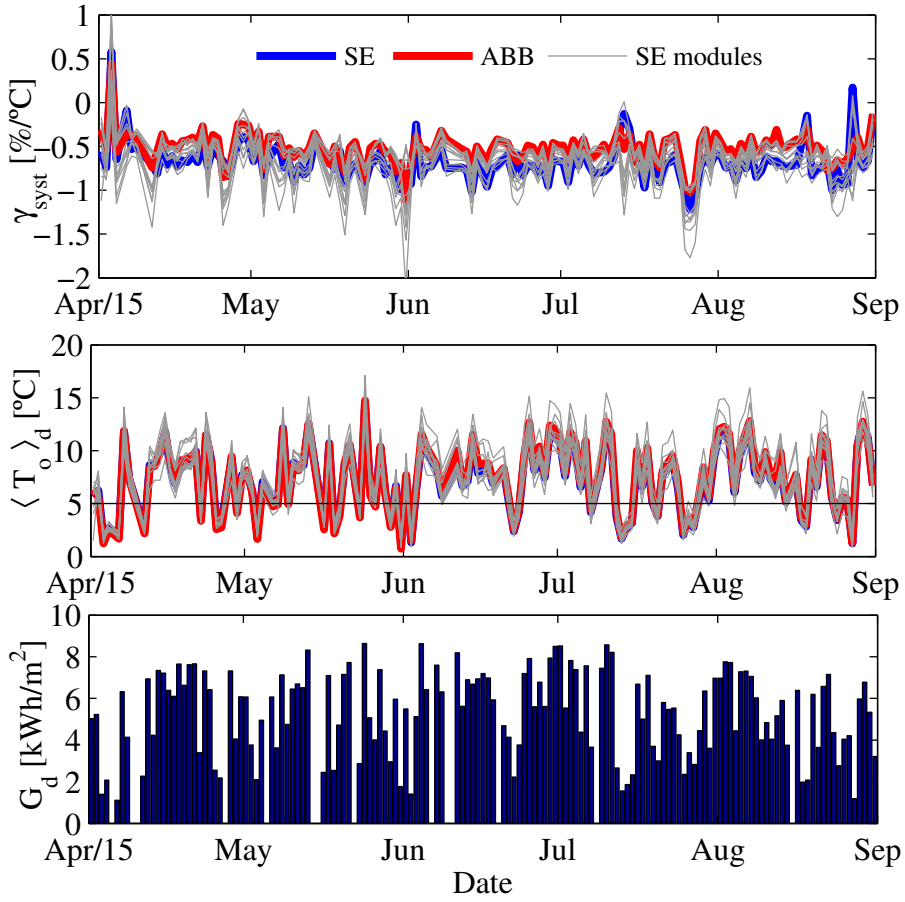

Figure 5.6: *Unfiltered* daily values of pyranometer- determined γ_{syst}, with T_o and G_d for *Smart PV* modules, April-August 2015. Days with errors in data have been removed in all subplots. The T_o filtering criterion line shows which days would be removed.

Figure 5.6 shows the variation in the daily determined γ_{syst} for April-August, which is sensitive in particular to two underlying effects: daily average over-temperature and irradiance fluctuations over the day, summarised by the natural variability index of irradiance (NVI) (the NVI is explained in more detail in Section 5.3).

Of these two effects, the daily average value of the over-temperature is most important, as the parameter γ_{syst} characterises performance related to

temperature changes. The temperature-efficiency relationship throughout a day should thus be sufficiently pronounced for it to be properly characterised by γ_{syst}.

The value of T_o contains information on the heating of the module during the day, as well as the amount of persistent cloud cover. However, large and fast irradiance variability can also lead to normalised efficiency fluctuations[11]. Both effects combine to make a regression analysis on those days largely untrustworthy, yet the obtained data is still useful, but for a different purpose - see Section 5.4.5.

The data for days such as 2 April, 31 May and 25 July (with a large deviation from the long-term trend of γ_{syst}), are removed by filtering using the criteria described above, in order to obtain the resulting averaged γ_{syst}, given in Table 5.2.

5.4.4 Calculation of the system temperature coefficient of power

The system temperature coefficient of power has been calculated for each module and system measured for April to August 2015, with the results summarised in Table 5.2. Both the summary values and the daily value for *PV055* (see Figure 5.4) are often larger in magnitude than expected from the modules' data sheets, which was also remarked by Makrides *et al* [132].

This can be explained using Equation (5.13), where the assumption is that the value of the temperature coefficient of power from the modules' data sheets is correct, and that therefore any deviation is a result of the rest (or balance) of the system (cables, inverter, ...) also showing a temperature-related response[12], the BOS temperature coefficient (γ_{BOS}), which is calculated using Equation (5.13):

$$\gamma_{syst} = \gamma_{module} + \gamma_{BOS}. \tag{5.13}$$

As the γ_{syst} is determined using module temperatures, the γ_{BOS} also relates to module temperatures. Over the period of April-August 2015, the values of the

[11] The *reference cell*-calculated η_N shows much larger sensitivity to irradiance fluctuations. This then affects the regression analysis per day, as many more outliers are present compared to pyranometer data. This thus requires more stringent filtering, and makes Figures 5.6 and 5.8 less useful for long-term comparisons.

[12] By extension, also an implicit irradiance-related response, e.g. for Joule losses in cables, as high over-temperatures correspond with high irradiance and thus power and currents in the system. A reduction in system efficiency with higher module temperatures measured may thus be larger (more negative) than just by looking at the relationship between ΔT_{STC} and γ_{module}.

standard deviation of γ_{syst} ($\sigma_{\gamma,syst}$) in Table 5.2 are shown both as absolute values (expressed in percentage points) and as relative values, compared to the long-term averaged value of γ_{syst}. While not shown, the MWT modules have a generally lower temperature than the other modules in the *Smart PV* system (∼1 °C to 3 °C less at high irradiance), which contributes to a smaller value of the γ_{syst}.

Table 5.2: Calculated values of for April to August 2015 for the three inverters and composing modules measured, for valid days.

Identifier	Technology	γ_{module} [%/°C]	γ_{syst} [%/°C]	$\sigma_{\gamma,syst}$ [pp]	$\sigma_{\gamma,syst}$ [d] [%]	γ_{BOS} [%/°C]
SE modules avg[b]	mc-Si/MWT	−0.41	−0.60	0.12	19	−0.20
SE inverter[c]	mc-Si/MWT	−0.41[b]	−0.68	0.13	20	−0.27
SGW inverter[c]	poly-Si	−0.50	−0.39	0.28	71	+0.11
PV052/ABB(N)	mono-Si	−0.42	−0.49	0.11	23	−0.07
PV052 (N)	mc-Si 3x20D	−0.42	−0.49	0.11	23	−0.07
PV053 (N)	mc-Si 3x20AB	−0.42	−0.57	0.11	20	−0.15
PV054 (N)	MWT 3x20D	−0.39	−0.50	0.12	23	−0.11
PV055 (N)	MWT 3x20AB	−0.39	−0.51	0.12	23	−0.13
PV060 (S)	MWT 10x6AB	−0.39	−0.53	0.12	22	−0.15
PV061 (S)	MWT 10x6D	−0.39	−0.54	0.12	22	−0.15
PV058 (S)	mc-Si 10x6AB	−0.42	−0.73	0.13	17	−0.31
PV059 (S)	mc-Si 10x6D	−0.42	−0.68	0.13	19	−0.26
PV051 (N)	mc-Si 10x6D	−0.42	−0.60	0.10	17	−0.18
PV056 (N)	mc-Si 10x6D	−0.42	−0.67	0.14	20	−0.25
PV057 (S)	mc-Si 10x6D	−0.42	−0.64	0.11	17	−0.22
PV062 (S)	mc-Si 10x6D	−0.42	−0.68	0.14	20	−0.26
PV063 (N)	mc-Si 10x6D	−0.42	−0.53	0.13	24	−0.11

[a] Added filters: $\langle T_o \rangle_d > 5$ °C, NVI<0.020 (classes 1–4).
[b] Average of all modules in SolarEdge array.
[c] DC inverter measurement data.
[d] $\frac{\sigma_{\gamma,syst}}{|\gamma_{syst}|}$ e.g. $\frac{0.12}{|-0.60|} = 19\,\%$, using non-rounded data.

One of the items that catches the attention in Table 5.2 is the *positive* value for the γ_{BOS} and larger variation of γ_{syst} for the Sungrow inverter system, with a *relative* $\sigma_{\gamma,syst}$ of 71 %. This is a result of the array of Solarex modules being undersized versus the Sungrow inverter: the total power of the PV modules used amounts to 1209 W_p, whereas the inverter has an AC power rating of 3000 W. As such, the fixed losses in the Sungrow inverter tend to dominate, and obfuscate the relationship between module temperatures and the change in their

efficiency. In this case, the value of γ_{syst} improves on days of high irradiance (and associated module temperatures), as the fixed losses in the inverter reduce in importance, compared to the variable losses in the balance-of-system.

The relatively large variation of the γ_{syst} values for the different modules in Table 5.2 could be due to temperature (and wind) effects. The inter-module temperature variations discussed in Section 4.11 suggested that the array edge modules should be among the most affected by wind. This is generally the case, with modules *PV058* and *PV059* also showing a similar large response to changes in temperature. The MWT modules do appear to be less sensitive to temperature variations with more similar values among the modules as well.

However, the results of Table 5.2 must be interpreted with caution, if attempting to compare one technology to another ("Are MWT cell modules better than mc-Si?"), as other explanations may be found. For example, random variations in the DC-DC converters used are possible, or the modules may also have had manufacturing and transport-related defects[13]. That said, the trends shown in this table may be used to understand and explain energy yield differences among the modules, as will be done in Sections 5.6 and 5.8.

5.4.5 Shading detection and monitoring

In general terms for crystalline silicon modules and systems, the system temperature coefficient of power γ_{syst}, similarly to the temperature coefficient of power γ, should be a negative value per °C of temperature rise above the STC temperature, as it quantifies the change in efficiency due to a temperature change. What happens then when a module or system is subjected to non-ideal conditions such as shading?

The mounting structure (for work on the building's façade) which was finished around 18 September 2015 has poles and horizontal bars which are up to 2 m above the roof and modules height. The pattern of shading that these poles generate can be complex, as can be observed in Figure 5.7.

Figure 5.8 can then be contrasted with Figure 5.6. The change is very clear is that from September onwards, the values of γ_{syst} vary strongly, much more[14] so than the preceding five months. During the high-irradiation days at the end of September-early October (e.g. 30 September and 1 October), the γ_{syst} for the modules closest to the poles causing shade deviate from their prior trend.

[13] Module *PV061* has a corner of a cell broken - this was noticed upon installation on the array.

[14] This is partly due to temperature: then *all* modules have these changes. For high irradiation days, the trends become decorrelated - which is due to shading.



Figure 5.7: Pole shading on the photovoltaic modules, with modules *PV061 & PV062* shaded, photograph taken on 04 December at 13:50. See also Figures 2.4, 2.6 and 4.1 for the lay-out of the array.

More importantly, the similar trends of γ_{syst} for different modules during the previous months become decorrelated from September onwards.

Figure 5.9 shows the variation in the normalised efficiency η_N for the four corner modules of the *Smart PV* array, modules *PV051, PV056, PV057* and *PV062*. The modules *PV051* is furthest from the poles, and thus suffers the least shading (modules *PV056* and *PV057* have approximately the same amount of shading, due to the pole placement at regular intervals and the $\sim$42° offset between the building and South - see also Figure 4.1). As the modules' temperatures do vary a bit because of the shading, the value of γ_{syst} becomes more positive for the day for the modules with most shading: the morning typically high values of the normalised efficiency are lowered due to shade, and the regression line which gives γ_{syst} for the daily data thus tilts upwards, instead of the expected downward trend.

Figure 5.9 also illustrates an issue which is difficult to predict using static[15] I-V curves and inverter (or DC-DC converter) efficiency and MPPT data: the behaviour of the *system* due to (pole) shading throughout a day. In particular, "clean" power and normalised efficiency local maximum power peaks seen in measured I-V curves, such as shown in Figure 5.10, do not directly translate

[15]By nature, an I-V curve is a static snapshot of a module's performance at the moment of measurement. Ideally, *all* conditions should be constant during the measurement, which can be problematic for I-V curves that require longer measurement intervals.

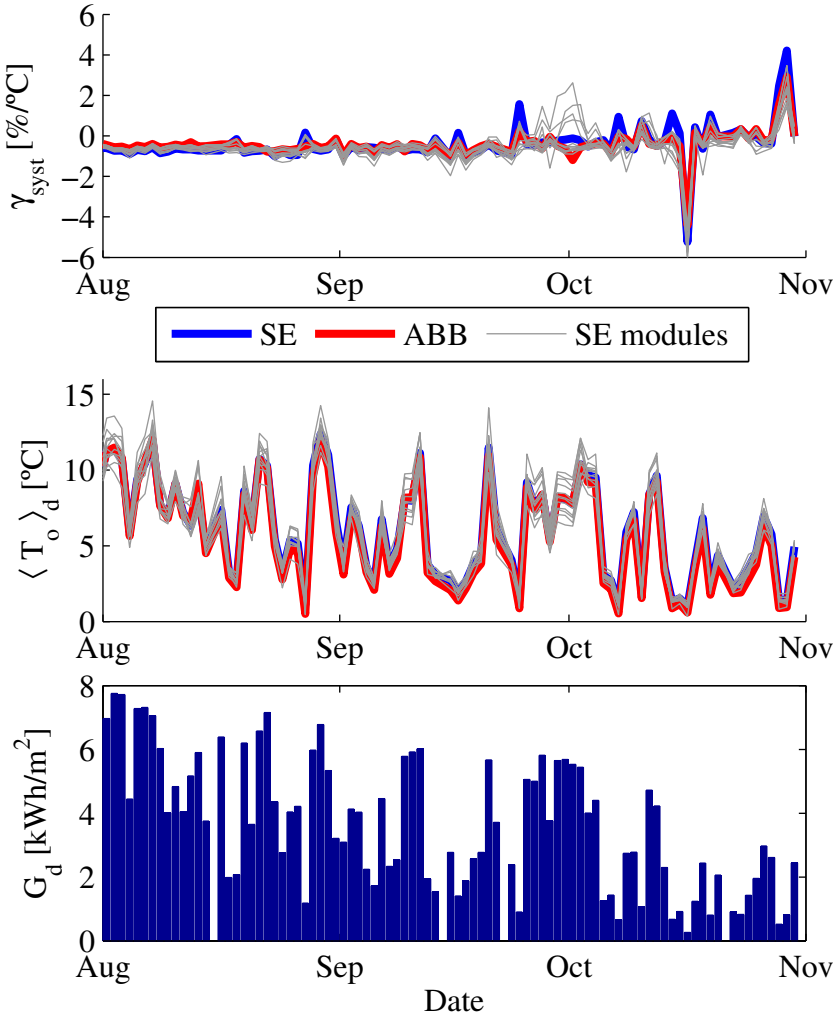

Figure 5.8: *Unfiltered* daily averaged values of γ_{syst}, T_o and G_d for modules of the *Smart PV* project, August-October 2015, with morning shading from September onwards. Days with errors in data have been removed in all subplots.

to equally clean or fully predictable behaviour when that module or system is connected to an inverter or converter, as is visible around 12:00 for *PV062*.

In part, this is because the shading is often more complex than modelled, with

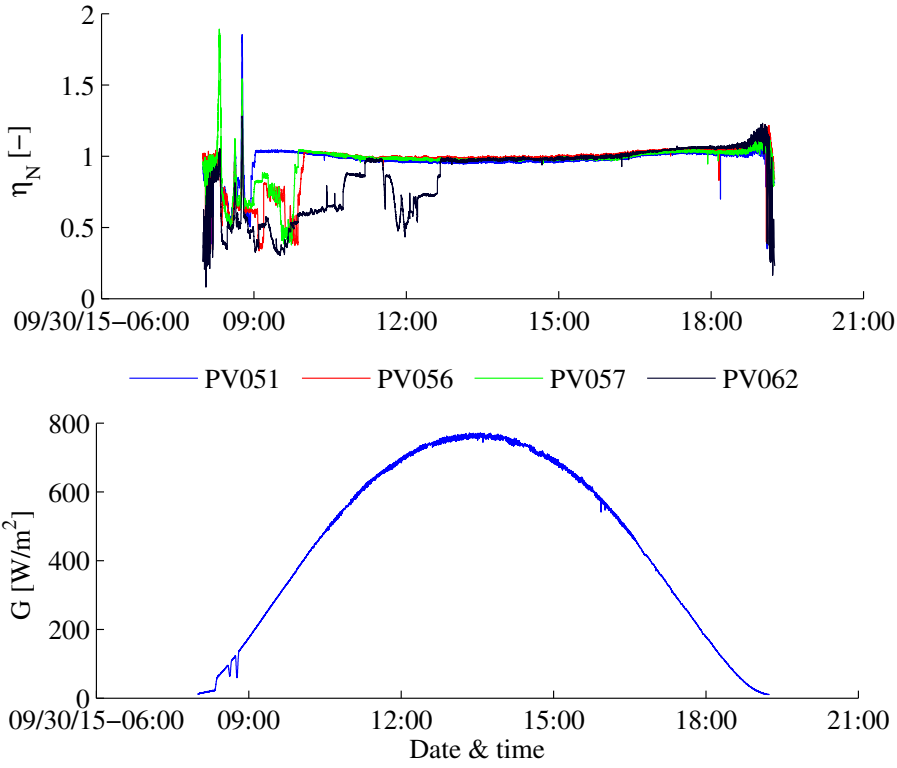

Figure 5.9: Variation in the reference cell normalised efficiency due to pole shading. The η_N peaks in the morning occur because the reference cell is shaded proportionally more than the modules.

larger areas and directions impacted. For example, shading of a cell may be just enough to lower the current yet not enough to cause the bypass element to turn on. Moreover, the bypassed areas of the module can lead to a voltage drop at which value the converter does not function as efficiently as it otherwise can, as well as that the multiple peak power values in the I-V curve can lead to MPP tracking errors and instabilities. Figure 5.10 illustrates the multiple maximum power points due to pole shading of the I-V curve measured of module *PV064* on 30 September. (This module has one bypass diode per 6 cells, which leads to this I-V curve shape for the shading encountered.)

As a general monitoring approach for (preferably) unshaded arrays and systems, the daily value of the system temperature coefficient of power (γ_{syst}) can be monitored. As long as the value stays within a certain system- and condition-

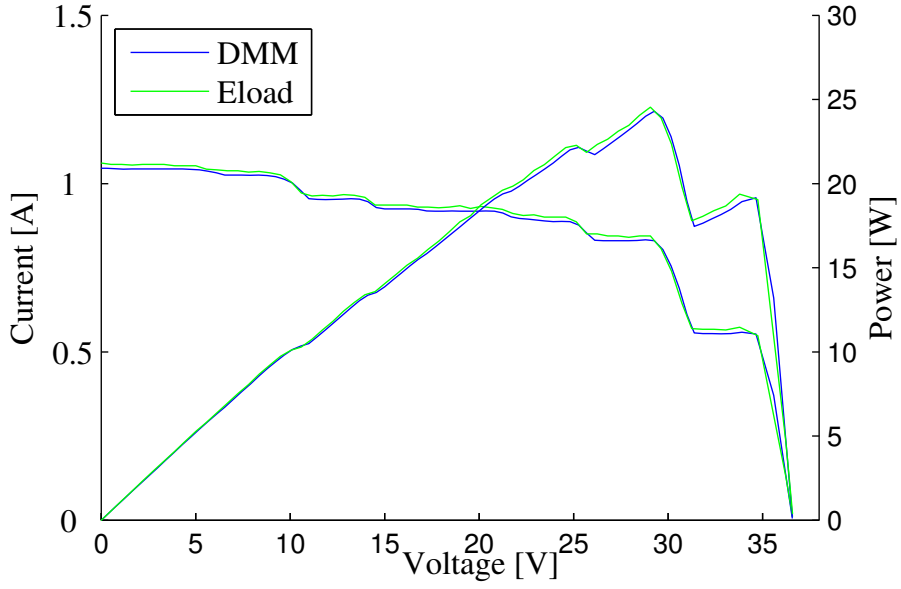

Figure 5.10: An I-V curve measured of module *PV064* during pole shading on 30 September 2015 at 8:39:26. $G \simeq 125\,\mathrm{W/m^2}$.

specific range (e.g. $\gamma_{syst} \pm \sigma_{\gamma,syst}$)[16], it behaves within specification. When a large change in the γ_{syst} is detected, it may point to a thermal or other system issue, e.g. shading. The normalised efficiency (η_N) during the day can subsequently be used to look into more detail to the system's behaviour, to ascertain the cause.

That the cause may not necessarily be an energy-loss inducing system error (such as unintended shading from a new nearby structure) can also be detected using the approach above. For example, as the determination of the γ_{syst} also depends on a proper temperature measurement, a large deviation of the daily value of γ_{syst} may point to a temperature sensor error, while the loose or broken temperature sensor has no impact on the system's electrical performance. The correctness of the indicated temperature values can then be verified using the methods described in Chapter 4.

Lastly, the daily PR and the temperature-corrected Performance Ratio PR* may also be used for shading or anomaly detection. Similarly, the averaged normalised efficiency $\langle \eta_N \rangle_\tau$ and its temperature-corrected form can also be

[16] With values of γ_{syst} excluded when the daily average of T_o<5 °C (or another system-appropriate value).

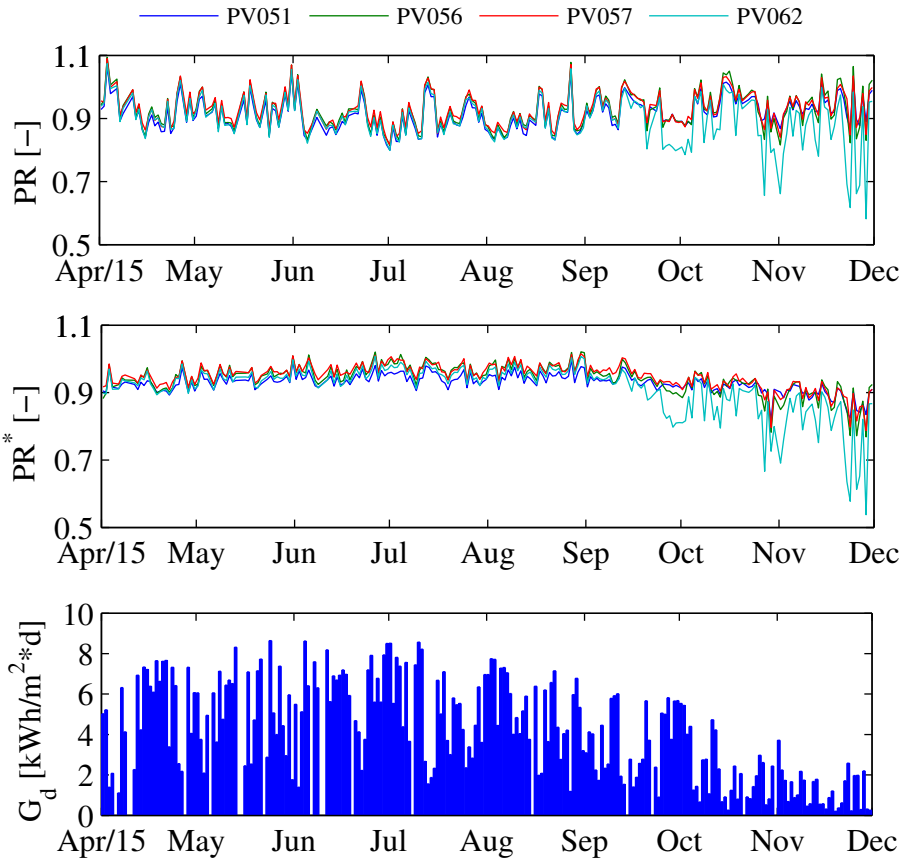

Figure 5.11: Daily PR and PR*, April-November 2015, with morning shading from early September. Days with errors in data have been removed in all subplots. Figure C.1 in Appendix C shows how this figure can also be created using the daily averaged value of the η_N for the same purpose.

used. As can be seen in Figure 5.11, the PR* is much more stable over time (its standard deviation is smaller) than the PR, and can thus also be used for shading analysis or anomaly detection.

5.5 Modelling of the normalised efficiency, power and energy

5.5.1 Initial theoretical considerations

For modelling, Huld *et al* [13, 124] used and defined a module-level model of the instantaneous relative efficiency η_{rel} and its hourly and yearly equivalent, by modifying the well-known model of King *et al* [114]. Their model depends on the measurement of multiple I-V curves over a long period (months), and subsequently solving the equations to obtain the parameters k_1 to k_6 of Equation (5.14).

As the energy yield measurements on the modules used in the measurement set-up excludes the practical use of such a large number of I-V curves being measured continuously per module due to, among other reasons, the energy loss associated with the I-V curve measurement, as described in Chapter 2, an alternative method must be developed. Moreover, a method which does not require the need for I-V curves to be measured increases the possibility of its use throughout the photovoltaic industry.

The model of Huld *et al* [13, 124] which served as a starting point for the modelling aspect is summarised in the equation of $\eta_{rel}(G', T') \equiv \eta_N(\frac{G}{G_{STC}}, \Delta T_{STC})$ (with the notation adapted to that of this text):

$$\begin{aligned}\eta_N(\frac{G}{G_{STC}}, \Delta T_{STC}) =& 1 + k_1 \cdot \ln(\frac{G}{G_{STC}}) + k_2 \cdot [\ln(\frac{G}{G_{STC}})]^2 \\ &+ \Delta T_{STC} \cdot \left(k_3 + k_4 \cdot \ln(\frac{G}{G_{STC}}) + k_5 \cdot [\ln(\frac{G}{G_{STC}})]^2 \right) \\ &+ k_6 \cdot (\Delta T_{STC})^2 \end{aligned} \tag{5.14}$$

The formulation of Huld *et al* is focused on the DC, *module-level* normalised efficiency and then the power. This approach is extended here to full photovoltaic systems, such the AC side of the inverter[17], by taking the inverter DC-AC conversion efficiency (η_{DCAC}) into account. This may either be the weighted[18] efficiency from inverter data sheets, or the measured average or weighted efficiency of the inverter.

[17] String inverter: SolarEdge and Sungrow, or micro inverter: ABB

[18] Irradiance-dependent weighting: Either the CEC or European formulation, depending on the irradiance profile of the region where the modelling is performed.

The AC normalised efficiency ($\eta_{N,AC}$) is modelled here as

$$\eta_{N,AC} = \eta_{DCAC} \cdot \eta_N. \tag{5.15}$$

The modelled normalised efficiency may either be obtained through fitting of the AC data, or the DC data of the inverter. Depending on the behaviour of the inverter, either of these paths may deliver the best results. From a practical perspective, the methods and results for the AC modelling of the inverters are shown for AC-fitted data, and similarly for the DC-locally measured data (e.g. measured data of the SolarEdge inverter's DC input, instead of measurements of the modules before the DC-DC converters and then using the DC normalised efficiency $\eta_{N,DC}$) in Sections 5.5.2 and 5.6.

The temperature-corrected normalised efficiency (η_N^*) is often easier to interpret than the normalised efficiency (η_N), as the impact of the variation in module temperature on the normalised efficiency is compensated. For modelling purposes, this means that $\Delta T_{STC} = 0$ can be used. As such, Equation (5.14) reduces to a polynomial depending only on the irradiance G, for every moment of time:

$$\eta^*_{N,mod}(G(t)) = 1 + k_1 \cdot \ln(\frac{G(t)}{G_{STC}}) + k_2 \cdot [\ln(\frac{G(t)}{G_{STC}})]^2. \tag{5.16}$$

The benefit of the formulation of Equation (5.16) is that it may also be used for educational and illustrative purposes. It lends itself to rapid modelling efforts, as only an irradiance value is required, which can be sourced from measured or modelled data. As an example, Figure 5.12 was generated for 21 and 22 August 2015 from measurements, and Figure 5.13 focuses on the morning of 21 August to better illustrate the variation in measured and modelled values during large irradiance changes.

The values chosen for this example ($k_1, k_2 = -0.1$) are equal in magnitude to indicate their relative importance in the final value of $\eta^*_{N,model}$. The determination of the optimal value of the coefficients k_1 and k_2 can lead to the modelled value of η^*_N to equal or closely approximate the measured value of η^*_N.

It can be seen that $k_2 \cdot [\ln(\frac{G}{G_{STC}})]^2$ strongly reduces the normalised efficiency at low irradiance values[19] and reaches its maximum at $G = G_{STC}$ for negative values of k_2. For $k_1 \cdot \ln(\frac{G}{G_{STC}})$, the parameter contributes positively to the value of $\eta^*_{N,model}$ for $G < G_{STC}$, and leads to a reduction of $\eta^*_{N,model}$ at irradiances above $1000\,\mathrm{W/m^2}$.

[19] This is clearly visible as $1 + k_2 \cdot [\ln(\frac{G}{G_{STC}})]^2$ becomes negative for G<43 W/m^2 and $k_2 = -0.1$.

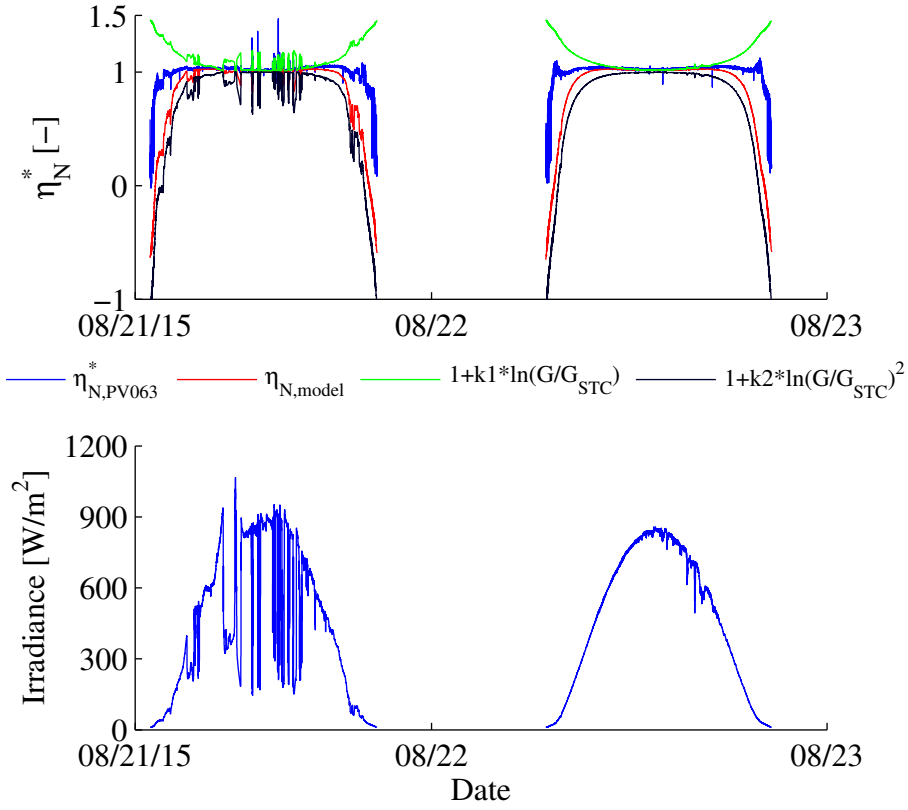

Figure 5.12: Comparison of initial model approximation to measured η_N^*, using $k_1 = k_2 = -0.1$, for 21 and 22 August 2015.

From the above analysis, the following conclusions can be drawn: the coefficient k_1 reduces high irradiance condition overestimations and it increases the modelled normalised efficiency at low irradiance conditions (below 500 $\mathrm{W/m^2}$)[20]. The coefficient k_2 strongly reduces the modelled normalised efficiency at low irradiance conditions (below 200 $\mathrm{W/m^2}$) and contributes in a limited - yet important - manner to the model in high irradiance conditions. For irradiances above G_{STC}, the coefficient k_2 reduces the modelled normalised efficiency as well, although its impact is less strong than the coefficient k_1.

As can be observed in Figure 5.13, the model of Equation (5.16) which joins the coefficients k_1 and k_2 approximates the measured temperature-corrected

[20]This varies depending on the value of the coefficient k_1, here, $k_1 = -0.1$

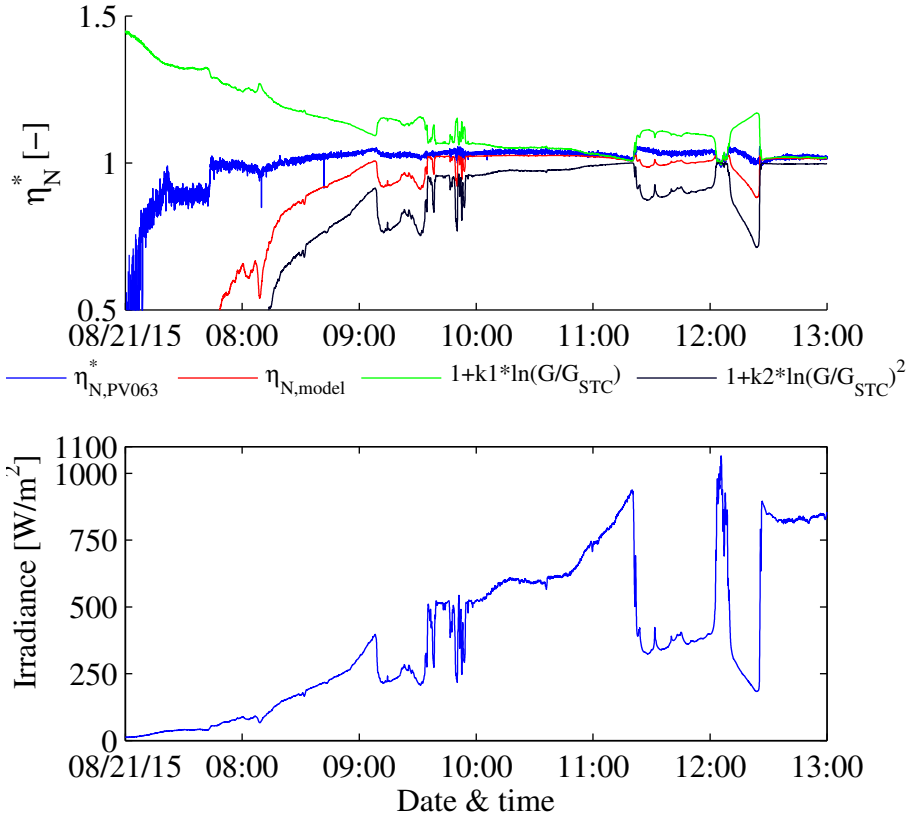

Figure 5.13: Comparison of initial model approximation to measured η_N^*, using $k_1 = k_2 = -0.1$, for the morning of 21 August 2015.

normalised efficiency, although it starts to do so correctly from $\sim$750 W/m^2. The impact of $k_2 \cdot [\ln(\frac{G}{G_{STC}})]^2$ appears to be too pronounced, leading to a strong reduction in the modelled η_N^*, compared to the measured η_N^*. Obtaining the module- or system-appropriate values of the coefficients k_1 and k_2 is therefore the next step to undertake.

5.5.2 Least-squares approximation of the normalised efficiency model coefficients

While the normalised efficiency is a very useful metric with multiple applications, the goal is to model the power and energy of photovoltaic modules and systems. As can be seen in Figures 5.4, 5.5, 5.12 and 5.13, the normalised efficiency (regular or temperature-compensated) includes the irradiance in the metric, yet does vary with the irradiance, which is clear for the high and low extremes. The importance of a model error for the normalised efficiency should therefore be weighted according to its contribution to power *and* energy, over a period of multiple days. This means that not only the magnitude of the model error at a certain irradiance value must be taken into account, but also the frequency at which rate these errors may occur.

The square root of the sum of squared errors (SSE) brings the power and energy requirements together to evaluate the model errors (note that the temperature-corrected normalised power P_N^* was defined in Equation (5.1)):

$$SSE = \sqrt{\sum (P^*_{N,model} - P^*_{N,meas})^2}. \tag{5.17}$$

By recognising the link between the (measured) irradiance scaled by G_{STC}, the normalised power and the normalised efficiency as in Equation (5.8), it is possible to calculate the temperature-corrected normalised power, from the temperature-corrected normalised efficiency η_N^* and the irradiance.

From [13, 124] and the analyses performed on figures such as Figures 5.12 and 5.13, it is known and expected that the coefficients k_1 and k_2 will be negative. In other words, as k_1 and k_2 differ from zero, the module or inverter for which the value of the SSE is calculated is non-ideal.

From statistical theory [160], when fitting model coefficients to a data set, the data set must be split in a training set and a validation data set. Otherwise, the model coefficients that are then determined will be with minimal errors, yet their applicability for the future is limited and more importantly, their untested errors not quantified. A further requirement for time series is that the training data set must be before[21] the validation data set.

The available data for the model is the measured data for April-August 2015. While data from September onwards is available, the pole shading will skew the results, and is thus not included in this part.

[21] Perhaps as this allows a training set to be up to "today", and validated for the future days.

The training set for the fitting of coefficients k_1 and k_2 is a therefore the reduced dataset of April and May. This reduced dataset is created by taking the filtered, error-corrected time series data for April and May and then appended to a data vector per module or inverter. These vectors are then used to calculate the minimal SSE over the total period. The value of k_1 and k_2 is determined using a step size of $-1 \cdot 10^{-4}$, with the starting point = 0 (an ideal system).

Algorithm 5.2 shows the steps followed to calculate the minimal SSE and the corresponding values of k_1 and k_2. The need for this form of algorithm is that it is not known a priori whether the minimum SSE is always obtained for $|k_1| > |k_2|$ (as the data from from [13, 124] suggests). While more sophisticated search methods can be employed to obtain the coefficients k_1 and k_2 which deliver the minimal SSE, Algorithm 5.2 satisfied the present state requirements, in particular as this is a step in the sequence of normalised efficiency, power and energy modelling. Additional work in this area may be performed in the future, a.o. to optimise Algorithm 5.2 so that it converges quicker to a solution, as well as ensure that the true minimum SSE is guaranteed to be found.

Algorithm 5.2 Method used to obtain coefficients k_1 and k_2 for Equation (5.16) using the square root of the sum of squared errors SSE

1: **Start**: Create training data set, **calculate** $P^*_{N,model} = \eta^*_{N,model} \cdot G_N$ using the *modelled* η^*_N and $k_1 = k_2 = 0$. Note: irradiance data is reference cell data. i=1.
2: i=i+1; Step size $st = -1 \cdot 10^{-4}$. $k_{1,new} = k_{1,old} + st$ and $k_{2,new} = k_{2,old} + st$. **Calculate** $SSE(k_{1,o,i}, k_{2,o,i})$, $SSE(k_{1,o,i}, k_{2,n,i})$, $SSE(k_{1,n,i}, k_{2,o,i})$, $SSE(k_{1,n,i}, k_{2,n,i})$, and minimum of all SSE. Compare to minimum of all SSE for i=i-1. Retain k_1, k_2.
3: **while** $MIN(SSE_i) > MIN(SSE_{i-1})$ **do**
4: i=i+1; Step size $st = -1 \cdot 10^{-4}$. $k_{1,new} = k_{1,old} + st$ and $k_{2,new} = k_{2,old} + st$. **Calculate** $SSE(k_{1,o,i}, k_{2,o,i})$, $SSE(k_{1,o,i}, k_{2,n,i})$, $SSE(k_{1,n,i}, k_{2,o,i})$, $SSE(k_{1,n,i}, k_{2,n,i})$, and minimum of all SSE. Compare to minimum of all SSE for i=i-1. Retain k_1, k_2.
5: **end while**
6: **Verify** that SSE decreases to end value (otherwise: use k_1 and k_2 for minimal SSE).
7: **return** Matrix with values of SSE and k_1 and k_2.

With the coefficients k_1 and k_2 for Equation (5.16) for the individual modules, the temperature-corrected normalised efficiency η^*_N can be modelled using irradiance data. To then obtain the regular normalised efficiency η_N, the formulation of Equation (5.10) can be applied using the system temperature coefficient of power γ_{syst} (instead of the temperature coefficient of power γ),

and then fully written out.

$$\eta_N = \eta_N^* \cdot T_{corr} \tag{5.18}$$

$$\eta_N = \left(1 + k_1 \cdot \ln(\frac{G}{G_{STC}}) + k_2 \cdot [\ln(\frac{G}{G_{STC}})]^2\right) \cdot (1 + \gamma_{syst} \cdot \Delta T_{STC}) \tag{5.19}$$

$$\eta_N = \left(1 + k_1 \cdot \ln(\frac{G}{G_{STC}}) + k_2 \cdot [\ln(\frac{G}{G_{STC}})]^2\right) \tag{5.20}$$

$$+ \Delta T_{STC} \cdot \left(\underbrace{\gamma_{syst}}_{k_3} + \underbrace{k_1 \cdot \gamma_{syst}}_{k_4} \cdot \ln(\frac{G}{G_{STC}}) + \underbrace{k_2 \cdot \gamma_{syst}}_{k_5} \cdot [\ln(\frac{G}{G_{STC}})]^2\right)$$

The similarity between Equation (5.20) and the formulation of Huld *et al* [13, 124]) from Equation (5.14) can be noticed, with the coefficient k_6 assumed to be zero in Equation (5.20).

One of the main advantages of the approach outlined in this chapter is that it can be applied to monitored systems without the need for I-V curve measurement capabilities, which are required in order to obtain the coefficients k_1 to k_6 for Equation (5.14). It is therefore much more broadly applicable, at a reasonable measurement and data processing cost. Moreover, the approach shown here requires only the three primary coefficients k_1, k_2, k_3 to be determined, as k_4 and k_5 are derived from these. The high-level summary of the different steps to calculate the best-fit model of the normalised efficiency using monitored data is given in Algorithm 5.3.

Algorithm 5.3 Steps to obtain the model coefficients for a system's performance from measurements, using the normalised efficiency, system temperature coefficient of power and Algorithm 5.2.

1: Start: **Measure** P, G, T_{cell}, T_{amb}.
2: **Calculate** P_N^*, G_N, η_N^*
3: **Determine** the system temperature coefficient of power γ_{syst}; remove data for days with average T_o<3 °C.
4: **Calculate** η_N^* using γ_{syst} and ΔT_{STC}.
5: **Determine** coefficients k_1, k_2 for minimal SSE.
6: **return** Model coefficients $k_1 = k_{1,fit}$, $k_2 = k_{2,fit}$, $k_3 = \gamma_{syst}$, $k_4 = k_1 \cdot \gamma_{syst}$ and $k_5 = k_2 \cdot \gamma_{syst}$; $k_6 = 0$.

The resulting averaged values for the fitted and calculated coefficients are given in Table 5.3, and contrasted with the averaged values from Huld *et al.* Purely as a numeric comparison, the fitted values of this work are larger in magnitude (more negative) for the coefficients k_1, k_3 and k_4, whereas k_2 is smaller in

magnitude and k_5 shows the effect of γ_{syst}: k_5 is smaller than given by Huld *et al* for the MWT modules, and larger for the standard mono-crystalline *Smart PV* modules.

To an extent, a likely explanation for the different values for the data from Huld *et al* is the difference in measurement equipment and calculation methods employed: the data for the model of Huld *et al* is obtained from I-V curves and weather measurements including module temperatures, whereas the methodology of this work uses monitored power data from modules connected to DC-DC converters and DC-AC inverters, as well as weather measurements including module temperatures. As such, the influence of the MPP tracking algorithms of the power electronic equipment of this work may play a role, on top of the module technologies, mounting methods and measurement equipment used.

Nevertheless, the methodology shown here allows the model and coefficients of Huld *et al* to be obtained using a different approach, which can be applied for monitored installations which have access to four measured parameters: the power (DC or AC) of a module or array, the (preferably) plane-of-array reference cell irradiance G, the cell temperature T_C and the ambient temperature T_{amb}. Better results are obtained at a higher level of granularity: module-level power and temperature give better results than array-total power and array-average or array-representative temperature, yet the approach works for both cases.

Table 5.3: Comparison of averaged DC module-level coefficients for the model of Huld *et al* and its modified form (this work).

Parameter	Huld *et al*[a]	This work (all)	This work (MWT)	Symbolic equivalent
k_1 [-]	$-0.017\,24$	$-0.068\,95$	$-0.048\,60$	$k_{1,fit}$
k_2 [-]	$-0.040\,47$	$-0.034\,89$	$-0.026\,18$	$k_{2,fit}$
k_3 [°C^{-1}]	-0.0047	-0.0059	-0.0053	γ_{syst}
k_4 [°C^{-1}]	$1.49 \cdot 10^{-4}$	$3.23 \cdot 10^{-4}$	$2.28 \cdot 10^{-4}$	$\gamma_{syst} \cdot k_{1,fit}$
k_5 [°C^{-1}]	$1.47 \cdot 10^{-4}$	$2.28 \cdot 10^{-4}$	$1.76 \cdot 10^{-4}$	$\gamma_{syst} \cdot k_{2,fit}$
k_6 [°C^{-2}]	$5 \cdot 10^{-6}$	0	0	-

[a] The data is from [13], albeit with the correction that the numbers are expressed with the exponent 10^{-4} and not 110^{-4} for k_5 and k_6. Coefficients are slightly different for [124], which was published earlier.
[b] 4 MWT modules: *PV054, PV055, PV060, PV061*, 9 mc-Si modules: *PV051, PV052, PV053, PV056-PV058, PV062, PV063*. See also Figure 2.6 and tables 2.1 and 5.2.
[c] April-May model fitting data.

The MWT modules' coefficients are smaller in magnitude than the average[22] of all modules - their model-fitted values are closer to the ideal than the mono-

[22] Which also includes the values of the MWT modules.

crystalline modules. Ideal is understood here to scale fully linearly to the irradiance and be largely insensitive to temperature deviations from STC, so that $k_1 = k_2 = k_4 = k_5 = k_6 = 0$ and only $k_3 = \gamma_{syst}$ remains. The equation for η_N would then reduce to

$$\eta_{N,ideal} = 1 + k_3 \cdot \Delta T_{STC} = 1 + \gamma_{syst} \cdot \Delta T_{STC}. \tag{5.21}$$

Two modules can thus be compared according to the fitted coefficients obtained, with the module whose values are consistently closer to the ideal values more likely to have a better performance. This performance must still be verified or modelled for the conditions where the module or system will be used. For example, a module with an anticipated poor low-light performance may be better than another, if it is used in a high-irradiance region.

One benefit of the approach outlined here is that it may be possible to transpose model data from one region to another. For example, the temperature-corrected data and model coefficients from modules measured in one region (e.g. Belgium) may then be used for another region (e.g. Spain), if local temperature data is available from measurements or other models. This will likely not be error-free[23], yet it may be an avenue for further research (see also Section 5.9.2).

5.6 Model validation

5.6.1 Introduction

The formulation of Equations (5.1), (5.2) and (5.7) allows the fitted model coefficients for the normalised efficiency to be used to calculate the normalised power P_N and a range of values of interest, such as the modelled versus measured energy and the daily Performance Ratio PR.

In Section 5.5.2 the data was described to be split up into a training and a validation data set. In this section, the validation of the modelled coefficients is displayed using the remaining data for June to August, and compared to the baseline - the model of Huld *et al.* (A longer period for the training and validation data sets, e.g. January-June for training and July-December for validation will likely result in different coefficient values. However, as shown in this section, the reduced period of time used does allow well-fitted coefficients to be determined.) As an additional comparison, the model of Hunt *et al* is also calculated from the temperature-corrected form, and then using the

[23] E.g. there may be local spectral effects not taken into account, or different mounting conditions.

measured temperature data for the temperature correction (from P^* to P using Equation (5.18)). Coincidentally, this also shows how measured and modelled data can be brought together, depending on data quality and availability.

With the model of the normalised efficiency η_N and its coefficients fitted, the comparisons and model validations can be performed on the total energy over the period, the daily PR and the power.

5.6.2 Total Energy

The total energy modelled in a period is a straightforward value to compare, which can highlight some trends (e.g. a sustained under- or over-estimation of power and energy), although other trends may be masked, as some errors may compensate each other over time.

The top subplot of Figure 5.14 shows the regular modelled and measured values of the normalised energy for the months of June to August. The bottom subplot shows the model errors versus the measured data, and the expanded uncertainty of energy U_E for the period shown. When an error bar exceeds the U_E limits, that indicates that that value is erroneous and one or more of the model coefficients should be re-fitted.

Table 5.4: Comparison of number of module or system models with modelled energy within expanded uncertainty of energy measurement limits, as shown in Figure 5.14.

	Huld *et al*	Huld *et al* with T_{corr}	This work
Within U_E limits (abs)	4/21 (3/20)	7/21 (6/20)	21/21 (20/20)
Within U_E limits (rel)	19 % (17 %)	33 % (33 %)	100 % (100 %)

[a] ABB/*PV052* AC *relative* U_E: ±31 %/kW_p - so very broad limits: values between parentheses denote removal of this data.

[b] T_{corr} is measured & calculated data: $1 + \underbrace{\gamma_{syst}}_{calculated} \cdot \underbrace{\Delta T_{STC}}_{measured}$.

[c] U_E: modules (DC) ±2.4 % to ±2.5 %, DC-DC converters ±3.7 %, SolarEdge ±2.5 %(DC), ±2.6 %(AC), Sungrow: ±6.6 %(DC), ±6.0 % (AC).

Table 5.4 gives the summary of the different model errors shown in Figure 5.14, and whether these errors are within the expanded uncertainty of energy measurement limits. From both Table 5.4 and Figure 5.14, it is clear that the module and system performance are generally better modelled using the methodology of this text. The temperature correction using T_{corr} also brings some improvements (in some cases) compared to the coefficients of the

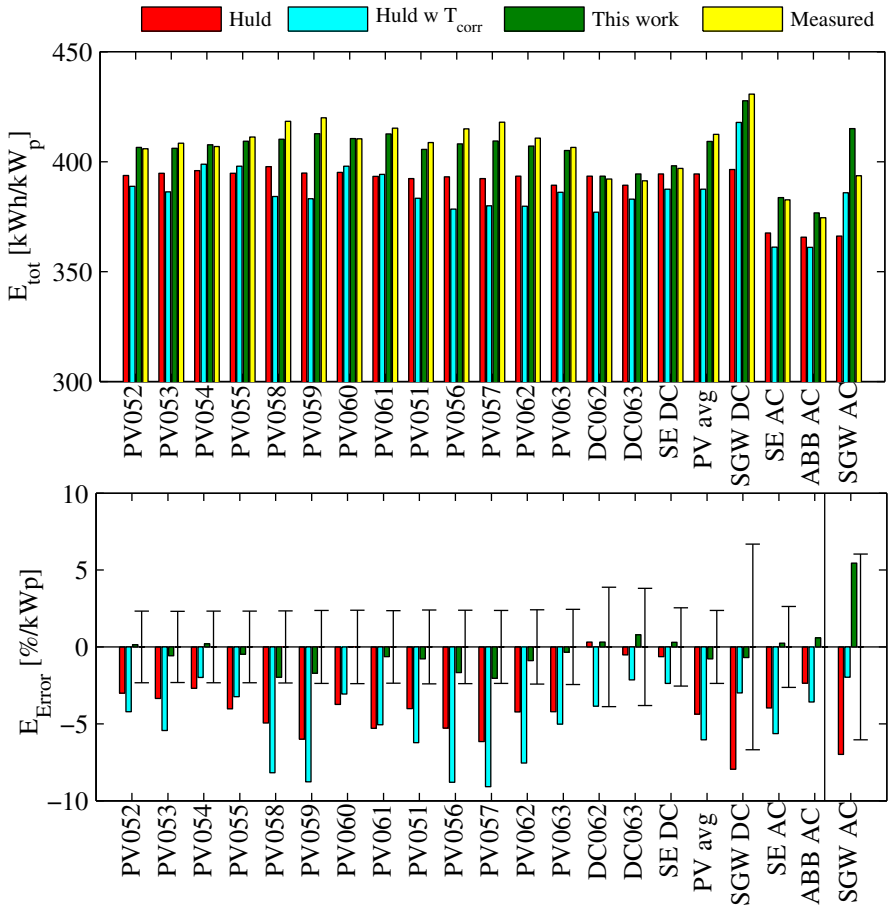

Figure 5.14: Total DC and AC energy production comparison for June to August, models versus measurements. Error bars are the relative measurement expanded uncertainty of energy (U_E) for the period shown.

temperature-corrected model of Huld *et al*, which highlights the applicability of the method described above.

5.6.3 Daily Performance Ratio

The Performance Ratio is the industry-standard by which the energetic performance of photovoltaic systems is evaluated. Thus, comparing the daily

measured and modelled values of the PR may highlight strengths and weaknesses of each model.

The models can be compared to the measurements per day, and then per module or system. As the amount of figures that can be generated is very large[24], the daily PR for module *PV54* is depicted for 9 to 31 July 2015. *PV054* was chosen as it is one where two of the models are within the energy uncertainty limits, with one over-estimation (this work) and two under-estimations, of which one beyond the measurement uncertainty limits. This can then point to areas of improvement, or show effects in a more pronounced manner than with the less error-prone models.

Comparing Figure 5.15 to Figure 5.14, the fitted model of this work appears to be generally better at predicting the PR than the two versions of the model of Huld *et al*, in particular for low irradiation days. On high irradiation days (e.g. 9-11, 16, 18, 29 and 31 July), the full model of Huld *et al* gives a similar error to the fitted model. The days where the average of ΔT_{STC} is close to zero or negative give the highest errors for the full model of Huld *et al*, and the fitted model generally performs better on those occasions.

The measurement uncertainty of the irradiance and irradiation has a strong impact on the expanded uncertainty of the PR (U_{PR}), shown in Figure 5.15 as the average of daily relative values. As the irradiance and the power (and by subsequent integration of both to energy and irradiation) are strongly correlated, their combined measurement uncertainties add up[25] (see Section 3.3.4). As a result, many of the modelled errors of the PR in Figure 5.15 are still within the limits of U_{PR}, although the trend does point to the fitted model behaving better in general than the two versions of the model of Huld *et al*, for module *PV054*.

Further evaluating the daily PR for an AC system (as an additional example of how the methodology can be applied), the SolarEdge system was chosen for analysis. In this case, Figure 5.14 suggested that the fitted model should be better than the model variants of Huld *et al*. Whether this conclusion also reappears for the daily PR is evaluated below.

Contrasting Figure 5.16 with Figures 5.14 and 5.15 shows the daily AC PR to be overestimated for the fitted model on a daily basis, yet the cumulative energy error (or the average PR for the period) is almost nil. On the other hand, the full model of Huld *et al* tends to have lower errors for the daily AC PR than

[24] 21 systems: 18 DC, 3 AC, 3 models plus the measurements as reference times the number of days.

[25] In reality, Equation (3.17) must still be applied, but it is a good approximation for this description.

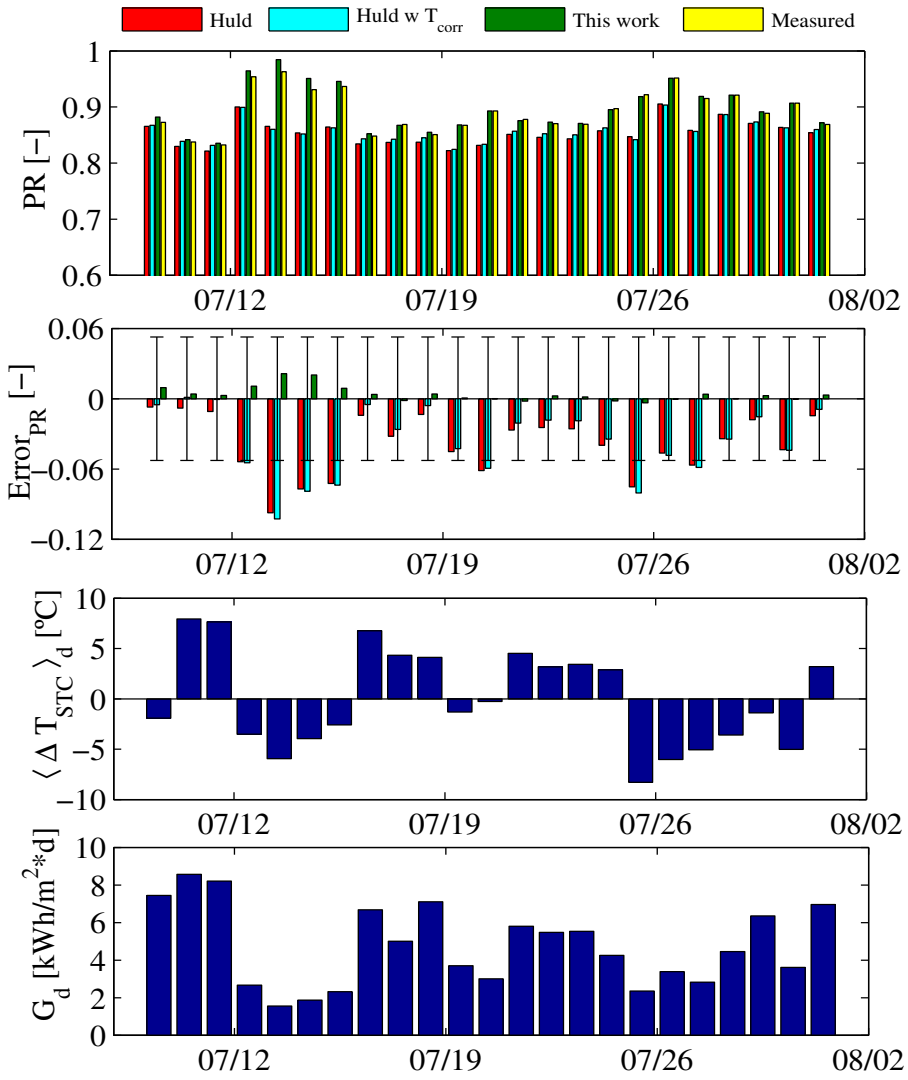

Figure 5.15: Daily PR comparison for module *PV054* for 9-31 July 2015, models versus measurements. Error bars are the averaged relative measurement expanded uncertainty of the PR (U_{PR}) for the period shown.

the fitted model, and yet the total energy was underestimated by 4.1 %/kW_p, exceeding the limits of the energy measurement uncertainty.

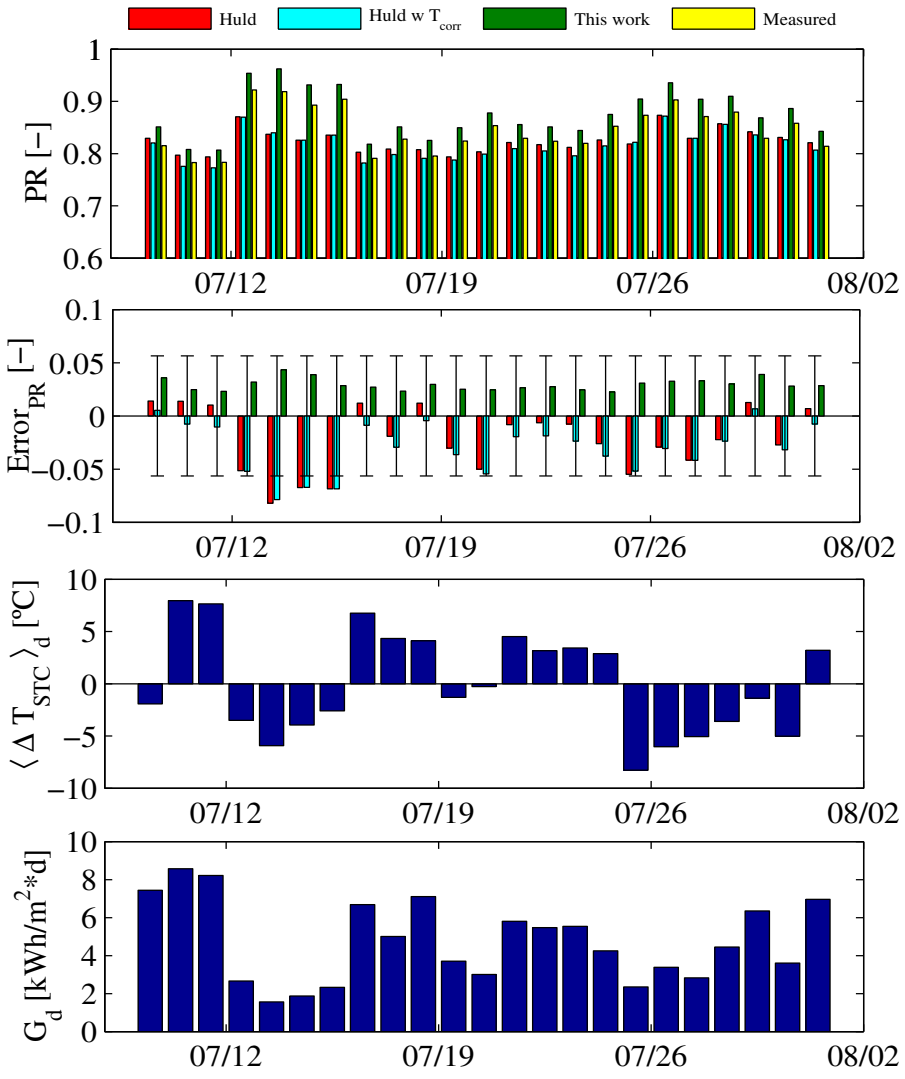

Figure 5.16: Daily AC PR comparison for the SolarEdge inverter for 9-31 July, models versus measurements. Error bars are the averaged relative measurement expanded uncertainty of the PR (U_{PR}) for the period shown.

Regardless, the full model of Huld *et al* shows smaller errors for the daily AC PR than the fitted model, in particular for the high-irradiation days. For low-irradiation days, the errors of the full model of Huld *et al* approach the

uncertainty limits, and consistently under-estimate the performance on these days. This may provide a partial explanation as to the longer-term energy underestimation by their model. The consistent trend (overestimating) shown by the model of this work for the AC SolarEdge data suggests that there is room for improvement, e.g. by re-evaluating the modelled coefficients, or the measured[26] DC-AC conversion efficiency (as done in this work) or data sheet value.

In both cases for the daily AC PR, the fitted model and the full model of Huld *et al* are mostly within the limits of the averaged expanded uncertainty of the PR, for the period of 9-31 July, compared to the total energy production calculated for June to August. As such, comparing models whose errors appear to be within the uncertainty limits on a daily basis (and thus "indistinguishable" from an uncertainty perspective) may have hidden trends, which then show up over longer (Section 5.6.4), or much shorter (Section 5.6.5), time periods.

5.6.4 Longer-term evaluation of the PR and its errors

The previous section illustrated how the modelled PR can vary from day to day, and occasionally not in the same manner as the measured PR. For longer-term evaluations of the modelled and measured PR, these results must be analysed differently. To do this, the mean value of the modelled and measured PR will be compared, with the variation around the mean. To evaluate the errors of the models, their mean value and standard deviation are also compared.

The spread in the modelled or measured PR is calculated as the standard deviation for the considered period[27], as in Equation (5.22). It indicates the variability of the PR, similar to the variation in the measured PR over the same period. The errors of the modelled PR are also compared for their trend (the mean) and variation (the standard deviation) over time. The standard deviation of the error of modelled PR is calculated using Equation (5.23)

$$\sigma_{PR} = \sigma(PR) \tag{5.22}$$

$$\sigma_{\Delta PR} = \sigma(PR_{model,d} - PR_{meas,d}). \tag{5.23}$$

Figure 5.17 is the comparison of the averaged PR with the spread (standard deviation) of values, together with the mean error and spread of the error. It is shown for the validation period of June to August for the 13 modules

[26] One possible explanation is the effect of the combined measurement uncertainty: the correct determination of the DC-AC conversion efficiency depends on the measurement uncertainty on the DC side *and* the AC side of the inverter.

[27] The number of valid, error-free days in June to August.

measured individually, whereas Figure 5.18 is the same comparison for the power electronic devices, on DC and AC sides.

The amount of model results shown in Figures 5.17 and 5.18 which are within the measurement uncertainty limits are summarised in Table 5.5.

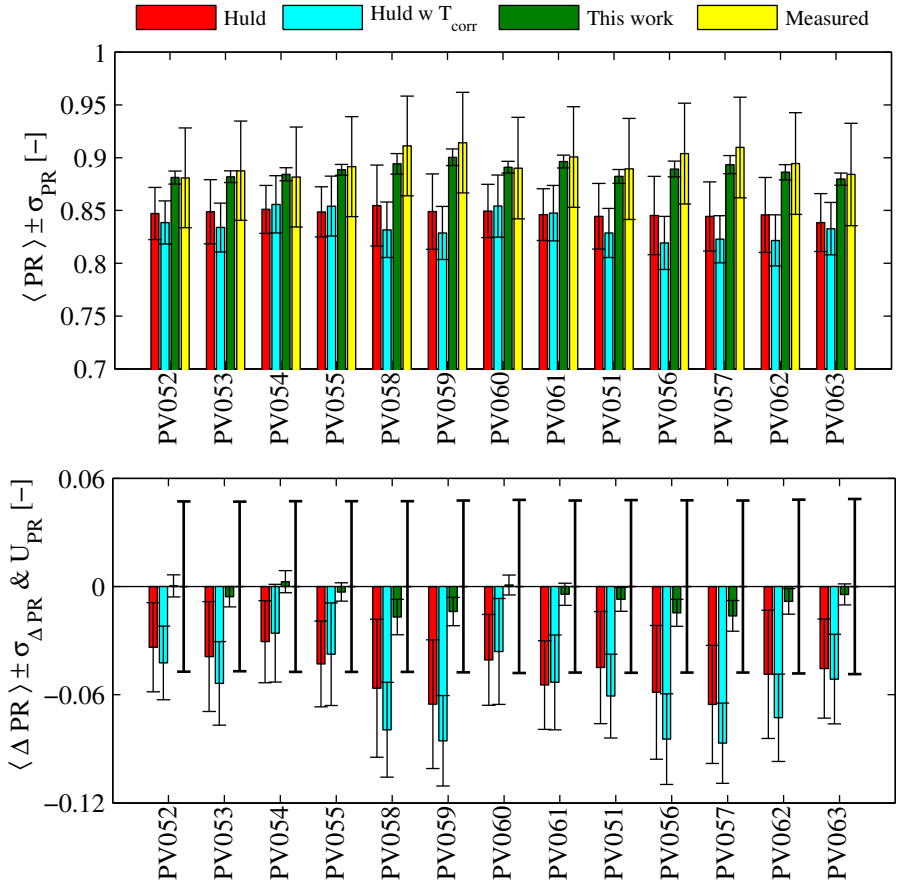

Figure 5.17: PR comparison of models for modules: average daily PR and standard deviation, and mean error and standard deviation of the error for June-August 2015. Thick error bars in bottom subplot are the relative measurement expanded uncertainty of the PR (U_{PR}) for the period shown.

Table 5.6 and Figures 5.17 and 5.18 show that, in general, the model of Huld *et al* underestimates the daily PR. In conjunction with Figures 5.14 to 5.16, this suggests that it consistently and most strongly underestimates performance

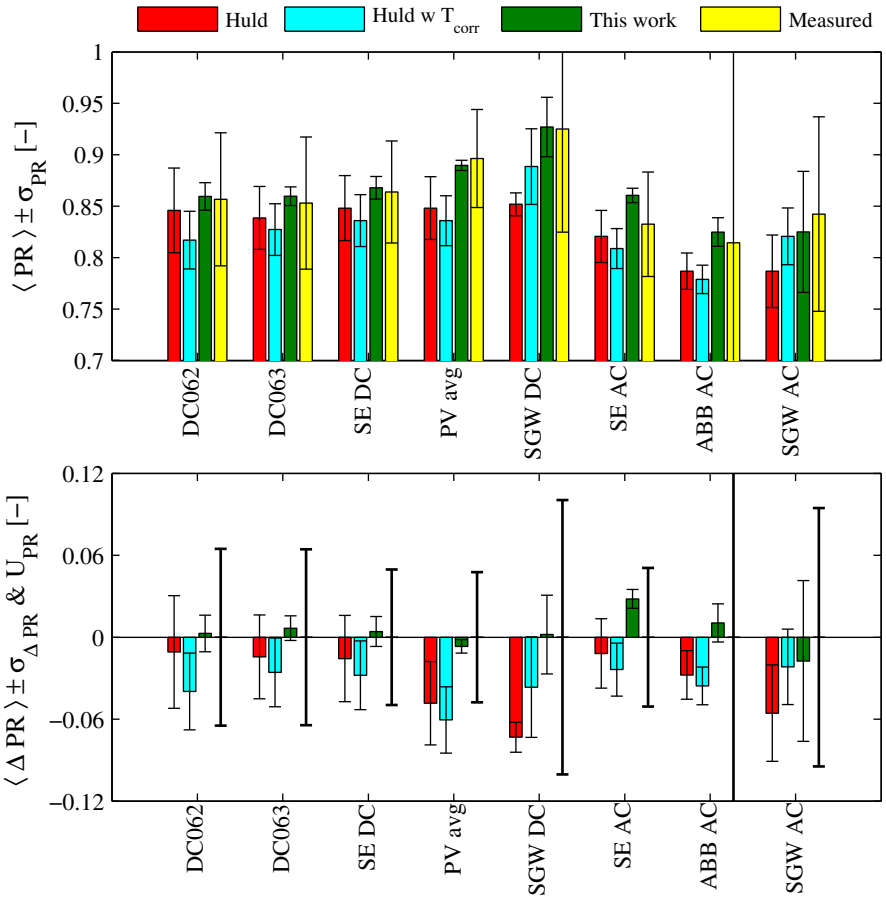

Figure 5.18: PR comparison of models for systems: average daily PR and standard deviation, and mean error and standard deviation of the error for June-August 2015. Thick error bars in bottom subplot are the relative measurement expanded uncertainty of the PR (U_{PR}) for the period shown.

on low irradiation days, which on aggregate result in an underestimated total energy yield.

For the modified or "mixed" model of Huld *et al* (i.e. coefficients k_1 and k_2 from Huld *et al* and measured T_{corr} data), the picture is diverse, with some total energy predictions better than the regular model (e.g. modules *PV054 & PV055*). The average modelled PR shows a similar trend to the total energy. The worst predictions happen with the modules and systems whose value of

Table 5.5: Comparison of number of module or system model results with modelled Performance Ratio within expanded uncertainty of the PR measurement limits, as shown in Figures 5.17 and 5.18.

	Huld *et al*	Huld *et al* with T_{corr}	This work
Within U_{PR} limits (abs)	21/21 (6/20)	16/21 (4/20)	21/21 (20/20)
Within U_{PR} limits (rel)	100 % (30 %)	76 % (20 %)	100 % (100 %)

[a] Values between parentheses: assume maximum error ($|\Delta PR| + \sigma_{\Delta PR}$) and removal of ABB AC data.
[b] U_{PR}: modules (DC) ±4.7 % to ±4.9 %, DC-DC converters ±6.4 % to ±6.5 %,ABB/PV052: ±4.7 % (DC), ±38.5 % (AC), SolarEdge ±5.0 %(DC), ±5.1 %(AC), Sungrow: ±10 %(DC), ±9.5 % (AC).

γ_{syst} shows the largest deviations from the datasheet value (see Table 5.2), such as modules *PV058 & PV059*.

This suggests that the "mixed" model of Huld *et al* could possibly perform better, if using datasheet values of γ. This is discussed further in Section 5.9.3.

From the above figures and tables, the model of this work with the fitted coefficients appears to be better than those of Huld *et al*, although the AC data appears to be overestimated. In the case of the SolarEdge data in Figure 5.16, the model appears to consistently overestimate the daily PR by ∼3 pp, and yet the total modelled energy production is off by only 0.25 %.

The measurement uncertainty associated with the above analyses is not negligible, and is further discussed in Section 5.7.

From Figures 5.17 and 5.18 and Table 5.6, it appears that the fitted model of this work has a smaller value of the PR error standard deviation ($\sigma_{\Delta PR}$) than either form of the model of Huld *et al*. While the evidence seen so far suggests that the fitted model of this work performs as well or better than that of Huld *et al*, one more test can be applied: comparing the normalised efficiency or the normalised power for one or more days. This is done in Section 5.6.5.

Table 5.6: Mean and standard deviation of model daily PR errors for June-August 2015.

Identifier	Huld		Huld w T_{corr}		This work	
	$\langle \Delta PR_d \rangle$ [pp]	$\sigma_{\Delta PRd}$ [pp]	$\langle \Delta PR_d \rangle$ [pp]	$\sigma_{\Delta PRd}$ [pp]	$\langle \Delta PR_d \rangle$ [pp]	$\sigma_{\Delta PRd}$ [pp]
PV052	−3.4	2.5	−4.3	2.1	+0.1	0.7
PV053	−3.9	3.1	−5.4	2.4	−0.6	0.6
PV054	−3.1	2.3	−2.6	2.8	+0.3	0.7
PV055	−4.3	2.4	−3.8	2.9	−0.4	0.6
PV058	−5.7	3.9	−8.0	2.7	−1.7	1.0
PV059	−6.6	3.6	−8.6	2.6	−1.4	0.8
PV060	−4.1	2.6	−3.7	3.0	+0.1	0.6
PV061	−5.5	2.5	−5.4	2.7	−0.5	0.7
PV051	−4.5	3.2	−6.1	2.4	−0.8	0.7
PV056	−5.9	3.8	−8.5	2.6	−1.5	0.8
PV057	−6.6	3.3	−8.7	2.3	−1.7	0.9
PV062	−4.9	3.6	−7.3	2.5	−0.9	0.8
PV063	−4.6	2.8	−5.2	2.5	−0.5	0.6
DC062	−1.1	4.2	−4.0	2.9	+0.7	1.0
DC063	−1.5	3.1	−2.6	2.6	+0.5	1.0
SE DC	−1.6	3.2	−2.8	2.6	+0.5	1.1
SE PV avg	−4.9	3.1	−6.1	2.5	−0.7	0.5
SGW DC	−7.4	1.2	−3.7	3.7	+0.2	2.9
SE AC	−1.2	2.6	−2.4	2.0	+2.7	0.7
ABB AC	−2.8	1.8	−3.6	1.4	−1.7	1.4
SGW AC	−5.6	3.6	−2.2	2.8	−1.8	5.9

5.6.5 Time series evaluation of the normalised efficiency and power

Comparing the model outputs for both the normalised efficiency and the normalised power in Figure 5.19, the fitted model generally appears to better follow the measured values, than the model forms of Huld *et al.* To an extent this is a logical and expected result, as the model of Huld *et al* was developed using other modules, and that conversely, a worse performance of the fitted model would indicate that the fitted coefficients were poorly chosen.

While not very easy to see on Figure 5.19 (it is an overview figure), the two

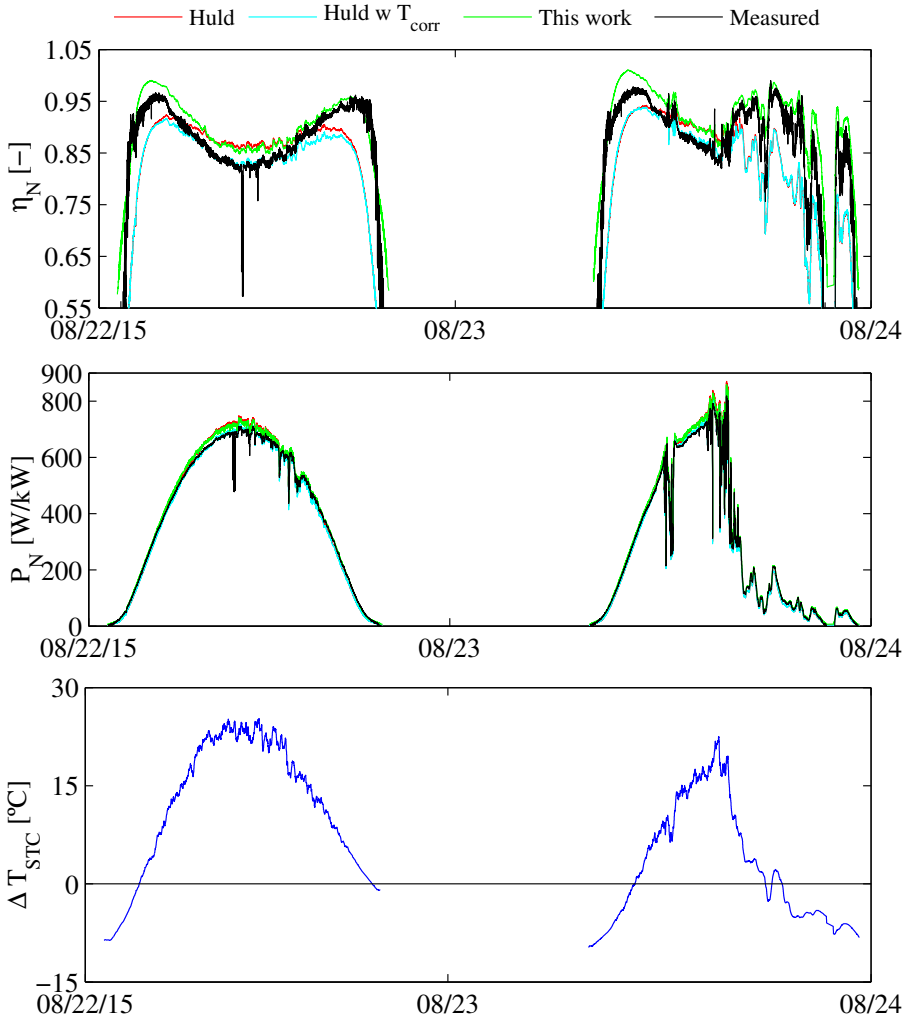

Figure 5.19: Comparison of models for AC side of SolarEdge inverter: η_N, P_N and measured ΔT_{STC} on 22 and 23 August 2015. The dip in the *measured* η_N and P_N on 22 August around 13h is measurement of I-V curves (see also Figure 2.12).

formulations of the model of Huld *et al* are generally quite close to each other, with the model as described in [13, 124] showing a response that is less temperature-sensitive. This effect is best observed around noon for the data of 22 August. The temperature response of the Huld *et al* normalised efficiency, which depends on the coefficients k_3 to k_6 (as shown in Table 5.3) could indeed

be expected to be less sensitive to module temperature than measured.

The irradiance response of the two model formulations of Huld *et al* are easier to identify, as they drop off faster for low irradiance than the measured data, and the fitted model of this work. Similarly, the much smaller magnitude of the coefficient k_1 than the values obtained from fitting explains why the modelled normalised efficiency η_N drops off faster for low irradiance: this may contrasted with Figure 5.12, which highlights the impact of the coefficient k_1 on the low irradiance response.

Combined with the knowledge from Table 5.3 and sections 5.6.2 and 5.6.3, it is now possible to conclude that the model formulations of Huld *et al* underestimate the low light performance (the higher uncertainty for low irradiance was also remarked by the authors in [13]), which is mostly due to the coefficient k_1 being too small in magnitude (-0.017 versus this work: -0.069 and -0.049), and similarly the (temperature) coefficient k_3.

The fitted model overestimates the (very) low light performance, which can be noticed in the morning periods in Figure 5.19, and after 18h on 23 August, when the heavy rain reduced the irradiance to $\sim$5 W/m^2 to 15 W/m^2, with the inverter temporarily shutting down[28]. By contrast, the fitted model predicted a value of the η_N of $\sim$60 % (and the models of Huld *et al* a more correct value of $\sim$25 %). However, the impact of errors for the irradiance below $\sim$30 W/m^2 on the measured and modelled total energy production is limited, as seen in the total energy, and the weighting of values using the SSE.

Figure 5.19 shows how the modelled and measured normalised power of the AC side of the SolarEdge inverter appear to lie quite close to each other, whereas the differences for the normalised efficiency are more pronounced. This reinforces the argument made in Section 5.4.1, that the normalised efficiency allows the performance of different systems (or models) to be compared, with more pronounced differences among the models than displaying the (normalised) power. Displaying both types of graphs on the same figure then allows a fast back-and-forth evaluation, depending on which question must be answered.

For example, the effect of the increase in temperature above T_{STC} (i.e. that the value of ΔT_{STC} is > 0) is better identified[29] in the top subplot of Figure 5.19.

Similarly, the relative power loss due to the I-V curves being measured on 22 August (as discussed in Section 2.7) resulted in a maximum dip of approximately 25 pp of the normalised efficiency, which, together with the temperature effects[30],

[28] This is not shown, in order to better see the more important high-irradiance behaviour.

[29] Q: How much is the efficiency drop due to temperature from the zero line crossing in the morning to the peak temperature on 22 August? A: From $\sim$95.5 % to $\sim$82.7 %: 12.8 pp.

[30] $\Delta\eta_N^* = \frac{\sim 0.25}{0.827} \simeq 0.31 \simeq 33\,\%$ - values read off the graph.

equal the power loss of four out of the twelve modules connected to the SolarEdge inverter (when four modules were selected for I-V curve measurement).

For other questions (e.g. "How much power is lost due to that building crane nearby?") the normalised power or nameplate power may help to express this answer faster. Cycling between the metrics is possible, as the normalised power can be calculated from the normalised efficiency, and then on to the nameplate or absolute power of the system considered, as shown in this chapter. This again indicates that the metrics and methods of this chapter can be used for many possible applications, yet as tools must be used judiciously, with the appropriate tool selected for the intended application.

In summary, the fitted model for the modules and systems considered in this text appears to generally perform better than the original or temperature-corrected forms of the model of Huld *et al.* This has been seen using the examples of the total energy calculated over three months, as well as the daily PR and the time series evaluation of the normalised efficiency and normalised power.

The applicability of the fitted model is higher and broader than the original model and measurement need of Huld *et al*: the measurement equipment needs for the fitted normalised efficiency model may be much less stringent than those associated with the long-term measurement of multiple I-V curves. In particular, the approach outlined here may be applied to any photovoltaic system which measures the irradiance, module and ambient temperature and the power of the system. As such, owners and users of monitored photovoltaic systems have an additional tool with which to verify system performance, and even compare the evolution of the modelled PR to the measured PR over time.

5.7 Importance of measurement uncertainty

Figure 5.17 highlights one of the most important issues for the monitoring of photovoltaic systems: measurement uncertainty. While the models discussed are generally close to the measured values, the expanded uncertainty of the PR is unfortunately so large that the models are indistinguishable from each other from an uncertainty perspective. To an extent, when comparing models to measurements, this can be "solved" by focusing on the power and energy production, as their respective expanded uncertainty is lower and differences among models or between models and measurements can come to the fore.

The issue for a customer who has invested (or is looking to invest) in a photovoltaic system is evaluating whether the system is performing as promised, or the extent that it deviates from projections. As Figure 5.17 shows, the

measurement uncertainty can be large (and this is assuming a properly maintained measurement set-up, not to mention faulty sensors), whereas the *model* uncertainty is rarely known, disclosed or discussed. Using the PR to evaluate performance compliance is thus subject to large uncertainties. From an intellectual complexity perspective, it is fully understandable that, given the large uncertainties, the *trend* of the PR is evaluated and that the uncertainties are (temporarily) ignored. The larger uncertainty limits of the PR reduces its discriminatory power - the ability to distinguish good from excellent or poor performance.

Why is this so important?

Bankability, feasibility, due diligence and pre-installation modelling depart from a range of characteristic values (e.g. the modules' P_{STC}, temperature coefficient of power γ, the inverters' efficiency, ...) and measured or assumed climatic conditions (irradiance and irradiation, ambient temperature, wind speed and direction, humidity, ...) and a photovoltaic performance model to predict or verify the performance of the system under consideration.

While a large number of contract modalities exist, one option has the system built and sold by a company, who is responsible (gives a performance warranty) for the first two years of operation of the system, after which the installation is handed over to the owner. The contracts typically specify a required value of the PR to be reached, either as an annual value or "Y % of the time, the daily PR must be above X %".

Yet, as Figure 5.17 shows, the uncertainty limits around the instrument-indicated (i.e. measured) values of the PR are quite large ($\sim \pm 5\,\%$). The monetary difference between a system which has a true initial PR of 81 % or 80 % is large, especially as the system's technical and financial lifetime spans decades - the differences cumulate over time. However, the difference between a *modelled* pre-installation value PR of 81 % or 80 % falls within the uncertainty limits of the PR determination.

As a consequence, depending on who performs the modelling and for whom, assumptions may be taken so that the modelled PR is higher or lower, with the possibility of large financial consequences, from the financing terms being more lenient to stringent, to a discrepancy between the modelled (and thus paid for) performance and the actual performance. A company aiming to finance a PV installation may approach the financier with a higher value of the modelled PR than the company hired by the financing institution to do the due diligence, yet both values will very likely be within the PR measurement uncertainty limits.

As much of this work has shown, the performance of photovoltaic modules and systems is subject to a large amount of technical and climatic variables ,

each with a varying degree of importance on the final result (which differs from installation to installation). For modelling as well as performance assessment, this also means that there are many variables that can be taken into account, and assumptions that can be made.

That these assumptions can play an important role was highlighted a.o. by [161], where professionals using the same software and base information (irradiance, array information) had modelled differences in predicted energy yield of up to $\pm 15\,\%$ from the control (what was actually measured). There is thus a need for additional transparency and disclosure of model assumptions, so that these may be objectively[31] evaluated and discussed. Otherwise, the risk exists that two experts tasked with performance analysis or prediction of a system may come to diverging conclusions, leaving the parties who paid for the evaluations none the wiser.

While the above points may give the impression that the PR suffers from weak discriminatory power due to the relatively large uncertainties, this is not the intended message. Rather, it is an argument against the indiscriminate use of the long-term computed value of the PR (or most other long-term values which are added or averaged over the total interval): as shown above, the calculation of the total energy or irradiation may lead to errors being masked.

Thus, Equation (5.24) is proposed as an alternative method to calculate the long-term value of the PR (which may be contrasted with the traditional definition of Equation (5.5)).

$$PR_y = \langle PR_d \rangle_y = \frac{\sum_1^{365} PR_d}{365}. \tag{5.24}$$

By then also calculating the standard deviation of the daily PR over the period considered, the variability around the mean computed value can be evaluated (as shown above in Section 5.6.4), which can then be combined to form a much more meaningful metric for a.o. inter-system comparisons (e.g. two PV systems in a similar geographic region).

Similarly, if two models present a similar PR value, then their respective standard deviations may indicate aspects which are otherwise hidden. For instance, a larger value in the standard deviation of the daily PR may point to model errors which cancel each other out, or it may highlight that the modelling follows the weather profile quite well and that counter-intuitively, the model with *smaller* standard deviation has certain assumptions which may be subject to discussion.

[31] In part, the work of IEA PVPS Task 13 is aimed at bringing best practices - e.g. modelling assumptions to be disclosed - to this field.

In this regard, the use of the temperature-corrected Performance Ratio may also be a complementary approach to the above, as its behaviour over time is (or should be) insensitive to variations in ambient and module temperature. In particular, the standard deviation of the measured PR* is much lower than the regular PR, as seen in Figure 5.11. (The daily averaged values of the η_N and η_N^* may be evaluated in a similar manner.)

Much more can be discussed about the choices for evaluation periods (days, months, years?), as well as model transparency and comparisons, of which a few suggestions are given in Section 6.4.

5.8 Quantifying energy losses due to shading

While interesting to detect shading or other effects on a photovoltaic installation, the economic impact of this effect must be quantified, in order to make an informed judgement on taking action to address the cause, or not. Moreover, quantifying these losses may indicate whether it is beneficial to opt for more complex[32] and likely more expensive photovoltaic modules, if partial shading can be anticipated, such as in the built environment.

For instance, if shading is detected or known, such as for the measurement set-up of this work, how much energy that *could* have been generated has been lost? To quantify the losses due to shading, the models calculate the energy from[33] 1 September 2015, the approximate start of the shading due to the poles being installed on the campus.

Figures 4.1 and 5.7, as well as the descriptions in this chapter indicate that the front row of the *Smart PV* array (modules *PV057-PV062*) are subject to the most shading from the poles. Of these, the cumulative normalised energy yield for modules *PV057–PV062* is compared to the reference (*PV052*) in Figure 5.20. Figure 5.20 thus shows how the modules' measured performance was consistently better than the reference, and how these trends are impacted by the amount of shading received per module.

As can be observed in Figure 5.20, the two model formulations of Huld *et al* estimate that the modules will perform worse than they do in reality, even with shading. The likely explanation for this is the models' poorer low-light performance (as shown in Figure 5.19) compared to measured performance. As from September onwards the amount of time with lower irradiance values

[32] A module with 10 substrings with associated bypasses for 6 cells each versus the simpler and currently standard 3 bypass elements for substrings of 20 cells.

[33] All models start from the measured energy at the end of August.

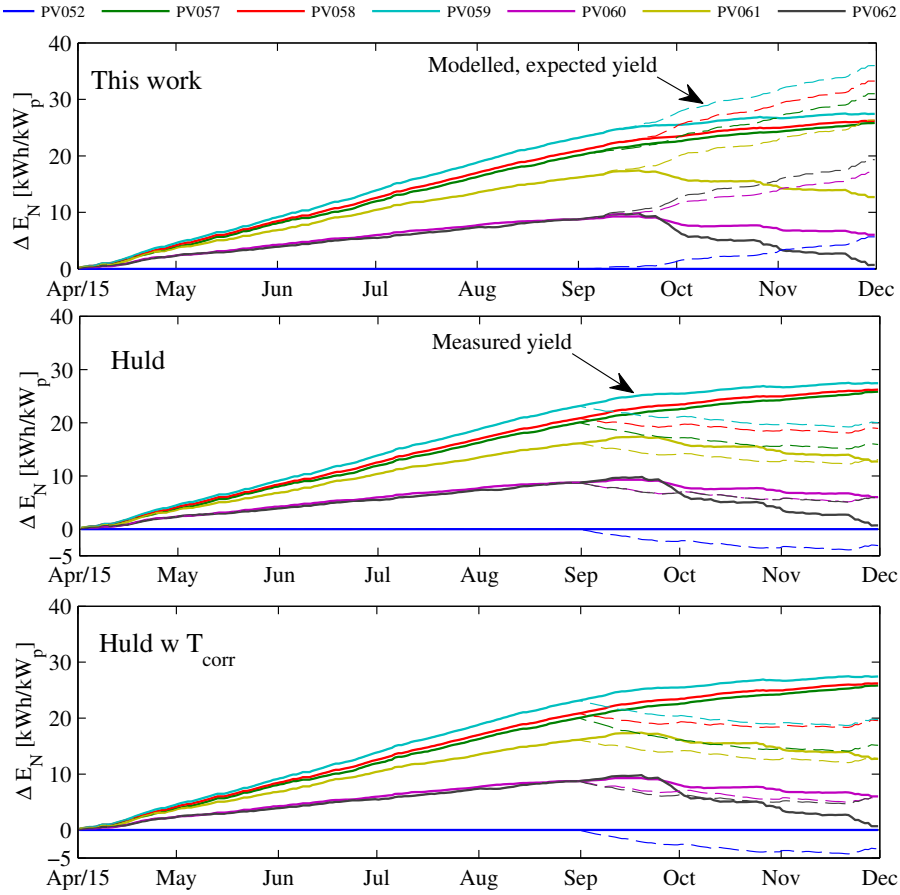

Figure 5.20: Energy yield difference to reference module, comparison of measured and modelled energy values, April-November 2015. Solid lines: measured data, marked lines: modelled (this work). Start of modelled data: 1 September. Measured cumulative production for *PV052* for period shown: 831 kWh/kW$_\mathrm{p}$. G_τ: 944.1 kWh/m^2.

becomes larger, the low light errors become more pronounced. However, as the two forms of the model by Huld *et al* predict the performance to be worse than measured (even with shading), they are not retained for further analyses.

By contrast, the model coefficients of this work result in modelled values which continue the expected trends: e.g. module *PV054* was performing better than the reference for April-August. It is reasonable to expect this trend to continue in the subsequent months, in the case of no shading. However, even with (limited)

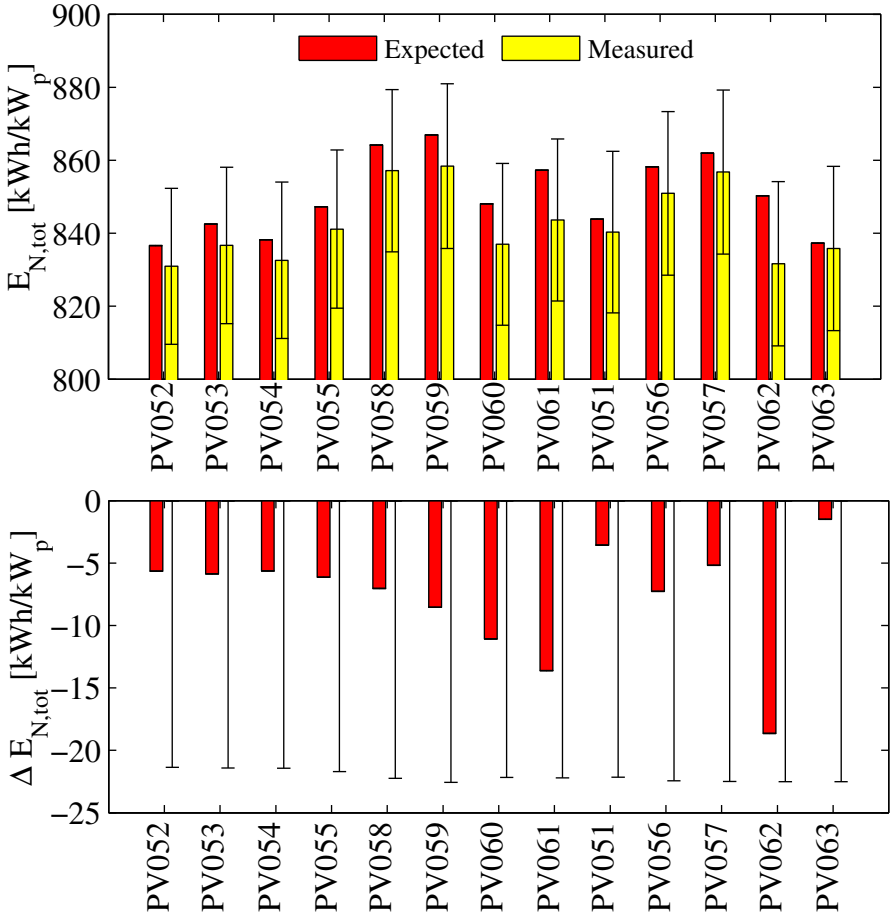

Figure 5.21: Total energy comparison of measured and expected (modelled) yield of individual modules, April-November 2015. G_τ: 944.1 kWh/m^2.

shading, the performance of modules *PV054* and *PV059* can be expected to have remained comparatively better than that of *PV052*. The effect of shading is most pronounced for module *PV062*: most of the previous energetic gains the module had made compared to *PV052* (which is subject to less shading) were wiped out in the course of the months of September-November.

By then comparing the expected - i.e. modelled - total energy production for the modules to the measured values, the normalised energy losses due to shading can be quantified for each module. This is shown in Figure 5.21. As

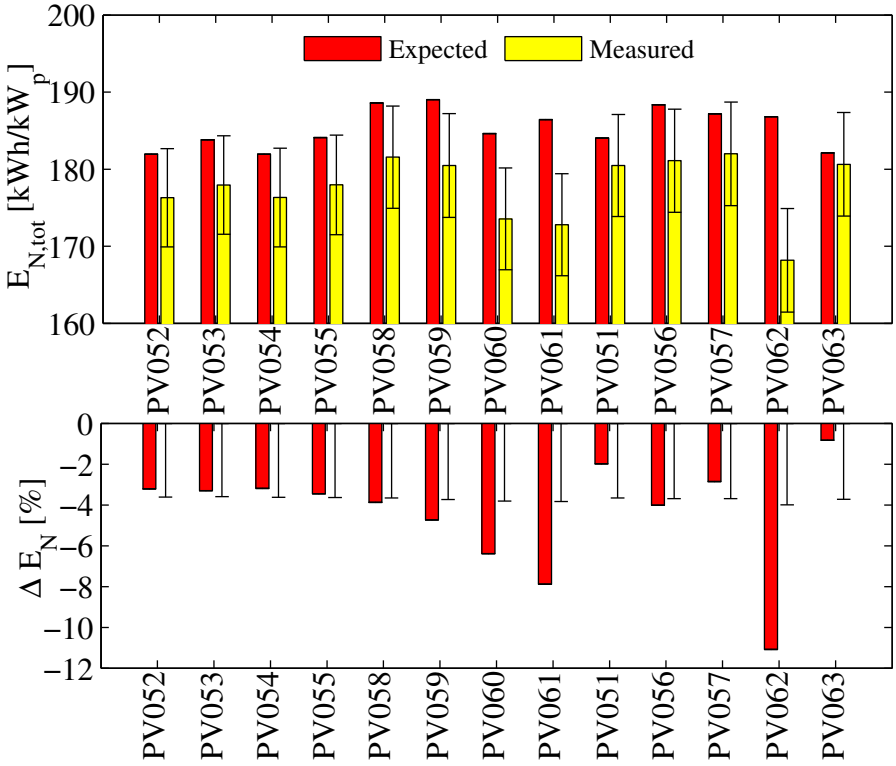

Figure 5.22: Comparison of measured and expected (modelled) energy yield,for September-November 2015. G_τ: 200.7 kWh/m^2.

was expected, module *PV062*, being the closest module to the roof ledge and the poles is subject to the largest amount of shading of the whole array, and thus suffers the largest loss of energy that could have been produced. By contrast, modules *PV051* and *PV063* are furthest from the poles, and their energetic losses due to shading are also the lowest.

In Table 2.1 the module configuration and type of bypass element were given. Modules *PV053, PV055, PV059* and *PV060* are outfitted with active bypass chips instead of industry-standard bypass diodes which were expected to lead to lower losses (and hence increased energy yield) because of their lower forward voltage drop when activated. From Figure 5.21, no definitive statement regarding their performance can be made, compared to regular diodes. By selecting the shading-only period (September-November), the relative differences between the modules can better be evaluated, as shown in Figure 5.22. It appears that

the physical location on the array - including shading and local wind access effects - dominates the performance result of the module, more than the module and bypass technology itself.

Nevertheless, the relative energy losses shown in Figure 5.22 can be significant, with up to 11 % of the expected energy yield (*PV062*) lost due to shading. The average modelled energy losses due to shading amount to 4.4 % for the individual modules in the array.

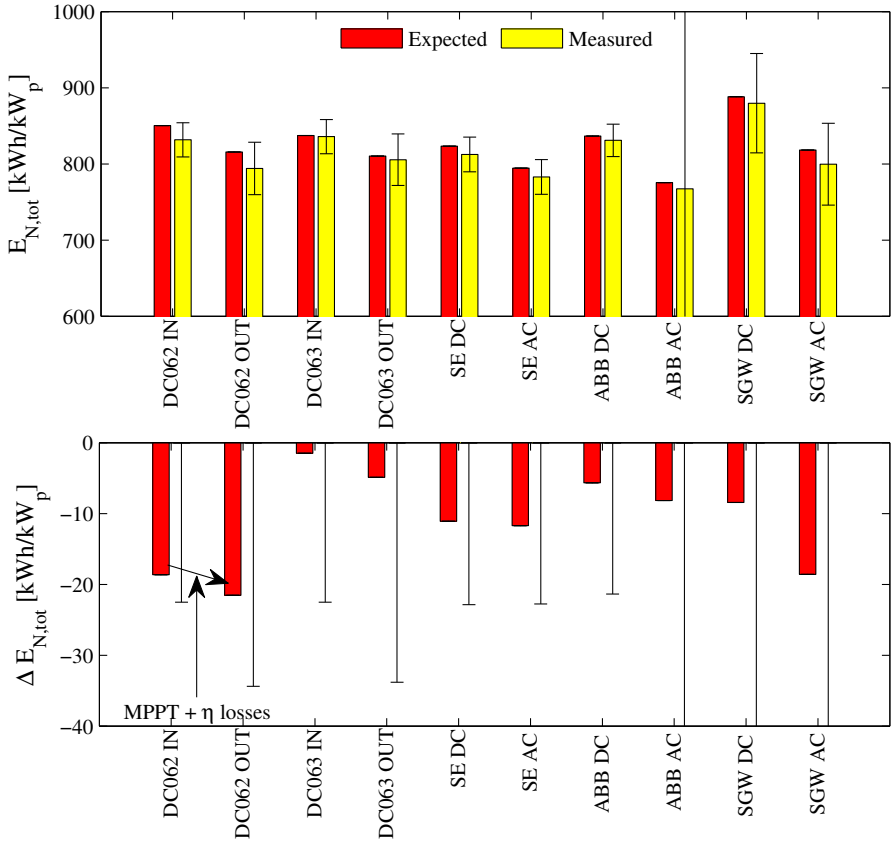

Figure 5.23: DC and AC system yield comparison, measured and expected of the DC-DC converters and inverters measured, for April-November 2015. G_τ: 944.1 kWh/m^2. DC062 IN: module-side input of DC-DC converter connected to module PV062, DC062 OUT: output of DC-DC converter. See also Figure 2.7.

For a standard string inverter (as is the case for the Solarex-Sungrow system), the losses due to shading are expected to be higher than for a system with

module-level DC-DC convers (the SolarEdge system). It can be expected that on the one hand bypass diodes would bypass the shaded areas, but the shade shapes would likely lead to additional current limitation losses: Figure 5.9 showed how part of the shadow resulted in additional losses, which are otherwise unexpected from I-V curves. This result is confirmed from the measurements and displayed in Figure 5.23: the modelled energy loss between September and November for the SolarEdge system is 11.7 $\mathrm{kWh/kW_p}$ whereas the Sungrow system lost 18.6 $\mathrm{kWh/kW_p}$.

In the case of Figure 5.23, the DC and AC yields - measured and expected - are compared. The large drop in energy yield from DC to AC for the Sungrow-Solarex system is a result of the DC array being undersized in power versus the inverter's nominal power, as was discussed in Section 5.4.4. As a result, the fixed losses of the Sungrow inverter dominate all losses inside the inverter. In the case of the SolarEdge inverter, almost no extra shading losses can be noticed between DC and AC side, as these losses and their impact on the individual DC-DC converters have already been taken into account on the DC side.

The losses for the DC-DC converter connected to module *PV062* are striking, and reinforce the point made above: not only will shading cause a loss of energy through the bypassed areas, it also "forces" the MPP algorithm of the inverter or converter to search more for the optimum MPP. This may result in MPPT oscillations, as could be noticed in Figure 5.9. Comparing the added losses due to shading of *DC062* to *DC063*, the effect of the location on the array on shading duration, and therefore losses, is clear (see also Figures 4.1, 5.7 and 5.9).

The effect of the loss of an active area inside a module thus also leads to added efficiency losses, as can be seen in Figure 5.23, for *DC062, DC063* and the ABB micro inverter connected to *PV052*: the converted losses are systematically higher than before the DC-DC or DC-AC converter. In particular, these three "systems" suffer among the largest amount of shading, relative to their size, and thus have the largest losses.

5.9 Applications of the normalised efficiency revisited

The range of analyses and applications that can be done using the η_N and η_N is very large, as has been illustrated so far. The following discusses some applications again, based upon the knowledge gained up to here and some other applications are briefly discussed.

5.9.1 Education and outreach

Efficiencies are well understood by many and thus the normalised efficiency may be used to illustrate and discuss photovoltaic system performance on a qualitative level. For example, while the decrease in module efficiency due to temperature is often well-known, it is less often well-understood. A figure (or sequence of figures) which illustrate how the system efficiency decreases during irradiance peaks and recovers during periods of passing clouds allows the concept to be better understood.

Similarly, informing a customer that the system is performing with the normalised efficiency at 80 % instead of "generating 2400 W at the STC irradiance" is functionally identical, yet more easily grasped: using the η_N, the need for the customer to remember the exact nameplate value of the system to evaluate the system's performance is removed. Additionally, the larger irradiance range over which the normalised efficiency is largely insensitive to irradiance changes (i.e. that it is possible that the η_N is above 90 % between 200 $\mathrm{W/m^2}$ and 1000 $\mathrm{W/m^2}$) allows it to be used to detect smaller changes in performance. Moreover, the normalised efficiency values can directly be read off a graph, instead of requiring additional calculations to arrive at the same conclusion.

5.9.2 Verification and comparison in multiple locations

In Section 5.5.2, the possibility of measuring the module (or system) coefficients in one location, and then use this model with data of another location was raised. This may contribute to model improvements, as well as validate the approach itself. On the other hand, a round-robin comparison of module coefficients determined in multiple locations (for example TÜV has multiple outdoor PV testing sites worldwide), could point to aspects that may not have shown up with this work - such as the use of other brands and types of module-level power electronics.

5.9.3 Coefficients for model by Huld *et al*

In Section 5.6.4, the combination of using the coefficients k_1 and k_2 from the model of Huld *et al* [13] together with measured temperature data (specifically, ΔT_{STC}) and datasheet values of γ was suggested. Depending on the quality of modelled and measured data, it may be possible to pick the most appropriate values for the system and location in question. Table 5.7 summarises the possibilities.

Table 5.7: Possible sources and uses for model of Huld *et al* coefficient values.

Parameter	All values from Huld *et al*[a]	This work symbolic equivalent	Mix-and-match
k_1 [-]	$-0.017\,24$	$k_{1,fit}$	Huld *et al*, this work, fit
k_2 [-]	$-0.040\,47$	$k_{2,fit}$	Huld *et al*, this work, fit
k_3 [$^\circ\mathrm{C}^{-1}$]	-0.0047	γ_{syst} $(= k_{3,fit})$	Huld *et al*, this work, fit, datasheet γ
k_4 [$^\circ\mathrm{C}^{-1}$]	$1.49 \cdot 10^{-4}$	$k_{3,fit} \cdot k_{1,fit}$	Huld *et al*, this work, fit
k_5 [$^\circ\mathrm{C}^{-1}$]	$1.47 \cdot 10^{-4}$	$k_{3,fit} \cdot k_{2,fit}$	Huld *et al*, this work, fit
k_6 [$^\circ\mathrm{C}^{-2}$]	$5 \cdot 10^{-6}$	0	Huld *et al*, this work, fit

[a] See [124, 13].

The original article of Huld *et al* was focused on the power rating of crystalline silicon modules. Similarly, the modifications to the model in this work are also applied to crystalline silicon modules. The modelling (and measurement) difficulties and spectral behaviour of other technologies, in particular thin-film technologies, would need to be tested in order to ascertain whether the approach of this work to determine the model coefficients works for all technologies. Nevertheless, the normalised efficiency can still be used as a means to analyse and monitor photovoltaic systems.

The theoretical meaning of the coefficients k_1 and k_2 can also be studied further, and their applications broadened. For example, providing the coefficients k_1, k_2, k_3 (with k_3 already known as γ) in photovoltaic module data sheets could be used as a differentiating factor, e.g. for region- or climate-specific modules. That way, low-light optimised modules with high values of γ (e.g. $\gamma = -0.5\,\%/^\circ\mathrm{C}$) could be chosen for higher-latitude applications. In a similar manner, high-temperature and high-irradiance modules could perform less well in low-irradiance regions.

Additionally, if the coefficients k_1, k_2, k_3 are provided in data sheets, they may serve for an *energy rating* and modelling benchmark. To an extent, I-V curves

measured for IEC 61853-1 [77] may already provide the necessary data to determine these coefficients using the I-V curve data fitting algorithm of Huld *et al* [13]. On the other hand, the method of this work, which uses more readily available data (or easier to measure), may also be used. In this case, more work can be done on standardising equipment used, e.g. specifications for the type of power electronic devices to ensure modules and systems perform at MPP.

Additionally, a consensus on the annual dataset(s) of irradiance-temperature pairs used for the energy rating calculation must still be reached. In this context, inspiration may be obtained from the approach for the CEC and European inverter weighted efficiencies, or the MotherPV method [162].

By having the coefficients k_1, k_2, k_3 available, together with a bankable[34] [163, 164] irradiance and temperature dataset, it would be possible to perform pre-feasibility and due diligence studies. More importantly, if such a shared framework would and can be applied, additional transparency can be achieved in how energy yield modelling is performed.

5.9.4 Real-time and near-real-time monitoring

The normalised efficiency can be used for real-time monitoring of photovoltaic performance. Depending on the ease of integration into the monitoring platform, it would be possible to integrate alarms and warnings, based on certain benchmarks e.g. a drop in the η_N greather than 25 %, for irradiance values greater than 200 W/m^2. These can be subject for further study, to find the optimum level at which an alarm or warning should be generated or not. (A very low value, e.g. 30 % of the η_N is perfectly normal close to sunset and sunrise, but may not be so for high irradiance conditions.) Additionally, having both the η_N and η_N^* monitored may help to distinguish between temperature-induced efficiency losses and other types of losses: temperature-related performance changes may mask other effects of module performance. By evaluating temperature-corrected metrics, it may be possible to detect other root causes, such as spectral effects, irradiance response, ...

In this context, for near-realtime analyses, using the modelled as well as the measured η_N and the additional values of normalised and absolute power and energy can allow PV system owners to react appropriately to performance deviations. One possibility is also the *Health Scan* developed by 3E [165] which may be expanded using the normalised efficiency and derived parameters, as well as some of the approaches discussed in the IEA PVPS Task 13 report [166].

[34] A high-quality, long-term and validated dataset of irradiance for certain locations that may be used by financing institutions (e.g. banks) to evaluate solar project risks.

5.9.5 Additional comments on the determination of the system temperature coefficient of power

A first approach for the determination of the system temperature coefficient of power γ_{syst} has been given in this dissertation, in Sections 5.4.3 and 5.4.4. It may be that the filtering requirements given here can be further optimised for certain locations, e.g. that the over-temperature requirement must be made more stringent for high-temperature and high-irradiance regions, or, that on the other hand, the natural variability index of irradiance requirement must be modified according to the local climatic conditions.

Given the importance of the γ_{syst} for the model fitting for detailed in this text, this is certainly an area where more research can lead to better results. From the experience of this work, the easiest approach is to apply very stringent limits, to essentially clear sky days only. This does result in the γ_{syst} being difficult to use for system anomaly detection as shown in Section 5.4.5 (i.e. one valid data point per 10 to 20 days is insufficiently fast in detecting important changes).

5.10 Conclusions

This chapter has introduced and discussed the application of the normalised efficiency η_N as a tool for photovoltaic module and system monitoring and analyses, as well as a number of derived metrics, such as the γ_{syst}. The principles of normalisation and temperature-correction have been made explicit, with which analyses can be performed as well.

The normalised efficiency η_N can be used as a stand-alone metric for multiple purposes:

- Real-time as well as *a posteriori* monitoring and performance analysis of photovoltaic modules and systems of different power ratings, on DC and AC levels.
- Qualitative and quantitative comparison of the performance of different systems ("Which one performs better?") throughout the day.
- Detection of shading of either the array or the irradiance sensor. While not shown or discussed above, it may also be used to calculate the instantaneous power loss due to shading, even for complex shading geometries - instead of needing to resort to modelling.

- The interaction between modules and the MPPT algorithms of inverters or converters may be studied, including the identification of MPPT instabilities due to shading - even for module-level equipment.
- Identifying or recognising temperature-induced efficiency changes throughout a day - this can be useful within an educational context, among others.

The normalised efficiency η_N also permits derivative metrics to be determined, of which the system temperature coefficient of power γ_{syst} is most salient. The γ_{syst} itself may then be used as a daily summary metric with which to determine shading, temperature sensor malfunctions as well as system performance (the stability of the γ_{syst} over time may be used for process control). For process control, having more data points of daily γ_{syst} available gives better results, and can be used as a better stability metric than the PR.

Care must be taken however with the determination and filtering employed for the γ_{syst}. While the linearity of reference cell-derived η_N can be useful (and possibly better) to determine the γ_{syst}, it is *very* sensitive to irradiance fluctuations throughout the day, which cause outliers in the regression analysis and thus require more stringent filtering. Using the pyranometer-derived η_N allows the γ_{syst} to be calculated on more days versus a reference cell (or with less effort), as its slower response to irradiance changes results in less η_N fluctuations throughout the day as well as results in a lower calculated value of the NVI. With strict(er) filtering, both the reference cell and pyranometer-derived η_N allows the γ_{syst} to be calculated with very similar results.

The approach of temperature correction using the γ_{syst} then permits evaluation of the system performance as if it were working at the reference (typically STC) temperature. As such, other aspects of system behaviour may be detected, free from the masking effect of the combination of irradiance and temperature. For example, modules may have spectral effects identified using the temperature-corrected normalised efficiency η_N^*. Similarly, the effect of inverter under-loading for the Solarex-Sungrow system was first identified by comparing the regular and temperature-corrected normalised efficiency.

The temperature-corrected normalised efficiency η_N^* is then the starting point to fit the coefficients k_1 and k_2 for the temperature-corrected formulation of the model of Huld *et al* [13]. By taking $k_3 = \gamma_{syst}$, the remaining coefficients k_4 and k_5 may be obtained, with which the full (non-temperature-corrected) model of the normalised efficiency can be calculated.

The method outlined in this chapter to obtain the model coefficients has the benefit to the original methodology of Huld *et al* is that the need for I-V curves is

reduced or removed, although it is still possible to use I-V curve data. However, the method shown here can obtain the model coefficients in the course of a few weeks or months for the system under consideration. The method scales from single modules to full arrays, and requires a limited number of data inputs. Important here is that most of the data inputs are quite standard for larger photovoltaic arrays as well as research systems.

The possibility to calculate system-specific coefficients can be used to self-verify the performance of a system, or set a benchmark for future performance (e.g. degradation). The modelled values can then further be contrasted with industry-standard models and modelling software (e.g. PVsyst, HOMER or SAM).

One added application of the modelled value of the normalised efficiency can be for real-time or quasi real-time performance monitoring of systems, by comparing the modelled value of η_N (or η_N^*) to the measured value of η_N (resp. η_N^*). Significant deviations between modelled and measured values can then be used to guide actions to be taken.

The validity and generally superior or equivalent performance to the original coefficients of Huld *et al* has been validated using the total (normalised) energy yield for the period of June to August 2015, as well as the daily PR and time series evaluation of the normalised efficiency. As a further application, the model of this work has been used to quantify energy losses due to shading for the modules, DC-DC converters and DC-AC inverters measured.

The effect of shading on module and system performance not only leads to bypass-area losses, it also results in additional MPPT losses and instabilities, which lead to overall larger losses. While module-level power electronic devices are a step forward from string inverters (despite the added efficiency losses), the type of shading encountered during the course of this work suggests that module sub-string level MPPT can be useful [167].

Similarly, the ability to switch the internal module topology could be useful, although likely to be more difficult to implement than sub-string MPPT, in particular with regards to cost. However, for the built environment where chimneys, trees and similarly wide sources of shading may frequently occur, the further subdivision of modules from three sub-strings of 20 or more cells to more (e.g. the studied 10x6 sub-string modules) can pay immediate, low-cost dividends.

For longer-term analyses, the PR may be made less sensitive to ambient temperature variations by applying the temperature correction methodology of this chapter to obtain the PR^*. The benefits include that the variability of PR^* is lower compared to the regular PR, and that subsequent variations in

the PR^* may be used as a starting point for subsequent analyses.

If possible, it is recommended to use the daily PR as the basis for the longer-term calculation of the PR_τ, together with the PR error standard deviation $\sigma_{\Delta PR}$. Statement of the *averaged* PR_τ with the $\sigma_{\Delta PR}$ further permits models to be compared between each other, and may point to avenues of further investigation.

Chapter 6

Conclusions and future outlook

6.1 Summary of the measurement set-up requirements and the results obtained

The measurement set-up in its current form can (and does) provide data with which the goals in Section 1.4 can be achieved, in some cases fully, in other cases providing a starting point. These goals and requirements are repeated here, with the current implementation and design choices highlighted, in order to identify the extent to which the requirements have been met.

6.1.1 High-level goals

- *Build a high-quality, high-speed outdoor measurement set-up, which will allow transient (rapidly changing) thermal and electrical effects to be observed.* **Achieved, with some aspects not in initial goals:** Both rapid thermal and electrical transient effects have been measured and analysed. Tools such as the normalised efficiency (η_N), the projected wind vector ($v_{w,proj}$) and BOS temperature coefficient (γ_{BOS}) aid the detection and analysis of transient effects, as well as a better understanding and communication of concepts such as efficiency decrease due to temperature or shading effects.

- *Contribute to the development of the detailed physics-based thermal-electrical-optical model for photovoltaic modules developed at IMEC, including providing data for model calibration and verification.* **Achieved:** The Electrical-Optical-Thermal model at IMEC has been validated, improved and calibrated using data from the set-up (and that of other measurement set-ups). The interested reader may consult the work of Hans Goverde on this topic. The conclusions of Chapter 4 on inter- and intra-module temperature variations may also be modelled, together with the data from Chapter 5.

- *Modelling of degradation and development/validation of test procedures for the energy rating of PV modules in the Belgian context by performing outdoor measurements and accelerated lifetime tests.* **Partially achieved:** The methodology based on the use of the normalised efficiency (η_N) is a new potential avenue for empirical energy rating methods. The accelerated lifetime tests have not been performed, due to the focus on the improvements on the outdoor measurement set-up. The measured I-V curves can be analysed at a future date for degradation analyses.

- **Achieved, not in initial goals:** The concept of the normalised efficiency (η_N) may be as useful for photovoltaic system analysis and inter-comparison as the Performance Ratio (PR); it shows a level of detail that was heretofore lacking and can be broadly applied.

- **Achieved, not in initial goals:** Development of an accurate, easy-to-implement and internally validated method to obtain module and system coefficients, which can be used to predict the normalised efficiency, normalised power and energy yield of photovoltaic systems. The method can be applied on any system which measures a limited number of variables (irradiance, power, module temperature). Moreover, the applications extend to quantifying potential energy losses, such as in the case of shading or system outages.

6.1.2 Actionable requirements

- *A flexible, expandable measurement set-up for distributed temperature measurements on PV modules, while also taking into account climatic and electric variables.* **Achieved:** The measurement set-up is flexible in use, has been expanded throughout the course of this PhD and may so again in the future. Multiple temperature measurements are possible, and the main weather and electric variables (DC voltage and current, AC voltage, current, power, ...) are measured per second.

- *Achieve the lowest measurement uncertainty within the budgetary constraints of time, skills and available resources.* **Achieved:** The measurement set-up has low measurement uncertainties throughout, which were obtained at the expense of time and resources, with a growth in skills as an additional result.
- *I-V curves should be measured at regular intervals, with the PV module in question held at its MPP between I-V curve measurements. I-V curves should be measured in* 1 s *or less, with the possibility of longer duration I-V curves if circumstances so dictated, e.g. for highly capacitive PV modules [14].* **Mostly achieved:** The measurement of I-V curves *does* happen in less than 1 s for sweep-mode, but the time between I-V curves in a sequence is ∼2.5 s and a loop time of typically 5 min. PV modules showing capacitive effects may be measured using the equipment, provided that the I-V curve measurement in list mode is further optimised.
- *To have the PV modules connected to a commercial converter or inverter. This resulted in the need for a commutation mechanism (which is described in (very) general terms in [15, 16]), to disconnect a PV module from a string without impeding the flow of power to the main inverter.* **Achieved:** The commutation mechanism works as designed, and has been used for thousands of I-V curves.
- *All values should be measured and stored per second to characterise photovoltaic modules and systems' transient behaviour. Compared to most descriptions in literature, this is a significant increase in the frequency, as other set-ups measured and stored data at intervals between* 5 s *average values up to* 15 min. **Achieved:** The weather VI, the DC voltage and current VI and the AC measurement VI log all data per second. This data may subsequently be averaged or resampled if so desired. The inverter and DC-DC converter behaviour removed the need for per-second I-V curves.
- **Achieved, not in initial goals:** Development of safe and, post linear transformation and calibration, SCBs with low measurement uncertainty for DC voltage and current measurements for module-level up to inverter-level energy yield comparisons.

6.2 Thermal characterization and measurements

The focus of this work on transient thermal and electrical characterisation has resulted in the need to reevaluate models and equations from literature.

For cell-to-backsheet corrections, the well-known equation by King *et al* has been modified and the relationship of the components to time made more explicit. In particular, the minimum time interval over which the running mean of the irradiance has to be calculated has been linked to the module's equivalent thermal time constant $\tau_{\vartheta,eq}$. The similarity between a backsheet-measurement-derived and the cell-measurement derived value of the $\tau_{\vartheta,eq}$ allows backsheet-measured data to be used, even for transient results. Nevertheless, significant discrepancies between measurements and modelled or corrected values may arise if the methods of this work are applied incorrectly.

Using the developed methods and data, temperature inhomogeneities across a modules' surface were evaluated, to provide a partial answer to the issue highlighted by Müllejans *et al*: how large are temperature non-uniformities, and how often do they occur at a certain magnitude? The answers to these questions suggest that for non-faulty modules, the intra-module temperature inhomogeneity is limited to less than 4 °C for 90 % to 97 % of the time. However, when temperature inhomogeneities do occur, they may reach up to 8 °C between the hottest and coldest area of the module. Similar to the absolute module temperature, the largest intra-module temperature differences are measured under conditions of high irradiance, with wind access to the module playing a role as well.

Inter-module (or array) temperature variations have been quantified for the modules studied, with most temperature deviations of the inter-module temperature variation ΔT_{m-m} to be in the range of ± 4 °C at high irradiance, with the value of the ΔT_{m-m} seen to scale with the irradiance.

6.3 Photovoltaic module and system analysis

Using the measurement set-up and its data to illustrate the concepts discussed, a number of tools for the analysis of photovoltaic modules, systems and influencing parameters have been introduced. Among these, the most important contributions are the normalised efficiency η_N and the framework of normalisation as a whole, as well the concept of temperature correction. With this terminology and framework, the performance of multiple systems may be qualitatively and quantitatively analysed. The normalised efficiency can be used to determine the system temperature coefficient of power γ_{syst} , with almost no human intervention (such as manual covering and uncovering of PV modules for I-V curve measurements) necessary. This may be applied for monitored systems of any power rating with the only requirements to be to measure module temperature(s), the irradiance, and the system power. The

methods of this work to measure and model the η_N and the P_N are broadly applicable. Much less stringent measurement requirements are necessary (but may still be used), and I-V curve measurements are now optional instead of mandatory.

Figure 6.1 summarises the main contributions of this work for the analysis of photovoltaic system performance. Where the Performance Ratio PR was the metric for energy evaluations, the normalised efficiency η_N is the metric for power evaluations. Figure 6.1 also contains notation used in literature for the irradiation G_τ (indicated as H), while the $E_{N,\tau}$ is also discussed in literature as $Y_{f,\tau}$. Figure 6.1 also indicates that the transition between energy and power leads to a loss of information, as only the average power over the interval τ can be calculated from the energy.

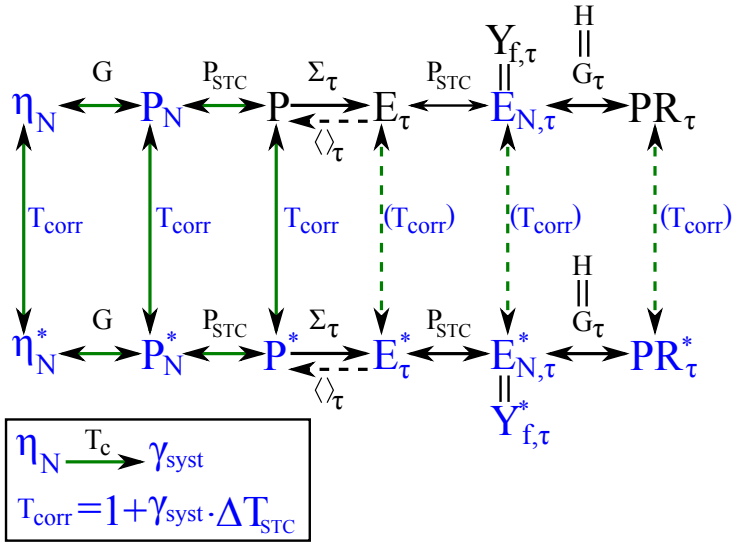

Figure 6.1: A visual summary of the main PhD contributions, which are indicated in colour. Dotted arrow lines indicate that the correction may be applied, but will suffer from averaging errors, compared to following the paths with full arrows. A double headed arrow indicates that it is possible to calculate from one level to the other without loss of information, e.g. from P_N to η_N and back to P_N. All steps shown may be applied for measured and modelled data.

The simplicity of the methodology of this work to determine and apply the coefficients for the modified power rating model of Huld *et al* may increase its likelihood of use, as it requires measurement of just three parameters which are quite standard for monitored photovoltaic systems: the irradiance (using a reference cell), module temperature and the module or system power. From

these, the three base coefficients (k_1, k_2 and $k_3 = \gamma_{syst}$) can be determined, which then allow the derivative coefficients k_4 and k_5 to be calculated. As shown in this work, the model with fitted coefficients generally outperforms the model with the original coefficients of Huld *et al.* The fitted normalised efficiency model can then be used for real-time normalised efficiency and power monitoring, up to energy production prediction or verification, and can thus serve as an easy-to-apply benchmark.

6.4 Performance analysis of systems

The discussion on measurement uncertainty for PR and energy yield evaluations (Section 5.7) suggests that there is still room for improvement for the calculation of the PR and similar evaluation metrics (e.g. total yield).

At issue here is how the choices are made to average data over longer time periods. Similar to the discussion on averaging of sampled data and the relative weights of values, the choice for the calculation of long-term (e.g. yearly) PR can be expressed as

$$PR_\tau = \frac{\langle Y_f \rangle_\tau}{\langle Y_r \rangle_\tau} \leftrightarrow \langle PR \rangle_\tau = \langle \frac{Y_{f,i}}{Y_{r,i}} \rangle_\tau. \tag{6.1}$$

For the climatic conditions of e.g. Belgium, the choice is between giving a much lower weight to low-irradiation days (the left side of Equation (6.1): PR_τ) on the whole, or to give each day of the year an equal weight in the longer-term average of the PR (the right side of Equation (6.1): $\langle PR \rangle_\tau$). The advantage with the form of $\langle PR \rangle_\tau$ is that, during the calculation of its value, it is almost no effort to also determine the standard deviation of the PR. Combined, these can much better quantify how the system under consideration performs on average, and how much variation around this mean can be expected.

Even if the choice remains with the continued use of the formulation of PR_τ, it can benefit from using the σ_{PR} as well. When considering or comparing models, the $\sigma_{\Delta PR}$ is an additional metric that can be employed. Similarly, if possible to determine, the temperature-corrected Performance Ratio shows less to no sensitivity to ambient temperature variations, and can be used to discriminate between temperature-induced effects and other effects, such as the irradiance spectrum variation over the year, or changes in the system environment, such as the shading condition illustrated in this text.

6.5 Future work

6.5.1 Normalised efficiency: measurements and modelling

While this work has introduced and illustrated a large range of analyses that may be performed and derivative parameters such as the γ_{syst} to be determined, much more can be done in this area.

On the measurement or monitoring side, more in-depth analyses can be performed, which may require more measurement equipment than available in this dissertation. The first and foremost test is to apply the methodology of the normalised efficiency in other photovoltaic systems. To date, this has been done in the course of a master thesis on a 968 kW_p system in Italy as well as using publicly available data from the Desert Knowledge Solar Centre in Alice Springs.

Integrating the (often separate) data streams of weather and system power to calculate the normalised efficiency is one step that must be performed, if real-time or near-real-time alarm generation is to function. Work can be done here to develop intelligent anomaly detection algorithms, where a challenge may be in dealing with false alarms generated throughout the day.

For modelling, the approach shown in this text may be tested and verified on other systems, with different photovoltaic technologies, mounting conditions and measurement equipment. This PhD has shown that less coefficients need to be determined (three base coefficients instead of six separate in the original formulation of Huld *et al*), at lower cost and complexity. Aspects that may need further study include:

- How broadly applicable is the methodology outlined in this work? Is it valid for thin-film technologies? Which modifications would have to be implemented for technology or system X? From the previous work of Huld *et al*, the focus has been on crystalline silicon modules, and this dissertation has also applied this to silicon crystalline modules and broadened the applicability to systems.
- Which period of time is necessary to properly determine the value of γ_{syst}? Are there system designs or filtering methods which allow γ_{syst} to be equal to γ? Are the filtering criteria proposed too strict, or too lax for the location where the photovoltaic system is located?

- The minimum duration for which a training data set and validation data sets must be obtained. At which point is the model sufficiently trained?

6.5.2 Measurement set-up

The measurement set-up may be seen as a continuous work-in-progress, with the need to keep it functioning as well as possible. Nevertheless, improvements to the set-up can be made in the following areas:

- Indoor flashers (or better yet, steady-state LED) I-V curve measurements can be used to perform measurements and validations when outdoor conditions are not conducive for best results. Moreover, as typically more of the conditions can be controlled, this is part of the reason that all large laboratories (NREL, Sandia, Fraunhofer, TÜV, ...) have these as well.
- Development of portable module or system loggers, yet with good measurement uncertainty. Industrial and other customers can not always afford (or want to) remove modules or inverters from the system for certain types of testing.
- Integration of the different data streams, so that automatic alarms can be generated, e.g. for partial shading or loose sensors.
- Humidity and rainfall sensors could provide the necessary background for analyses. The rainfall-temperature aspect for bias corrections can thus be better optimised from the current approach. As the measurement connections are available in the cabinets, this is not insurmountable.
- Spectral measurements can further lead to a better understanding of which are the root causes of performance deviations between neighbouring modules.
- An automated shading rack could be useful to perform *controllable* and *repeatable* shading experiments, and may also help for cover-uncover steps for I-V curves.
- Round-robin comparisons of measurements. While all feasible methods have been applied to account for and reduce sources of error and uncertainty, some hidden biases may only surface when performing comparisons of measurements with other laboratories.

6.5.3 Degradation analyses

The use of I-V curves for degradation analyses is suggested in Section 2.4, per the approach of Jordan and Kurtz [23].

This may also be supplemented by the fitted model coefficients for the set-up: if the fitting is repeated at a later date (without shading), the variation in the coefficients may also indicate whether degradation can be detected and quantified.

6.5.4 Measurement uncertainty: absolute, relative and application

Determining the applicable absolute measurement uncertainty according to the methods outlined in the *GUM* [12] is no easy task, with the *GUM* the international consensus by the largest scientific bodies (BIPM, IEC, IUPAC, ...) on the topic. However, the complexity of the matter and the prerequisite knowledge and *understanding* of statistical principles result in a situation where scientists, researchers and industry often adhered to different practices. To an extent, the work of IEA PVPS Task 13 is aimed at ensuring that measurements are performed and reported according to the same principles, so that comparisons can be objectively and rapidly made. One example of an area where semantic differences must still be resolved is where measurement uncertainty is often stated as "accuracy"[1], and without an indication to the coverage factor k used, as well as the coverage interval.

One aspect that is for future analyses is the application of relative comparisons. The *Law of Propagation of Uncertainties* results in combined (e.g. relative) measurements to have a larger combined measurement uncertainty than the original, composing measurement uncertainties. However, the trend remains the same: if a module has a higher power and normalised power P_N than its neighbour, then this trend reappears for the normalised efficiency η_N. In terms of measurement uncertainty, the P_N will have a lower measurement uncertainty than the η_N. For absolute comparisons, where these results would be compared to those of other modules located elsewhere, it is logical to compare absolute measurement uncertainties. However, for relative comparisons to the same instrument, the resolution of measurements may be of more use, so that

[1] Accuracy is the closeness of mean of measured values to the true value, whereas measurement uncertainty characterises the width of the population of measurements, in absolute terms. It is possible to have accurate data and yet have a large measurement uncertainty.

observed trends can be used for conclusions, even if the absolute uncertainty would suggest that the measurements fall within the uncertainty interval.

6.5.5 Temperature measurements and effects on energy yield calculations

Section 4.9 showed how longer-interval temperature measurements may lead to under-estimated temperature variations. It may be possible that temperature effects play a larger role in the energy yield of photovoltaic systems than previously analysed, because of this use of longer-interval data, e.g. per minute or longer. More analyses (both modelling and measurements on varying time scales) in this area can help to quantify the effects on the energy yield.

Regarding the determination of the thermal time constant discussed in Section 4.9, much more work can be done for both outdoor use and for models. In particular, the relationship to the wind speed *and* direction is worthy of study. Not only is this suggested for open-rack mounted modules, but also for roof-mounted and roof-integrated modules. In this regard, the possibility to filter for wind direction with the projected wind vector may be of use.

The effect of intra-module temperature inhomogeneities discussed in Section 4.10 requires more study, using a variety of methods. One possibility may be to use multiple IR thermographic cameras for long-term measurements, together with information on the local weather conditions, such as the wind speed and direction.

The Equivalent Cell Temperature determination according to IEC 60904-5 [129] and one-diode thermal models assume the module temperature to be homogeneous, yet do not specify what to do when this is not the case, nor the limits where the assumption breaks down. Furthermore, it can be useful to determine the permitted intra-module temperature inhomogeneities, to know when more complex modelling efforts are required. While the effect of an intra-module temperature variation on the current of modules is limited, it may be useful to determine how large the effect is on the annual energy yield, and whether this is one of the last steps toward “perfect” energy yield modelling.

6.5.6 Classification of irradiance variability

For the classification and identification of variable irradiance days, the concept of the natural variability index of irradiance (NVI), can be improved, by working

on identifying the limits of each class according to the irradiance measurement technology.

Ideally, a combined metric of the *VI* of Stein *et al* [152] with the NVI of Willy *et al* [153] could yield the clearest answers. In this regard, the *VI* may be improved by combining the already available data of clear sky irradiance (and thus irradiation) with the measured irradiance: the daily clear sky index is one possibility. Alternatives would include the value of G_d (but are essentially the clear sky index by another name).

6.5.7 SCBs

While the SCBs have shown to be stable and accurate in use, they may still be improved, albeit in a different direction: by abandoning the need for analog signal interpretation using the NI 9205 voltage cards, and attempting to measure in a fully distributed manner, where portable "measurement boxes" can be installed with minimal effort on any standard photovoltaic array.

By stepping away from the need for analog signal interpretation and conversions, it is possible to develop low-cost yet very accurate DC voltage, current, power, ... measurement boards. For example, 24-bit Analog-to-Digital Converters (ADCs) are now available at reasonable prices which can then be read out on embedded computers.

It is foreseeable that in the coming years, the "standard" photovoltaic system performance studies can be done at a fraction of the cost, although some components (e.g. pyranometers, anemometers) have not yet gone through the same aggressive cost reductions. Nevertheless, with high-quality distributed measurement capabilities, additional functionalities can become available, such as detecting cloud movements or measurements with more granularity than typically available for utilities.

6.6 Improvements and long-term future prospects

An issue that impacts all photovoltaic performance assessments is the measurement uncertainty associated with weather parameters. Compared to the well-known measurement methods employed for electrical measurements where a DMM may have a measurement uncertainty of 0.0040 % [63], an uncertainty of ∼2 % (e.g. many higher-quality secondary standard pyranometers) is a few

orders of magnitude away. The uncertainty of the reference irradiance and irradiation measurement then impacts performance analyses [58, 168] and their uncertainty.

If manufacturers of reference cells, pyranometers and irradiance measurement devices are able to significantly reduce the measurement uncertainty by an order of magnitude, new conclusions will be able to be drawn, such as a better understanding of both power changes and degradation over time. Furthermore, models which use this data can then also profit from the improvements. To an extent, pyranometer manufacturers have already made inroads in this direction, with the instruments of today having less measurement uncertainty and often a shorter time constant than before.

However, one of the take-home messages of this work is that without (correct) measurements, including weather inputs, *no* conclusions can be drawn regarding the quality and performance of the system. A system which is not monitored using at least one irradiance sensor is like a car with a broken or unreliable speed indicator (the module's temperature is then the heat gauge). It may be moving in the correct direction (as seen by the absolute energy yield), yet very little information is available about the correctness of this value, compared to what was paid for. For photovoltaic systems which have an expected technical and economical lifetime of twenty years or more, a systematic deviation may result in large financial implications.

Computing costs have rapidly decreased and inverters and external measurement devices have become cheaper over the past years. One of the next steps here is for irradiance measurement devices to become cheaper while maintaining or improving on the measurement uncertainty, so that photovoltaic system owners and investors can correctly verify that the promised performance is delivered. Not only will this contribute to better-maintained systems, but this will allow additional business services to be created. Examples here may range from using (aggregated and anonymised) system performance data to detect cloud movements for grid stability control, to needs-based maintenance checks instead of fixed but unnecessary maintenance checks.

The different weather and electrical measurements such as irradiance, module temperature, and power can be see as legs of a stool: removal of one may not always be critical, yet the whole may become unstable. With data lost or untrustworthy, a large range of questions becomes unanswerable, less trustworthy on its own or more uncertain. Expressed in simple financial terms, an increase in the uncertainty of photovoltaic measurements and models results in a financial penalty in one form or another. As such, continuous and sustained efforts to maintain system quality, reliability and reduce uncertainties are important. Conversely, adding functionalities to well-maintained measurement set-ups bring

more benefits, as the results can build on each other, and may aid to eliminate possible hypotheses and to faster reach relevant conclusions.

Lastly, the ideal photovoltaic system will be self-aware and self-reporting, so that photovoltaic modules, converters and inverters can evaluate and compare their performance to their neighbours or similar systems elsewhere. If a component then starts to fail, integrated sensors or intelligent algorithms may report this and where possible take corrective measures - similar to going to the doctor if one is ill. One such possibility is module (or intra-module)-level power electronic devices which obtain or locally measure irradiance, module temperature and power data, apply the model fitting as shown in this work to "learn" the behaviour of the module, and then generate alarms based on real-time deviations from previous behaviour.

Appendix A

Worst-case scenario temperature measurement results

A working hypothesis during the PhD has been that photovoltaic modules *routinely* experience intra-module temperature variations, as a result of rapidly varying weather conditions. To an extent, the modelling work at IMEC [11] strongly pointed in this direction.

During the period of the prototype measurement set-up working (March-August 2013), its location strongly affected the measured results *and* the conclusions that could be drawn from it. On the one hand, the location near the roof edge (see also Figure 2.3) was an unrepresentative roof location, with a highly turbulent wind flow. Worse than this was the nearby pipes which emitted hot, humid air. An example of this is given in Figure A.1.

For temperature homogeneity measurements on the PV modules, the fumes coming from the pipes disturbed the measurements, particularly in winter months. This effect can be seen in Figure A.2, where the effect of human activity can be remarked between 9:30 until 19:00 approximately, with the hot air affecting the bottom of the PV module most strongly.

The weather conditions for the day shown in Figure A.2 are given in Figure A.3, where it *may have been* the case that the irradiance dips between 12:00 and 15:00 are due to hot humid air from the nearby pipes (this can not be know for sure based on the available data, but is a likely conclusion). The sensor



Figure A.1: Hot humid air from nearby pipes affecting module performance on the prototype set-up. Photograph taken on 4 March 2013, but representative for 1 April 2013 as well.

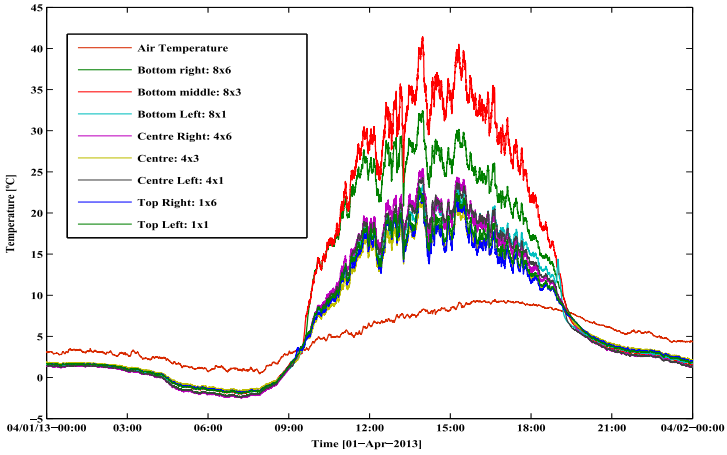

Figure A.2: Temperatures measured on multiple points of a PV module (project code PV003) on 1 April 2013.

placement notation is row x column (1x1 is top left, 8x6 is bottom right). The localised heating at the bottom of the module due to hot air coming from the nearby exhaust pipes is clearly visible. Intra-module temperature differences of up to 20 °C were measured around noon. Note that the sensors on the PV

module show almost no difference at night, indicating proper measurement.

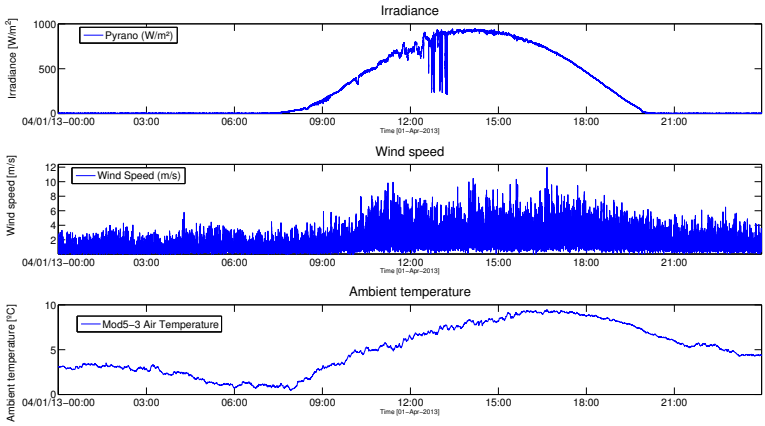

Figure A.3: Irradiance, wind speed and ambient temperature measured on 1 April 2013.

The issue with Figures A.1 to A.3 is that the results were not generally applicable, but more indicative of a worst-case placement scenario (in such a case, temperature differences of up to 20 °C in a module are possible).

The measurements performed on the second and the final iterations of the measurement set-up were therefore aimed at learning from the above experiences.

Appendix B

Additional data for the thermal constant for other wind directions

To complement the data shown in Chapter 4 (Section 4.9), the following Figure B.1 and Table B.1 were generated. Compared to the data shown in Table 4.6, the dominant wind direction is from West and South (it is more variable in direction than in the main text).

As can be observed from the data in Table B.1, the modules on the Southern side of the array have a lower value of the thermal time constant τ_ϑ than on the Northern rack. The values for the Southerly modules are also more similar than the Northerly modules, in particular for the step-up of the irradiance. The heating of the modules is, as described in Section 4.9, counteracted by the wind, while the cooling of the modules sees both a removal of heat due to the reduction in irradiance and the presence of wind.

The effect of installing an array flush with the roof surface thus strongly limits cooling effects, due to the thermal mass of the roof and much reduced wind access to the back surface. Ye *et al* [139] have also looked at this issue, and classified mounting structures according to their effect on the module temperature.

Table B.1: Calculated values of the thermal time constant τ_ϑ for the modules shown in Figure B.1.

Module	Heating τ_ϑ [min:s]	Cooling τ_ϑ [min:s]	Average τ_ϑ [min:s]
PV052 (N,ref)[b]	5:56	3:16	4:36
PV053 (N)[b]	6:23	3:18	4:50
PV054 (N)[c]	7:26	3:24	5:25
PV055 (N)[c]	7:07	3:21	5:14
PV058 (S)[b]	5:02	3:29	4:15
PV059 (S)[b]	4:52	3:19	4:06
PV060 (S)[c]	5:19	3:31	4:25
PV061 (S)[c]	5:33	3:30	4:32
Average (N)	6:43	3:20	5:01
Average (S)	5:12	3:27	4:19
Average all	5:57	3:24	4:40

[a] Prevailing wind direction during measurements: W.
[b] Mono-crystalline silicon cell technology.
[c] MWT cell technology.

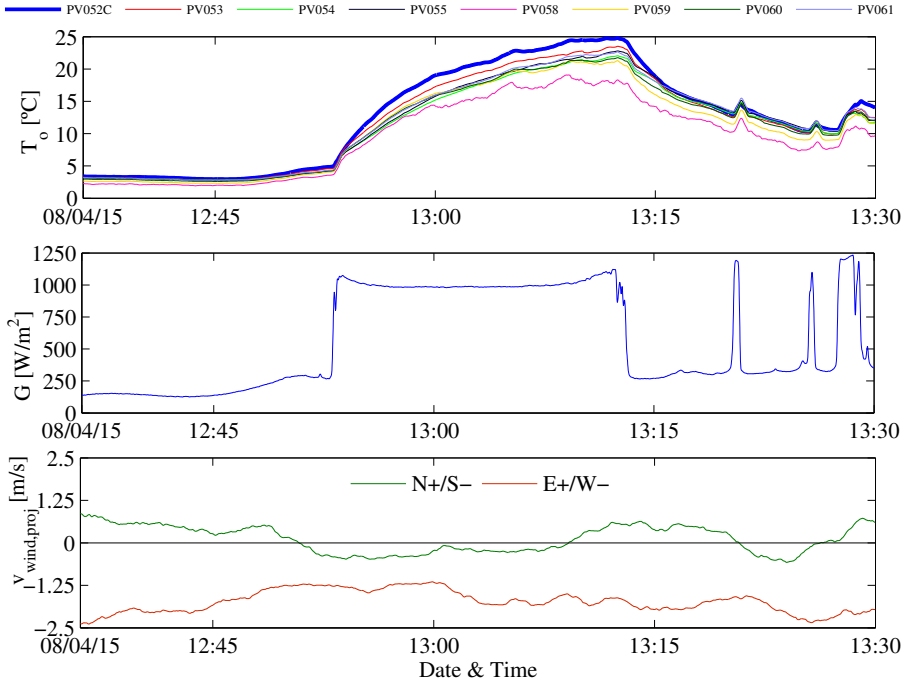

Figure B.1: Cell- and backsheet-measured temperature responses to changing irradiance and wind on 4 August 2015 for central *Smart PV* modules. Projected wind vector averaged over 5 min. Physical module lay-out: Figure 2.6.

Appendix C

Additional information for the normalised efficiency

C.1 Shading detection using daily averaged values of the normalised efficiency

Figure 5.11 in Section 5.4.5 shows how (partial) shading (or a similar anomaly) may be detected using the daily values of the PR. Similarly, the daily averaged values of the (regular and temperature-corrected) normalised efficiency η_N may also be used for this purpose. The daily averaged value of the η_N will generally be lower than the daily PR value, as the (normalised) efficiency below $\sim$100 W/m^2 contributes *negatively* to the daily average, whereas the energy for these low irradiance values still contribute *positively* to the PR.

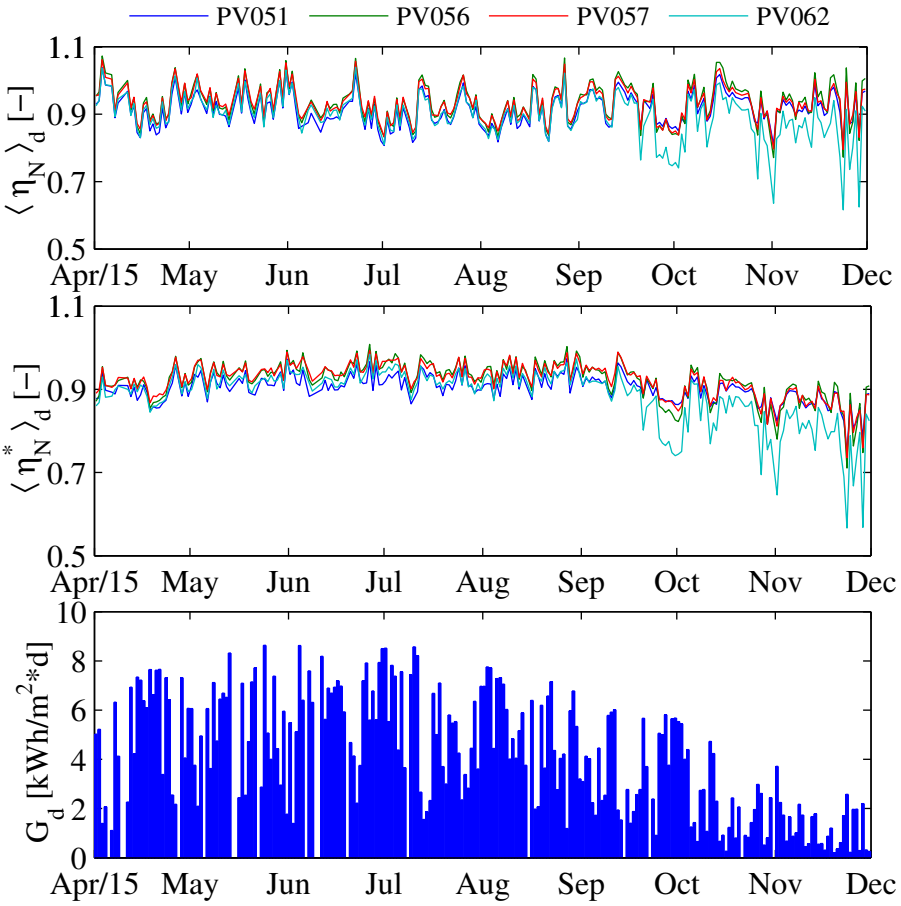

Figure C.1: Daily averaged η_N and η_N^*, April-November 2015, with morning shading from early September. Days with errors in data have been removed in all subplots. Figure 5.11 mirrors this figure, using the PR.

C.2 Determination of the system temperature coefficient of power

The comparison between using a reference cell or pyranometer to calculate the normalised efficiency η_N and then the system temperature coefficient of power γ_{syst} is a topic worthy of more study. Below are the reference-cell determined graphs, which mirror those shown in Chapter 5. Figure C.4 is not shown in Chapter 5, although it does point out the effect of filtering, and the need for increased filtering for reference cell data, versus pyranometer data.

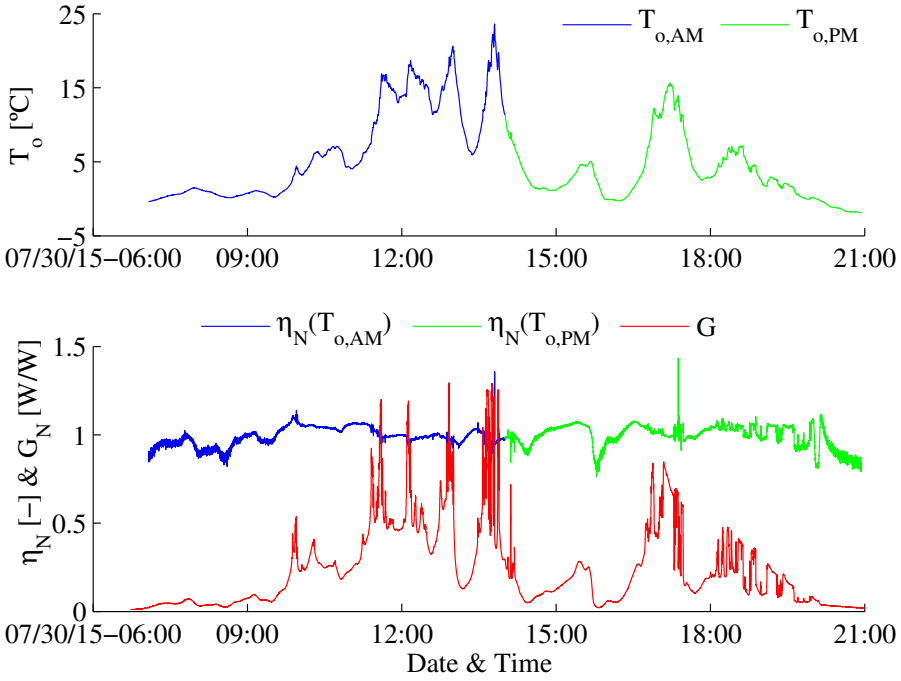

Figure C.2: Over-temperature T_o and normalised efficiency η_N for a day with multiple temperature peaks and troughs.

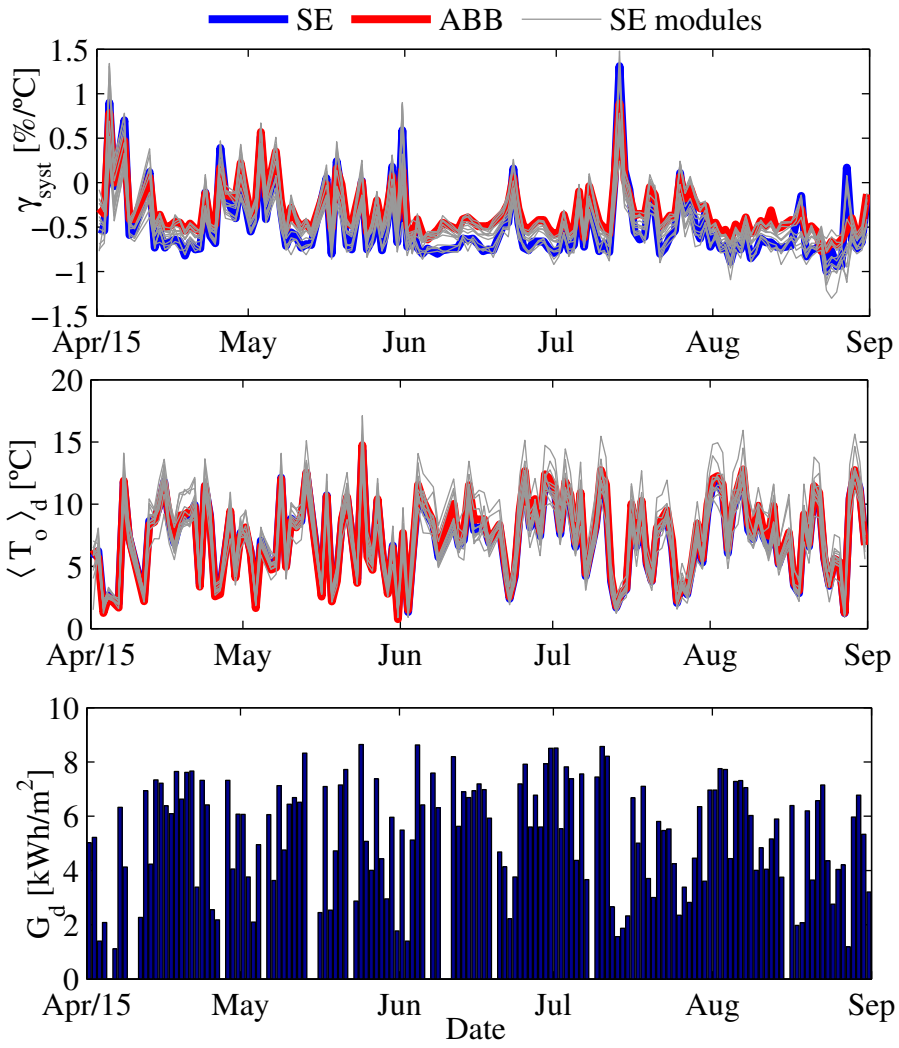

Figure C.3: *Unfiltered* daily values of γ_{syst} determined using reference cell data, T_o and G_d for *Smart PV* modules, April-August 2015. Days with errors in data have been removed in all subplots.

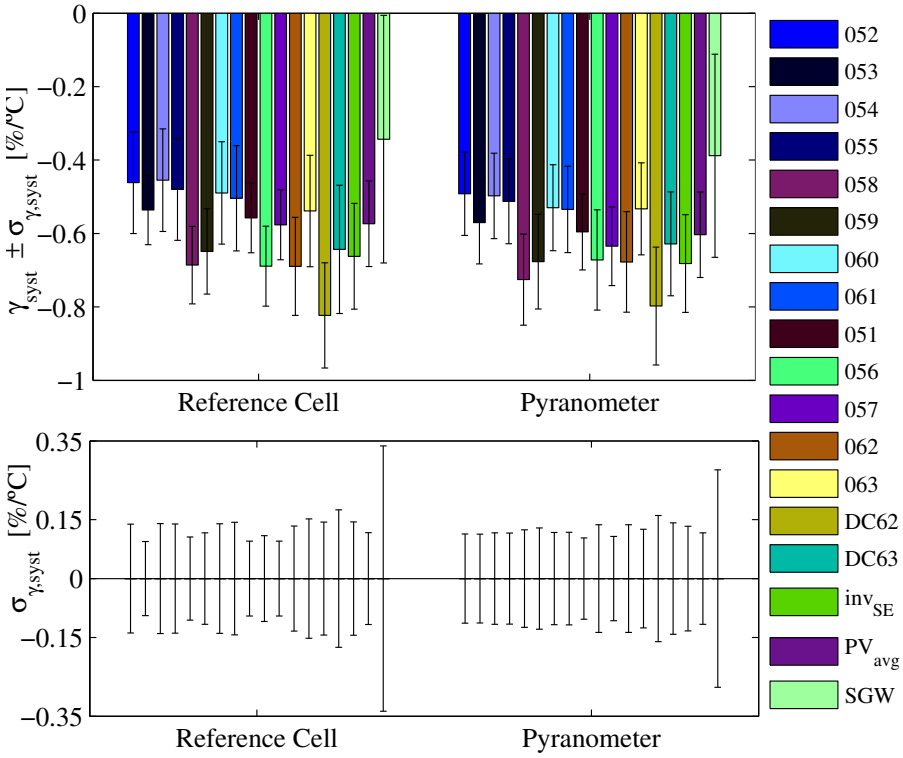

Figure C.4: Comparison of γ_{syst} values, determined using reference cell or pyranometer for April-August 2015. Filters used: T_o>5 °C and $NVI_{RC} < 0.020$ and $NVI_{pyr} < 0.025$.

Appendix D

Data and its treatment for analyses

The data of the measurement set-up is gathered and stored using LabVIEW on the dedicated PC. While LabVIEW has contributed to more rapid development of the measurement set-up[1], its use for data analysis and subsequent publication has not been as straightforward. Matlab on the other hand has more strengths on the side of data analysis and publication of graphics, on top of the benefit of working in a scripting language, rather than a visually interpreted language (LabVIEW).

The technical data management streaming (TDMS) file format developed by National Instruments combines the benefits of human-readable files (e.g.) and binary files (less data overhead per file). The Weather, DC inverter and AC inverter files have their data stored in the TDMS format, which is not readily opened by Matlab. The popularity of LabVIEW and Matlab has resulted in Matlab users writing TDMS-to-MAT file converters, so that the data can be opened and interpreted by Matlab.

Whereas each file of the *Weather*, *DC Voltage and Current (Smart PV* or *Residential)* and *AC logging* VIs has the data assigned a LabVIEW timestamp per second by the same computer (as all VIs run in parallel, see also Figure 2.5), the exact moment of logging (or writing to memory) may vary slightly ($\sim$100 ms

[1]It is, among others, a powerful programme for interaction with instruments, as many of the necessary communication and data protocols are provided as (sub)VIs, which reduces or eliminates the need to program instrument-to-instrument communication, such as with the I-V curve measurements.

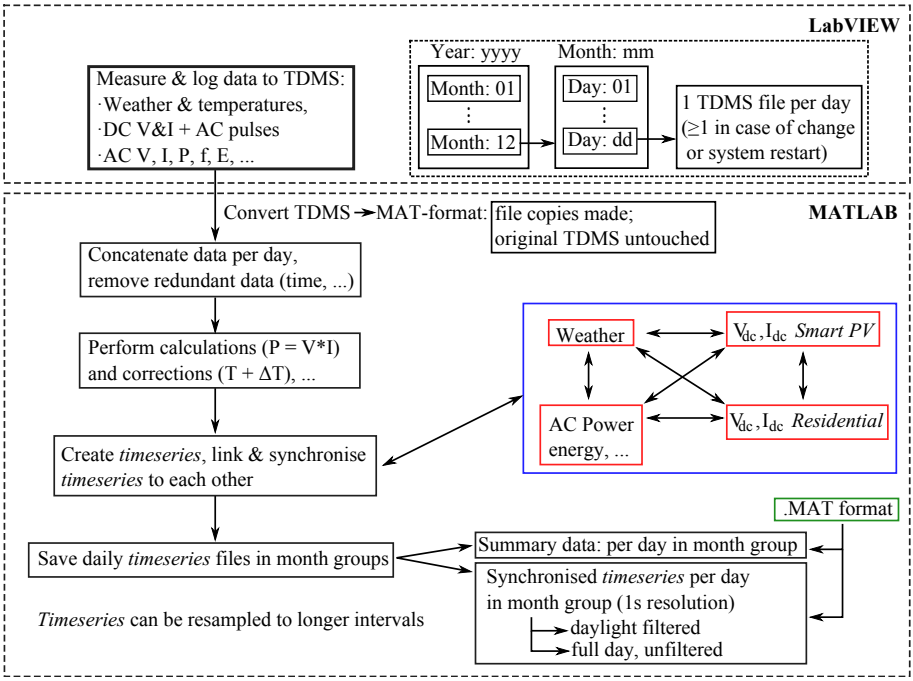

Figure D.1: Flow for TDMS to MAT files and *timeseries* conversion for analyses. TDMS to Matlab converter: web link.

to 400 ms). To ensure proper synchronisation and comparison, the Matlab *timeseries* format is used, which encodes the time and the data together. The Matlab *timeseries* format allows multiple *timeseries* to be synchronised to a fixed basis, e.g. per second. An additional advantage is that it permits data to be resampled to longer intervals, and the selection (or filtering) of data according to time as well as the data contents itself. This means that filtering can be done between 10:00 and 12:00 during a day, or for an irradiance value of $200\,\mathrm{W/m^2} < G < 500\,\mathrm{W/m^2}$, as well as combinations of these.

The TDMS files may be opened individually, using a free Excel plug-in by National Instruments. For such cases, human-readable data columns are included: Year, Month, Day, Hour, Minute, Second, DST (Daylight Saving Time). These columns can be replaced by the LabVIEW *timestamp* or, by calculation, the Matlab *datenum* format. For the data analysis performed in Matlab, the data which is superfluous (i.e. the human-readable time and date columns) is removed (cf Figure D.1), as the LabVIEW *timestamp* has been recalculated to the Matlab *datenum* format.

For the latest iteration of the measurement set-up, data has been collected reliably from March 2015 for Weather, IV and the module-level DC measurements. From April 2015, the AC data is properly logged and saved as well. (The focus of many analyses is therefore for the period from April onwards). The data from the first and second iterations of the measurement set-up is available and stored, although often not converted to the Matlab-friendly data format, as the data from the latest measurement set-up iteration is more interesting for analyses.

Data losses have unfortunately occurred at a relatively high rate (one to three days of incomplete data per month, occasionally more), as a result of a variety of situations:

- Power cuts to the complete campus (this happened a few times during the PhD).
- Power cuts and works on the electrical switchboards which power the measurement set-up. Also: short-circuits on this switchboard, affecting all installations.
- A voltage dip, resulting in the Digital Multimeters or Electronic Load freezing or suffering a restart. If this happened during the I-V curve measurement sequence, this occasionally led to LabVIEW generating an error, which required human intervention and in the meantime froze all VIs, and their data gathering.
- Voltage dips or similar AC problems also led to the measurement PC restarting. Because of the contactors used, the LabVIEW VIs must be restarted with human verification.
- A loose Ethernet connection between the CompactRIO and the PC: wind gusts moved the outdoor cabinet, affecting the contact of the Ethernet connection. As LabVIEW is an events-based language, this resulted in data losses through "data skipping" (no data recorded for a period ranging from seconds to hours) or prolonged errors which again required human intervention.
- Human actions turning off all equipment, despite warnings not to do so.

While most of the above situations have been detected and solved (e.g. through the use of an UPS for the PC), data losses may still occur.

When daytime data losses have occurred, a manual "untrustworthy" flag is stored in an events worksheet, which is then used as input for the monthly summary data. By then using the trustworthy/untrustworthy flag as a data

selector, data analysis can be performed for the days which can be trusted. The untrustworthy days may still have useful information, yet the additional programming requirements (and range of possible issues for these days) lead to these being excluded from energy yield measurements, as well as any other form of long-term (more than one day) type of analysis.

A similar method is applied for loose or faulty temperature sensors as well as DC and AC logging.

Bibliography

[1] "Climate Change 2014 Synthesis Report," IPCC, Tech. Rep., 2014. [Online]. Available: http://www.ipcc.ch/pdf/assessment-report/ar5/syr/AR5_SYR_FINAL_All_Topics.pdf

[2] J. S. Pal and E. A. B. Eltahir, "Future temperature in southwest asia projected to exceed a threshold for human adaptability," *Nature Clim. Change*, October 2015.

[3] M. Kelly. (1992, October 31) The 1992 Campaign: The Democrats – Clinton and Bush Compete to Be Champion of Change; Democrat Fights Perceptions of Bush Gain. The New York Times. [Online]. Available: http://nyti.ms/1emUItJ

[4] D. Coady, I. Parry, L. Sears, and B. Shang, "How large are global energy subsidies?" IMF, Working Paper, May 2015. [Online]. Available: https://www.imf.org/external/pubs/ft/wp/2015/wp15105.pdf

[5] "Renewable energy cost analysis - solar photovoltaics," IRENA, Working Paper, June 2012, volume 1: Power Sector Issue 4/5. [Online]. Available: http://www.irena.org/DocumentDownloads/Publications/RE_Technologies_Cost_Analysis-SOLAR_PV.pdf

[6] F. Niehörster, M. Aichinger, R. Murnane, N. Ranger, and S. Surminski, "Warming of the oceans and implications for the (re)insurance industry," The Geneva Association, Tech. Rep., June 2013. [Online]. Available: https://www.genevaassociation.org/media/616661/ga2013-warming_of_the_oceans.pdf

[7] "Sunpower 2015 analyst day," Sunpower Corporation, Tech. Rep., 2015. [Online]. Available: http://files.shareholder.com/downloads/SPWR/1022777484x0x861169/C9FCA34A-DC93-41DC-8CC8-9D52F1ACB49D/2015_SPWR_Analyst_Day.pdf

[8] T. Roessler and K. Sauer, "Modeling of pv module power degradation to evaluate performance warranty risks," in *27th European Photovoltaic Solar Energy Conference and Exhibition*. WIP, 2012, pp. 3142–3147.

[9] B. V. Mihaylov, J. W. Bowers, T. R. Betts, R. Gottschalg, T. Krametz, R. Leidl, K. Berger, S. Zamini, N. Dekker, G. Graditi *et al.*, "Results of the Sophia module intercomparison part-1: STC, low irradiance conditions and temperature coefficients measurements of c-Si technologies," in *29th European Photovoltaic Conference and Exhibition*. WIP, 2014, pp. 2443 – 2448.

[10] D. Kahneman and A. Tversky, "Choices, values, and frames." *American psychologist*, vol. 39, no. 4, p. 341, 1984.

[11] V. Dubey, J. Govaerts, F. Catthoor, H. Oprins, U. Chatterjee, B. Lefevre, and K. Baert, "3d thermal model with high spatial and temporal resolution," in *27th European Photovoltaic Solar Energy Conference*. WIP, 2012, pp. 1339 – 1342.

[12] "Evaluation of measurement data —- Guide for the expression of uncertainty in measurement." BIPM, IEC, IFCC, ILAC, IUPAC, IUPAP, ISO and OIML, Tech. Rep., 2008.

[13] T. Huld, G. Friesen, A. Skoczek, R. P. Kenny, T. Sample, M. Field, and E. D. Dunlop, "A power-rating model for crystalline silicon PV modules," *Solar Energy Materials and Solar Cells*, vol. 95, no. 12, pp. 3359–3369, 2011.

[14] N. Taylor, Ed., *Guidelines for PV Power Measurement in Industry*, 2010, EUR 24359 EN.

[15] "Iec61829:1995: Crystalline silicon photovoltaic (pv) array - on-site measurement of i-v characteristics," IEC, standard (withdrawn on 22-10-2015), March 1995.

[16] "IEC 61724: Photovoltaic system performance monitoring: Guidelines for measurement, data exchange and analysis," IEC, Standard, 1998.

[17] Y. Tsuno, Y. Hishikawa, and K. Kurokawa, "Modeling of the I–V curves of the PV modules using linear interpolation/extrapolation," *Solar Energy Materials and Solar Cells*, vol. 93, no. 6, pp. 1070–1073, 2009.

[18] V. L. Brano, A. Orioli, and G. Ciulla, "On the experimental validation of an improved five-parameter model for silicon photovoltaic modules," *Solar Energy Materials and Solar Cells*, vol. 105, pp. 27–39, 2012.

[19] M. M. Mahmoud, "Transient analysis of a PV power generator charging a capacitor for measurement of the I–V characteristics," *Renewable Energy*, vol. 31, no. 13, pp. 2198–2206, 2006.

[20] E. Q. B. Macabebe, C. J. Sheppard, and E. E. van Dyk, "Parameter extraction from i–v characteristics of pv devices," *Solar Energy*, vol. 85, no. 1, pp. 12–18, 2011.

[21] C. R. S. Reinoso, D. H. Milone, and R. H. Buitrago, "Simulation of photovoltaic centrals with dynamic shading," *Applied Energy*, vol. 103, pp. 278–289, 2013.

[22] A. Dolara, G. C. Lazaroiu, S. Leva, and G. Manzolini, "Experimental investigation of partial shading scenarios on PV (photovoltaic) modules," *Energy*, vol. 55, pp. 466–475, 2013.

[23] D. C. Jordan and S. Kurtz, "Analytical improvements in PV degradation rate determination," in *Photovoltaic Specialists Conference (PVSC), 2010 35th IEEE*. IEEE, 2010, pp. 002 688–002 693.

[24] "IEC 61215: Crystalline silicon terrestrial photovoltaic (pv) modules – design qualification and type approval," IEC, Standard Ed 2.0, 2005.

[25] "IEC 61646: Thin-film terrestrial photovoltaic (pv) modules – design qualification and type approval," IEC, Standard Ed 2.0, 2008.

[26] "IEC 60904-1: Measurement of photovoltaic current-voltage characteristics," IEC, Standard, 2006.

[27] "IEC 60891:2009: Photovoltaic devices – procedures for temperature and irradiance corrections to measured i-v characteristics," IEC, Standard, 2009.

[28] H. Müllejans, W. Zaaiman, and R. Galleano, "Analysis and mitigation of measurement uncertainties in the traceability chain for the calibration of photovoltaic devices," *Measurement Science and Technology*, vol. 20, no. 7, 2009.

[29] J. Kurnik, M. Jankovec, K. Brecl, and M. Topič, "Outdoor testing of PV module temperature and performance under different mounting and operational conditions," *Solar Energy Materials and Solar Cells*, vol. 95, no. 1, pp. 373–376, 2011.

[30] R. Eke, A. S. Kavasoglu, and N. Kavasoglu, "Design and implementation of a low-cost multi-channel temperature measurement system for photovoltaic modules," *Measurement*, vol. 45, no. 6, pp. 1499–1509, 2012.

[31] E. Van Dyk, A. Gxasheka, and E. Meyer, "Monitoring current–voltage characteristics and energy output of silicon photovoltaic modules," *Renewable Energy*, vol. 30, no. 3, pp. 399–411, 2005.

[32] J. Kurnik, M. Jankovec, K. Brecl, and M. Topič, "Development of outdoor photovoltaic module monitoring system," *Informacije MIDEM*, vol. 38, no. 2, pp. 75–80, 2008.

[33] A. Imenes, G. Yordanov, O. Midtgard, and T. Saetre, "Development of a test station for accurate in situ IV curve measurements of photovoltaic modules in southern Norway," in *Photovoltaic Specialists Conference*. IEEE, 2011, pp. 003 153–003 158.

[34] D. Craciun, V. Helmbrecht, S. Tselepis, A. Kyritsis, N. Hatziargyriou, K. Latoufis, S. Misara, P. Funtan, P. Strauss, A. Ellis, and R. Bründlinger, "Harmonised procedures on photovoltaic modules long-term energy yield measurements and performance evaluation under outdoor conditions," in *27th European Photovoltaic Solar Energy Conference and Exhibition*. WIP, 2013.

[35] "Ni 9144 user guide and specifications," National Instruments, Manual, 2013. [Online]. Available: http://www.ni.com/pdf/manuals/372498g.pdf

[36] "Contactor, 3p+1n/o, 3kw/400v/ac3," Eaton Industries GmbH, Data sheet, 2015. [Online]. Available: http://datasheet.moeller.net/Eaton-276570-DILM7-10(VDC)-en_GB.pdf?model=276570&locale=en_GB&_lt=&type=pdf

[37] "Ni 9472/9474 operating instructions and specifications," National Instruments, Manual, 2008. [Online]. Available: http://www.ni.com/pdf/manuals/373509e.pdf

[38] A. Woyte, "Design issues of photovoltaic systems and their grid integration," Ph.D. dissertation, KU Leuven, 2003.

[39] "Se3000-4000-16a inverter," SolarEdge, Data sheet, 2014. [Online]. Available: http://www.solaredge.com/files/pdfs/products/inverters/se-single-phase-16a-inverter-datasheet.pdf

[40] "Micro-0.25-0.3-0.3HV data sheet," ABB, Datasheet, 2015. [Online]. Available: http://new.abb.com/power-converters-inverters/solar/micro/micro

[41] "SG3KTL-M/SG4KTL-M/SG4K6TL/SG5KTL-M PV Grid-Connected Inverter," Sungrow Power Supply Co., Ltd., User Manual, 2015. [Online]. Available: http://sungrowpower.com/sungrow-english/down_file.php?type=product&item=190

[42] "Single-phase energy meter WSZ12B-32A with MID approval," Eltako GmbH, Data sheet, 2009. [Online]. Available: http://www.eltako.com/fileadmin/downloads/en/_bedienung/WSZ12D-32A_28032612-3_gb.pdf

[43] "Single-phase energy meter WSZ12DE-32A without approval," Eltako GmbH, Data sheet, 2008. [Online]. Available: http://www.eltako.com/fileadmin/downloads/en/_bedienung/WSZ12E-32A_4861_gb.pdf

[44] "PM3200 Series," Schneider Electric, User manual DCOA0006EN-04, 2014. [Online]. Available: http://download.schneider-electric.com/files?p_File_Id=792030648&p_File_Name=DOCA0006EN-04.pdf

[45] "NI 9422 operating instructions and specifications," National Instruments, Manual, June 2009. [Online]. Available: http://www.ni.com/pdf/manuals/374183c.pdf

[46] J. Kleissl, Ed., *Solar Energy Forecasting and Resource Assessment*. Academic Press, 2013.

[47] R. Perez, R. Stewart, C. Arbogast, R. Seals, and J. Scott, "An anisotropic hourly diffuse radiation model for sloping surfaces: description, performance validation, site dependency evaluation," *Solar energy*, vol. 36, no. 6, pp. 481–497, 1986.

[48] D. Yang, Z. Ye, A. M. Nobre, H. Du, W. M. Walsh, L. I. Lim, and T. Reindl, "Bidirectional irradiance transposition based on the perez model," *Solar Energy*, vol. 110, pp. 768–780, 2014.

[49] M. Sengupta, P. Gotseff, and T. Stoffel, "Evaluation of photodiode and thermopile pyranometers for photovoltaic applications," in *27th European Photovoltaic Solar Energy Conference*. WIP, 2012, pp. 3705–3708.

[50] A. Woyte, M. Richter, D. Moser, N. Reich, M. Green, S. Mau, and H. G. Beyer, *Analytical Monitoring of Grid-connected Photovoltaic Systems*, 2014, Report IEA-PVPS T13-03:2014. [Online]. Available: http://www.iea-pvps.org/index.php?id=95&eID=dam_frontend_push&docID=2307

[51] M. Zehner, M. Hartmann, J. Weizenbeck, T. Gratzl, T. Weigl, B. Mayer, G. Wirth, M. Krawczynski, T. Betts, R. Gottschalg *et al.*, "Systematic analysis of meteorological irradiation effects," in *25th European Photovoltaic Solar Energy Conference*. WIP, 2010, pp. 4545–4548.

[52] WMO, *Guide to Meteorological Instruments and Methods of Observation*, 7th ed., 2008. [Online]. Available: https://www.wmo.int/pages/prog/gcos/documents/gruanmanuals/CIMO/CIMO_Guide-7th_Edition-2008.pdf

[53] "CM 11 Pyranometer / CM 14 Albedometer - Manual," Kipp & Zonen B.V., Manual, 2005. [Online]. Available: http://www.kippzonen.com/Download/48/CM-11-Pyranometer-CM-14-Albedometer-Manual

[54] M. Sengupta, A. Habte, S. Kurtz, A. Dobos, S. Wilbert, E. Lorenz, T. Stoffel, D. Renné, C. Gueymard, D. Myers, S. Wilcox, P. Blanc, and R. Perez, "Best practices handbook for the collection and use of solar resource data for solar energy applications," NREL, Technical Report NREL/TP-5D00-63112, February 2015. [Online]. Available: http://www.nrel.gov/docs/fy15osti/63112.pdf

[55] "Manual - Pyranometers - CMP series - English," Kipp & Zonen B.V., Manual, 2005. [Online]. Available: http://www.kippzonen.com/Download/72/Manual-Pyranometers-CMP-series-English

[56] L. Dunn, M. Gostein, and K. Emery, "Comparison of pyranometers vs. pv reference cells for evaluation of pv array performance," in *38th IEEE Photovoltaic Specialists Conference (PVSC)*, 2012, pp. 002 899–002 904.

[57] "Si-Sensoren Flyer," Ingenieurbüro Mencke & Tegtmeyer GmbH, Data sheet. [Online]. Available: http://www.imt-solar.com/fileadmin/docs/en/products/Si-Sensoren_Flyer_E.pdf

[58] N. H. Reich, B. Mueller, A. Armbruster, W. G. Sark, K. Kiefer, and C. Reise, "Performance ratio revisited: is PR> 90% realistic?" *Progress in Photovoltaics: Research and Applications*, vol. 20, no. 6, pp. 717–726, 2012.

[59] "Temperature-sensor *compact*," Thies Clima, Datasheet, 2012. [Online]. Available: http://www.thiesclima.com/electrical_transmitters.html#TemperatureSensorcompact

[60] "Omegafilm Platinum RTD sensors," OMEGA Engineering Inc., Datasheet, April 2012, Model F2020-100-1/3B. [Online]. Available: http://www.omega.nl/Temperature/pdf/F1500_F2000_F4000.pdf

[61] "Wind sensor first class advanced," Thies Clima, Datasheet, 2012. [Online]. Available: http://www.thiesclima.com/windsensor_first_class_e.html

[62] "Windvane type DIR21+," Ekopower, Datasheet, 2012. [Online]. Available: http://www.ekopower.nl/pdf/DIR21.pdf

[63] "34410a and 34411a multimeters - data sheet," Keysight Technologies, Data sheet, April 2013. [Online]. Available: http://literature.cdn.keysight.com/litweb/pdf/5989-3738EN.pdf?id=737854

[64] "Solar module yield measurement," Photon laboratory GmbH, Brochure, 2014. [Online]. Available: http://www.photon.info/upload/Lab_Yield_Measurement_Brochure_EN_2014_4191.pdf

[65] Photon laboratory GmbH. (2015) Solar module yield measurement "Germany". [Online]. Available: http://www.photon.info/photon_lab_modul_ertragsm_en.photon?ActiveID=1289

[66] T. Glotzbach and J. Kirchhof, "Novel measuring system for long term evaluation of photovoltaic modules," in *24th European Photovoltaic Solar Energy Conference and Exhibition*. WIP, 2009, pp. 3660 – 3663.

[67] A. Dolara, G. C. Lazaroiu, S. Leva, and G. Manzolini, "Experimental investigation of partial shading scenarios on pv (photovoltaic) modules," *Energy*, vol. 55, pp. 466–475, 2013.

[68] M. Bliss, T. R. Betts, R. Gottschalg, and D. Infield, "Improved outdoor monitoring of photovoltaic modules," 2005. [Online]. Available: https://dspace.lboro.ac.uk/2134/17772

[69] W. Durisch, D. Tille, A. Wörz, and W. Plapp, "Characterisation of photovoltaic generators," *Applied Energy*, vol. 65, no. 1, pp. 273–284, 2000.

[70] H. Belmili, S. M. A. Cheikh, M. Haddadi, and C. Larbes, "Design and development of a data acquisition system for photovoltaic modules characterization," *Renewable Energy*, vol. 35, no. 7, pp. 1484–1492, 2010.

[71] N. Forero, J. Hernández, and G. Gordillo, "Development of a monitoring system for a pv solar plant," *Energy Conversion and Management*, vol. 47, no. 15, pp. 2329–2336, 2006.

[72] "DS-1000 PV I-V Curve Tracer," Daystar Inc., Data sheet, 2014. [Online]. Available: http://www.daystarpv.com/TracerBroc.pdf

[73] "Kepco bop family brochure p/n 146-1971," Kepco, Inc, Brochure, 2011. [Online]. Available: http://www.kepcopower.com/1461971.pdf

[74] "Using kepco bop 1kw for solar device testing," Kepco, Inc, Application Note, 2009. [Online]. Available: http://www.kepcopower.com/bop-solar.pdf

[75] "N3300 series dc electronic loads data sheet," Keysight Technologies, Data sheet, August 2014. [Online]. Available: http://literature.cdn.keysight.com/litweb/pdf/5980-0232E.pdf?id=1000070562:epsg:dow

[76] D. C. Jordan and S. R. Kurtz, "Photovoltaic degradation rates – an analytical review," *Progress in photovoltaics: Research and Applications*, vol. 21, no. 1, pp. 12–29, 2013.

[77] "IEC 61853–1: Photovoltaic (PV) module performance testing and energy rating," IEC, Standard Ed 1.0, 2011.

[78] H. Goverde, B. Herteleer, D. Anagnostos, G. Köse, D. Goossens, B. Aldaladi, J. Govaerts, K. Baert, F. Catthoor, J. Driesen *et al.*, "Energy yield prediction model for PV modules including spatial and temporal effects," in *29th European Photovoltaic Solar Energy Conference*. WIP, 2014, pp. 3292–3296.

[79] "Op250-lv / op300-mv / op400-mv / op400-ev power optimizers specifications," SolarEdge, Data sheet, 2013. [Online]. Available: http://www.solaredge.com/files/pdfs/products/power-optimizers/op-us-application-note.pdf

[80] "Msx-110 and msx-120 photovoltaic modules," Solarex, Data sheet, 1999.

[81] A. Woyte, R. Belmans, J. Nijs, L. Verbeeck, and J. Lemmens, "Optimised application of grid-connected photovoltaics," in *Proceedings of Power-Gen 2001*, p. 16.

[82] "Ni 9205 operating instructions and specifications," National Instruments, Manual, 2008. [Online]. Available: http://www.ni.com/pdf/manuals/374188d.pdf

[83] "Data sheet - acpl-c78a, acpl-c780, acpl-c784, miniature isolation amplifiers," Avago Technologies, Data sheet, August 2008. [Online]. Available: http://www.avagotech.com/docs/AV02-1436EN

[84] "EVBD-ACPL-C87B/C87A/C870 Isolated Voltage Sensor Evaluation Board," Avago Technologies, Data sheet, November 2013. [Online]. Available: http://docs.avagotech.com/docs/AV02-4293EN

[85] "INA 337, 338: High-Temperature, Precision, Instrumentation Amplifier," Texas Instruments, Data sheet, June 2002. [Online]. Available: http://www.ti.com/lit/gpn/ina337

[86] "CSN Series Magnetoresistive (MR) Closed Loop Current Sensor," Honeywell, Data sheet, June 2010. [Online]. Available: http://sensing.honeywell.com/index.php?ci_id=49807

[87] "Digital multimeters — tektronix dmm4050 and dmm4040," Tektronix, Data sheet, 2013. [Online]. Available:

http://www.tek.com/sites/tek.com/files/media/media/resources/Tektronix-DMM4050-and-DMM4040-Digital-Multimeter-Datasheet-8.pdf

[88] "EA-PSI 8000 2u 640w-3000w programmable laboratory power supplies," EA Elektro-Automatik GmbH & Co. KG, Data sheet, 2013. [Online]. Available: EAELEKTRO-AUTOMATIKGMBH&CO.KG

[89] H. Castrup, "Estimating and combining uncertainties," in *8th Annual International Test And Evaluation Association Instrumentation Workshop*, 2004. [Online]. Available: http://www.isgmax.com/Articles_Papers/Estimating%20and%20Combining%20Uncertainties.pdf

[90] Evaluating uncertainty components: Type B. NIST. [Online]. Available: http://physics.nist.gov/cuu/Uncertainty/typeb.html

[91] G. E. Box, J. S. Hunter, and W. G. Hunter, *Statistics for Experimenters: Design, Discovery, and Innovation*, 2nd ed. John Wiley & Sons, Inc., 2005.

[92] Hawai'i Natural Energy Institute, "Report on pv test sites and test protocols," 2012. [Online]. Available: http://www.hnei.hawaii.edu/node/338

[93] "Accuracy of the solaredge monitoring system," SolarEdge, Technical Note, March 2014.

[94] A. M. Al-Sabounchi, S. A. Yalyali, and H. A. Al-Thani, "Design and performance evaluation of a photovoltaic grid-connected system in hot weather conditions," *Renewable Energy*, vol. 53, pp. 71–78, 2013.

[95] E. Fuentealba, P. Ferrada, F. Araya, A. Marzo, C. Parrado, and C. Portillo, "Photovoltaic performance and LCoE comparison at the coastal zone of the Atacama Desert, Chile," *Energy Conversion and Management*, vol. 95, pp. 181 – 186, 2015. [Online]. Available: http://www.sciencedirect.com/science/article/pii/S0196890415001491

[96] G. Makrides, B. Zinsser, M. Schubert, and G. E. Georghiou, "Energy yield prediction errors and uncertainties of different photovoltaic models," *Progress in Photovoltaics: Research and Applications*, vol. 21, no. 4, pp. 500–516, 2013.

[97] "Measurement accuracy - Energy values and efficiency for PV Inverter Sunny Boy and Sunny Mini Central," SMA, Technical Information Messgenau-UEN092520, 2009. [Online]. Available: http://files.sma.de/dl/7418/Messgenau-UEN092520.pdf

[98] S. M. Wilcox and D. R. Myers, "Evaluation of radiometers in full time use at the national renewable energy laboratory solar radiation research laboratory," 2008. [Online]. Available: http://www.nrel.gov/docs/fy09osti/44627.pdf

[99] M. C. Di Vincenzo and D. Infield, "Detailed pv array model for non-uniform irradiance and its validation against experimental data," *Solar Energy*, vol. 97, pp. 314–331, 2013.

[100] S. Krauter and A. Preiss, "Comparison of module temperature measurement methods," in *Photovoltaic Specialists Conference (PVSC)*. IEEE, 2009, pp. 000 333–000 338.

[101] V. Benda, Z. Machacek, and K. Stanek, "Non-uniform temperature distribution on a photovoltaic field under real operating conditions," in *Solar 2007: 45th ANZSES Annual Conference*, October 2007. [Online]. Available: http://solar.org.au/papers/07papers/Paper44.pdf

[102] M. Koehl, M. Heck, S. Wiesmeier, and J. Wirth, "Modeling of the nominal operating cell temperature based on outdoor weathering," *Solar Energy Materials and Solar Cells*, vol. 95, no. 7, pp. 1638–1646, 2011.

[103] M. A. García and J. Balenzategui, "Estimation of photovoltaic module yearly temperature and performance based on nominal operation cell temperature calculations," *Renewable Energy*, vol. 29, no. 12, pp. 1997–2010, 2004.

[104] F. Mavromatakis, E. Kavoussanaki, F. Vignola, and Y. Franghiadakis, "Measuring and estimating the temperature of photovoltaic modules," *Solar Energy*, vol. 110, pp. 656–666, 2014.

[105] D. Faiman, "Assessing the outdoor operating temperature of photovoltaic modules," *Progress in Photovoltaics: Research and Applications*, vol. 16, no. 4, pp. 307–315, 2008.

[106] J.-A. Jiang, J.-C. Wang, K.-C. Kuo, Y.-L. Su, J.-C. Shieh, and J.-J. Chou, "Analysis of the junction temperature and thermal characteristics of photovoltaic modules under various operation conditions," *Energy*, vol. 44, no. 1, pp. 292–301, 2012.

[107] M. Mattei, G. Notton, C. Cristofari, M. Muselli, and P. Poggi, "Calculation of the polycrystalline pv module temperature using a simple method of energy balance," *Renewable Energy*, vol. 31, no. 4, pp. 553–567, 2006.

[108] E. Skoplaki, A. Boudouvis, and J. Palyvos, "A simple correlation for the operating temperature of photovoltaic modules of arbitrary mounting,"

Solar Energy Materials and Solar Cells, vol. 92, no. 11, pp. 1393–1402, 2008.

[109] E. Skoplaki and J. Palyvos, "On the temperature dependence of photovoltaic module electrical performance: A review of efficiency/power correlations," *Solar Energy*, vol. 83, no. 5, pp. 614–624, 2009.

[110] R. Ross Jr, "Interface design considerations for terrestrial solar cell modules," in *12th Photovoltaic Specialists Conference*, vol. 1, 1976, pp. 801–806.

[111] E. Skoplaki and J. Palyvos, "Operating temperature of photovoltaic modules: A survey of pertinent correlations," *Renewable Energy*, vol. 34, no. 1, pp. 23–29, 2009.

[112] "En 50380: Datasheet and nameplate information for photovoltaic modules," CENELEC, European Standard EN 50380, March 2003.

[113] D. T. Lobera and S. Valkealahti, "Dynamic thermal model of solar pv systems under varying climatic conditions," *Solar energy*, vol. 93, pp. 183–194, 2013.

[114] D. King, W. Boyson, and J. Kratochvill, "Photovoltaic array performance model." [Online]. Available: http://prod.sandia.gov/techlib/access-control.cgi/2004/043535.pdf

[115] M. Jankovec and M. Topič, "Intercomparison of temperature sensors for outdoor monitoring of photovoltaic modules," *Journal of Solar Energy Engineering*, vol. 135, no. 3, p. 031012, 2013.

[116] M. A. M. Bohórquez, J. M. Enrique Gómez, and J. M. Andújar Márquez, "A new and inexpensive temperature-measuring system: Application to photovoltaic solar facilities," *Solar energy*, vol. 83, no. 6, pp. 883–890, 2009.

[117] B. Herteleer, B. Morel, B. Huyck, J. Cappelle, R. Appels, B. Lefevre, F. Catthoor, and J. Driesen, "High frequency outdoor measurements of photovoltaic modules using an innovative measurement set-up," in *29th European Photovoltaic Solar Energy Conference*. WIP, September 2014, pp. 2700 – 2706.

[118] A. Jones and C. Underwood, "A thermal model for photovoltaic systems," *Solar Energy*, vol. 70, no. 4, pp. 349–359, 2001.

[119] S. Armstrong and W. Hurley, "A thermal model for photovoltaic panels under varying atmospheric conditions," *Applied Thermal Engineering*, vol. 30, no. 11–12, pp. 1488 – 1495, 2010.

[120] M. Prorok, W. Kolodenny, T. Zdanowicz, R. Gottschalg, and D. Stellbogen, "Reducing uncertainty of pv module temperature determination based on analysis using data gained during outdoor monitoring," in *23rd European Photovoltaic Solar Energy Conference, Valencia, Spain, September*. WIP, 2008, pp. 2865 – 2871.

[121] G. TamizhMani, K. Paghasian, J. Kuitche, M. G. Vemula, and G. Sivasubramanian, "Photovoltaic module power rating per iec 61853-1 standard–a study under natural sunlight," Solar America Board for Codes and Standards, Report, 2011. [Online]. Available: www.solarabcs.org/ratingper61853

[122] R. P. Kenny, D. Viganó, E. Salis, G. Bardizza, M. Norton, H. Müllejans, and W. Zaaiman, "Power rating of photovoltaic modules including validation of procedures to implement iec 61853-1 on solar simulators and under natural sunlight," *Progress in Photovoltaics: Research and Applications*, vol. 21, no. 6, pp. 1384–1399, 2013.

[123] E. Lorenzo, "Quality assurance of pv plants connected to the grid," in *27th European Photovoltaic Conference and Exhibition Parallel Event: Grid-connected PV systems: Field testing, performance monitoring, and energy storage*, September 2014. [Online]. Available: https://www.photovoltaic-conference.com/images/stories/29th/5_parallelevents/grid-connected/02_Eduardo_LORENZO.pdf

[124] T. Huld, R. Gottschalg, H. G. Beyer, and M. Topič, "Mapping the performance of PV modules, effects of module type and data averaging," *Solar Energy*, vol. 84, no. 2, pp. 324–338, 2010.

[125] B. Herteleer, B. Huyck, F. Catthoor, J. Driesen, and J. Cappelle, "Normalised efficiency of photovoltaic systems: Going beyond the performance ratio," *Submitted to Solar Energy*, 2015.

[126] L. Pratt and D. L. King, "The effect of uncertainty in modeling coefficients used to predict energy production using the sandia array performance model," in *35th Photovoltaic Specialists Conference (PVSC)*. IEEE, 2010, pp. 002 718–002 723.

[127] D. L. King, J. A. Kratochvil, and W. E. Boyson, "Temperature coefficients for pv modules and arrays: measurement methods, difficulties, and results," in *Photovoltaic Specialists Conference, 1997., Conference Record of the Twenty-Sixth IEEE*. IEEE, 1997, pp. 1183–1186.

[128] G. Tina, "A coupled electrical and thermal model for photovoltaic modules," *Journal of Solar Energy Engineering*, vol. 132, no. 2, p. 024501, 2010.

[129] "Iec 60904-5: Determination of the equivalent cell temperature (ect) of photovoltaic (pv) devices by the open-circuit voltage method," IEC, standard, February 2011.

[130] D. L. King, J. Kratochvil, M. A. Quintana, and T. McMahon, "Applications for infrared imaging equipment in photovoltaic cell, module, and system testing," in *Photovoltaic Specialists Conference, 2000.* IEEE, 2000, pp. 1487–1490.

[131] M. Köntges, S. Kurtz, C. Packard, U. Jahn, K. A. Berger, K. Kato, T. Friesen, H. Liu, and M. V. Iseghem, *Review of Failures of Photovoltaic Modules*, March 2014, Report IEA-PVPS T13-01:2014. [Online]. Available: http://www.iea-pvps.org/index.php?id=275&eID=dam_frontend_push&docID=2064

[132] G. Makrides, B. Zinsser, G. E. Georghiou, M. Schubert, and J. H. Werner, "Temperature behaviour of different photovoltaic systems installed in cyprus and germany," *Solar energy materials and solar cells*, vol. 93, no. 6, pp. 1095–1099, 2009.

[133] "Iec/ts 62446-3 ed. 1.0 grid connected photovoltaic (pv) systems - part 3: Outdoor infrared thermography of photovoltaic modules and plants," IEC, standard working draft, 2015, first Committee Draft deadline: 31 December 2015.

[134] "Ni 9212 with ni tb-9212," National Instruments, datasheet, March 2015. [Online]. Available: http://www.ni.com/pdf/manuals/374389a.pdf

[135] "Ni 9217 4-channel, 100 ohm rtd, 24-bit analog input module," National Instruments, data sheet, November 2014. [Online]. Available: http://www.ni.com/datasheet/pdf/en/ds-193

[136] "3m™vhb™tapes product information," 3M, Product Information, July 2013. [Online]. Available: http://multimedia.3m.com/mws/media/764998O/iatd-product-info.pdf

[137] "Phoenix solar - phx-160/170/175," Phoenix Solar, Data sheet, February 2010. [Online]. Available: http://www.sonnenberg-solar.de/cms/fileadmin/downloads/phx175-ger-0210_safe.pdf

[138] B. Herteleer, H. Goverde, F. Catthoor, J. Driesen, and J. Cappelle, "Spatial and temporal photovoltaic module temperature variations in outdoor conditions," in *6th World Conference on Photovoltaic Energy Conversion.*

[139] Z. Ye, A. Nobre, T. Reindl, J. Luther, and C. Reise, "On pv module temperatures in tropical regions," *Solar Energy*, vol. 88, pp. 80–87, 2013.

[140] (2015, 12) Pv performance modelling collaborative. Sandia National Laboratories. [Online]. Available: https://pvpmc.sandia.gov/

[141] H. Goverde, D. Goossens, J. Govaerts, V. Dubey, F. Catthoor, K. Baert, J. Poortmans, and J. Driesen, "Spatial and temporal analysis of wind effects on pv module temperature and performance," *Sustainable Energy Technologies and Assessments*, vol. 11, pp. 36–41, 2015.

[142] H. Goverde, D. Anagnostos, B. Herteleer, J. Govaerts, K. Baert, B. Aldalali, F. Catthoor, J. Driesen, and J. Poortmans, "Model requirements for accurate short term energy yield predictions during fast-varying weather conditions," in *31st European Photovoltaic Solar Energy Conference*. WIP, 2015, pp. 1556 – 1559.

[143] S. O. Ojo, S. Grivet-Talocia, and M. Paggi, "Model order reduction applied to heat conduction in photovoltaic modules," *Composite Structures*, vol. 119, pp. 477–486, 2015.

[144] J. Copper, A. Bruce, T. Spooner, M. Calais, T. Pryor, and M. Watt, "Australian technical guidelines for monitoring and analysing photovoltaic systems," 2013. [Online]. Available: http://apvi.org.au/wp-content/uploads/2013/11/Australian-PV-System-Monitoring-Guideline-2013.pdf

[145] J. K. Kaldellis, M. Kapsali, and K. A. Kavadias, "Temperature and wind speed impact on the efficiency of pv installations. experience obtained from outdoor measurements in greece," *Renewable Energy*, vol. 66, pp. 612–624, 2014.

[146] R. Moreton Villagra, E. Lorenzo Pigueiras, J. Leloux, and J. M. Carrillo Salinas, "Dealing in practice with hot-spots," in *29th European Photovoltaic Solar Energy Conference*, 2014, pp. 2722 – 2727.

[147] A. Dimitrios, H. Goverde, B. Herteleer, F. Catthoor, S. Dimitrios, J. Driesen, and J. Poortmans, "Demonstration and validation of an energy yield prediction model suitable for non-steady state non-uniform conditions," in *The 6th World Conference on Photovoltaic Energy Conversion*, 2014, pp. 1181–1182.

[148] J. Leloux, L. Narvarte, and D. Trebosc, "Review of the performance of residential PV systems in Belgium," *Renewable and Sustainable Energy Reviews*, vol. 16, no. 1, pp. 178–184, 2012.

[149] J. Leloux, L. Narvarte, and D. Trebosc, "Review of the performance of residential PV systems in France," *Renewable and Sustainable Energy Reviews*, vol. 16, no. 2, pp. 1369–1376, 2012.

[150] M. Gostein, "Update on Edition 2 of IEC 61724: PV System Performance Monitoring," in *Photovoltaic Module Reliability Workshop 2014: February 25-26, 2014*. [Online]. Available: http://www.nrel.gov/pv/pdfs/2014_pvmrw_84_gostein.pdf

[151] D. L. King, "More "efficient" methods for specifying and monitoring pv system performance," in *Photovoltaic Specialists Conference (PVSC), 37th IEEE*, 2011, pp. 000 219–000 224.

[152] J. S. Stein, C. W. Hansen, and M. J. Reno, "The variability index: a new and novel metric for quantifying irradiance and PV output variability," in *World Renewable Energy Forum, Denver, CO*, 2012.

[153] D. M. Willy, T. L. Acker, and R. K. Flood, "Natural variability of irradiance and power - simple variability metrics for photovoltaic power plants," in *Proceedings of 43rd ASES Annual Conference*, vol. 1, San Francisco, 2014, pp. 552–558.

[154] T. E. Hoff and R. Perez, "Quantifying PV power output variability," *Solar Energy*, vol. 84, no. 10, pp. 1782–1793, 2010.

[155] M. Lave, J. Kleissl, and J. Stein, *Solar Energy Resource Forecasting and Assessment*. Academic Press, 2013, ch. Quantifying and Simulating Solar-Plant Variability Using Irradiance Data, pp. 150–171.

[156] M. Lave, J. Kleissl, and J. S. Stein, "A wavelet-based variability model (wvm) for solar pv power plants," *Sustainable Energy, IEEE Transactions on*, vol. 4, no. 2, pp. 501–509, 2013.

[157] R. Perez and T. E. Hoff, *Solar Energy Forecasting and Resource Assessment*. Academic Press, 2013, ch. Solar Resource Variability, pp. 133–149.

[158] B. Herteleer, J. Cappelle, and J. Driesen, "Quantifying low-light behaviour of photovoltaic modules by identifying their irradiance-dependent efficiency from data sheets," in *27th European Photovoltaic Solar Energy Conference*, 2012, pp. 3714 – 3719.

[159] T. Ishii, K. Otani, T. Takashima, and S. Kawai, "Estimation of the maximum power temperature coefficients of pv modules at different time scales," *Solar Energy Materials and Solar Cells*, vol. 95, no. 1, pp. 386–389, 2011.

[160] P. I. Good and J. W. Hardin, *Common Errors in Statistics (and How to Avoid Them)*, 4th ed. John Wiley & Sons, Inc., 2012.

[161] C. P. Cameron, J. S. Stein, and C. A. Tasca, "PV performance modeling workshop summary report," Sandia National Laboratories, Report Sandia Report, SAND2011-3419, 2011. [Online]. Available: http://prod.sandia.gov/techlib/access-control.cgi/2011/113419.pdf

[162] A. G. de Montgareuil, "Description of motherpv, the new method developed at ines/cea for the assessment of the energy production of phovoltaic modules," in *22nd European Photovoltaic Conference and Exhibition*, Milan, 2007.

[163] F. Vignola, C. Grover, N. Lemon, and A. McMahan, "Building a bankable solar radiation dataset," *Solar Energy*, vol. 86, no. 8, pp. 2218–2229, 2012.

[164] J. Kleissl, Ed., *Solar Energy Forecasting and Resource Assessment*. Academic Press, 2013, ch. Bankable Solar-Radiation Datasets, pp. 98–132.

[165] K. de Brabandere, F. Assiandi, M. Richter, O. Gammoh, and A. Woyte, "PV array characterisation from operational data," in *29th European Photovoltaic Solar Energy Conference and Exhibition*, 2014.

[166] T. Nordmann, L. Clavadetscher, W. G. van Sark, and M. Green, *Analysis of Long-Term Performance of PV Systems*, 2014, Report IEA-PVPS T13-05:2014. [Online]. Available: http://www.iea-pvps.org/index.php?id=95&eID=dam_frontend_push&docID=2307

[167] R. C. Pilawa-Podgurski and D. J. Perreault, "Submodule integrated distributed maximum power point tracking for solar photovoltaic applications," *Power Electronics, IEEE Transactions on*, vol. 28, no. 6, pp. 2957–2967, 2013.

[168] M. Strobel, T. Betts, G. Friesen, H. G. Beyer, and R. Gottschalg, "Uncertainty in photovoltaic performance parameters–dependence on location and material," *Solar Energy Materials and Solar Cells*, vol. 93, no. 6, pp. 1124–1128, 2009.

Curriculum Vitae

Bert Herteleer was born in Tiraque, Bolivia on 15 September 1985. He spent most of his youth in South America and Europe in the following countries: Bolivia-England-Chile-Belgium-Ecuador-Bolivia-Ecuador. He graduated in 2004 from The British School, Quito, Ecuador with a Bilingual International Baccalaureate Diploma.

After a sabbatical year spent working in Belgium and travelling in South America, he started his studies of Civil Engineering at the University of Ghent in 2005. He switched to the Katholieke Hogeschool Sint-Lieven in 2006, from where he graduated in 2011 with an MSc in Industrial Sciences (Electrical Engineering): specialization Electrotechnics, cum laude. His Master's thesis was "Calculating and sizing of autonomous photovoltaic systems for offices in Africa", which led to two subsequent conference articles.

During his employment period (September-December 2011) at the Katholieke Hogeschool Sint-Lieven, he successfully applied for an IWT individual PhD scholarship, which started in January 2012. His PhD supervisors were prof. Jan Cappelle (ESAT-ETC, KU Leuven), prof. Johan Driesen (ESAT-ELECTA, KU Leuven) and prof. Francky Catthoor (ESAT-IMEC, KU Leuven and IMEC).

List of publications

Journal articles

1. **B. Herteleer**, B. Huyck, F. Catthoor, J. Driesen, and J. Cappelle, "Normalised efficiency of photovoltaic systems: Going beyond the performance ratio," *Submitted to Solar Energy*, 2015.

2. R. Appels, B. Lefevre, **B. Herteleer**, H. Goverde, A. Beerten, R. Paesen, K. De Medts, J. Driesen, and J. Poortmans, "Effect of soiling on photovoltaic modules," *Solar energy*, vol. 96, pp. 283–291, 2013.

Articles in conference proceedings

1. H. Goverde, D. Anagnostos, **B. Herteleer**, J. Govaerts, K. Baert, B. Aldalali, F. Catthoor, J. Driesen, and J. Poortmans, "Model requirements for accurate short term energy yield predictions during fast-varying weather conditions," in *31st European Photovoltaic Solar Energy Conference*. WIP, September 2015, pp. 1556 – 1559.

2. G. Van den Broeck, **B. Herteleer**, H. Goverde, F. Catthoor, K. Baert, and J. Driesen, "Substring-level energy-yield assessment of photovoltaic modules subject to partial shading conditions," in *31st European Photovoltaic Solar Energy Conference*. WIP, September 2015, pp. 2592 – 2597.

3. **B. Herteleer**, B. Rotthier, S. Beck, J. Rotsaert, P. Van den Bossche, and J. Cappelle, "Synergy between electric vehicles and photovoltaic installations in Belgium," in *International Electric Vehicle Symposium and Exhibition*, Goyang, Korea, May 2015.

4. **B. Herteleer**, H. Goverde, F. Catthoor, J. Driesen, and J. Cappelle, "Spatial and temporal photovoltaic module temperature variations in outdoor conditions," in *6th World Conference on Photovoltaic Energy Conversion*, Kyoto, Japan, November 2014.

5. A. Dimitrios, H. Goverde, **B. Herteleer**, F. Catthoor, S. Dimitrios, J. Driesen, and J. Poortmans, "Demonstration and validation of an energy yield prediction model suitable for non-steady state non-uniform conditions," in *The 6th World Conference on Photovoltaic Energy Conversion*, Kyoto, Japan, November 2014.

6. **B. Herteleer**, B. Morel, B. Huyck, J. Cappelle, R. Appels, B. Lefevre, F. Catthoor, and J. Driesen, "High frequency outdoor measurements of photovoltaic modules using an innovative measurement set-up," in *29th European Photovoltaic Solar Energy Conference*. WIP, September 2014, pp. 2700 – 2706.

7. H. Goverde, **B. Herteleer**, D. Anagnostos, G. Köse, D. Goossens, B. Aldaladi, J. Govaerts, K. Baert, F. Catthoor, J. Driesen *et al.*, "Energy yield prediction model for PV modules including spatial and temporal effects," in *29th European Photovoltaic Solar Energy Conference*. WIP, 2014, pp. 3292–3296.

8. **B. Herteleer**, J. Cappelle, R. Appels, B. Lefevre, J. Driesen, and F. Catthoor, "PV-battery sizing for stand-alone lighting applications," in *28th European Photovoltaic Solar Energy Conference*. WIP, 2013, pp. 4437 – 4442.

9. R. Appels, B. Lefevre, **B. Herteleer**, H. Goverde, G. Etienne, K. De Medts, J. Driesen, and J. Poortmans, "Practical implementation of spectrum splitting for solar cells," in *28th European Photovoltaic Solar Energy Conference*. WIP, 2013, pp. 309–311.

10. **B. Herteleer**, J. Cappelle, and J. Driesen, "Quantifying low-light behaviour of photovoltaic modules by identifying their irradiance-dependent efficiency from data sheets," in *27th European Photovoltaic Solar Energy Conference*, WIP, 2012, pp. 3714 – 3719.

11. **B. Herteleer**, J. Cappelle, and J. Driesen, "An autonomous photovoltaic system sizing program for office applications in Africa," *Renewable Energy & Power Quality Journal (RE&PQJ)*, 2012.

Science popularisation

1. **B. Herteleer**, B. Huyck, and J. Cappelle, "De energieopbrengst van een zonnepaneel," in *Ecotips*, vol. 5, G. Redant, Recorder, October 2014, vol. 19, pp. 6–8.



FACULTY OF ENGINEERING TECHNOLOGY
DEPARTMENT OF ELECTRICAL ENGINEERING
E& A
Gebroeders De Smetstraat 1
B-9000 Gent
bert.herteleer@kuleuven.be
http://www.kuleuven.be/eena